Origin and evolution of parental magmas associated with Pliocene-Quaternary low-silica volcanism within the Altiplano-Puna Volcanic Complex of northern Chile

Osvaldo Patricio González Maurel

Thesis Presented for the Degree of

DOCTOR OF PHILOSOPHY

in cotutelle between

Department of Geological Sciences – University of Cape Town – South Africa &

Departamento de Ciencias Geológicas – Universidad Católica del Norte – Chile

April 2020

Plagiarism declaration

I know the meaning of plagiarism and declare that all the work in the thesis, save for that is properly acknowledged, is my own.

Signed by candidate

Declaration of free licence

I hereby:

a) grant the University free licence to reproduce the above thesis in whole or in part, for the purpose of research;

b) declare that:

I. the above thesis is my own unaided work, both in conception and execution, and that apart from the normal guidance from my supervisor(s), I have received no assistance except as stated below;

II. neither the substance nor any part of the thesis has been submitted in the past, or is being, or is to be submitted for a degree at this University or at any other University, except as stated below.

I am now presenting the thesis for examination for the Degree of PhD.

Declaration on inclusion of publications

I confirm that I have been granted permission by the University of Cape Town's Doctoral Degrees Board to include the following publication(s) in my PhD thesis, and where co-authorships are involved, my co-authors have agreed that I may include the publications:

a. González-Maurel, O., le Roux, P., Godoy, B., Troll, V.R., Deegan, F.M., Menzies, A., 2019. The great escape: Petrogenesis of low-silica volcanism of Pliocene to Quaternary age associated with the Altiplano-Puna Volcanic Complex of northern Chile (21° 10′-22° 50′ S). Lithos, 346-347:105162. https://doi.org/10.1016/j.lithos.2019.105162

b. González-Maurel, O., Godoy, B., le Roux, P., Rodríguez, I., Marín, C., Menzies, A., Bertin, D., Morata, D., Vargas, M., 2019. Magmatic differentiation at La Poruña scoria cone, Central Andes, northern Chile: Evidence for assimilation during turbulent ascent processes, and genetic links with mafic eruptions at adjacent San Pedro volcano. Lithos, 338-339:128-140. https://doi.org/10.1016/j.lithos.2019.03.033

c. González-Maurel, O., Deegan, F.M., le Roux, P., Harris, C., Troll, V.R., Godoy, B., 2020. Constraining the sub-arc, parental magma composition for the giant Altiplano-Puna Volcanic Complex, northern Chile. Scientific Reports, 10(1):1-10. https://doi.org/10.1038/s41598-020-63454-1

Signature: Signed by candidate Date: 03 April 2020

Student name: Osvaldo Patricio González Maurel Student number: GNZOSV001

Dedication

To my family, especially to Camila and Nala.

Acknowledgements

This PhD thesis would not have been possible without the strong support of many people during this time. I am exceedingly grateful to my supervisors and collaborators at different stages throughout my PhD. A very special thanks to Dr. Petrus le Roux, my principal supervisor, for his guidance, enthusiasm and never-ending support, even during difficult times. Thank you, Dr. Andrew Menzies, for the unexpected invitation to the 2014 Andean field trip, where the opportunity to undertake a PhD came true. To Dr. Rodrigo Riquelme, for his role as UCN supervisor in Chile. Thank you to Dr. Benigno Godoy, for being the friend-collaborator that any PhD student should have. I also thank Dr. Frances Deegan and Prof. Valentin Troll, for encouraging this Andean work, for stimulating a novel crystal-forensic approach study, and for making me feel at home during my visits to Sweden. Prof. Chris Harris is further thanked for providing invaluable advice and expertise whose extensive work on oxygen isotopes refined this thesis.

This PhD was funded by the Comisión Nacional de Investigación Científica y Tecnológica (CONICYT-PCHA/Doctorado Nacional/2015-21150403). I would also like to thank the Department of Geological Sciences, University of Cape Town (South Africa), SERNAGEOMIN (Chile), MAINI-UCN (Chile), the Department of Earth Sciences, Uppsala University (Sweden), the Nordsim ion microprobe facility, Swedish Museum of Natural History (Sweden), and all their technical staff for precious analytical support. A special thanks to Prof. Martin J. Whitehouse, Dr. Heejin Jeon and Kerstin Lindén for technical support and assistance with SIMS procedures at Nordsim.

No tengo palabras suficientes para agradecer a mi familia en Chile y a todos mis amigos repartidos por el mundo. Cada uno de ustedes son una pieza clave en mi vida, y el resultado final de esta Tesis de Doctorado también es producto de su incondicional apoyo y cariño. Finalmente, agradezco el amor infinito recibido por mi Camila y mi Nalita, los amores de mi vida. ¡Gracias! (*Thanks!*).

[V. Surrender, Trust and Passion]

"To really feel the joy in life

You must suffer through the pain

When you surrender to the light

You can face the darkest days

If you open up your eyes

And you put your trust in love

On those cold and endless nights

You will never be alone

Passion glows within your heart

Like a furnace burning bright

Until you struggle through the dark

You'll never know that you're alive"

Illumination Theory – Dream Theater

Abstract

The Andean continental arc is built upon the thickest crust on Earth, whose eruption products reflect varying degrees of crustal assimilation. Physical interactions between mafic and felsic magmas for this arc are therefore difficult to recognize due to the differentiation of mantle-derived magma during ascent through the thickened crust and a corresponding lack of erupted primitive lavas. However, a rare concentration of less evolved rocks is located marginal to the partially molten Altiplano-Puna Magma Body (APMB) in the Altiplano-Puna Volcanic Complex of northern Chile, between 21°10'S and 22°50'S. To unravel the petrogenesis of these less evolved eruptives and their spatiotemporal assessment, this work makes use of new major and trace element data, and Sr and Nd isotope ratios of fourteen Pliocene to Quaternary volcanoes. Whole-rock compositional and Sr and Nd isotope data reveal a large degree for compositional heterogeneity (e.g. SiO_2 = 53.2 to 63.2 wt%, MgO = 1.74 to 6.08 wt%, Cr = 2 to 382 ppm, Sr = 304 to 885 ppm, $^{87}Sr/^{86}Sr$ = 0.7055 to 0.7088, and $^{143}Nd/^{144}Nd$ = 0.5122 to 0.5125). The least evolved products erupted along the periphery of the APMB and are likely equivalent to the replenishing magmas that thermally sustain the large APMB system. Here it is found that the investigated mafic to intermediate eruptives reflect mafic melt injections that underplate the APMB and escape along the sides of the large felsic body to avoid significant compositional modifications during ascent (e.g. La Poruña, San Pedro, Palpana, Chela volcanoes). Investigating these magmas therefore assist in assessing the evolution of the APMB through space and time. Additionally, individual volcanoes demonstrate that contamination of parental melts was caused by different differentiation processes (e.g. magma mixing, fractional crystallization, crustal assimilation) as a function of their spatiotemporal framework relative to the APMB and its melt fraction variation from peripheral (ca. 4 vol%) to central (up to 25 vol%) portions.

New insight into the petrological processes that governed the magmatic evolution of La Poruña, one of the centres that exhibit the least evolved eruptions in the area, is presented. La Poruña is a 100 ka scoria cone, composed of pyroclastic material and an extensive basaltic-andesite to andesite lava flow, with magmatic evolution related to the neighbouring larger San Pedro stratovolcano. New petrography, geochemistry and radiogenic isotope data describe a set of porphyritic mafic samples, comprising olivine- and pyroxene-rich rocks, with well-defined major element compositional trends, as well as trace and rare earth element characteristics, that reflect magmatic differentiation at mid-upper crustal levels. Additionally, magma mixing as well as assimilation and fractional crystallization processes acted on these La Poruña magmas. A remarkable compositional feature is the unusual reversed isotopic behaviour of increasing silica with decreasing $^{87}Sr/^{86}Sr$ compositions related to later magmatic evolution involving selective assimilation during turbulent ascent at shallow crustal levels prior to eruption, therefore differing from the broadly accepted Central Andean magmatic model.

In order to robustly model magma evolution and assimilation at subduction zones such as the Andes, the compositions of parental magmas feeding crustal magma reservoirs need to be defined. Here, new olivine and clinopyroxene oxygen isotope data from six volcanoes located at the margins of the giant APMB is presented, as these data provide robust constraints on parental magma genesis and further contamination processes. Existing olivine and pyroxene $\delta^{18}O$ values for the Central Andes are highly variable and potentially not representative of sub-arc parental compositions. However, new olivine (n = 6) and clinopyroxene (n = 12) $\delta^{18}O$ values obtained by Laser Fluorination (LF) analysis display a narrow range, with averages at 6.0‰ ± 0.2 (2σ S.D.) and 6.7‰ ± 0.3 (2σ S.D.), consistent with a common history for the investigated minerals. Additionally, the first *in-situ* Secondary Ionisation Mass Spectrometry (SIMS) oxygen isotope data for mafic mineral phases from La Poruña and Palpana is presented in order to ensure a robust parental melt $\delta^{18}O$ composition, since unlike in LF analysis fractures or mineral/melt inclusions can be avoided. Crystal cores show a density peak at

5.6‰ for both La Poruña and Palpana, whereas rims have either relatively high (6.0‰) or low (5.4‰) peaks. Intra-crystal differences (up to ± 1.1‰) in $\delta^{18}O$ values between crystal cores and rims accurately record crustal assimilation that postdate cores formation at 13 to 19 km depth. Based on the more robust dataset of LF results, a $\delta^{18}O$ value for sub-arc, parental melts of ca. 7.0‰ ± 0.2 (2σ S.D.) can be estimated. SIMS core data, on the other hand, indicate a lower, but less well-constrained parental melt value of 6.3‰ ± 0.4 (2σ S.D.).Parental melts feeding the APMB and associated volcanic centres are proposed to form in the felsic continental crust following assimilation of up to 28 vol% high $\delta^{18}O$-high $^{87}Sr/^{86}Sr$ basement rocks by mantle-derived magmas.

Contents

Chapter 1

Introduction and overview

1.1 General

A parental magma is the least-differentiated melt from which an igneous rock series begins to evolve to more differentiated magmatic products (Best, 2003). Mafic volcanic rocks, including their early phases (e.g. olivine and pyroxene), are of major interest in the study of parental magmas as they are surface evidence of magmas which left their mantle source and erupted with low degrees of differentiation (e.g. Baker et al., 1994; Danyushevsky et al., 2000; Davidson, 1996; Hildreth and Moorbath, 1988; Portnyagin et al., 2008; Wallace and Carmichael, 1999). Mafic rocks are the most abundant lithology type on Earth (i.e. basalts; Best, 2003) and potentially present in all tectonic settings. However, true basalts are scarce in some areas such as the Central Andes of South America where basaltic-andesite are commonly the least-evolved volcanic product, e.g. the Pliocene-Quaternary low-silica volcanism, found within the Altiplano-Puna Volcanic Complex province.

On the western margin of South America is the development of the Andean magmatic arc as a consequence of the subduction of Nazca and Antarctic oceanic lithosphere beneath the continental South American Plate. This magmatic arc also includes more than two hundred potentially active Quaternary volcanoes and at least twelve larger caldera systems (Stern, 2004). These volcanic structures of the Andean Cordillera are grouped into four segments, namely: the Northern (NVZ; 2°N-5°S), Central (CVZ; 14°S-28°S), Southern (SVZ; 33°S-46°S) and the Austral (AVZ; 49°S-55°S) Volcanic Zones (Fig. 1.1).

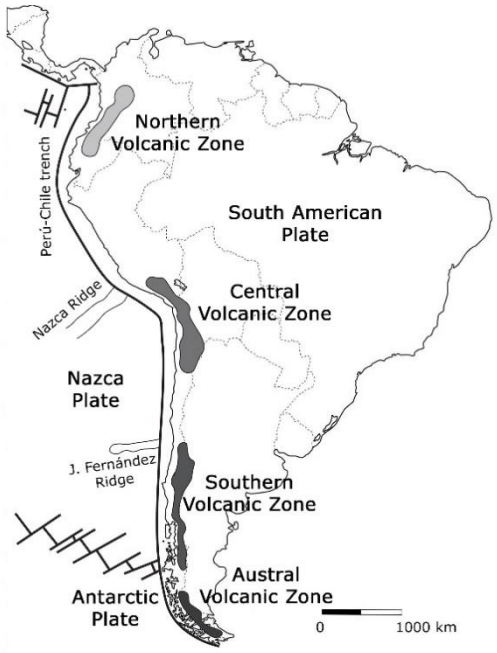

Fig. 1.1. Location of the active volcanic segments of the Andes.

The Neogene-Quaternary magmatic arc of the Central Andes is located in the Western Cordillera (Fig. 1.1), 120 km above the subducted slab, and 240-300 km east of the Peru-Chile trench (Stern, 2004). This arc is developed under a compressive regional tectonic setting over thick continental crust, reaching up to 70-74 km (Beck et al., 1996) and below which the subducting plate is dipping at an angle of ca. 17° (Hayes et al., 2012). The subduction angle is well-defined by the Wadati-Benioff Zone with earthquakes occurring at depths of less than 150 km (Hayes et al., 2012). A distinctive feature of this region is the progressive eastward migration of the volcanic arc since the Jurassic (ca. 200 Ma ago; Coira et al., 1982; Haschke, 2002; Mpodozis and Kay, 1990; Pichowiak et al., 1990; Trumbull et al., 2006). This migration is generally attributed to the change of the subduction angle with time, and to subduction erosion at the plate boundary (Stern, 1991). The subduction erosion process has been considered an important source of mantle enrichment below the Central Andes, particularly during the Neogene (Maro et al., 2017, and references therein). Volcanism associated with the modern magmatic arc of the Central Andes is distributed through southern Peru, western Bolivia, northwestern Argentina and northern Chile and more than 1100 Neogene to Quaternary

volcanic edifices (stratovolcanoes, calderas, monogenetic cones and domes) have been identified. At least sixteen volcanoes are considered active (Allmendinger et al., 1997; de Silva and Francis, 1991; Trumbull et al., 2006). The stratovolcano complexes constitute the major volcanic chains of the Central Andes, comprised mainly of andesitic to dacitic lava flows, with less common basalts, basaltic-andesites and rhyolites, the latter usually associated with pyroclastic deposits and felsic domes (Allmendinger et al., 1997; Davidson et al., 1991). The volcanism from caldera systems is of siliceous andesitic to dacitic ignimbrite eruptions dated as late Miocene to Pliocene (Allmendinger et al., 1997; de Silva and Francis, 1991; Mamani et al., 2010; Stern, 2004; Trumbull et al., 2006) and small-volume Quaternary rhyolitic ignimbrite complexes (e.g. Cerro Blanco caldera Chiodi et al., 2019; Incapillo caldera, Goss et al., 2011). The mafic monogenetic cones are built mainly by scoriaceous material and basaltic-andesite lava flows (Davidson et al., 1990; Kay and Kay, 1993; Maro et al., 2017; O'Callaghan and Francis, 1986; Wörner et al., 1994) and in some cases the cones are considered as peripheral edifices to larger stratovolcanoes (e.g. La Poruña cone, O'Callaghan and Francis, 1986; Incahuasi cone, Kay et al., 1999).

The Neogene-Quaternary volcanic centres are clustered mainly in the Western Cordillera and Altiplano-Puna Plateau between 20°S to 26°S (Trumbull et al., 2006). Four main regional NW-SE fault zones (Lipez-Coranzuli, Calama-Olacapato-El Toro, Archibarca-Galan and Culampaja-Farallon Negro) are recognized in this area (Fig. 1.2; Matteini et al., 2002; Mazzuoli et al., 2008; Richards et al., 2001; Riller et al., 2001; Salfity, 1985), which coincide with the distribution of several of the volcanic complexes (e.g. Godoy et al., 2014; Matteini et al., 2002; Norini et al., 2013; Richards and Villeneuve, 2002; Trumbull et al., 2006). Several volcanoes are also found in local N-S and NE-SW fault zones (e.g. Tibaldi et al., 2017; Trumbull et al., 2006). Many authors therefore argue that volcanism in the region is associated with these extensional faulting (e.g. de Silva et al., 2006; Matteini et al., 2002; Mazzuoli et al., 2008; Riller et al., 2001; Tibaldi et al., 2006, 2017; Trumbull et al., 2006). This volcano-faulting association likely facilitated magma ascent for eruption sites at

stratovolcanoes (e.g. Giambiagi et al., 2016; Trumbull et al., 2006) and caldera systems (e.g. de Silva, 1989), for rapid magma ascent (e.g. Mattioli et al., 2006), and potentially control the collapse of volcanic edifices (e.g. Riller et al., 2001; Tibaldi et al., 2006).

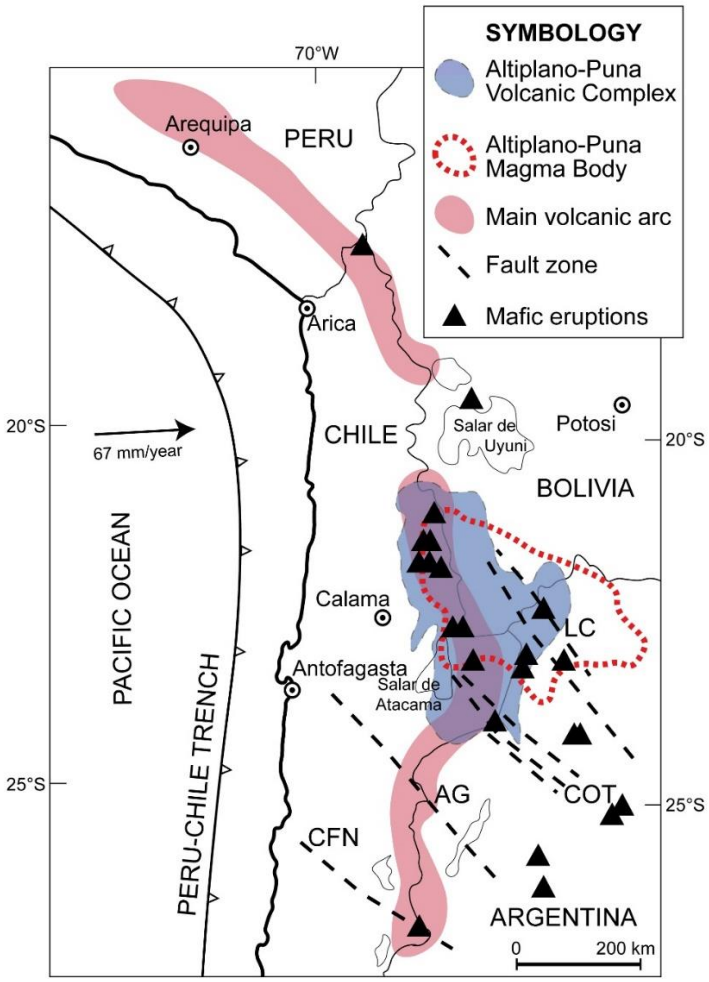

Fig. 1.2. Map of the Neogene-Quaternary arc of the Central Andes showing the location of mafic erupted materials (black triangles) relative to the Altiplano-Puna Volcanic Complex (de Silva, 1989) and the Altiplano-Puna Magma Body partial melt anomaly (Chmielowski et al., 1999). Abbreviations: LC – Lipez-Coranzuli fault system, COT – Calama-Olacapato-El Toro fault system, AG – Archibarca-Galan fault system, CFN – Culampaja-Farallon Negro fault system (after Salfity, 1985; Richards et al., 2001). The distribution of the Altiplano-Puna Volcanic Complex and the surface projection of APMB are based on Zandt et al. (2003). Nazca-South American convergence rate is based on Métois et al. (2014).

A relevant volcanic feature for this study is the occurrence of the volcano-tectonic province called the Altiplano-Puna Volcanic Complex (de Silva, 1989; Fig. 1.2). This complex is characterized by the presence of massive Miocene-Pleistocene ignimbrite sheets, concentrated in the Western Cordillera, southern Altiplano and northern Puna at 21°-24°S. These cover a surface area greater than 70,000 km^2, constituting one of the largest ignimbrite provinces in the world (de Silva, 1989; de Silva et al., 2006; Kay et al., 2010; Salisbury et al., 2011). An ignimbrite flare-up of at least 15,000 km^3 of magma erupted as regional-scale ignimbrites between 10 and 1 Ma from large caldera systems (de Silva et al., 2006; Salisbury et al., 2011, and references therein). A minor amount of young (< 100 ka) volcanism related to the Altiplano-Puna Volcanic Complex has also been reported as rhyodacitic domes and coulées (de Silva et al., 1994; Tierney et al., 2016; Watts et al., 1999).

Arguments for partially melted material in the upper crust, at 4-30 km depth beneath the Altiplano-Puna Volcanic Complex, have been based on electrical conductivity, and thermal and seismic anomaly studies (e.g. Brasse et al., 2002; Chmielowski et al., 1999; Haberland and Rietbrock, 2001; Schilling and Partzsch, 2001; Schilling et al., 1997; Schnurr et al., 2007; Ward et al., 2014; Zandt et al., 2003). The surface projection of this partial melting zone overlaps widely with the Altiplano-Puna Volcanic Complex distribution, and the magma body is referred to as the Altiplano-Puna Magma Body (APMB, Chmielowski et al., 1999; Fig. 1.1). It is estimated that the amount of partial melting of the upper crust in the APMB exceeds 20 vol% (Comeau et al., 2015; Schilling et al., 1997; Zandt et al., 2003), and is a consequence of heat advection related to stagnation of mantle-derived magmas during their ascent to the surface (Annen and Sparks, 2002; Hildreth, 1981; Huppert and Sparks, 1988; Laube and Spring, 1998).

Previous studies within the Altiplano-Puna Volcanic Complex suggest that the parental magmas of ignimbrite deposits, and other evolved volcanic products, were generated by anatectic melts of the upper crust (related to the APMB) mixed with mantle-derived magmas at 4 to 25 km depth (de Silva,

1989; de Silva et al., 2006; Freymuth et al., 2015; Kay et al., 2010; Lindsay et al., 2001; Schmitt et al., 2001). This is consistent with overall constraints in the whole Central Andean region. On the basis of trace element compositional and isotope geochemistry, several authors have argued for strong compositional modification of ascending mantle magmas by differentiation processes, such as crustal assimilation, magma mixing or fluid alteration, as might be expected in a thickened crustal setting with high rates of subduction erosion (e.g. Davidson et al., 1991; Francis and Hawkesworth, 1994; Mamani et al., 2010).

1.2 Geochemistry

Several authors have identified a wide compositional range for the Central Andean volcanism (ca. 48 to 80 wt% SiO_2; Fig. 1.3), however, most of the erupted materials are andesitic to dacitic (58 to 66 wt% SiO_2; Fig. 1.3) displaying high-K calc-alkaline trends and a strong subduction signature (Haschke, 2002; Mamani et al., 2010). Rhyolite lavas (> 69 wt% SiO_2) are unusual in stratovolcanoes, although ignimbrites are commonly dacitic to rhyolitic in composition (> 65 wt% SiO_2; de Silva et al., 1994; Salisbury et al., 2011; Watts et al., 1999). On the other hand, low to intermediate silica rocks (commonly referred as "mafic") are rare and concentrated in a few volcanoes, with basaltic-andesite being the most common least-evolved volcanic product erupted at many volcanoes (Godoy et al., 2019). Central Andean rocks are characterized by high concentrations of incompatible trace elements with an enrichment of large ion lithophile elements (LILE) with respect to high field strength elements (HFSE) and a pronounced negative Nb-Ta anomaly (e.g. Davidson et al., 1991; de Silva et al., 1994; Feeley and Davidson, 1994; Godoy et al., 2014; Kay et al., 1994; Mamani et al., 2010). The presence of variable plagioclase, garnet, amphibole or clinopyroxene may affects certain trace element ratios, such as Sr/Y, Dy/Yb or La/Yb, indicating an increasing or decreasing role of these phases in the evolution of parental magmas (Wörner et al., 2018). These rocks generally reveal elevated Sm/Yb and Sr/Y ratios and are depleted in heavy rare earth elements (HREE), consistent with significant garnet fractionation and thus indicating a magmatic evolution in a high-pressure

differentiation environment (Mamani et al., 2010), however, not all parental magmas evolve under this condition in the region (e.g. Burns et al, 2015; Godoy et al., 2014; Taussi et al., 2019). For example, lavas erupted within the Altiplano-Puna Volcanic Complex show overall lower Sr/Y and Sm/Yb ratios than other lavas erupted along the rest of the entire Central Andes (Godoy et al., 2019). Most magmas have high $^{87}Sr/^{86}Sr$ ratios (>0.706) and low $^{143}Nd/^{144}Nd$ ratios (<0.5125) (e.g. Davidson et al., 1990, 1991; Feeley and Sharp, 1995; Francis et al., 1974; Godoy et al., 2014, 2017; Kay et al., 1994; Mamani et al., 2010; Taussi et al., 2019) compared to other lavas derived from primitive magmas (i.e. $^{87}Sr/^{86}Sr = 0.703$; Harmon et al., 1981; $^{143}Nd/^{144}Nd > 0.5129$; Davidson et al., 1991). Oxygen isotope values obtained for whole-rocks and monomineralic crystal separates are offset towards higher $\delta^{18}O$ values, reaching up to 14.6 ‰ (e.g. Feeley and Sharp, 1995; Freymuth et al., 2015; Kay et al., 2010, 2011; Lister, 2019). This is significantly higher than the established value for mantle-derived melts (5.7‰ ± 0.3 for MORB; Ito et al., 1987).

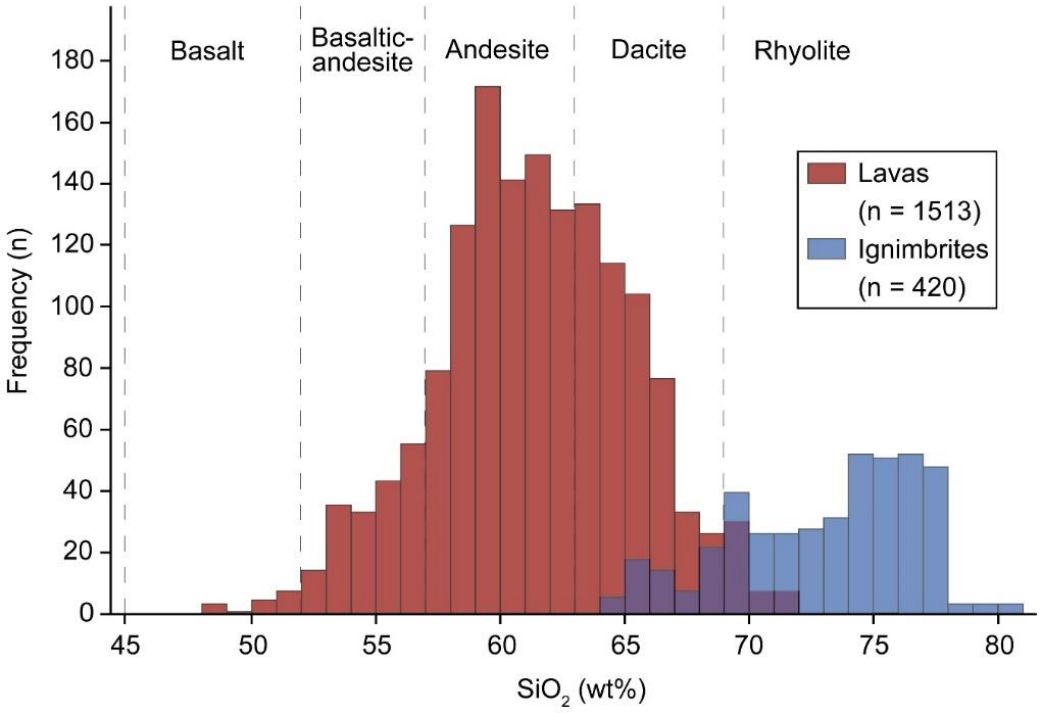

Fig. 1.3. Frequency distribution plot showing SiO_2 ranges for Neogene-Quaternary lavas and ignimbrites from the Central Andes (*after* Wörner et al., 2018).

1.3 Mafic volcanism

True basalts are extremely rare in the Central Andes (Fig. 1.3), with basaltic-andesite being the most common least-evolved volcanic product at many volcanoes, although mafic Neogene-Quaternary rocks with geochemical and isotopic compositions close to those for presumed parental magmas have been recognized in the area (Fig. 1.1; e.g. Davidson and de Silva, 1995; Davidson et al., 1990; Drew et al., 2009; Figueroa et al., 2009; Kay and Kay, 1993; Mamani et al., 2010; Maro et al., 2017; van Alderwerelt, 2017). Some authors have proposed that these relatively primitive rocks are derived from basaltic magmas from the mantle (e.g. Davidson and de Silva, 1995; Davidson et al., 1990; Kay and Kay 1993). Comprehensive petrological studies along the back-arc (the Central Andean Altiplano-Puna Plateau) have led to the association of the mafic magmatism with lithospheric delamination, which also induced a high degree of crustal partial melting as a consequence of upwelling asthenospheric mantle (Kay et al., 1994; Davidson and de Silva; 1995; Risse et al., 2013; Murray et al., 2015; Maro et al., 2017). Mafic volcanism within the main volcanic arc, on the other hand, has been studied with some detail (e.g. Davidson et al., 1990; Feeley and Davidson, 1994; Wörner et al., 1994; Mattioli et al., 2006; Figueroa et al., 2009; Godoy et al., 2014, 2017; Burns et al., 2015, 2020) and the basaltic-andesite magmatism is considered a result of mantle-derived primitive melts having assimilated lower crustal material at high pressures (e.g. deep crustal hot zone; Annen et al., 2006) and related to MASH-type processes (Melting-Assimilation-Storage-Homogenization; Hildreth and Moorbath, 1988). Within the Altiplano-Puna Volcanic Complex, this magmatism has been interpreted as the result of the rapid ascent of a superheated hydrous basaltic magma, derived from the MASH zone, that likely exploited the extensional tectonics due to crustal relaxation (de Silva, 1989; Mattioli et al., 2006). In addition, some authors have suggested that the presence of evolved mafic magmatism may be related in some degree to the interaction between the primitive mafic magmas and the partially molten crustal material of the large-volume felsic Altiplano-Puna Magma Body (Godoy et al., 2017), whose surface projection overlaps with the Altiplano-Puna Volcanic Complex distribution (Zandt et al., 2003).

Neogene-Quaternary volcanism within the Altiplano-Puna Volcanic Complex province is largely represented by massive ignimbrite deposits and complexes of stratovolcanoes, but other minor volcanic features, such as scoria cones and domes, can be found (González-Ferrán, 1995). In the main volcanic arc and back-arc region, the rare mafic volcanism is restricted to olivine-pyroxene-rich basaltic-andesite to andesite products exposed as monogenetic centres (i.e. scoria cones or maar deposits), lava flows (isolated or associated to stratovolcanoes) or mafic enclaves hosted in silicic domes (e.g. Davidson and de Silva, 1992, 1995; Drew et al., 2009; Feeley et al., 1993; Figueroa et al., 2009; Francis et al., 1974; Godoy et al., 2014; Kay et al., 1994; Maro et al., 2017; van Alderwerelt, 2017; Wörner et al., 2000). Notably, a concentration of Pliocene-Quaternary mafic magmas erupted within the western border of the Altiplano-Puna volcanic province in northern Chile, i.e. in the main volcanic arc between 21º10'S to 22º50'S, from scoria cones and stratovolcanoes (e.g. Bertín and Amigo, 2019; Figueroa et al., 2009; Godoy et al., 2019; Mattioli et al, 2006; Sellés and Gardeweg, 2017; Wörner et al., 2000). The most-common mafic rock type identified at 21°10'-22°50'S is pyroxene-basaltic-andesite to pyroxene-andesite with a medium-K to high-K calc-alkaline signature and large variability in major and trace element composition (1.0-6.5 wt% MgO; 2.6-7.1 wt% K_2O + Na_2O; 6-501 ppm Cr; 2-127 ppm Ni; 236-777 ppm Sr; Ramírez and Huete, 1981; Marinovic and Lahsen, 1984; Wörner et al., 1994; Mattioli et al, 2006; Figueroa et al., 2009; Mamani et al., 2010; Sellés and Gardeweg, 2017). The reported $^{87}Sr/^{86}Sr$ ratios (0.706-0.708) and $^{143}Nd/^{144}Nd$ ratios (0.5123-0.5124) of these rocks are in agreement with the Sr and Nd isotope array for the lavas of the Central Andes ($^{87}Sr/^{86}Sr$ = 0.705-0.715; $^{143}Nd/^{144}Nd$ = 0.5121-0.5124; Figueroa et al., 2009; Godoy et al., 2017; Mamani et al., 2010; Scott et al., 2018). In contrast, stable oxygen isotopic characteristics of parental magmas to these mafic eruptives are considerably less constrained in this area. The published whole-rock and mineral $\delta^{18}O$ data generally display high values (average = 8.0‰ for whole-rock, Feeley et al., 1995, Harmon et al., 1984; average = 7.0‰ for olivine, Godoy, 2014; average = 7.8‰ for plagioclase, Feeley et al., 1995; average = 9.1‰ for quartz, Lister, 2019), although some mafic crystals record arc-type mantle source values (e.g. < 6.2‰, Dallai et al., 2019).

1.4 Scope of the thesis

Parental basaltic-andesite magmas in the Central Andes are conventionally proposed to form in the lithospheric mantle-lower crust boundary by deep MASH-type processes (Davidson et al., 1991; Hildreth and Moorbath, 1988). Thus, before eruption, the parental magmas of the concentrated mafic volcanics within the western border Altiplano-Puna Volcanic Complex (21°10'-22°50'S) had to pass through the thickest crust on Earth (70-74 km, Beck et al., 1996) in a portion of the Central Andes that also includes the largest known zone of partial melting in the continental crust throughout the world, the felsic Altiplano-Puna Magma Body melt anomaly (Ward et al., 2014). Even though previous field constraints and geochemical studies identified this mafic volcanism (Section 1.3), the nature of the relevant source and parental magma evolution through time and space have been poorly studied in this region. This incomplete information related to mafic volcanics in the northern Chilean Andes at 21°10'-22°50'S forms the basis for the current study. New petrography, whole-rock and mineral geochemistry, radiogenic and stable isotope data provide an approach to evaluate the petrogenesis of the mafic volcanism and the degree of crustal material contribution in the parental magmas within the Altiplano-Puna Volcanic Complex. The aim of this work is to gain new insight into the nature of the parental magmas in this region, and to constrain the parental source(s) and the magmatic evolutionary processes that modified their composition during storage and ascent through the thick crust and the felsic APMB.

This thesis is divided as follows: Chapter 2 addresses the petrogenesis of the mafic volcanism within the western margin of the Altiplano-Puna Volcanic Complex, by petrographic and geochemical constraints, focused on a spatiotemporal relation with the Altiplano-Puna Magma Body; Chapter 3 traces the differentiation regimes of the parental magmas, based on petrography and geochemistry, in one of the volcanoes that reported the least evolved eruptions in the area; Chapter 4 provides the first known approach to constrain the parental signature for the Altiplano-Puna Volcanic Complex by an oxygen isotope study on mafic crystals; Chapter 5 discusses the overall observations of this study in

the Altiplano-Puna Volcanic Complex and Central Andes geological context; finally, Chapter 6 concludes and summarizes the main findings.

Chapter 2

Petrogenesis of low-silica volcanism within the Altiplano-Puna Volcanic Complex

This chapter is based on the work published as:

González-Maurel, O., le Roux, P., Godoy, B., Troll, V.R., Deegan, F.M., Menzies, A., 2019. The great escape: Petrogenesis of low-silica volcanism of Pliocene to Quaternary age associated with the Altiplano-Puna Volcanic Complex of northern Chile (21° 10′-22° 50′ S). Lithos, 346-347:105162. https://doi.org/10.1016/j.lithos.2019.105162.

The modern volcanic arc of the Central Andes formed on 70-74 km thick continental crust. Physical interaction between mafic and felsic magmas in this arc are therefore difficult to recognize due to the differentiation of mantle-derived magma during ascent through this thickened crust and a corresponding lack of erupted primitive lavas. However, a rare concentration of less evolved rocks is located marginal to the partially molten Altiplano-Puna Magma Body (APMB) in the Altiplano-Puna Volcanic Complex of northern Chile, between 21º10'S and 22º50'S. To unravel the petrogenesis of these rare mafic lava flows, new major and trace element data, and Sr and Nd isotope ratios of fourteen volcanoes erupted at different ages are presented here. These new data also provide an approach to evaluate the relationship between this less evolved magmatism and the APMB, which in turn aids in assessing the evolution of the APMB through space and time.

The following text is reproduced verbatim from the published paper mentioned above and only reformatted to comply fully with the Doctoral Degree Board (University of Cape Town) guidelines for Doctoral Thesis. A final Section 2.7 concludes the chapter in order to discuss examiners' non-typographic corrections and comments.

2.1 Introduction

The Pliocene to Quaternary volcanic arc of the Central Andes is spread over southern Peru, western Bolivia, northwestern Argentina and northern Chile (14°S-28°S) and developed on the world's thickest continental arc crust (70-74 km; Beck et al., 1996; Fig. 2.1). Several authors have identified a wide compositional range for the Pliocene to Quaternary volcanic rocks in this region and most of the erupted materials are andesitic to dacitic in composition, usually displaying high-K calc-alkaline trends and a strong subduction signature (e.g. Mamani et al., 2010; Wörner et al., 2018). Most magmas in the region have high $^{87}Sr/^{86}Sr$ (> 0.706) and low $^{143}Nd/^{144}Nd$ (< 0.5125) ratios relative to primitive mantle-type magmas (i.e. $^{87}Sr/^{86}Sr$ = 0.703, Harmon et al., 1981; $^{143}Nd/^{144}Nd$ > 0.5129, Davidson et al., 1991) and several authors have thus argued for compositional modification of parental magma by fractional crystallization and assimilation during ascent through the thickened Andean crust (Davidson et al., 1991; Francis and Hawkesworth, 1994; Mamani et al., 2010). Accordingly, primitive (parental) mafic compositions are rare, with olivine and pyroxene phyric basaltic-andesite to andesite rocks (commonly referred as "mafic") representing the most primitive volcanic products in the region (Fig. 2.1; e.g. Davidson et al., 1990; Drew et al., 2009). The mafic volcanism within the modern arc has been studied in some detail (e.g. Burns et al., 2015; Mattioli et al., 2006) and is considered the result of primitive mantle wedge melts having assimilated crustal material at high pressures during deep MASH-type processes (Hildreth and Moorbath, 1988; de Silva and Kay, 2018; Wörner et al., 2018).

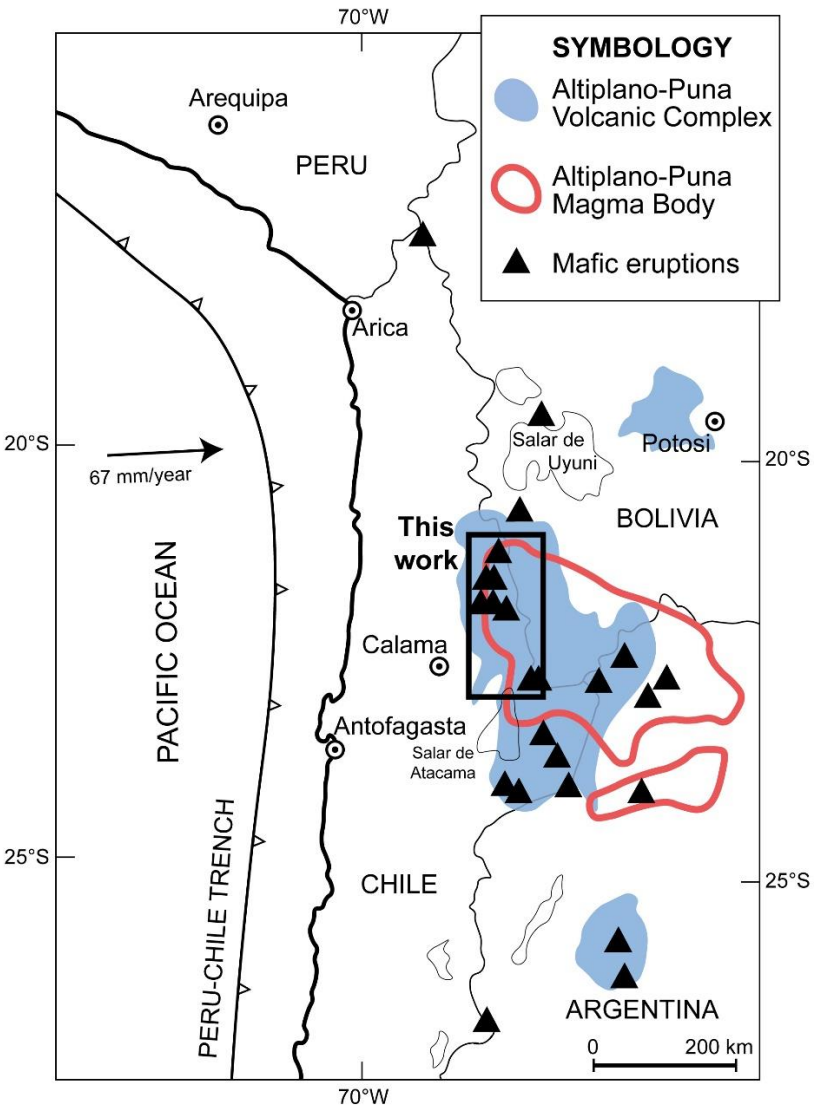

Fig. 2.1. Map of the Pliocene to Quaternary arc of the Central Andes showing the location of mafic erupted materials (black triangles) relative to the Altiplano-Puna Volcanic Complex (APVC) and Altiplano-Puna Magma Body (APMB) partial melt anomaly. The distribution of the APVC and the surface projection of APMB are based on Zandt et al. (2003).

Modern volcanic activity generally produced stratovolcanoes and few monogenetic volcanoes but also extensive ignimbrite deposits (Mamani et al., 2010). The volcano-tectonic ignimbrite province of the Altiplano-Puna Volcanic Complex (APVC, de Silva, 1989; Fig. 2.1) covers a surface area >70,000 km^2, constituting one of the largest ignimbrite provinces in the world. Within this province,

the scarce mafic magmatism has been interpreted as a result of direct, and possibly rapid, ascent of a superheated hydrous basaltic magma from the mantle as a result of extensional tectonics and crustal relaxation (Mattioli et al., 2006). Alternatively, some authors have suggested that the presence of slightly more evolved mafic magmatism within the APVC may be related to interaction between ascending mafic magmas and the partially molten crustal material of the large-volume felsic Altiplano-Puna Magma Body (APMB; Godoy et al., 2017), whose surface projection overlaps with the APVC distribution (Fig. 2.1). However, a concentration of mafic to intermediate, olivine-pyroxene-rich lavas erupted within the western border of the Altiplano-Puna volcanic region in northern Chile, i.e. between 21º10'S and 22º50'S (Fig. 2.1), from Pliocene to Quaternary stratovolcanoes and monogenetic cones (e.g. Godoy et al., 2019; Sellés and Gardeweg, 2017; Taussi et al., 2019). In this chapter, I present new petrography, geochemistry and radiogenic isotope data to evaluate the petrogenesis of these olivine and/or pyroxene phyric mafic to intermediate rocks and assess their spatiotemporal relationship with the evolved APMB with the goal to evaluate the nature of the parental magmas in the region and to unravel evolutionary processes during storage and ascent through the crust.

2.2 Geological background

The Altiplano-Puna Magmatic Body (APMB, Chmielowski et al., 1999; Fig. 2.1) is a region of partially molten material in the upper crust, at 4 to 30 km depth, defined by electrical conductivity, thermal and seismic anomalies (e.g. Araya Vargas et al., 2019; Ward et al., 2014; Zandt et al., 2003). The fraction of partial melt in the upper APMB is thought to exceed 20 vol% (Comeau et al., 2015; Ward et al., 2014), resulting from large-scale heat advection related to stagnation of mantle-derived mafic magmas (de Silva and Gosnold, 2007; del Potro et al., 2013). The surface projection of the Altiplano-Puna partial melting zone (i.e. APMB) is reflected on the surface by the Altiplano-Puna Volcanic Complex (APVC, de Silva, 1989), which is characterized by the presence of massive Miocene to Pleistocene high-silica ignimbrite sheets that are concentrated in the Western Cordillera,

southern Altiplano and northern Puna between 21° and 24°S (Fig. 2.1; de Silva, 1989). The APMB is thus considered as the source region of the APVC ignimbrites (Zandt et al., 2003), which were likely generated by mafic magmas and anatectic melts of the upper crust that accumulated at 5 to 10 km depth (e.g. Freymuth et al., 2015; Kay et al., 2010; Kern et al., 2016). In addition to this regional scale ignimbritic activity, occasional mafic magma eruptions have been recognized around the margins of the APMB in the form of lava flows erupted from Miocene to Quaternary stratovolcano complexes and scoria cones (Fig. 2.1; e.g. Davidson and de Silva, 1995; Godoy et al., 2019). The mafic to intermediate volcanism in the Chilean Western Cordillera (between 21°10'S and 22°50'S) has been sampled from fourteen volcanoes with olivine and/or pyroxene-rich rocks among their erupted materials (Fig. 2.2), comprising volcanic activity at Araral, Ascotán, Cerro Carcote, Chela and Palpana volcanoes during the Pliocene (Table 2.1; Fig. 2.2), and Apacheta, Cerro La Quebrada, Cordón Inacaliri, Juriques, Licancabur, La Poruña, La Poruñita, Paniri and San Pedro volcanoes during the Quaternary (Table 2.1; Fig. 2.2). Several volcanoes occur in NW-SE trending alignments (i.e. Araral-Ascotán, San Pedro-Paniri, Apacheta-Cordón Inacaliri, Licancabur-Juriques), which are parallel to principal local tectonic structures in the region (Fig. 2.2; Giambiagi et al., 2016; Sellés and Gardeweg, 2017; Tibaldi et al., 2017), whereas others appear clustered (i.e. Chela-Palpana-Cerro Carcote; San Pedro-La Poruña; Fig. 2.2).

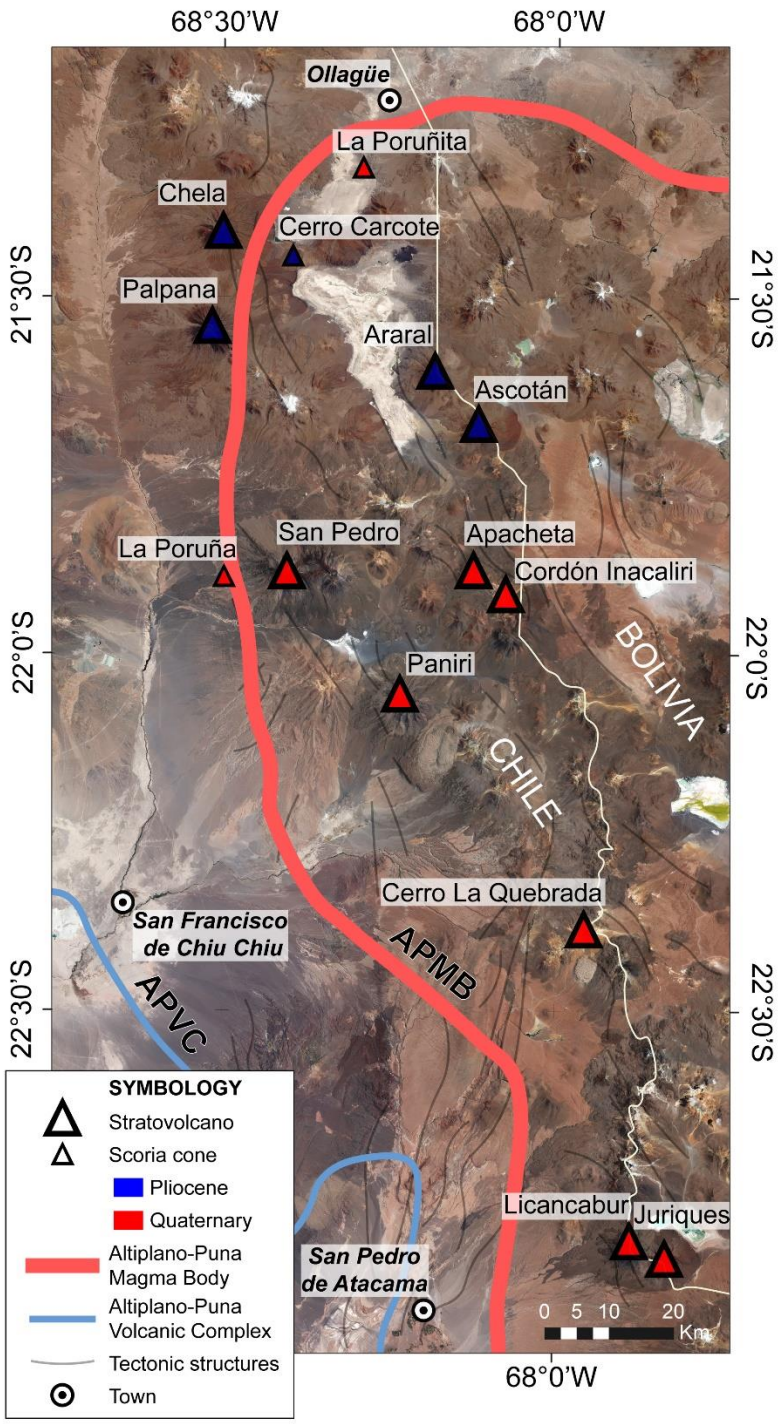

Fig. 2.2. Satellite image (Google Earth™) showing the location of the Pliocene and Quaternary volcanoes included in this study. The distribution of the APVC and the surface projection of the APMB are based on Zandt et al. (2003). Pliocene to Quaternary tectonic structures based on Giambiagi et al. (2016), Sellés and Gardeweg (2017) and Tibaldi et al. (2017).

Table 2.1. Summarized K-Ar, $^{40}Ar/^{39}Ar$, U-Pb and relative published dating for the Pliocene and Quaternary studied volcanoes at 21°10'S to 22°50'S.

Volcano	Sample	Latitude (S)	Longitude (W)	Age (Ma)	Uncertainty (2σ)	Method	Reference
Pliocene							
Chela	CHE 08	21º 24' 20"	68º 27' 0"	4.11	0.25	K-Ar (whole-rock)	Wörner et al. (2000)
	CHE 07	21º 25' 30"	68º 25' 50"	3.75	0.5	K-Ar (whole-rock)	Wörner et al. (2000)
Palpana	PAL 04	21º 34' 0"	68º 29' 40"	3.81	0.3	K-Ar (whole-rock)	Wörner et al. (2000)
	PAL 01	21º 33' 55"	68º 29' 55"	3.65	0.15	K-Ar (whole-rock)	Wörner et al. (2000)
Cerro Carcote	CAR 01	21º 26' 10"	68º 23' 10"	3.34	0.3	K-Ar (whole-rock)	Wörner et al. (2000)
	CAR 01	21º 26' 10"	68º 23' 10"	2.82	0.11	K-Ar (whole-rock)	Wörner et al. (2000)
Araral	AI-040	21º 35' 29"	68º 14' 3"	2.75	0.04	$^{40}Ar/^{39}Ar$ (amphibole)	Sellés and Gardeweg (2017)
Ascotán	AI-053	21º 42' 18"	68º 11' 4"	2.67	0.02	$^{40}Ar/^{39}Ar$ (groundmass)	Sellés and Gardeweg (2017)
Quaternary							
Cordón Inacaliri	AI-226	21º 51' 22"	68º 6' 52"	1.43	0.02	$^{40}Ar/^{39}Ar$ (groundmass)	Sellés and Gardeweg (2017)
	AI-201	21º 55' 28"	68º 10' 1"	1.109	0.023	$^{40}Ar/^{39}Ar$ (groundmass)	Sellés and Gardeweg (2017)
	AI-256	21º 56' 1"	68º 5' 9"	1.094	0.016	$^{40}Ar/^{39}Ar$ (groundmass)	Sellés and Gardeweg (2017)
Cerro La Quebrada	M2	22º 24' 52"	67º 57' 10"	0.9	-	U-Pb (zircon)	Bidart (2014)
Licancabur	-	-	-	> 1.35	-	Relative	Figueroa et al. (2009)
Juriques	-	-	-	> 1.35	-	Relative	Marinovic and Lahsen (1984)
Paniri	PAE-090	22° 0' 0"	68° 14' 8"	1.39	0.29	$^{40}Ar/^{39}Ar$ (amphibole)	Godoy et al. (2017)
	PAE-55	22° 3' 45"	68° 11' 24"	0.64	0.14	$^{40}Ar/^{39}Ar$ (amphibole)	Godoy et al. (2017)
	PAE-43	22° 7' 55"	68° 15' 16"	0.625	0.093	$^{40}Ar/^{39}Ar$ (amphibole)	Godoy et al. (2017)
	ZZ-27a	22º 8' 30"	68º 16' 3"	0.5	0.1	K-Ar (whole-rock)	Seelenfreund et al. (2009)
	ZZ-46	22º 8' 30"	68º 16' 3"	0.4	0.1	K-Ar (whole-rock)	Seelenfreund et al. (2009)
	PAE-03	22º 2' 50"	68º 12' 29"	0.325	0.008	$^{40}Ar/^{39}Ar$ (groundmass)	Godoy et al. (2017)
	ZZ-42	22º 5' 19"	68º 11' 48"	0.3	0.1	K-Ar (whole-rock)	Seelenfreund et al. (2009)
	PAE-02	22º 2' 47"	68º 12' 35"	0.264	0.099	$^{40}Ar/^{39}Ar$ (amphibole)	Godoy et al. (2017)
	PAE-25	22º 3' 44"	68º 15' 31"	0.164	0.003	$^{40}Ar/^{39}Ar$ (groundmass)	Godoy et al. (2017)
	PAE-08	22º 6' 13"	68º 17' 49"	0.15	0.006	$^{40}Ar/^{39}Ar$ (amphibole)	Godoy et al. (2017)
Apacheta	AA-067	21º 51' 0"	68º 12' 40"	0.97	0.11	$^{40}Ar/^{39}Ar$ (groundmass)	Taussi et al. (2019)
La Poruñita	PORU 02	21º 17' 40"	68º 15' 35"	0.68	0.2	K-Ar (whole-rock)	Wörner et al. (2000)
	PORU 02	21º 17' 40"	68º 15' 35"	0.65	0.2	K-Ar (whole-rock)	Wörner et al. (2000)
	PORU 02 (bomb)	21º 17' 40"	68º 15' 35"	0.42	0.2	K-Ar (whole-rock)	Wörner et al. (2000)

Table 2.1. Continued.

Volcano	Sample	Latitude (S)	Longitude (W)	Age (Ma)	Uncertainty (2σ)	Method	Reference
Quaternary							
San Pedro	DB251114-5	21º 49' 5"	68º 23' 10"	0.166	0.012	$^{40}Ar/^{39}Ar$ (groundmass)	Bertin and Amigo (2019)
	DB190714-1	21º 54' 28"	68º 22' 0"	0.166	0.016	$^{40}Ar/^{39}Ar$ (groundmass)	Bertin and Amigo (2019)
	DB060911-2	21º 54' 15"	68º 29' 2"	0.160	0.050	$^{40}Ar/^{39}Ar$ (groundmass)	Bertin and Amigo (2019)
	DB170714-2	21º 57' 22"	68º 23' 6"	0.159	0.003	$^{40}Ar/^{39}Ar$ (groundmass)	Bertin and Amigo (2019)
	DB060911-3	21º 53' 58"	68º 28' 11"	0.140	0.040	$^{40}Ar/^{39}Ar$ (groundmass)	Bertin and Amigo (2019)
	DB251114-4	21º 52' 21"	68º 23' 59"	0.139	0.033	$^{40}Ar/^{39}Ar$ (groundmass)	Bertin and Amigo (2019)
	GO060911-1	21º 49' 29"	68º 27' 59"	0.130	0.040	$^{40}Ar/^{39}Ar$ (amphibole)	Bertin and Amigo (2019)
	SP12-02A	21º 56' 4"	68º 30' 36"	0.107	0.012	$^{40}Ar/^{39}Ar$ (groundmass)	Delunel et al. (2016)
	DB140613-3	21º 51' 42"	68º 29' 55"	0.097	0.014	$^{40}Ar/^{39}Ar$ (groundmass)	Bertin and Amigo (2019)
	DB200714-2B	21º 57' 41"	68º 27' 24"	0.096	0.036	$^{40}Ar/^{39}Ar$ (groundmass)	Bertin and Amigo (2019)
	DB060911-4	21º 52' 23"	68º 29' 15"	0.090	0.080	$^{40}Ar/^{39}Ar$ (groundmass)	Bertin and Amigo (2019)
	DB200714-2C	21º 57' 41"	68º 27' 24"	0.068	0.027	$^{40}Ar/^{39}Ar$ (groundmass)	Bertin and Amigo (2019)
	DB140613-2	21º 50' 26"	68º 30' 18"	0.060	0.006	$^{40}Ar/^{39}Ar$ (groundmass)	Bertin and Amigo (2019)
La Poruña	DB120613-2	21º 54' 13"	68º 30' 52"	0.11	0.05	$^{40}Ar/^{39}Ar$ (whole-rock)	Bertin and Amigo (2019)

2.3 Analytical methods

To fully characterise the olivine and/or pyroxene-rich rocks erupted in the Chilean Western Cordillera, new petrography, whole-rock major element, trace element and radiogenic isotope data of forty-eight (48) fresh volcanic rock samples from Pliocene to Quaternary lava flows from Central Andean stratovolcanoes and scoria cones are presented (Fig. 2.2). All 48 samples were crushed and pulverized at the Department of Geological Sciences, University of Cape Town (South Africa). Major and trace elemental abundance and isotope measurements were performed at UCT.

2.3.1 XRF method

Bulk-rock major element compositions were obtained by routine X-ray fluorescence spectrometry (XRF) using a Panalytical Axios wavelength dispersive XRF spectrometer in the Department of Geological Sciences, University of Cape Town. Typical internal two-sigma analytical errors for individual analyses were < 2 %RSD.

Major elements analyses were done on prepared fusion discs. The routine process starts with approximately 2 g of whole rock powder being weighed into a crucible of known mass and dried overnight at 110°C. Once cooled down this is reweighed with the mass difference being recorded as the volatile content. Each sample is then reheated to 800°C for 4 hours to determine loss on ignition (LOI) and ensure all Fe is oxidised to Fe^{3+}. Meanwhile, lithium tetraborate/metaborate flux is dried in a furnace at 450ºC overnight. Once cooled, 6 g of flux, to act as a releasing agent, and 0.7 g of sample are measured into a labeled vial and sealed with mylar film and a lid. Finally, the flux and sample mixture are fused in a Claisse gas burner in order to form the fusion disc.

Trace elements analyses were done on prepared powder pellets. This routine process involves 6 g of powdered sample being weighed out and mixed with 3 drops of binding agent. The sample and the binding agent are mixed thoroughly before being poured into a mould (a combination of a hollow

tube within a larger mould) where a small amount of pressure is applied to form the initial shape of the pellet; the tube is then removed. A small amount of boric acid powder is added to the mould and a cylinder is inserted into the mould on top of the combination of sample and acid. A hydraulic press is then used to apply 10 tons of pressure to the cylinder to form the combined sample pellet with acid backing. Finally, the pellet is carefully removed from the mould and labeled.

For major and trace element calibration, the routine instrument analysis method uses a combination of natural standards from the USGS, SARMS (South African producers of Metallurgical and Geological Certified Reference Materials). These standards were prepared identically to the samples being analysed. Matrix corrections are made using the Fundamental Parameter method as described in Rousseau et al. (1996) or Willis and Duncan (2008). Volatiles and loss of ignition (LOI) were calculated using a mass balance described above.

2.3.2 Quad-ICP-MS method

A ThermoFisher Xseries 2 inductively coupled plasma mass spectrometer (ICP-MS) in the Department of Geological Sciences, University of Cape Town, was used to obtain bulk trace element data by analysis of sample solutions. The routine method involves the digestion of accurately weighed ~50 mg of rock powder of each sample in 4 ml of 4:1 concentrated HF:HNO_3 mixture for 48 hours at 140°C in closed Teflon beakers to ensure complete digestions. Samples are then dried down, redissolved in < 1 ml of concentrated HNO_3 only and repeated twice. Finally, samples were redissolved in 2M HNO_3 and quantitatively split by weight into two aliquots; Split 1 for elemental abundance analysis (±0.2 mL) and Split 2 for radiogenic isotope composition analysis (±1.5 mL). Split 1 aliquot was then again dried down and taken up in 5 % HNO_3 solution containing 10 ppb Re, Rh, In, and Bi, used as internal standards. Calibration curves were obtained using artificial multi-element standards from which standard solutions were made (for details also see Harris et al. (2015)

and Howarth et al. (2019)). Routine internal two-sigma analytical errors for individual analyses were < 3%RSD.

2.3.4 MC-ICP-MS method

A Nu Instruments NuPlasma HR multi-collector inductively couple plasma mass spectrometer (MC-ICP-MS) equipped with a DSN-100 desolvating nebulizer in the MC-ICP-MS facility, housed in the Department of Geological Sciences, UCT, was used for all isotope analyses. The ±1.5 mL Split 2 aliquot of the dissolved sample (see quad-ICP-MS method above) was processed for Sr and Nd elemental separation following the sequential column chemistry outlined in Mikova and Denkova (2007). This methodology is based on previous protocols of Pin and Zalduegui (1997) and Pin et al. (1994). Strontium isotope ratios were analysed in 200 ppb 0.2 % HNO_3 solution and data were referenced to an $^{87}Sr/^{86}Sr$ normalizing value of 0.710255 for the bracketing analyses of NIST SRM987 with on-peak background measurements. Strontium isotope data were corrected for Rb interference using the measured signal for ^{85}Rb and the natural $^{85}Rb/^{87}Rb$ ratio. Instrumental mass fractionation was corrected using the exponential law and an $^{86}Sr/^{88}Sr$ value of 0.1194. Internal 2σ analytical uncertainty for $^{87}Sr/^{86}Sr$ were <0.000015, similar to the long-term 2σ external reproducibility for $^{87}Sr/^{86}Sr$ analysis in this facility of 0.000020. Neodymium isotope ratios were analysed in 50 ppb 2 % HNO_3 solutions and data were referenced to a $^{143}Nd/^{144}Nd$ normalizing value of 0.512115 for the bracketing analyses of JNdi-1, after Tanaka et al. (2000) with half-amu off-set background measurements. All Nd isotope data were corrected for Sm and Ce interference using the measured signal for ^{147}Sm and ^{140}Ce, and natural Sm and Ce isotope abundances. Instrumental mass fractionation was corrected using the exponential law and a $^{146}Nd/^{144}Nd$ value of 0.7219. Internal 2σ analytical uncertainty for $^{143}Nd/^{144}Nd$ ranged from <0.000015, similar to the long-term 2σ external reproducibility for $^{143}Nd/^{144}Nd$ analysis in this facility of 0.000020 (for details also see Harris et al. (2015) and Howarth et al. (2019)).

2.4 Results

2.4.1 Petrography and mineral assemblage

With respect to mineralogy, the petrographic description follows a definition of phenocrysts = 0.2-2.5 mm, microcrysts = 0.2-0.03 mm and microlite ≤ 0.03 mm. Most of the olivine and/or pyroxene-rich rock samples are dark-coloured, fine-grained and porphyritic. The phenocrysts (up to 40 vol%) comprise plagioclase, orthopyroxene, clinopyroxene and olivine. Amphibole and biotite occur only rarely as microcrysts and/or microlites. Phenocrysts and microcrysts are generally suspended in a very finely crystalline groundmass with interstitial glass and microlites of, in order of decreasing abundance, plagioclase, pyroxene, olivine, amphibole and Fe-Ti oxides. A hypocrystalline texture is common in many of the rocks, however glassy lavas can also be found. Groundmass varies from compact to vesicular. Although vesicular rocks are not common, vesicularity is high (>40 vol%) in scoria samples from La Poruña, La Poruñita and San Pedro. Three Pliocene samples from Cerro Carcote, Chela and Palpana have a reddish-brown groundmass colour, due to the presence of very fine-grained hydrothermal alteration minerals (e.g. illite, anhydrite, K-rich clays). Secondary quartz was observed in a few samples, either as interstitial mineral grains or as vesicle infill (Table 2.2).

Plagioclase is the most abundant phase (>50 vol%) and typically appears as euhedral to subhedral crystals, ranging in size from microlites to phenocrysts (<2.5 mm). Plagioclase displays a diversity of morphologies and textures, including equant and/or tabular crystals with sieve, resorption, or regrowth rims, frequently displaying seriate and/or normal zonation. In consideration of the ferromagnesian phenocryst phases, the samples are either (i) olivine-pyroxene-bearing or (ii) pyroxene-bearing. Photomicrographs of representative mineral assemblages are presented in Fig. 2.3.

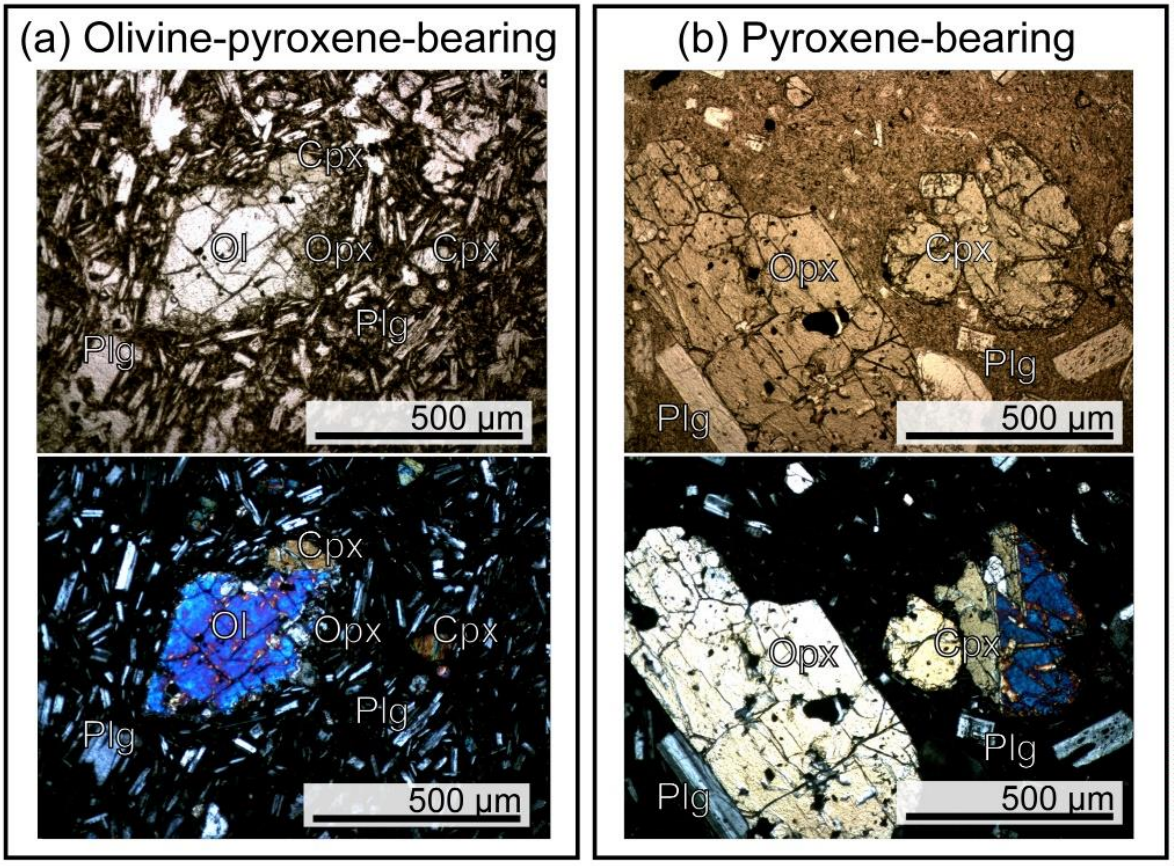

Fig. 2.3. Representative photomicrographs of the studied sample groups: (a) olivine-pyroxene-bearing and (b) pyroxene-bearing. Upper and lower panels show examples of plane-polarized light and cross-polarized light photomicrographs, respectively.

Table 2.2. Petrography and phenocryst main assemblages of the studied Pliocene to Quaternary volcanism at 21°10'S to 22°50'S. Geochemical data from Table S1.

Volcano	Sample	SiO_2 (wt%)[a]	Chemical classification[a]	Rock type	Mineral assemblage
Olivine-pyroxene-bearing rocks					
Pliocene					
Araral	ARA-01	63.04	Andesite	glassy fine-grained plg-ol-px seriate glomerophyric	plg>opx=cpx>ol
	ARA-04	61.15	Andesite	glassy fine-grained plg-ol-px seriate glomerophyric	plg>opx=cpx>ol
	ARA-10	62.29	Andesite	glassy fine-grained plg-ol-px seriate glomerophyric	plg>opx=cpx>ol
Cerro Carcote	CAR-01	57.07	Basaltic trachyandesite	fine-grained ol-px phyric	plg (only microlite)>ol>opx=cpx
	CAR-03	59.42	Trachyandesite	fine-grained ol-px phyric	plg (only microlite)>opx>ol>cpx
	CAR-04	56.03	Basaltic trachyandesite	vesicular fine-grained ol-cpx phyric	plg (only microlite)>cpx>ol>opx
Chela	CHE-01	57.92	Basaltic-andesite	fine-grained ol-cpx phyric	plg (only microlite)>ol>cpx>opx
	CHE-02	56.68	Basaltic-andesite	fine-grained plg-ol-px seriate phyric	plg>opx=cpx>ol
	CHE-03	55.50	Basaltic-andesite	fine-grained plg-ol seriate phyric px glomerophyric	plg>ol>cpx>opx
	CHE-04	57.30	Basaltic-andesite	fine-grained plg-px seriate phyric	plg>opx=cpx>ol
	CHE-05	58.75	Andesite	fine-grained plg-px seriate phyric	plg>opx=cpx>ol
Palpana	PAL-02	58.36	Andesite	fine-grained plg-px seriate phyric	plg>cpx>opx>ol
	PAL-03	59.48	Trachyandesite	fine-grained plg-px seriate phyric	plg>cpx>opx>ol
Quaternary					
Cerro La Quebrada	QUE-01	58.87	Andesite	vesicular glassy fine-grained plg-ol seriate phyric	plg>ol>opx=cpx
Juriques	JUR-05	53.70	Basaltic-andesite	fine-grained plg-ol seriate phyric px glomerophyric	plg>opx=cpx>ol
La Poruña	POR-01	57.47	Basaltic-andesite	vesicular fine-grained plg-ol-px seriate phyric	plg>ol>opx=cpx
	POR-02	57.46	Basaltic-andesite	vesicular fine-grained ol phyric plg-px glomerophyric	plg>ol>opx=cpx
	POR-03	57.48	Basaltic-andesite	fine-grained plg-ol-px seriate phyric	plg>ol>opx=cpx
	POR-04	59.85	Andesite	glassy fine-grained plg-ol-px seriate phyric	plg>ol>opx=cpx
	POR-05	59.21	Basaltic trachyandesite	fine-grained plg-ol-cpx seriate phyric	plg>ol>cpx>opx
	POR-06	56.30	Basaltic-andesite	glassy fine-grained plg-ol-px seriate phyric	plg>ol>cpx>opx
	POR-07	56.86	Basaltic-andesite	glassy fine-grained plg-ol-px seriate phyric	plg>ol>cpx>opx
	POR-08	56.63	Basaltic-andesite	fine-grained plg-ol-px seriate phyric	plg>ol>opx=cpx
	POR-09	57.51	Basaltic-andesite	vesicular fine-grained plg-ol-px seriate phyric	plg>ol>opx>cpx
	POR-10	58.23	Andesite	vesicular fine-grained plg-ol-px seriate phyric	plg>ol>opx=cpx
La Poruñita	PORU-01	56.56	Basaltic trachyandesite	vesicular fine-grained ol-px phyric	plg (only microlite)>ol>opx=cpx
	PORU-02	56.72	Basaltic trachyandesite	vesicular fine-grained ol-px phyric	plg (only microlite)>ol>opx=cpx
Paniri	PANI-03	57.74	Basaltic trachyandesite	fine-grained ol phyric plg-opx glomerophyric	plg>ol=opx>cpx
	PANI-05	57.04	Basaltic-andesite	fine-grained plg phyric ol-px glomerophyric	plg>ol=opx=cpx
San Pedro	SPE-01	58.31	Andesite	vesicular fine-grained plg-ol-px seriate phyric	plg>opx=cpx>ol
	SPE-09	56.60	Basaltic-andesite	vesicular fine-grained plg-ol-px phyric	plg>ol>opx=cpx
	SPE-10	56.29	Basaltic-andesite	vesicular fine-grained plg-ol-px phyric	plg>ol>cpx>opx

Table 2.2 Continued.

Volcano	Sample	SiO_2 (wt%)[a]	Chemical classification[a]	Rock type	Mineral assemblage
Pyroxene-bearing rocks					
Pliocene					
Ascotán	ASC-01	64.46	Dacite	glassy fine-grained plg-px seriate glomerophyric	plg>opx>cpx
	ASC-04	64.78	Dacite	glassy fine-grained plg-px seriate glomerophyric	plg>opx>cpx
	ASC-06	62.88	Andesite	glassy fine-grained plg-px seriate glomerophyric	plg>opx>cpx
Cerro Carcote	CAR-02	59.64	Trachyandesite	fine-grained opx phyric	plg>opx>cpx
Palpana	PAL-01	62.02	Trachyandesite	glassy fine-grained plg-px seriate phyric	plg>cpx>opx
Quaternary					
Apacheta	APA-01	57.30	Basaltic trachyandesite	glassy fine-grained plg-px seriate phyric	plg>opx=cpx
	APA-02	61.27	Andesite	glassy fine-grained plg-px-amp seriate phyric	plg>opx=cpx>amp
Cordón Inacaliri	INA-01	63.30	Trachyandesite	glassy fine-grained plg-px phyric	plg>opx>cpx
Juriques	JUR-01	55.45	Basaltic-andesite	fine-grained plg-opx seriate glomerophyric	plg>opx>cpx
Licancabur	LIC-01	58.99	Andesite	glassy fine-grained plg-ox phyric	plg>ox>cpx>opx
Paniri	PANI-01	59.88	Andesite	glassy fine-grained plg-px-ox seriate glomerophyric	plg>opx=cpx>ox
	PANI-14	59.33	Basaltic-andesite	glassy fine-grained plg-px-ox phyric	plg>opx>ox
	PANI-15	57.14	Basaltic-andesite	glassy fine-grained plg-px seriate phyric	plg>opx>cpx
San Pedro	SPE-02	62.84	Trachyte	glassy fine-grained plg-px seriate glomerophyric	plg>opx=cpx
	SPE-07	56.38	Basaltic-andesite	fine-grained plg-ol-px seriate glomerophyric	plg>opx=cpx

[a] Recalculated to 100% anhydrous

Olivine-pyroxene-bearing rocks are the most common mafic volcanic type in our sample set (Fig. 2.3a) and are found at both Pliocene and Quaternary volcanoes (Table 2.2). These lavas differ however among each other in terms of their average crystal sizes and frequent seriate texture, ranging from very fine- to fine-grained. They contain dominantly olivine, orthopyroxene, clinopyroxene and plagioclase with minor amphibole, magnetite and ilmenite. The olivine crystals (up to 2 mm; < 10 vol%) include subhedral and rare skeletal forms, frequently contain Fe-Ti oxide inclusions, and often display disequilibrium textures around their outer edges such as embayments and orthopyroxene microcrysts. Orthopyroxene is common as a pristine phenocryst (up to 1 mm) and microcryst (up to 0.2 mm) with usual abundance < 20 vol%. Orthopyroxene crystals are euhedral to subhedral and occur individually or in small clusters with plagioclase and clinopyroxene. Clinopyroxene occurs as euhedral to subhedral crystals (up to 2 mm; < 15 vol%) or as reaction rims surrounding orthopyroxene phenocrysts and, similar to orthopyroxene, clinopyroxene crystals may occur individually or as glomerocrysts. A few samples contain olivine ± orthopyroxene or olivine ± clinopyroxene only, but plagioclase occurs as a phenocryst phase (up to 2.5 mm; < 40 vol%) in all but six olivine-pyroxene-bearing lavas from Cerro Carcote, Chela and La Poruñita (Table 2.2).

Pyroxene-bearing lavas from individual volcanic centres show similar mineral assemblages (Fig. 2.3b), although optical microscope observations highlight some variability in modal mineralogy, texture, and grain size between different samples (Table 2.2). These lavas are very fine- to fine-grained (seriate texture) with variable phenocryst and microcryst abundances (> 5 to ca. 55 vol%). The most common assemblage is, in order of decreasing abundance, plagioclase, orthopyroxene, clinopyroxene as phenocrysts (Fig. 2.3b), with amphibole, olivine, Fe-Ti oxides as microcrysts. Alternatively, some samples show elongated amphibole (up to 1.2 mm; < 2 vol%) and/or magnetite ± ilmenite (0.2 to 0.7 mm; < 3 vol%) as phenocrysts. Orthopyroxene and/or clinopyroxene can also appear as minor phases. Plagioclase usually occurs as individual phenocrysts, up to 2.5 mm, (< 50 vol%) or in orthopyroxene-clinopyroxene-magnetite glomerocrysts. Orthopyroxene (up to 2 mm; <

15 vol%) and clinopyroxene (up to 2 mm; < 10 vol%) occur as subhedral to euhedral tabular crystals. Replacement of olivine by orthopyroxene or orthopyroxene by clinopyroxene is common around the phenocryst outer edges. Some pyroxenes show resorption features and/or Fe-Ti oxide inclusions. Crystals are then set in a glassy to hypocrystalline groundmass with microlites of plagioclase, orthopyroxene, clinopyroxene, amphibole, magnetite, ilmenite and olivine. These lavas are rather compact and show low vesicularity (< 10 vol%).

2.4.2 Whole-rock geochemical and isotope composition

The full geochemical dataset of the samples from this study is provided in the Supplementary Material 1 (Table S1). The suite of samples comprises medium- to high-K calc-alkaline basaltic-andesites to dacites, with some rare basaltic-trachyandesite and trachyandesite compositions (Fig. 2.4). All studied rocks are subalkaline (Fig. 2.4a) and metaluminous in terms of the aluminum saturation index (molar A/CNK = 0.70-0.93; Zen, 1986). The variation of the major elements shows an increase in K_2O (Fig. 2.4b) and a decrease in FeO*, MnO and CaO with increasing silica, whereas Al_2O_3, Na_2O and P_2O_5 remain nearly constant.

The Pliocene lavas have a wide range of SiO_2 contents (SiO_2 = 54.6 to 63.2 wt%; Fig. 2.4), however most are classified as high Mg# lavas (44-57 Mg#; Kelemen et al., 2003). These samples show a well-defined negative trend of MgO against SiO_2 (Fig. 2.5a) and MgO correlates positively with Ni and Cr but scatters somewhat around 4 wt% MgO (Fig. 2.5b-c). Conversely, Sr shows no correlation with MgO (Fig. 2.5d). Quaternary lava samples (SiO_2 = 53.2 to 62.8 wt%; Fig. 2.4) classify as evolved, high Mg# and primitive lavas (Kelemen et al., 2003), ranging from 35 to 62 Mg#. These samples reveal the same correlations between silica and compatible trace elements with respect to MgO as seen in the Pliocene samples (Fig. 2.5).

All samples are enriched in large ion lithophile elements (LILE) relative to high field strength element (HFSE) normalized to primitive mantle concentrations (McDonough and Sun, 1995; Fig. 2.6a), consistent with typical continental arc compositions. The primitive mantle-normalized multi-element diagram (Fig. 2.6a) exhibits a pronounced negative Nb-Ta anomaly, a positive anomaly in Sr, K and Pb, and enrichment in Rb, Th and U. Chondrite-normalized rare earth element (REE; McDonough and Sun, 1995) patterns of the studied rock samples are enriched in light REE (LREE) relative to the depleted heavy REE (HREE) (La/Yb_N = 4.28-19.13; Fig. 2.6b). A weak negative Eu anomaly (Eu/Eu* = 0.65-0.91) characterizes all studied samples (Fig. 2.6b).

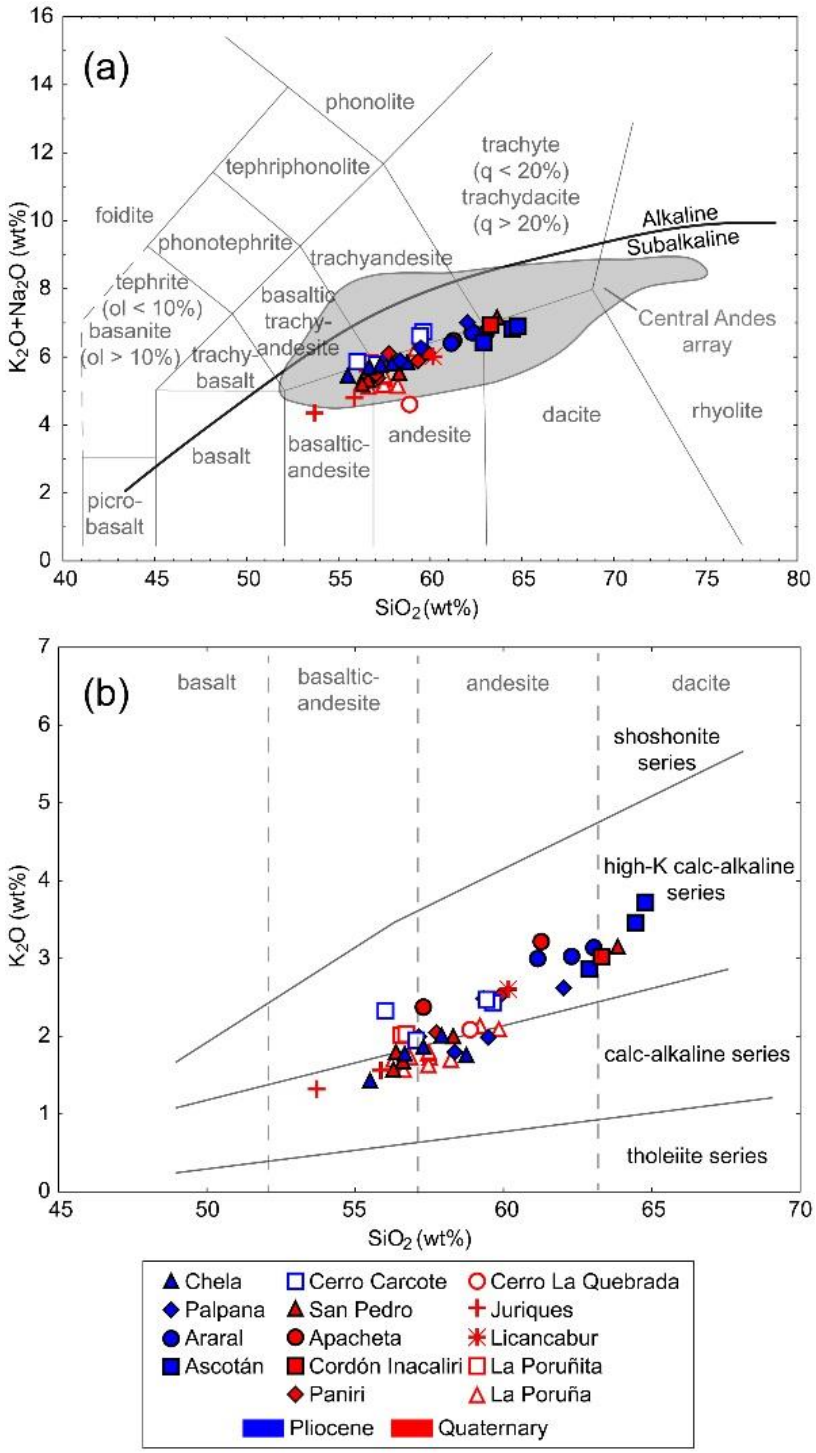

Fig. 2.4. (a) TAS diagram (Le Maitre et al., 1989) for volcanic rocks from the studied volcanoes. Solid line discriminates between alkaline and subalkaline rocks (Irvine and Baragar, 1971). Grey field represents the Central Andes array (Mamani et al., 2010). (b) K_2O vs. SiO_2 classification diagram after Peccerillo and Taylor (1976).

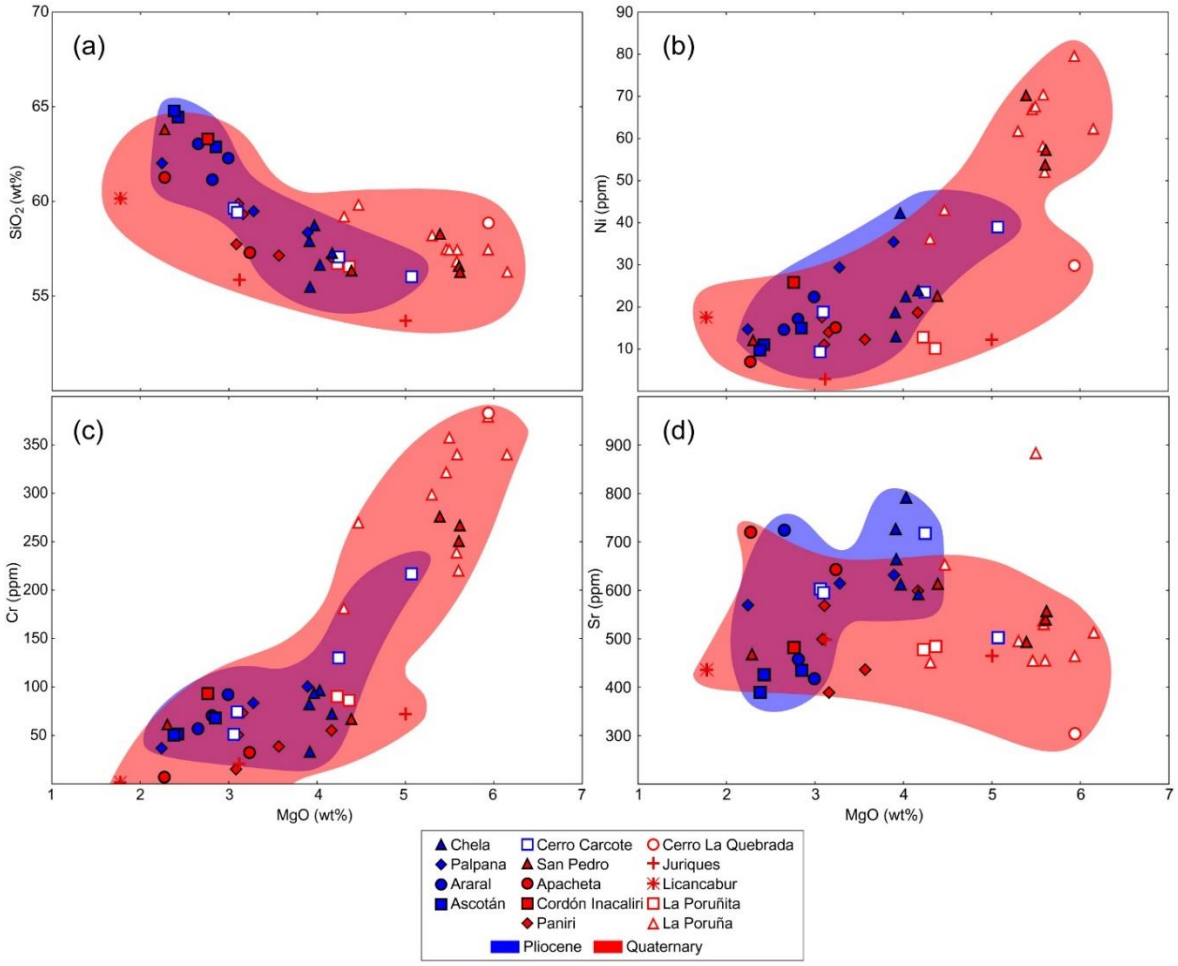

Fig. 2.5. Variation diagrams for the samples studied: (a) SiO_2 (wt%) vs. MgO (wt%). (b) Cr (ppm) vs. MgO (wt%). (c) Ni (ppm) vs. MgO (wt%). (d) Sr (ppm) vs. MgO (wt%). Note that the Pliocene samples (blue) tend to show slightly more restricted compositional ranges than the Quaternary samples (red).

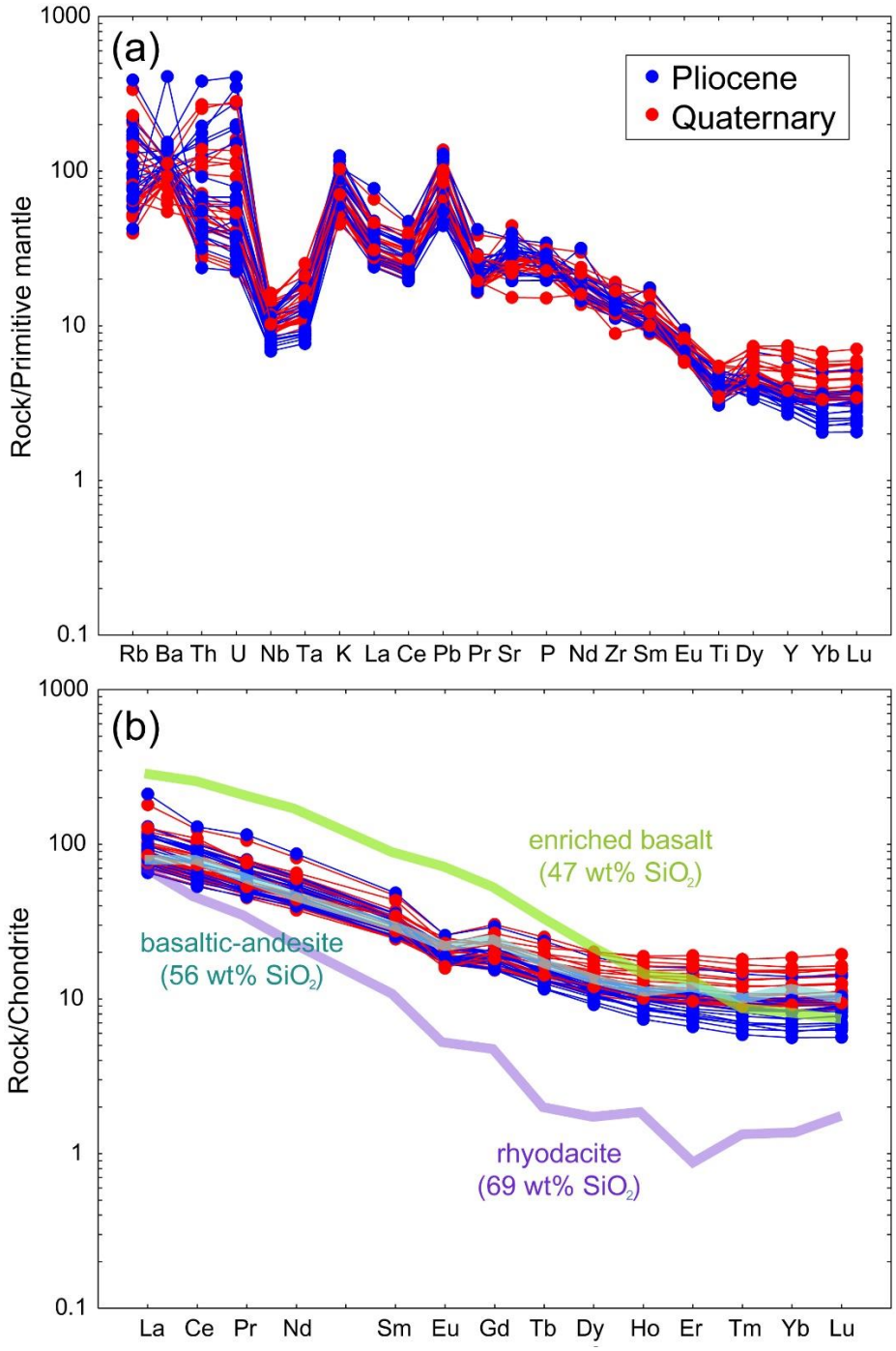

Fig. 2.6. Multi-element diagrams for analysed samples normalized to (a) primitive-mantle and (b) chondrite. (b) Chondrite-normalized rare earth element patterns of the studied rock samples are compared with the end-members suggested for the Central Andean magmatism (Blum-Oeste and Wörner, 2016), overlapping widely with the basaltic-andesite trend. Normalization values from McDonough and Sun (1995).

The $^{87}Sr/^{86}Sr$ and $^{143}Nd/^{144}Nd$ ratios range from 0.705541 to 0.708746, and 0.512208 to 0.512513, respectively. From the Sr-Nd isotope diagram (Fig. 2.7), a pronounced negative correlation is observed, with a few samples showing scattered $^{143}Nd/^{144}Nd$ ratios with respect to Sr isotope ratios at ca. 0.7065. Nd isotopes ratios from the Quaternary rocks have a relatively restricted range compared to the variability revealed for the Pliocene samples (Fig. 2.7). The correlation of Sr and Nd isotope ratios with respect to silica and Sr contents reveal well-defined differentiation trends for Pliocene lavas, whereas Quaternary rocks show an overall scattered distribution (Fig. 2.8).

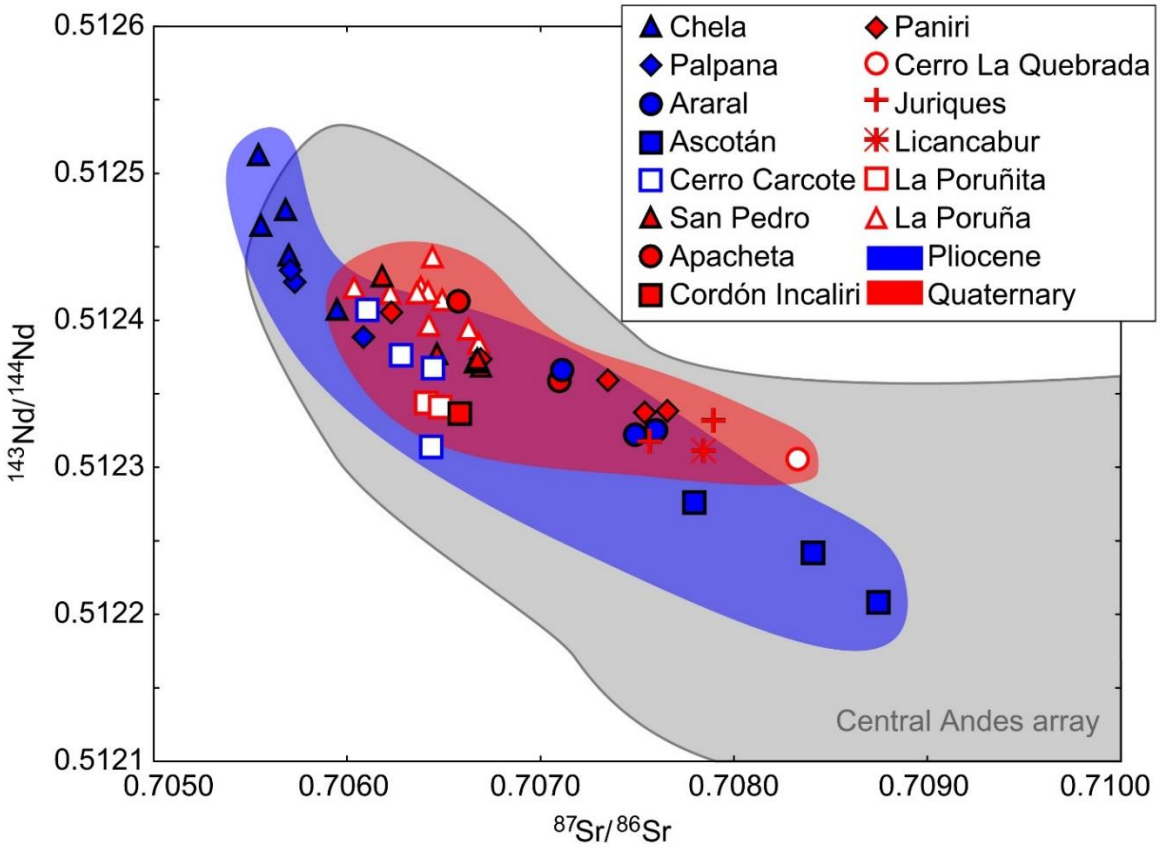

Fig. 2.7. $^{143}Nd/^{144}Nd$ vs. $^{87}Sr/^{86}Sr$ diagram for the studied samples. Grey field represents the isotope composition of Central Andes modern volcanism (Scott et al., 2018, and references therein). There is a strong correlation between $^{87}Sr/^{86}Sr$ and $^{143}Nd/^{144}Nd$ overall, with a differentiation trend more restricted to the Quaternary samples (red) relative to the Pliocene rocks (blue).

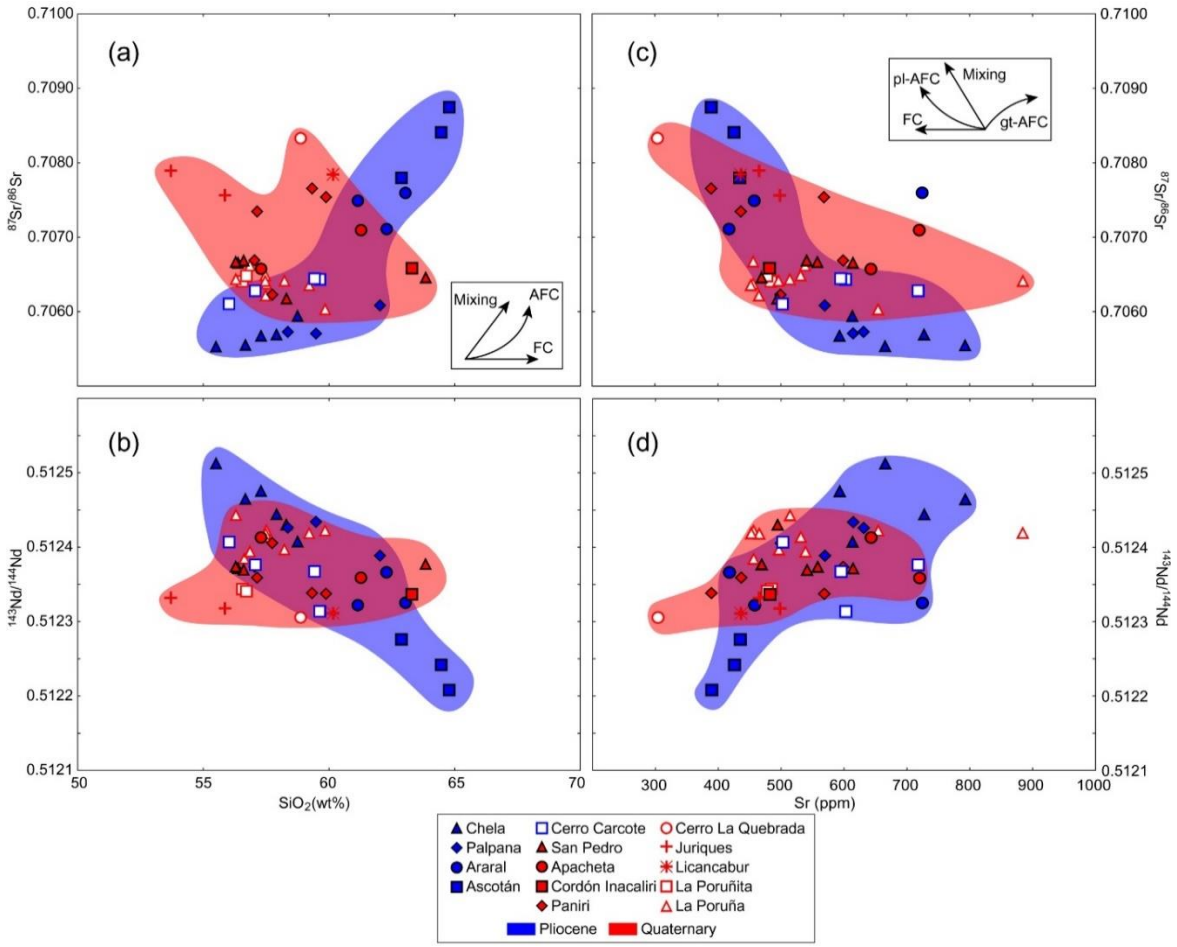

Fig. 2.8. $^{87}Sr/^{86}Sr$ and $^{143}Nd/^{144}Nd$ vs. SiO_2 (wt.%) (a, b) and Sr (wt.%) (c, d). Isotopic data demonstrate a large isotopic variation even in the less evolved melts. Inset shows the typical trends for: (a) mixing, assimilation and fractional crystallization (AFC), and fractional crystallization (FC) processes; and (c) mixing, plagioclase- and garnet-dominated assimilation and fractional crystallization (pl-AFC and gt-AFC, respectively), and fractional crystallization (FC) processes.

2.5 Discussion

2.5.1 Magmatic differentiation processes and temporal variations

The major and trace element compositions define a strong subduction-related arc signature, typical for lavas in the Central Andes (e.g. Davidson et al., 1991; Hildreth and Moorbath, 1988; Mamami et al., 2010). There is a large variation in the Th-U concentrations of the samples (Fig. 2.6a) that is influenced by different degrees of differentiation in the continental crust as the most differentiated samples (>60 wt% SiO_2) show the higher Th and U concentrations (e.g. Fig. 2.9a). The overall REE element character of the samples generally resembles the basaltic-andesite end-member proposed by Blum-Oeste and Wörner (2016) (Fig. 2.6b), suggested to reflect an originally asthenospheric mantle source for the studied rocks. Their $^{87}Sr/^{86}Sr$ and $^{143}Nd/^{144}Nd$ ratios overlap consistently with the overall Central Andes array (Fig. 2.7). Petrographic descriptions reveal a relative homogeneity of mineral assemblages of (in order of decreasing abundance) plagioclase, orthopyroxene, clinopyroxene and olivine (Fig. 2.3; Table 2.2) and plagioclase, orthopyroxene and clinopyroxene crystal morphologies suggest they are usually in equilibrium with the host magma. The negative correlation between Eu/Eu* and SiO_2 (Fig. 2.9b) and positive trends of CaO, FeO, Cr and Ni with regard to MgO (Fig. 2.5) are consistent with fractional crystallization of the mineral assemblages observed in the samples (plagioclase + pyroxene ± olivine; Fig. 2.3) (McKay, 1989; Taylor and McLennan, 1988). However, disequilibrium textures in plagioclase (i.e. sieve textures) and in pyroxene (i.e. resorption features) are locally present and embayments are relatively common in olivine (Fig. 2.3). Embayments and orthopyroxene corona rims on olivine crystals (Fig. 2.3a) indicate chemical and thermal disequilibrium between the crystals and the melt (Streck, 2008), probably caused by the reaction of early formed olivine with SiO_2 in the melt.

The most widely accepted generation model for basaltic-andesite arc magmas in the Central Andes comprises a lower crustal MASH (Melting-Assimilation-Storage-Homogenization) zone at ca. 70 km crustal depth where mantle-derived magmas stagnate and mix and homogenise with lower crustal

melts (e.g. Davidson et al., 1991; Hildreth and Moorbath, 1988; Wörner et al., 2018). The Sr and Nd isotope data presented here reveal large isotopic variation even in the basaltic-andesite melts (Figs. 2.7 and 2.8), and some individual volcanoes demonstrate that further differentiation of such basaltic-andesite melts has been caused by coupled fractionation and assimilation of the continental crust (AFC, DePaolo, 1981; e.g. Cerro Carcote, Chela, Palpana), or by mixing with evolved contaminated melt (i.e. APMB) in the magma reservoir (e.g. Ascotán, Juriques, Paniri) (Fig. 2.8a-b). The occurrences of relatively low silica lavas with high Sr isotope ratios (Fig. 2.8a; e.g. La Poruña, San Pedro) can possibly be explained by selective assimilation of partial melts and low-temperature melting components, e.g. as a consequence of selective incorporation of evolved crustal components or partial crustal melts into the rising mafic magmas (e.g. Meade et al., 2014; Troll et al., 2005). Most samples have depleted Sr/Y ratios compared with the Central Andean array (Fig. 2.9c), although they reflect that the differentiation processes were likely controlled by either mid (Sr/Y > 30) and/or shallow crustal sources (Sr/Y < 30). The relatively flat slopes for the HREE of the studied lavas may suggest a magmatic evolution dominated by low-pressure (garnet-free) processes (Fig. 2.6b; cf. Davidson et al., 2007; O'Callaghan and Francis, 1986). Indeed, low Sr/Y and La/Yb ratios support significant plagioclase fractionation and the absence of garnet or amphibole, in the source (Fig. 2.9c-d). Since garnet and amphibole are capable of controlling La/Yb ratios (Davidson et al., 2013), the Dy/Yb ratios versus silica is also plotted (Fig. 2.9e), as this ratio is sensitive to the presence of these phases. Low Dy/Yb ratios are indicative of the absence of garnet fractionation but may show evidence for the involvement of residual amphibole during differentiation (Fig. 2.9e), consistent with the main petrographic observations, as amphibole crystals appeared as minor phase in most samples (Section 2.4.1). Therefore, magma mixing, AFC or selective assimilation processes in a garnet-free differentiation environment at mid to upper crustal levels are required to fully explain most of the petrographic and geochemical characteristics of the studied samples.

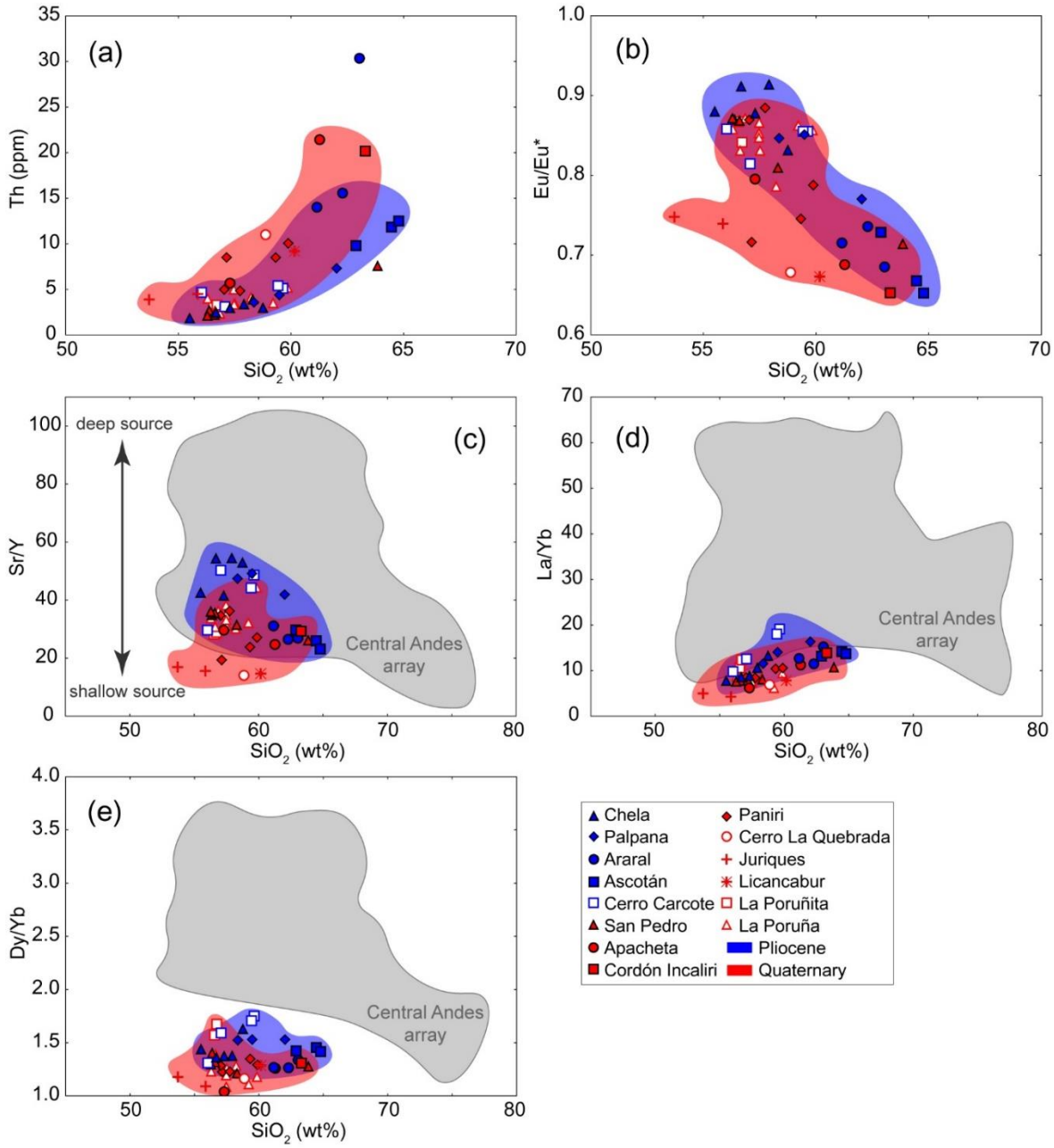

Fig. 2.9. Diagrams of (a) Th (ppm), (b) Eu/Eu*, (c) Sr/Y, (d) La/Yb and (e) Dy/Yb vs. SiO_2 for the studied samples. Grey field represents the Central Andes array (Mamani et al., 2010). There is no significant temporal variation in these parameters between the analysed samples in this work, apart from that incompatible element ratios are slightly higher in the Pliocene samples in respect to the Quaternary samples, but still low enough to be related to mid-shallow crustal sources.

As noted above, major and trace element concentrations and the radiogenic Sr and Nd isotopes support varied magmatic differentiation processes and variable degrees of crustal additions. Pliocene and Quaternary samples have wide ranges of e.g. SiO_2 (Fig. 2.4), MgO (Fig. 2.5), $^{87}Sr/^{86}Sr$ and $^{143}Nd/^{144}Nd$ ratios (Fig. 2.7), but these are relatively restricted when each volcano is examined individually. Thus, a remarkable compositional heterogeneity among the eruptive centres is recognized from the studied samples. It is also noted an apparent compositional variability with time, for example, in $^{87}Sr/^{86}Sr$ and $^{143}Nd/^{144}Nd$ ratios. Radiogenic isotope data for Pliocene samples leads to an expectation of a systematic increase of magma differentiation with time, however variable ratios are recognized in the Quaternary samples (Fig. 2.10). These compositional variations between the studied rocks is perhaps in part related to the spatial distribution of the volcanoes and may be linked to the projected APMB reservoir (Ward et al., 2014; Zandt et al., 2003). Thus, it is particularly relevant to discuss the influence of the APMB on the magmatic plumbing system of the erupted mafic to intermediate lavas of our study (Figs. 2.1 and 2.2).

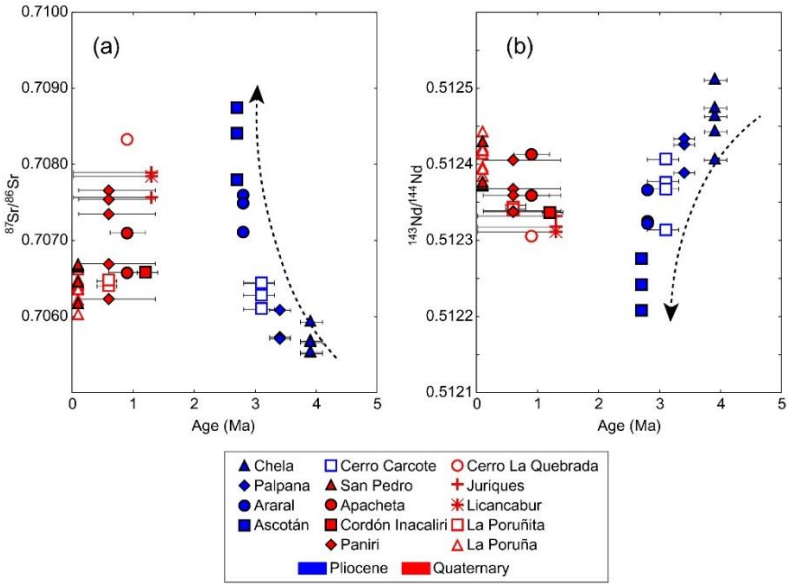

Fig. 2.10. (a) $^{87}Sr/^{86}Sr$, and (b) $^{143}Nd/^{144}Nd$ vs. average Age (Ma) for the studied samples. Bars indicate maximum and minimum ages (Table 2.1). The Pliocene samples show a systematic increase and decrease of Sr and Nd isotope ratios through the time, respectively, whereas Quaternary samples show a scattered distribution.

2.5.2 Spatiotemporal relation with the Altiplano-Puna Magma Body

To further understand the magmatic evolution of the studied mafic to intermediate Pliocene to Quaternary Andean volcanism at 21°10'-22°50'S, the spatiotemporal framework of our samples relative to the APMB ought to be considered. A 3-D S-wave velocity model defines the dimensions of the APMB (Fig. 2.11), as of 4-30 km crustal depth and with the largest lateral extension of the partial melt body at a depth of 15 km (2.9 km/s velocity contour; Ward et al., 2014). The APMB is viewed as the source of the APVC ignimbrites (Zandt et al., 2003) and as a contaminant to the recent volcano plumbing systems (e.g. Godoy et al., 2019; Taussi et al., 2019). A major ignimbrite pulse manifested locally at 8.3 Ma (e.g. Sifon ignimbrite, Salisbury et al., 2011) as well as the extensive Pliocene to Quaternary volcanism (Fig. 2.11) allow the assertion that the APMB has remained active over the last 8 Myr beneath this study area. It is thus proposed that the compositional variability observed here, as larger variations are reflected against differentiation indexes (Section 2.5.1; e.g. SiO_2, MgO, $^{87}Sr/^{86}Sr$; Figs. 2.7, 2.8 and 2.10), was influenced by the APMB reservoir. A systematic increase of the degree of crustal assimilation by ascending magmas as the vertical thickness of the APMB increased for the < 2 Ma volcanism was proposed by Godoy et al. (2017), however the temporal variation prior to the < 2 Ma volcanism is also considered as our samples span a longer time period. To evaluate the effect of variable isotope composition as a function of silica and assess the difference between volcanoes for mafic starting compositions, baseline isotopic values of the least silicic sample at each volcano are considered. Baseline isotopic compositions are thought to be inherited in the lower crustal MASH zone and are affected to a limited degree by crustal processes before eruption (Davidson et al., 1990; Freymuth et al., 2015; Hildreth and Morbath, 1988). A compilation of geochemical data of the low silica (< 64 wt% SiO_2) lavas erupted in the western border of the APMB, dated from Pliocene to the present (Fig. 2.11), it was used to determine the baseline isotopic values (Supplementary material 2, Table S2.1). Reference data in Fig. 2.12 (Supplementary material 2, Table S2.2) include Sr and Nd baseline radiogenic isotope ratios of twenty-seven (27) stratovolcanoes and monogenetic centres, including Uturuncu volcano (Bolivia) located in the centre

of the current APMB. Pliocene and Quaternary volcanoes with the least evolved baseline values overlap with the borders of the APMB, whereas volcanoes located further inwards of this boundary show a more differentiated character (Fig. 2.12). This is further consistent with the variation in the petrography between the analysed samples in this work, as the olivine-pyroxene-bearing rocks are more common along the outer edge of the APMB (Table 2.2; Fig. 2.3). The olivine-pyroxene-bearing rocks generally show less evolved compositions compared with the pyroxene-bearing samples (Table 2.2), and remarkably La Poruña and San Pedro preserve the less evolved characteristics among the studied volcanoes in terms of compatible element contents (e.g. MgO, Cr, Ni; Fig. 2.5), which may be interpreted as local escape of mafic magma around the APMB. As the differentiation processes such as magma mixing, AFC, or selective assimilation vary from volcano to volcano (Section 2.5.1), the petrological variations seem also spatially related to the areal extent of the different velocity contours estimated for the APMB (Fig. 2.12). S-wave velocities indicate an increase in melt/fluid percentage from the margin to the centre of the partially molten body from ca. 4 vol% (3.2 km/s) to ca. 10 vol% (2.9 km/s), and up to 25 vol% (<1.9 km/s) (Ward et al., 2014; Fig. 2.12). Since portions of the APMB with low S-wave velocities (≤2.9 km/s) contain higher amounts of melt and/or fluids (Ward et al., 2014), the ascending mafic magmas would be affected by high degrees of crustal assimilation and contamination. Therefore, such parental magmas passing through the APMB result in more evolved final compositions, whereas those erupted outside likely involved more restricted incorporation of derivate melts from the APMB (Figs. 2.11 and 2.12). These spatiotemporal variations of the baseline isotopic values into the S-wave velocity contours also lead us to suggest a possible APMB evolution through time. Most of the volcanoes located outside or within the 3.2 km/s contour share similar $^{87}Sr/^{86}Sr$ and $^{143}Nd/^{144}Nd$ baseline ratios (Fig. 2.12), which may suggest fixed spatial limits for a relatively stationary APMB in time. Conversely, volcanoes constructed in the portions of low velocities (≤2.9 km/s) exhibit more evolved but variable baseline compositions (Fig. 2.12), which it is interpreted as a reflection of continuous replenishment of magma from the mantle to the mid to upper crust that keep the APMB thermally active with contours of high partial melt potentially

fluctuating in time. Judging on the location of Pliocene volcanoes (i.e. Araral and Ascotán) and younger volcanoes (e.g. Cerro del Azufre, Apacheta, Paniri) on the same velocity contour (Fig. 2.12a), and the elevated baseline Sr-isotope ratios in the Pliocene samples (Fig. 2.12b), the APMB contours with high percentages of partial melting (>10 vol%) may have been slightly more areally extensive in the Pliocene suggesting that these contours have shrunk since then.

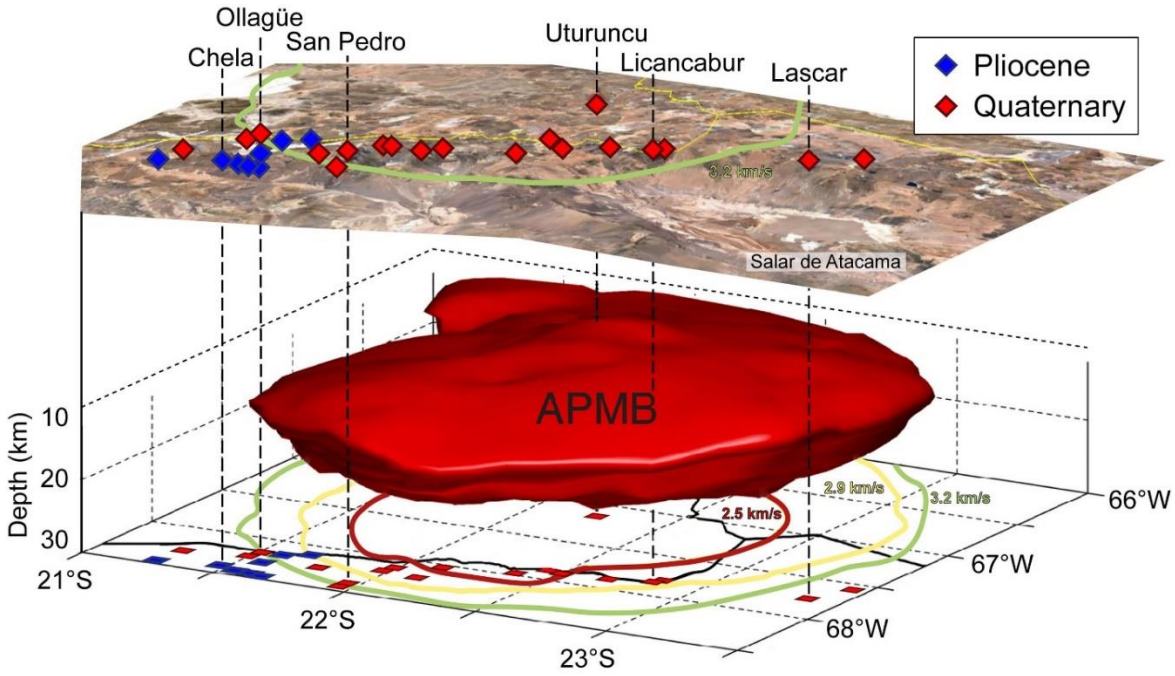

Fig. 2.11. 3-D volume model of the 2.9 km/s velocity contour (after Ward et al., 2014) showing the distribution of the Altiplano-Puna Magma Body and location of representative Pliocene to Quaternary volcanoes erupted above the partial melt anomaly.

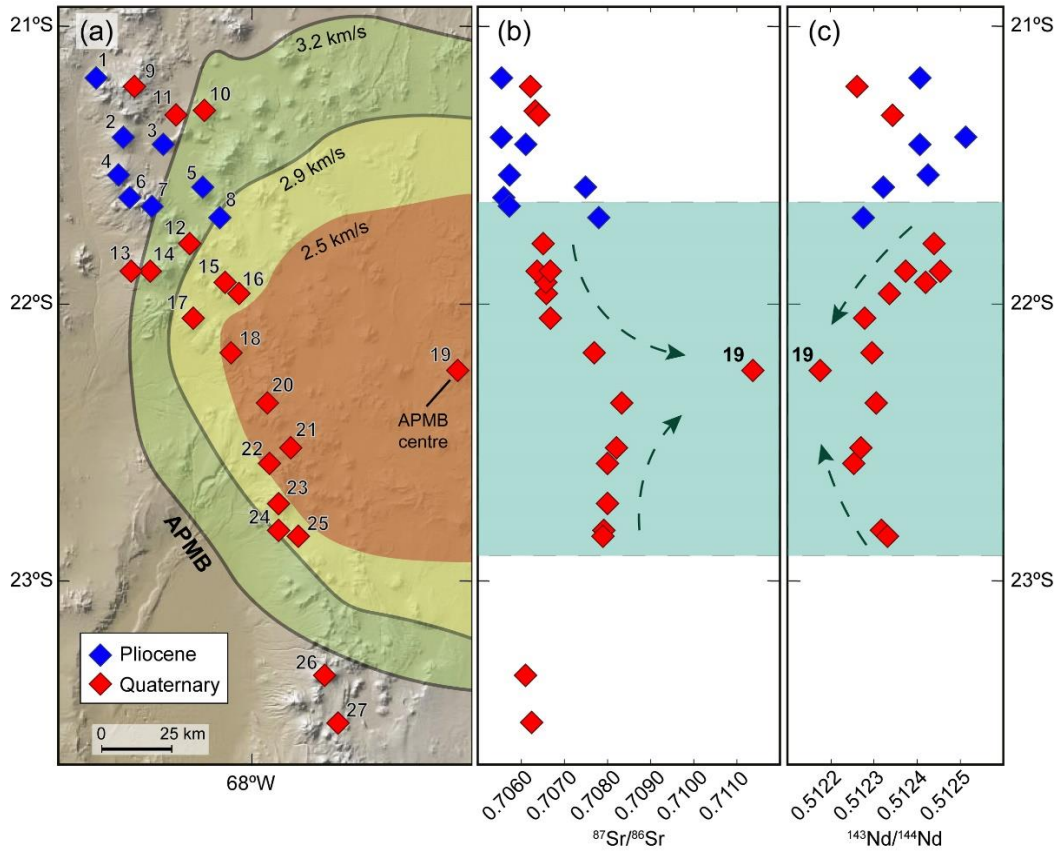

Fig. 2.12. (a) Global Multi-Resolution Topography (www.geomapapp.org; Ryan et al., 2019) image showing the location of the Pliocene and Quaternary volcanoes included in this study. Coloured areas indicate the estimated cross-section and extent of the APMB based on the joint ambient noise-receiver function inversion S-velocity model from Ward et al. (2014). (b, c) Baseline Sr (b) and Nd (c) isotopic values as a discriminant to assess the spatial and temporal evolution of the less silicic volcanism. Most of the Pliocene and Quaternary volcanoes outside or within the margin of the APMB show similar least evolved baseline values, whereas more evolved baseline values tend to appear further inwards of the melt body. Pliocene: 1 – Miño, 2 – Chela, 3 – Cerro Carcote, 4 – Palpana, 5 – Araral, 6 – Cerro de las Cuevas, 7 – Cebollar and 8 – Ascotán. Quaternary: 9 – Aucanquilcha, 10 – Ollagüe, 11 – La Poruñita, 12 – Cerro del Azufre, 13 – La Poruña, 14 – San Pedro, 15 – Apacheta, 16 – Cordón Inacaliri, 17 – Paniri, 18 – Toconce, 19 – Uturuncu, 20 – Cerro La Quebrada, 21 – Putana, 22 – Colorado, 23 – Sairecabur, 24 – Licancabur, 25 – Juriques, 26 – Lascar and 27 – Cerro Overo. All data shown here are presented in Supplementary material 2 (Table S2.2).

Most petrological models include distinct levels of melt accumulation and melting in the continental crust where the basaltic-andesite magmas from the lower crust become progressively more evolved at shallower depths (e.g. de Silva et al., 2006; Hildreth, 1981; Hildreth and Moorbath, 1988). The presence of the large APMB system implies a steady supply of basaltic-andesite melts into the crust that accumulate in an underplating zone beneath the APMB in the mid-crust (Perkins et al., 2016; Fig. 2.13). These dense mafic magmas in the underplating zone are not able to penetrate easily into the overlying low density APMB body and so tend to accumulate in the lower part of the reservoirs (e.g. Huber et al., 2009), however a larger thermal aureole surrounding the APMB is suggested by highest S-wave seismic velocities of 2.9 to 3.2 km/s (Ward et al., 2014), which could represent a particularly ductile zone in the Central Andes that facilitated the movement of the ascending mafic magmas through a lined route and gave rise to the crustal melts of the uppermost crust. This implies that after the late Miocene initiation of the APMB, parental basaltic-andesite escape the lower crustal MASH zone and the APMB by lateral migration and ponding from where these finally escape by e.g. direct ascent, likely exploiting upper crustal weakness zones (e.g. Giambiagi et al., 2016; Sellés and Gardeweg, 2017; Tibaldi et al., 2017) to migrate to the surface on the periphery of the APMB (Figs. 2.2 and 2.13). This model allows for variable degrees of parental magma-crust interaction with respect to their variable ascent routes either passing through or bypassing the APMB on their way to the surface, as the compositions of our mafic to intermediate magmas are strongly dependent on their eruption location relative to the larger APMB (Figs. 2.12 and 2.13).

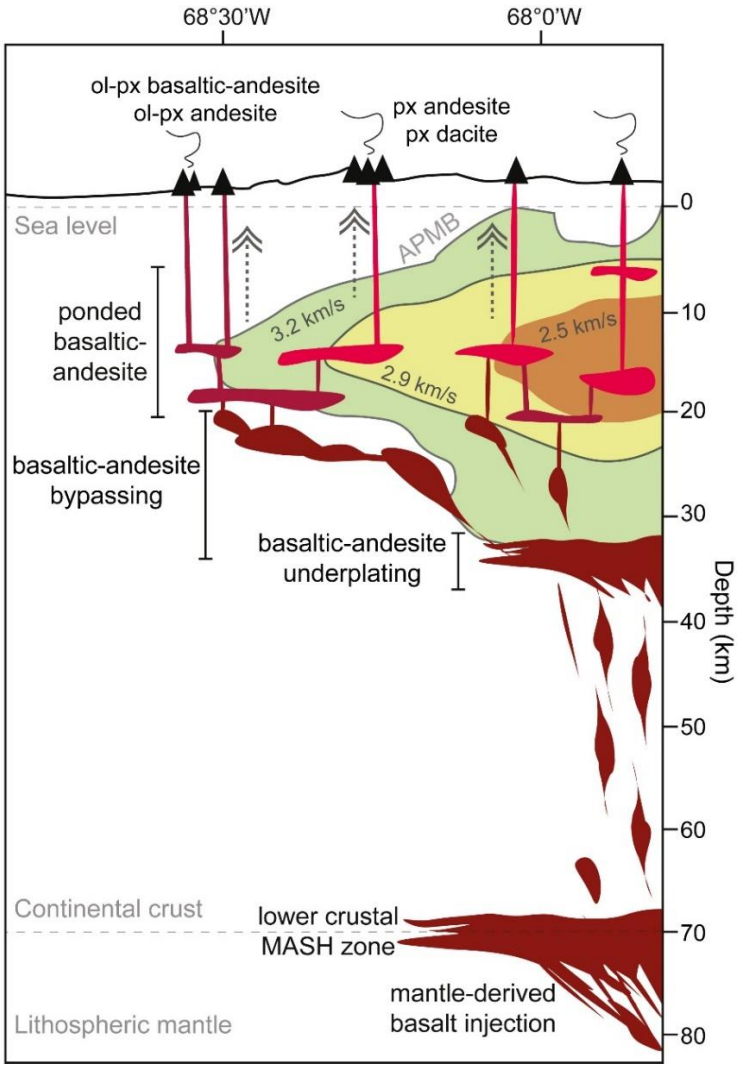

Fig. 2.13. Schematic cross-section of the continental crust showing the proposed magmatic evolution of the Pliocene to Quaternary least silicic magmas beneath the Altiplano-Puna Volcanic Complex province. Coloured areas indicate the estimated cross-section of the APMB based on the joint ambient noise-receiver function inversion S-velocity model from Ward et al. (2014). It is suggested that parental magmas are injected beneath the APMB in an underplating zone after avoiding significant fractional crystallization in the MASH zone. A fraction of basaltic-andesite magma is diverted to the margins of the APMB, where it stalls, differentiates and fractionates in a mid to upper crustal plumbing system before ascent and eruption. Magmas that ascend through more central portions of the APMB, in turn, show higher rates of magma-crust interaction, reflecting higher uptake of APMB material during their journey.

2.6 Conclusions

The mafic to intermediate Pliocene to Quaternary volcanism that is concentrated on the western boundary of the Altiplano-Puna Volcanic Complex (between 21º10' to 22º50'S) occurs as lava flows from stratovolcanoes and as monogenetic cones. The investigated volcanic rocks are olivine and two-pyroxene phyric and range from medium-K to high-K calc-alkaline basaltic-andesite to dacite magmas with large compositional heterogeneity in major and trace element concentrations (e.g. SiO_2 = 53.2 to 63.2 wt%, MgO = 1.74 to 6.08 wt%, Cr = 2 to 382 ppm; Sr = 304 to 885 ppm) and in Sr and Nd isotopes ($^{87}Sr/^{86}Sr$ = 0.7055-0.7087; $^{143}Nd/^{144}Nd$ = 0.5122-0.5125). This compositional variability is explained by the interplay of parental basaltic-andesite magma assimilating continental crust or various amounts of APMB derivate melts. Differentiation processes such as magma mixing, AFC, or selective assimilation occur at relatively low pressures in the middle to upper crust, but the development of these processes appears spatially variable from volcano to volcano. The least evolved eruptions occurred outside or just within the outer borders of the APMB, with volcanoes further inward from this border showing more differentiated overall geochemical and mineralogical features. The spatial isotope development of the magmatic system appears to be a useful indicator to evaluate the temporal evolution of mafic rocks in the region. The APMB remained thermally active since the late Miocene due to a steady replenishment of mafic melt from depth, represented by the investigated mafic to intermediate eruptives but may have slightly reduced its molten extent below the region at least since the Pliocene. The more evolved Pliocene samples possibly record a somewhat larger areal extent of the APMB contours with high percentages of partial melting (>10 vol%). Finally, it is proposed that the location of the less evolved magmas of the modern arc in the Altiplano-Puna Volcanic Complex is linked to the APMB borders where ascending parental basaltic-andesite magmas are diverted to avoid significant compositional modification prior to eruption. The study of these low-silica magmas thus offers a window into the 'parental' magma chambers that underplate the APMB and the state and size of the underlying larger APMB.

2.7 Examiners' non-typographic corrections and comments

To fully characterise the studied rocks new petrography, whole-rock major element, trace element and radiogenic isotope data of forty-eight (48) fresh volcanic rock samples are presented. This study started with detailed standard optical petrography of 48 thin sections (one per sample) and complemented with automated mineralogical analyses (See Chapter 3, Section 3.3.2 for analytical details). All 48 samples were crushed in an iron jaw crusher and pulverized in agate mills at the Department of Geological Sciences, University of Cape Town (South Africa).

The primitive mantle-normalized multi-element diagram (Fig. 2.6a) exhibits a pronounced negative Nb-Ta anomaly, a negative Ti anomaly, a positive anomaly in Sr, K and Pb, and enrichment in Rb, Th and U, which is expected for lavas in the Central Andes. The trace element ratios, LILE/HFSE and REE patterns (Fig. 2.6) may suggest a magmatic evolution dominated by low-pressure (garnet-free) processes at mid-upper crustal levels (ca. < 50 km depth; Godoy et al., 2014). The overall REE patterns of the studied samples are similar to the basaltic-andesite end-member, with lower LREE and higher HREE with respect to the enriched basalt and rhyodacite end-members, respectively (Fig. 2.6b).

The Sr and Nd isotope data reveal large isotopic variations by individual volcanoes (Fig. 2.8), such variability is postulated to reflect parental magmas assimilating variable amounts of basement rocks with highly radiogenic Sr isotope ratios (e.g. $^{87}Sr/^{86}Sr$ = 0.7085 to 0.7278, Lucassen et al., 2001; See also Section 5.2 in Chapter 5), or mixing felsic and evolved melts derived from the APMB (Fig. 2.13).

Please note that in Fig 2.11 the upper part is in approximate coincidence with the lower part.

Chapter 3

Differentiation regime in the Altiplano-Puna Volcanic Complex: case studies of La Poruña mafic eruptions

This chapter is based on the work published as:

González-Maurel, O., Godoy, B., le Roux, P., Rodríguez, I., Marín, C., Menzies, A., Bertin, D., Morata, D., Vargas, M., 2019. Magmatic differentiation at La Poruña scoria cone, Central Andes, northern Chile: Evidence for assimilation during turbulent ascent processes, and genetic links with mafic eruptions at adjacent San Pedro volcano. Lithos, 338-339:128-140. https://doi.org/10.1016/j.lithos.2019.03.033.

Individual volcanoes demonstrated that contamination of parental melts has been caused by different differentiation processes as a function of their spatiotemporal framework (Chapter 2). New insight into the petrological processes that governed the magmatic evolution of weakly evolved mafic lavas erupted from La Poruña are presented. La Poruña is a well-preserved Quaternary scoria cone erupted on the western border of the APMB and composed of mafic pyroclastic material and an extensive basaltic-andesite to andesite lava flow. New petrography, geochronology, geochemistry and radiogenic isotope data describe a suite of olivine- and pyroxene-phyric mafic samples. These data are used to constrain magmatic evolutionary processes acting on these La Poruña magmas, which slightly differ from the broadly accepted Central Andean magmatic model.

The following text is reproduced verbatim from the published paper mentioned above and only reformatted to comply fully with the Doctoral Degree Board (University of Cape Town) guidelines for Doctoral Thesis. A final Section 3.7 concludes the chapter in order to discuss examiners' non-typographic corrections and comments.

3.1 Introduction

The Neogene to Quaternary Central Andean magmatic arc, located in the Western Cordillera, is built on a 70 km thick continental crust (Beck et al., 1996). Modern volcanic activity is characterized by calc-alkaline to shoshonitic magmas and mainly comprised of andesitic to rhyolitic lava flows, the latter usually associated with ignimbrite deposits and felsic domes (Haschke, 2002; Mamani et al., 2010; Stern, 2004). Due to the magma chambers being emplaced within a very thick continental crust, true erupted basalts are scarce in the Central Andes, although mafic eruptives have been recognized in both the Western Cordillera and back-arc region (Fig. 3.1; e.g. Davidson and de Silva, 1992; 1995; Figueroa et al., 2009; Godoy et al., 2014; Kay et al., 1994; Maro et al., 2017; Mattioli et al., 2006; Wörner et al., 1994). While this unusual volcanism is associated with lithospheric delamination in the back-arc (e.g. Davidson and de Silva, 1995; Kay et al., 1994; Maro et al., 2017), within the modern arc it has been related to limited degrees of interaction with the Altiplano-Puna Magma Body (Godoy et al., 2017), a partially molten low-seismic velocity layer related to the construction of the Altiplano-Puna Volcanic Complex (Chmielowski et al., 1999; Schilling and Partzsch, 2001; Ward et al., 2014; Zandt et al., 2003). Within the western boundary of the Altiplano-Puna Volcanic Complex, between 21ºS to 22º50'S (Fig. 3.1), individual volcanoes demonstrated that contamination of the parental melts has been caused by different differentiation processes related to the spatiotemporal framework of the Altiplano-Puna Magma Body (Chapter 2). From these, the less evolved magmas are located marginal to the projected APMB reservoir, as the ascending parental mafic magmas avoided significant contamination by interaction with derivate melts from the large felsic body. La Poruña (21º53'S; 68º30'W) is one of the studied centres in Chapter 2 that reported the least evolved eruptions in the area and located in the western border of the current APMB (Fig. 3.1). This centre represents a unique, well-preserved scoria cone despite being a hundred thousand years old (Bertin and Amigo, 2019; Wörner et al., 2000). This cone is built of scoriaceous material and a basaltic-andesite flow field made up of innumerable small and large flow lobes and channels (Francis and Oppenheimer, 2004). La Poruña is considered a monogenetic peripheral edifice to the San Pedro stratovolcano, one of the

highest and best-preserved volcanic edifices of the Central Andes, representing the last eruptive episode on its evolutionary stage (Bertin and Amigo, 2019; Francis et al., 1974; O'Callaghan and Francis, 1986). A few petrological studies describe the nature and composition of the eruptions and the volcanic history of San Pedro in particular (e.g. Bertin and Amigo, 2019; Francis et al., 1974; O'Callaghan and Francis, 1986), however none account for either the petrogenesis of La Poruña nor the relation of the coeval mafic occurrences from both volcanoes. This unresolved possible relationship between the mafic eruptions from La Poruña and San Pedro motivates the current chapter. In this paper, new petrography, ^{40}Ar-^{39}Ar geochronology, and geochemistry and radiogenic isotope data are presented, together with a compilation of published datasets, of selected samples from La Poruña and San Pedro. The aim of this work is to present new insight into the differentiation regime(s) that controlled the magmatic evolution of the mafic eruptions from La Poruña and to determine their genetic relation with San Pedro mafic rocks.

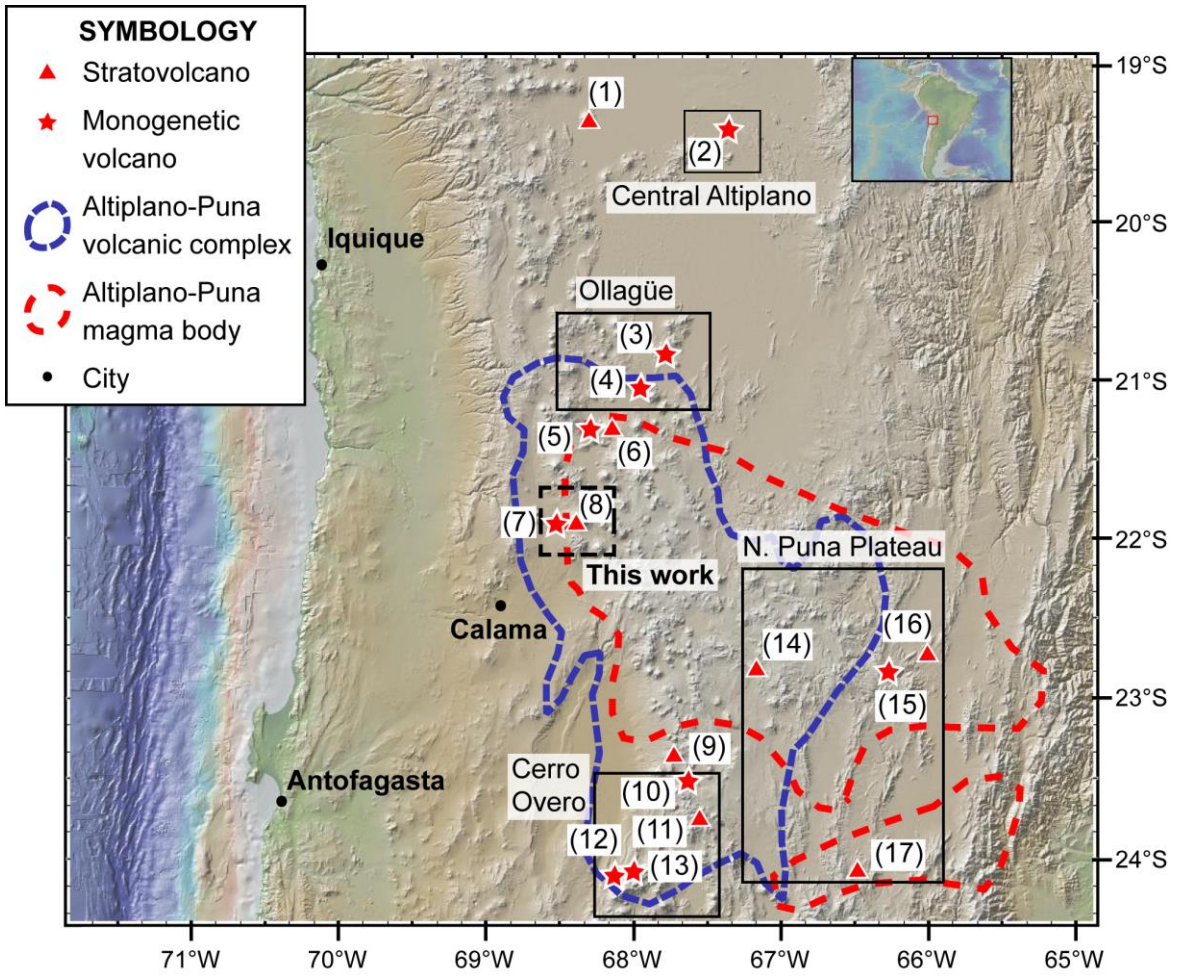

Fig. 3.1. Global Multi-Resolution Topography (www.geomapapp.org; Ryan et al., 2019) image of the Central Andes between 19º-24º30'S. Location of Central Altiplano and Ollagüe (Davidson and de Silva, 1992; 1995), northern (N.) Puna Plateau (Maro et al., 2017), and Cerro Overo (van Alderwerelt, 2017) regions are shown. Dashed black square indicates location of Fig. 3.2. Volcanic structures are: (1) Tata Sabaya; (2) Chiar Kkollu; (3) Cerro Luntapa; (4) Cerro Chiguana; (5) La Poruñita; (6) Ollagüe; (7) La Poruña; (8) San Pedro; (9) Lascar; (10) Cerro Overo; (11) Puntas Negras; (12) Tilocalar; (13) Cerro Tujle; (14) Cerro Zapaleri; (15) Cerro Barro Negro; (16) Cerro Rachaite; (17) Cerro Tuzgle.

3.2 Geological background

La Poruña is a 140 m high, 800 m in diameter, scoria cone composed of pyroclastic material and an extensive basaltic-andesite lava flow that is up to 8 km in length to the south-west of the vent (Fig. 3.2). This cone is located in the western margin of the APMB (Fig. 3.1; Bertin and Amigo, 2019; Francis et al., 1974; O'Callaghan and Francis, 1986), and was built on a basement of late Miocene ignimbrites (Bertin and Amigo, 2019; Salisbury et al., 2011; Sellés and Gardeweg, 2017), in the proximity of the San Pedro stratovolcano. Similar compositional patterns have been recognized in the mafic lavas of San Pedro and La Poruña (e.g. Godoy et al., 2014; O'Callaghan and Francis, 1986), whose related magmatic evolution is associated with local crustal structures that further facilitated magma ascent (Giambiagi et al., 2016; Marín, 2016; Sellés and Gardeweg, 2017; Tibaldi et al., 2017). Radiometric dating of the La Poruña lava flow has yielding two eruption $^{40}Ar/^{39}Ar$ ages of 110 ± 50 ka in whole-rock and 54 ± 24 ka in groundmass (Fig. 3.2; Bertin and Amigo, 2019), of which only one is consistent with the 103 ± 2 ka age measured in olivine crystals by the ^{3}He exposure method (Wörner et al., 2000). The whole volcanic deposit of La Poruña is considered monogenetic generating a relatively small-volume and short-lived singular eruption, thus a long-term eruption or a significant break in the eruptive activity cannot be expected, hence motivating for new geochronology. With regard to the last San Pedro eruptive events, dating of different volcanic products gave a wide range of $^{40}Ar/^{39}Ar$ ages from 160 to 68 ka (Fig. 3.2; Bertín and Amigo, 2019; Delunel et al., 2016); although, confident ages of a few lava flows are still lacking (Fig. 3.2).

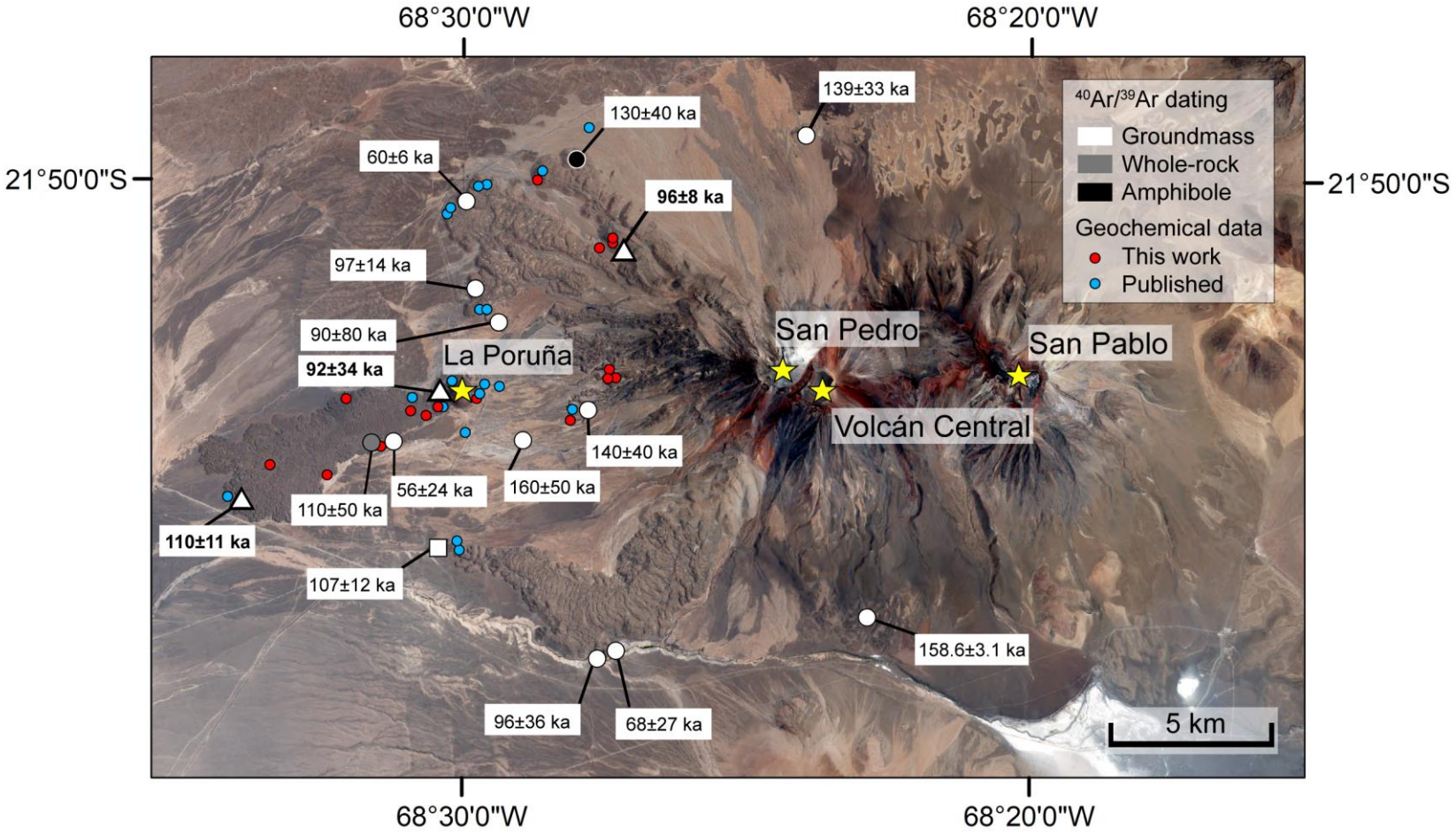

Fig. 3.2. Satellite image (Google Earth™) of La Poruña area showing the location of published (Godoy et al., 2014, 2017) and new geochemical data, and ^{40}Ar/^{39}Ar geochronological data from Bertin and Amigo (2019) (circles), Delunel et al. (2016) (squares), and the new ^{40}Ar/^{39}Ar dating (triangles). All ages are in ka, with error at 2σ.

3.3 Methods

This study presents whole-rock major- and trace-element concentrations, as well as $^{87}Sr/^{86}Sr$ and $^{143}Nd/^{144}Nd$ isotope data for sixteen (16) fresh volcanic rock samples from La Poruña and San Pedro volcano. The interpretations in this paper are based on a larger dataset in which these new and published data from Godoy et al. (2014, 2017) are combined (Supplementary material 3; Table S3). Additionally, two (2) samples from La Poruña and one (1) from San Pedro volcano were feasible for $^{40}Ar/^{39}Ar$ dating (Table 3.1), and nine (9) samples were selected for automated mineralogical analysis.

3.3.1 $^{40}Ar/^{39}Ar$ geochronology

New $^{40}Ar/^{39}Ar$ ages on unaltered groundmass from fresh samples from La Poruña and San Pedro were measured at the Servicio Nacional de Geología y Minería (SERNAGEOMIN, Chile). Crushing and mineral separation, and sample preparation were carried out following the procedures and parameters established by Salazar et al. (2018). Analysis were done using an ARGUS VI mass spectometer, with characteristics as indicated at www.sernageomin.cl/laboratorio-geocronología, and parameters indicated in Klug et al. (2018). Obtained plateau and isochron data, and parameters are presented in Supplementary Material 4.

Results of analysis by ARGUS VI mass spectrometer are presented on Table S4.1. These data were used to obtain ages by using the Isoplot excel spreadsheet (Ludwig, 2012). Plateau ages were defined as containing >60% of the total ^{39}Ar released (Fig. S4) and considering results with positive ages. Age plateaus and inverse isochron ages are in concordance at the 95% confidence level (Table S4.2; Fig. S4).

3.3.2 Automated mineralogical analyses

To complement standard optical petrography, nine (9) samples from La Poruña and San Pedro were analysed by automated mineralogical analysis to fully characterise the mineralogical properties. The samples were mounted in 30 mm circular briquettes using epoxy resin, then polished and carbon coated. The automated mineralogical analyses were made using a QEMSCAN model E430, which is based on a ZEISS EVO 50 SEM combined with Bruker Series 4 EDS detectors at the Unidad de Equipamiento Científico (MAINI), Universidad Católica del Norte (UCN, Chile). Measurements were performed using iMeasure v5.3.2 and for data reduction using iDiscover v5.3.2. The samples were compositionally mapped in Fieldscan operating mode at a field size of 1500 μm (approximate magnification of 50x) or 2500 μm (approximate magnification of 30x). A detailed description of the QEMSCAN theory and analytical modes were published by Gottlieb et al. (2000) and Pirrie et al. (2004).

3.3.3 Whole-rock geochemistry and isotope analyses

All 16 samples were crushed in an iron jaw crusher and pulverized in agate mills at the Departamento de Geología, Universidad de Chile in preparation for whole-rock geochemical and isotope analyses. Major and trace elemental abundance and isotope measurements were performed at UCT and detailed sample preparation procedures and standard values, as well as equipment descriptions for the analytical methods were as presented previously in Chapter 2 of this thesis. Bulk-rock major element compositions were obtained by X-ray fluorescence spectrometry (XRF) using a Panalytical Axios wavelength dispersive XRF spectrometer following the procedures, standards and parameters outlined in Chapter 2 (see also Frimmel et al., 2001). A ThermoFisher Xseries II inductively coupled plasma mass spectrometer (ICP-MS) was used to obtain bulk trace element data by analysis of sample solutions using the methodology in Harris et al. (2015). A Nu Instruments NuPlasma HR multi-collector inductively couple plasma mass spectrometer (MC-ICP-MS) equipped with a DSN-100 desolvating nebulizer was used for Sr and Nd isotope analyses. Full details of the isotope analysis

method were published by Harris et al. (2015). Typical internal two-sigma analytical errors for individual analyses were < 2 %RSD for XRF, < 3 %RSD for ICP-MS, and < 0.003 %RSD for $^{87}Sr/^{86}Sr$ and $^{143}Nd/^{144}Nd$ ratios.

3.4 Results

3.4.1 $^{40}Ar/^{39}Ar$ geochronology

A summary of the new $^{40}Ar/^{39}Ar$ results are presented in Table 3.1. Plateau ages were defined as containing > 60% of the total ^{39}Ar released. Age plateaus and inverse isochron ages are in concordance at the 95% confidence level (Table 3.1). Selected ages were used taking into account the plateau values. Full geochronological data and age spectra and inverse isochron plots of the new ages are detailed in the Supplementary Material 4 (Table S4.1; Fig. S4). Two new ages correspond to the main lava flow of La Poruña (Fig. 3.2), showing groundmass $^{40}Ar/^{39}Ar$ ages of 92 ± 34 and 110 ± 11 ka. These ages agree with published dates of 103 ± 1 ka (Wörner et al., 2000) and 110 ± 50 ka (Bertin and Amigo, 2019) and, within error, 56 ± 24 ka (Bertin and Amigo, 2019) (Fig. 3.2). For San Pedro, an $^{40}Ar/^{39}Ar$ groundmass age of 96 ± 8 ka was measured, which is in agreement with previous obtained ages for this area (Fig. 3.2; Bertin and Amigo, 2019; Delunel et al., 2016).

3.4.2 Petrography and mineral assemblage by automated mineralogy

The results from automated mineralogical analysis, summarized on Table 3.2, for La Poruña samples obtained from the scoria cone (POR 15 03) and the lava flow (POR 14 01, POR 15 02, POR 15 05 and POR 16 01), respectively, agree with the optical petrography and previous studies (e.g. Bertin and Amigo, 2019; Marín, 2016). All samples are dark-coloured, fine-grained and porphyritic (up to 30 vol% phenocrysts). The main mineral assemblage, in order of decreasing abundances, consists of plagioclase, olivine, orthopyroxene and clinopyroxene (Fig. 3.3a), with amphibole, magnetite and ilmenite as minor phases. Plagioclase appears as euhedral to subhedral crystals in a seriate crystal size distribution as phenocryst and microlite (< 2.5 mm; < 40 vol%; Fig. 3.3c-e). This mineral phase

displays crystals with resorption, regrowth rims and/or generally normal zonation. The morphology of olivine crystals (< 1.5 mm; < 7 vol%) includes subhedral and common embayments and skeletal textures (Fig. 3.3b). Pyroxene reaction rims on olivine crystal are also frequent (Fig. 3.3c). Orthopyroxene (< 0.2 to 1 mm; < 9 vol%) and clinopyroxene (< 0.2 to 1 mm; < 6 vol%) are common as pristine phenocrysts and occur individual or in small clusters (Fig. 3.3e). Clinopyroxene rims on orthopyroxene crystals are recognized, but rare. Phenocrysts are in a very finely crystalline groundmass, with microlites of plagioclase, ortho- and clinopyroxene, olivine, amphibole, and ilmenite ± magnetite, with interstitial glass (Fig. 3.3a, c-e), although glassy groundmass can also be recognized (Fig. 3.3b). Vesicularity is high, up to 40 vol% in some samples.

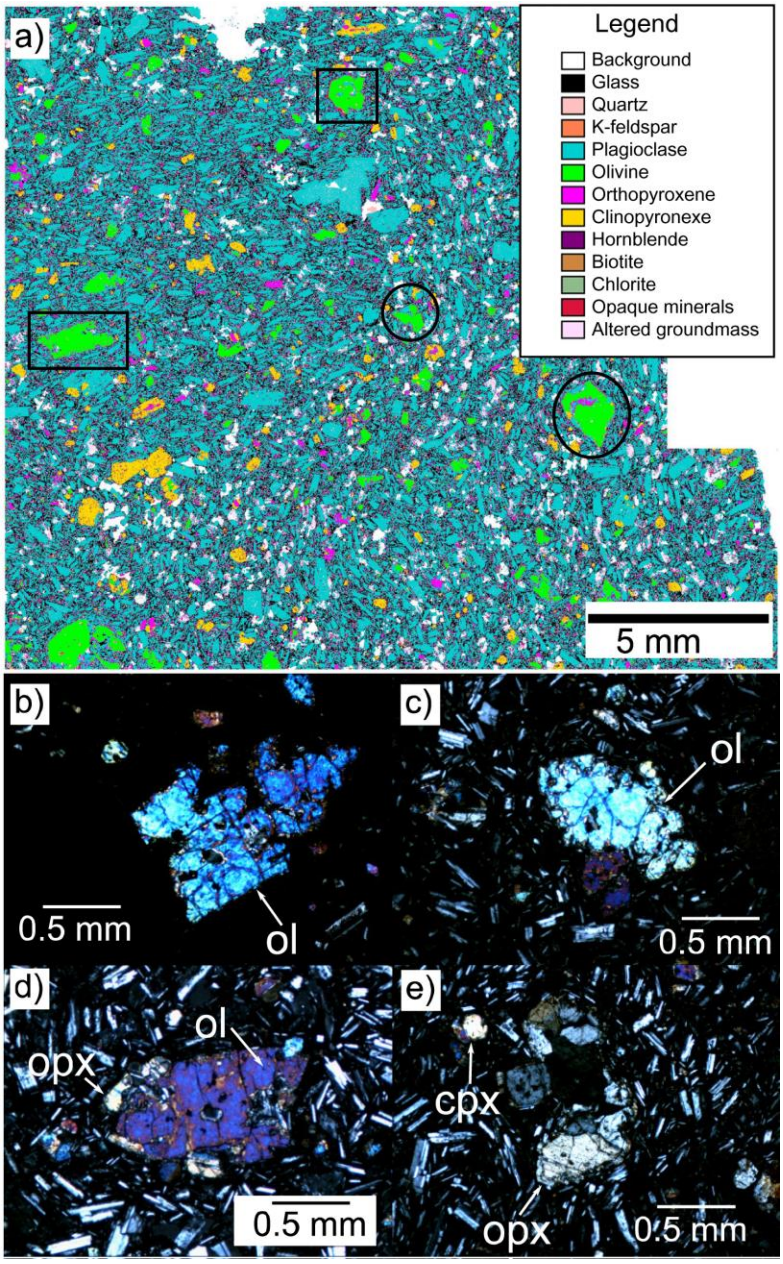

Fig. 3.3. (a) Automated mineralogical map; and (b-e) optical microscope photomicrographs of selected samples from La Poruña. The mineralogical map shows embayed olivine crystals (a; black squares) as observed in the thin sections (b-c). Moreover, orthopyroxene corona rims on olivine crystal are recognized in both mineralogical map (a; black circles) and thin sections (d). Orthopyroxene and clinopyroxene can also be found as glomeroporphyric textures (e). Thin sections under cross-polarized light; white bars indicate 0.5 mm length. ol – olivine; opx – orthopyroxene; cpx – clinopyroxene.

Table. 3.1. $^{40}Ar/^{39}Ar$ results from step heating of selected studied samples by groundmass at *SERNAGEOMIN Geochronological Laboratory* (Chile). Location of analysed samples and published ages on Fig. 3.2.

Sample	Latitude (S)	Longitude (W)	Sample description	Age Plateau					Inverse Isochron Analyses					
				Age (ka)	Error (2σ)	^{39}Ar (%)	n##	MSWD	Age (ka)	Error (2σ)	n##	$^{40}Ar/^{36}Ar$ intercept	Error (2σ)	MSWD
POR 15 04	21º 53' 35"	68º 30' 19"	Western lava flow at the base of the scoria cone	**92**	**34**	97	6/7	**0.26**	111	56	6/7	295.2	0.5	0.27
POR 15 05	21º 55' 32"	68º 34' 2"	Western flank of the 8 km lava flow	**110**	**11**	100	7/7	**0.84**	94	22	7/7	296.6	1.5	0.90
SPSP 16 01	21º 51' 13"	68º 27' 12"	Upper north-western flank of San Pedro	**96**	**8**	64	4/9	**0.24**	94	12	4/9	296.0	2.6	0.28

Preferred ages are in bold.
Number of data points used in plateau and isochron calculations; each step heating represents one data point.

Table 3.2. Petrography and phenocryst main assemblages obtained by automated mineralogical analyses of nine selected samples from La Poruña and San Pedro. Geochemical data from Table S3 (Supplementary Material 3).

Sample	SiO_2 (wt%)*	Chemical classification*	Rock type	Mineral assemblage
La Poruña				
POR 14 01	57.0	Basaltic-andesite	glassy medium-grained plg-ol-px seriate phyric	plg>ol>cpx>opx
POR 15 02	58.4	Andesite	vesicular medium-grained ol phyric plg-px glomerophyric	plg>ol>opx=cpx
POR 15 03	57.9	Andesite	medium-grained plg-ol-px seriate phyric	plg>ol>opx=cpx
POR 15 05	60.2	Andesite	glassy medium-grained plg-ol-px seriate phyric	plg>ol>opx=cpx
POR 16 01	60.2	Andesite	vesicular medium-grained plg-ol-px seriate phyric	plg>ol=opx>cpx
San Pedro				
BG SPL 004	58.5	Andesite	vesicular medium-grained plg-ol-px seriate phyric	plg>opx=cpx>ol (A. I)
SPSP 16 05	64.1	Dacite	glassy medium-grained plg-amp-ox seriate glomerophyric	plg>amp>ox (A. II)
SPSP 16 06	57.2	Andesite	glassy medium-grained plg-ol-px seriate glomerophyric	plg>opx=cpx>ol (A. I)
SPSP 16 07	56.8	Basaltic-andesite	vesicular medium-grained plg-ol-px phyric	plg>ol>cpx>opx (A. I)

*Recalculated 100% water free
A. I and A. II correspond to Assemblage I and II, respectively.

Automated mineralogical analyses of San Pedro samples are summarized in Table 3.2. By obtained mineral maps (Fig. 3.4a-b) and optical petrography (Fig. 3.4c-f), the analysed lavas were described as porphyritic (> 15 to ca. 40 vol% phenocrysts), with plagioclase, olivine, orthopyroxene, clinopyroxene and amphibole as phenocrysts (up to 2.5 mm), defining two main mineral assemblages: (i) Assemblage I, consisting of plagioclase ± orthopyroxene ± clinopyroxene ± olivine, mainly as phenocrysts, with scarce, or no, amphibole ± ilmenite ± magnetite (Fig. 3.4a, c-d; < 0.2 mm); and (ii) Assemblage II constituted by plagioclase ± amphibole ± magnetite phenocrysts, with minor orthopyroxene ± clinopyroxene (Fig. 3.4b, e-f). Plagioclase (< 50 vol%) generally occurs as single microlites to phenocrysts (< 0.2 to 3 mm) or forming glomerocrysts with orthopyroxene-clinopyroxene (Assemblage I) or with amphibole-magnetite (Assemblage II) (Fig. 3.4e-f). Plagioclase generally forms euhedral prismatic or tabular zoned and/or sieve-textured crystals. If present, olivine (Assemblage I; < 0.2 to 1.5 mm; < 8 vol%) shows varied morphologies including subhedral, embayed and resorbed crystals (Fig. 3.4a, c), and rare reaction rims of pyroxene (Fig. 3.4a). Orthopyroxene (< 0.2 to 0.8 mm; < 10 vol%) and clinopyroxene (< 0.2 to 1.5 mm; < 7 vol%) appear as euhedral tabular to subhedral crystals (Fig. 3.4d). Fe-Ti oxides inclusions can be found in olivine and pyroxene crystal. Pristine amphibole crystals were recognized in differentiated samples, up to 20 vol% abundance (Fig. 3.4b), which was also reported previously (e.g. Bertin and Amigo, 2019; O'Callaghan and Francis, 1986). This mineral phase occurs as euhedral, tabular to acicular crystals, ranging from microlite to phenocrysts (up to 3 mm in the length axis), often with magnetite inclusions (Fig. 3.4f). Glassy-compact (Fig. 3.4c-d), and hypocrystalline groundmass (Fig. 3.4e-f) with microlites of plagioclase, orthopyroxene, clinopyroxene (Fig. 3.4e-f), amphibole, and minor or no K-feldspar, magnetite, ilmenite, olivine and quartz, were recognized. Some samples show vesicular groundmass, with vesicularity > 30 vol%.

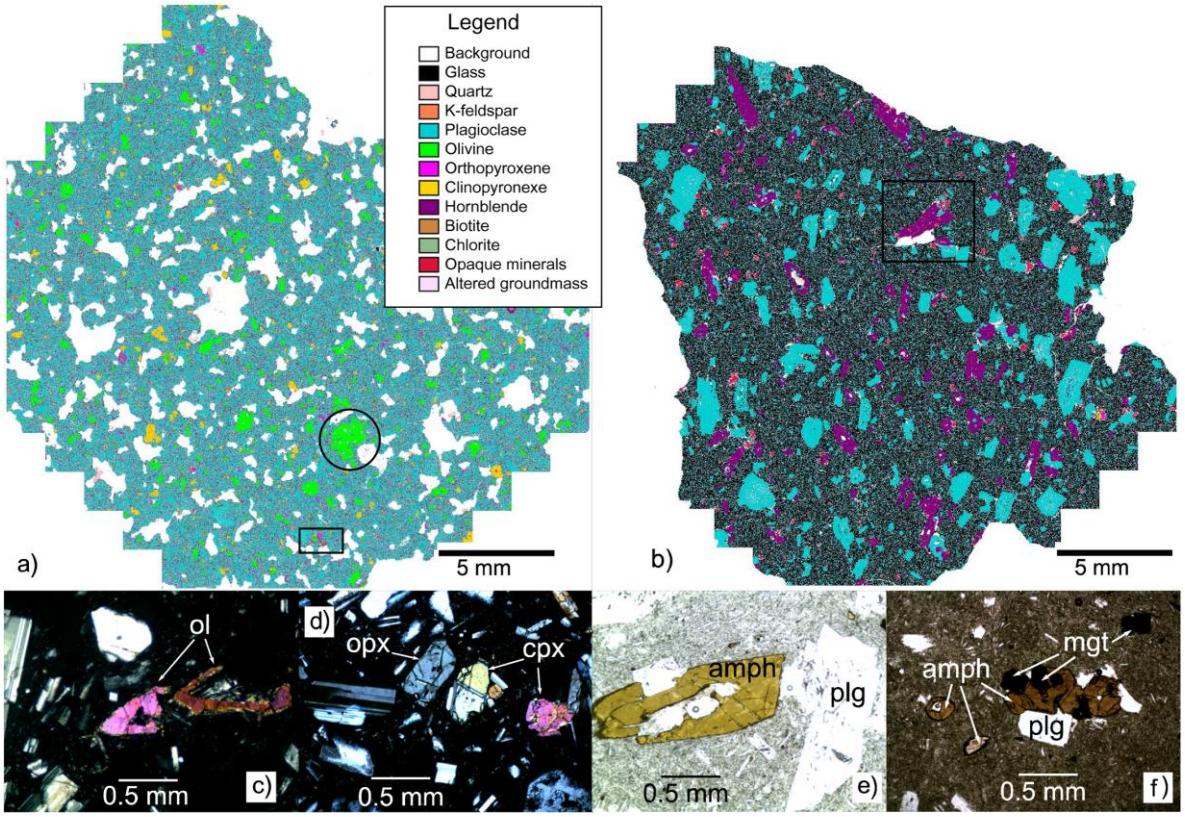

Fig. 3.4. (a-b) Automated mineralogical map; and (c-f) optical microscope photomicrographs of selected samples from San Pedro. Mineralogical map a) shows the Assemblage I type, characterized by embayed olivine crystals (black circle), reaction rim orthopyroxene growth on olivine (black square), and pyroxene and plagioclase phenocrysts, as shown on c and d. Figure b) shows the typical mineralogy of the Assemblage II type, with amphibole, plagioclase and magnetite as main mineralogical phases (black square). This is also observed in the thin sections (e-f). Thin sections under cross-polarized (c-d) and plane-polarized (e-f) light. ol – olivine; opx – orthopyroxene; cpx – clinopyroxene; amph – amphibole; plg – plagioclase; mgt – magnetite.

3.4.3 Whole-rock geochemistry and Sr and Nd isotopes

The complete elemental abundance and isotope composition dataset of all studied samples is provided in Table S3. La Poruña samples show basaltic-andesite to andesite composition (56.0-59.6 wt% SiO_2; Fig. 3.5) with calc-alkaline compositions (after Irvine and Baragar, 1971). Considering that Mg# is < 62 for all samples (Table S3), SiO_2 as differentiation index is used (Fig. 3.6 and 3.7). Most of the La Poruña samples form defined trends in most of the bivariate diagrams, except with Sr and Cr (Fig. 3.6 and 3.7). While SiO_2 correlates positively with K_2O, Na_2O, Al_2O_3, Ba and Rb, silica shows a negative correlation with FeO*, MgO and CaO (Fig. 3.6 and 3.7). Samples from San Pedro volcano are calc-alkaline (after Irvine and Baragar, 1971), varying from basaltic-andesite to dacite (Le Maitre et al., 1989; Fig. 3.5), with a gap between 59 and 63 wt% SiO_2. Nearly all the San Pedro samples follow the same trends of those for La Poruña (Figs. 3.6 and 3.7), except for Al_2O_3, which shows a scatter distribution with silica (Fig. 3.6f), and for Sr, which reveals a negative correlation with the most evolved samples. The variation of trace elements ratios with respect to silica contents for La Poruña samples shows a positive correlation in Sr/Y (Fig. 3.7e); and Sm/Yb remains almost constant during differentiation (Fig. 3.7f). San Pedro samples reveal a scatter distribution of both ratios with SiO_2 (Fig. 3.7e-f).

All studied rocks display enrichment in large ion lithophile elements (i.e. Rb, Ba, Pb, and Sr) and some high field strength elements (i.e. Th, U, Nb, Ta, Zr and Hf), and exhibit a pronounced negative Nb-Ta anomaly relative to N-MORB (Sun and McDonough, 1989; Fig. 3.8a). Chondrite-normalized rare earth element (REE; Sun and McDonough, 1989) patterns overlap for all studied lavas. Light REE are enriched with respect to the depleted heavy REE (La/Yb_N = 7.58-18.44), showing slightly steep slopes (Fig. 3.8b).

$^{87}Sr/^{86}Sr$ and $^{143}Nd/^{144}Nd$ ratios of La Poruña samples vary between 0.70618 and 0.70664, and 0.51239 to 0.51245, respectively (Table S3). The Sr-isotope ratios show a trend of slightly increasing

with decreasing $^{143}Nd/^{144}Nd$ ratios (Fig. 3.9). For San Pedro, $^{87}Sr/^{86}Sr$ values range from 0.70615 to 0.70672, and from 0.51236 to 0.51243 for $^{143}Nd/^{144}Nd$, defining a slight negative trend among them (Fig. 3.9). These radiogenic isotopes values have a relatively restricted range compared to those measured in different monogenetic centres and stratovolcanoes with mafic eruptives in the Central Andes (Fig. 3.9).

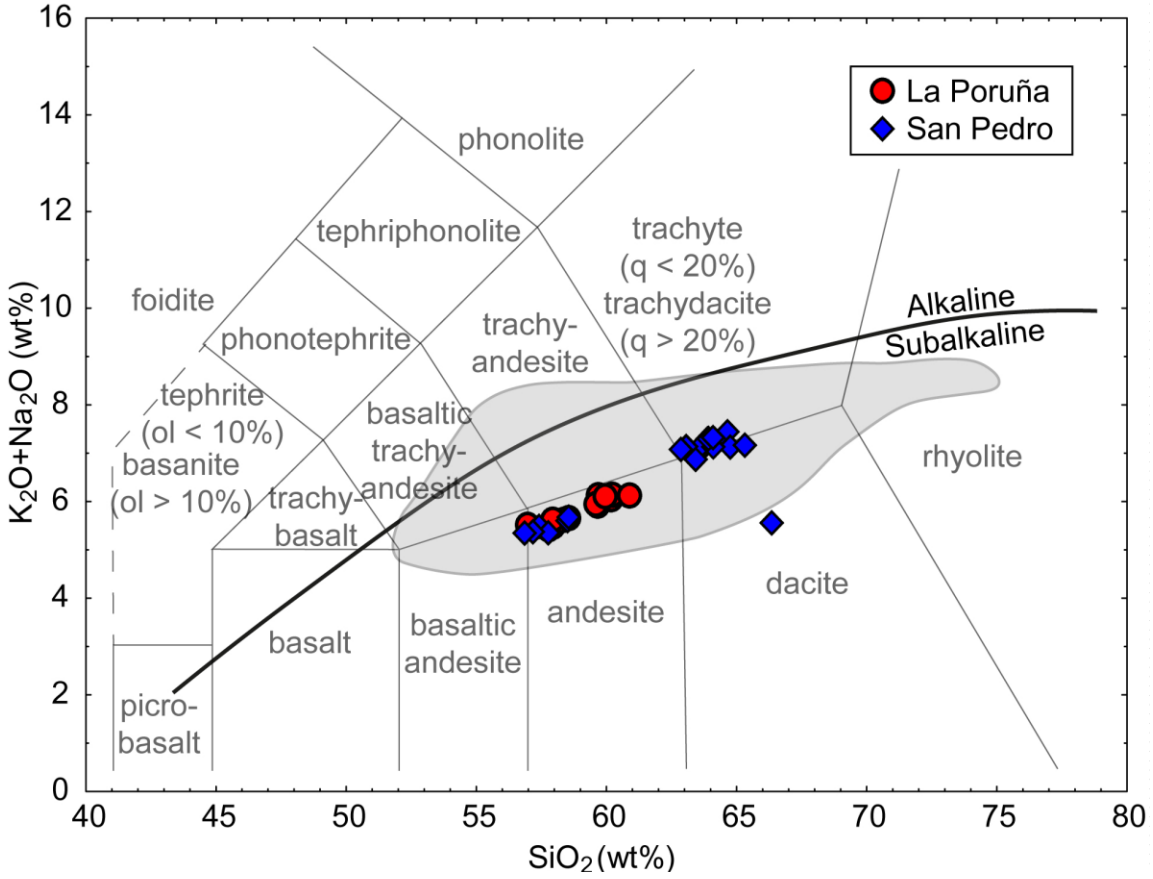

Fig. 3.5. Total-Alkali vs. Silica (TAS) diagram (after LeMaitre et al, 1989) for studied samples of La Poruña and San Pedro (Table S3). Lava samples show a well-defined sub-alkaline trend, varying from basaltic-andesite to rhyolitic, with few trachytic compositions. A gap between 60 and 63 wt% SiO_2 is observed on samples from San Pedro volcano. Gray field represents the composition of Central Andes lavas (after Mamani et al., 2010). Solid line represents subdivision of alkaline and subalkaline lavas (after Irvine and Baragar, 1971).

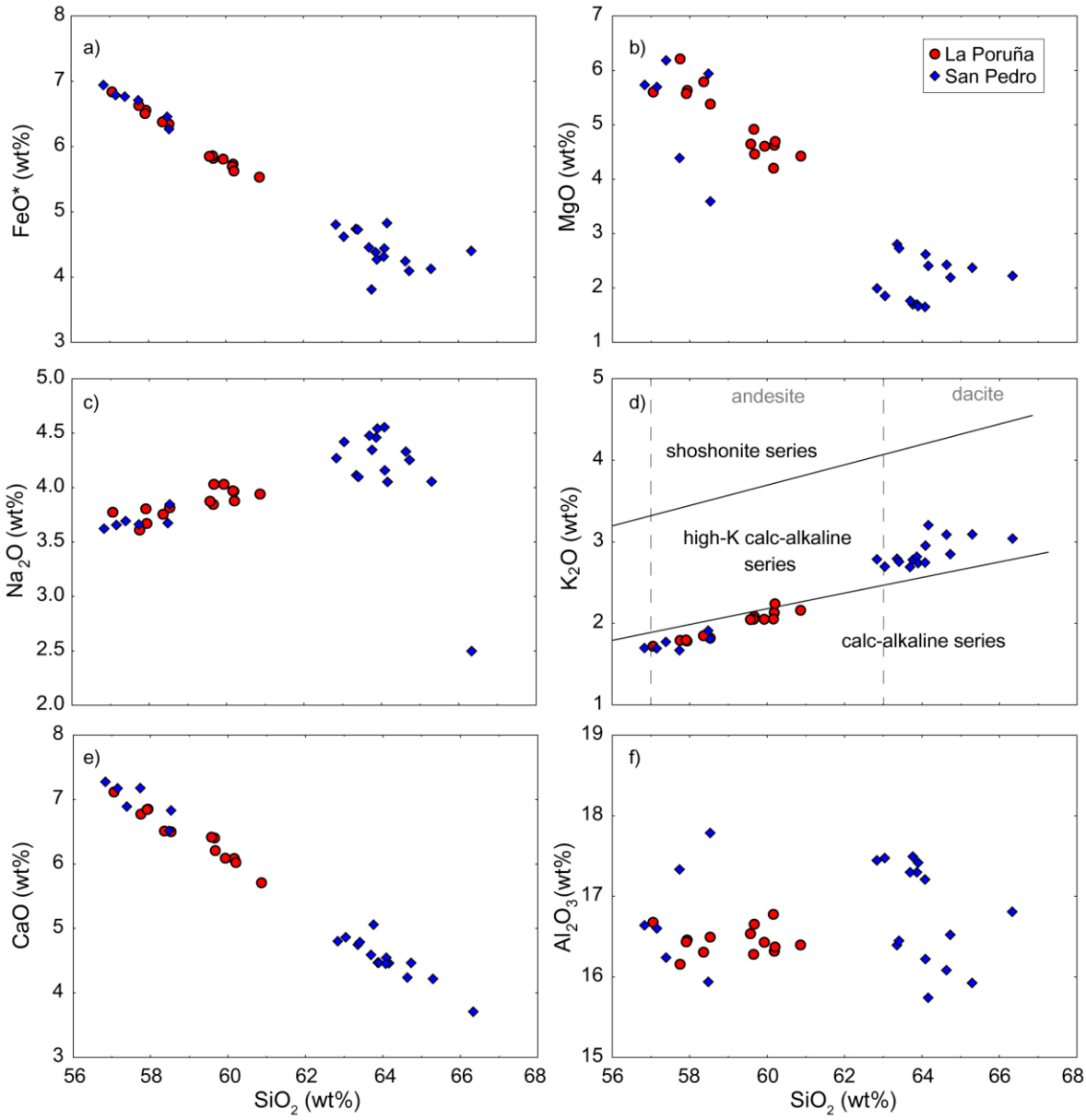

Fig. 3.6. Selected Harker diagrams for (a) total Fe oxide (as FeO*), (b) MgO, (c) Na_2O, (d) K_2O, (e) CaO, and (f) Al_2O_3 (all in wt%), vs. SiO_2 (wt%) for analysed samples of La Poruña and San Pedro volcanoes. For (d) lines and nomenclature after Rickwood (1989).

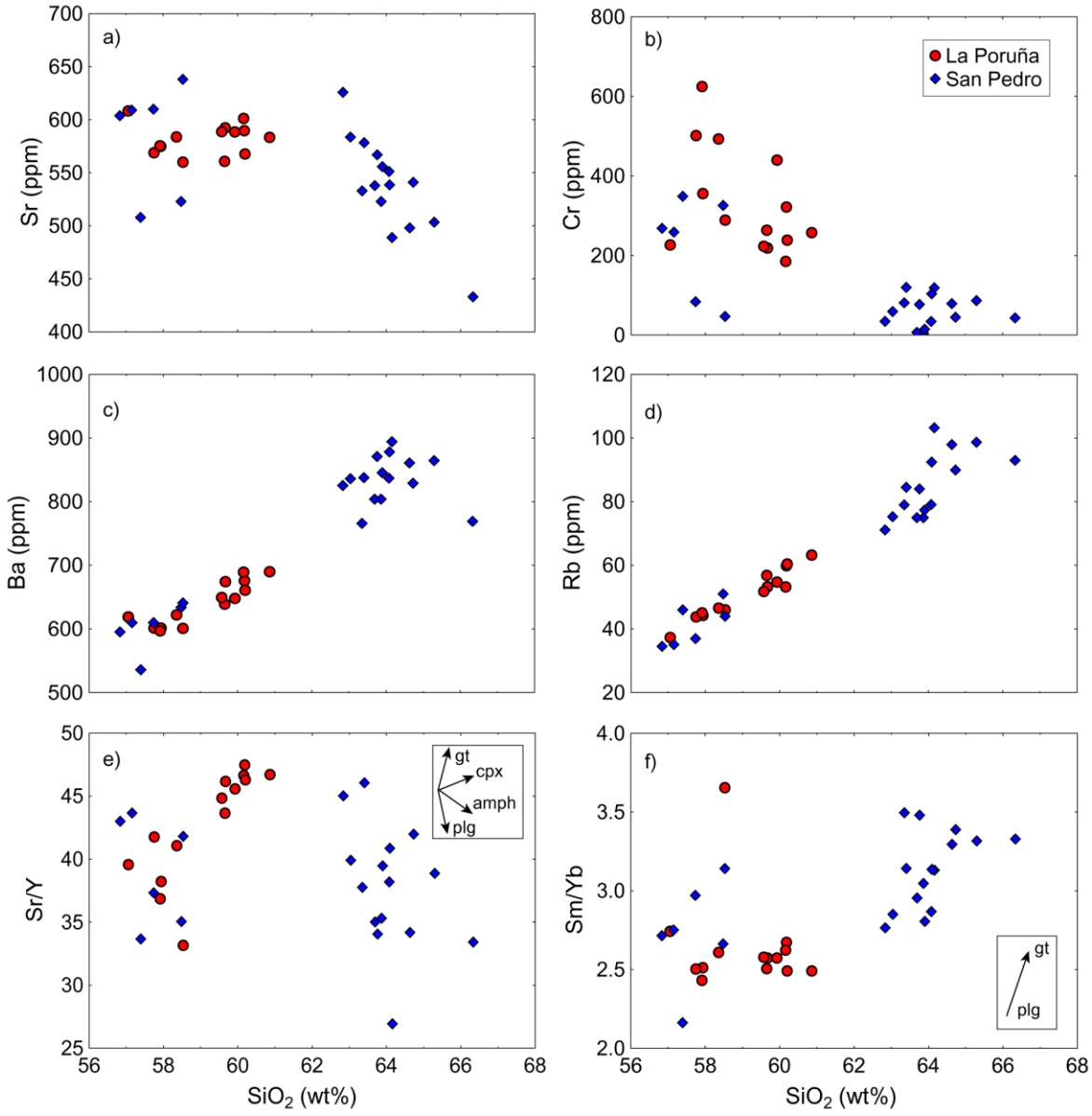

Fig. 3.7. Selected Harker diagrams for (a) Sr, (b) Cr, (c) Ba, and (d) Rb vs. SiO_2 (wt%) for samples of La Poruña and San Pedro. Also, variation diagrams are shown for (f) Sr/Y and (g) Sm/Yb ratios vs. SiO_2 (wt%). Inset shows the typical trends for garnet- (gt), clinopyroxene- (cpx), amphibole- (amph) or plagioclase-dominated (plg) fractionation.

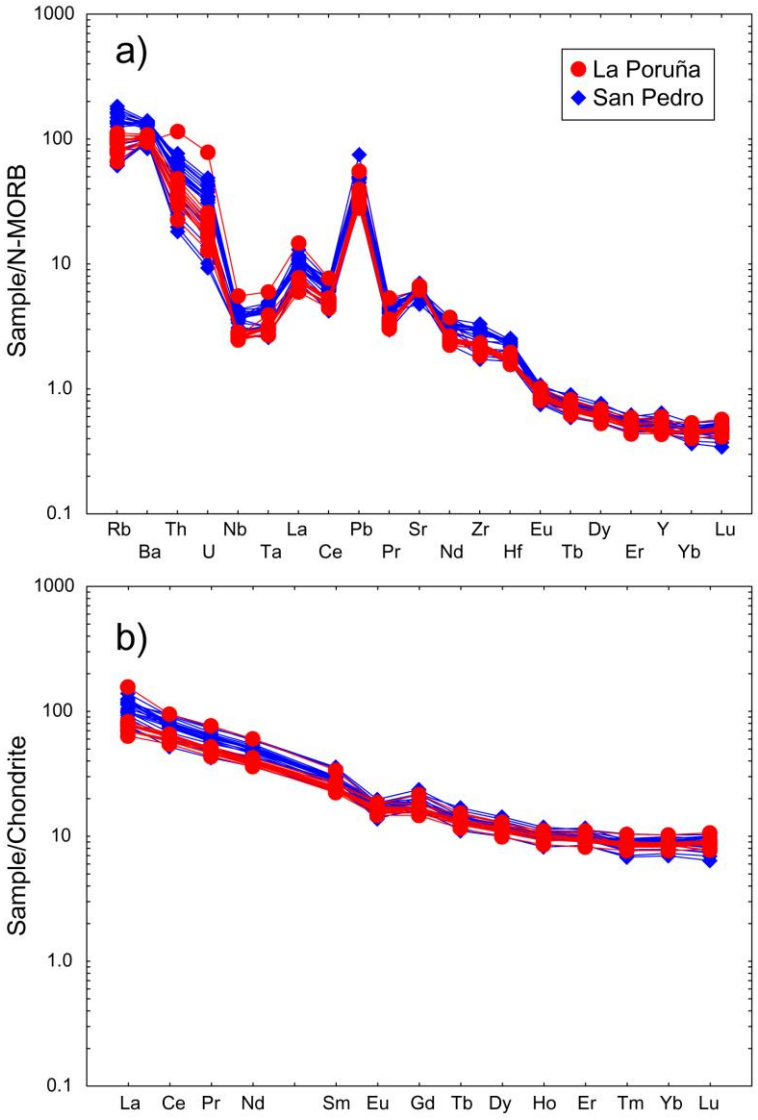

Fig. 3.8. Multi-element diagrams for samples from La Poruña and San Pedro volcanoes normalized to (a) N-MORB and (b) chondrite. Normalization values from Sun and McDonough (1989).

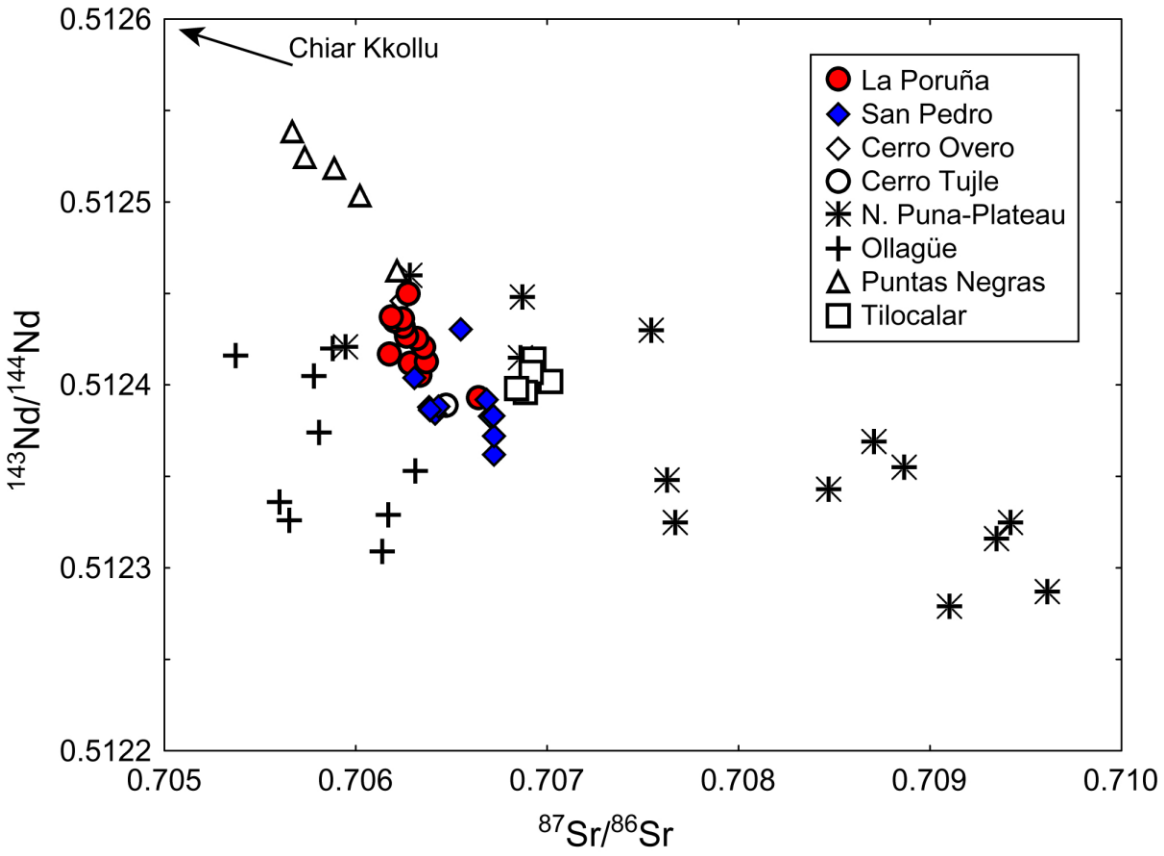

Fig. 3.9. $^{87}Sr/^{86}Sr$ vs. $^{143}Nd/^{144}Nd$ diagram for La Poruña and San Pedro volcanoes, and other local mafic rocks from the northern Puna Plateau (Maro et al., 2017), Ollagüe and Chiar Kkollu regions (Davidson and de Silva, 1992; 1995), and Cerro Overo, Cerro Tujle, Puntas Negras and Tilocalar (van Alderwerelt, 2017). Arrow points to position of the Chiar Kkollu sample (Miocene; Davidson and de Silva, 1992; 1995), which lies outside the diagram ($^{87}Sr/^{86}Sr$ = 0.704; $^{143}Nd/^{144}Nd$ = 0.5128).

3.5 Discussion

3.5.1 Eruption age and petrogenesis of La Poruña scoria cone

The published $^{40}Ar/^{39}Ar$ ages (110 ± 50 ka and 54 ± 24; Bertin and Amigo, 2019) could be related to a significant break in the eruptive activity at La Poruña. However, the morphology of this monogenetic volcano and overlap of most new (Table 3.1) and published age data (110 ± 50 ka $^{40}Ar/^{39}Ar$, Bertin and Amigo, 2019; 103 ± 2 ka ^{3}He, Wörner et al., 2000) strongly suggest a singular eruption, which broadly occurred around 100 kyr ago. This common age is contemporaneous with the last eruptives of the San Pedro volcano, whose petrogenetic relation is discussed thoroughly in the following section (Section 3.5.2).

The regular trends between major (FeO*, Na_2O, CaO) and trace elements (Ba, Rb, Sr/Y) with respect to SiO_2 as differentiation index (Figs. 3.6 and 3.7) defined by La Poruña samples are consistent with fractional crystallization of the observed phenocryst of plagioclase and pyroxene. Also, the negative anomaly of Eu (Fig. 3.8) and the negative correlation between Eu/Eu* and SiO_2 (Fig. 3.15) reflect an increasing role of plagioclase fractionation during differentiation (McKay, 1989). The variation of Sr/Y (33.2-47.5; Fig. 3.7e) and the low Sm/Yb ratios (2.4-3.7; Fig. 3.7f) are likely a result of multiple magmatic events (e.g. magma mixing with APMB melts and/or crustal assimilation) potentially at shallow depths to produce evolved basaltic-andesite to andesite compositions. A typical subduction-related arc signature is recognized through enrichment in LILE relative to HFSE and a strong negative anomaly in Nb-Ta (Fig. 3.8a). The REE patterns of the studied samples indicate a magma evolution dominated by a low-pressure garnet-free source which has also been proposed by other authors for Central Andean volcanoes (Fig. 3.8b; e.g. Burns et al., 2015; Davidson et al., 1990a; Godoy et al., 2014; Michelfelder et al., 2013; O'Callaghan and Francis, 1986). Thus, the variability revealed by the data is a clear indication of magmatic evolution at upper crustal levels. The La Poruña sample set shows relatively narrow ranges for Sr and Nd isotope ratios with respect to other local volcanoes (Figs. 3.9 and 3.10). In the $^{87}Sr/^{86}Sr$ variation diagrams (Figs. 3.11 and 3.12), a reverse isotopic

behaviour of decreasing radiogenic Sr values during differentiation is observed particularly in all samples from La Poruña. The $^{87}Sr/^{86}Sr$ vs. SiO_2 diagram reveals a decreasing of the Sr-isotope ratio with increasing silica content (i.e. differentiation) (Fig. 3.11). This behaviour is opposite to that expected for a typical AFC process, which increases the $^{87}Sr/^{86}Sr$ ratio values of the magmas by crustal assimilation of older material with higher $^{87}Sr/^{86}Sr$ compositions during differentiation (Fig. 3.11; e.g. Davidson and de Silva, 1995; Davidson et al., 1990a; Hildreth and Moorbath; 1988; Wörner et al., 2018). There is also a reversed isotopic behaviour of decreasing Sr-isotope ratios at lower Sr (ppm) contents (Fig. 3.12). These reversed trends cannot consistently be explained only by mixing or assimilation; along with plagioclase and pyroxene fractional crystallization at low pressures. A subsequent stage after the magma mixing-AFC phase for the La Poruña mafic magmas is thus suggested. Huppert and Sparks (1985) pointed out that decreasing assimilation during differentiation is associated with ascending mafic magmas under turbulent conditions. This process is described as assimilation during turbulent ascent (ATA; Huppert and Sparks, 1985; Moorbath and Thompson, 1980), which is based on the turbulent rapid ascent of hot mafic magmas effectively generating selective fusion and assimilation of felsic crust over relatively short time scales (e.g. Huppert and Sparks, 1985; Kerr et al., 1995; Maro et al., 2017; Peccerillo et al., 2004). Thus, the poor establishment of 'armoured' magma pathways and the high temperatures of rising mafic magmas can lead to excessive assimilation of crustal material and the corollary that the least-evolved magmas may ultimately be the most contaminated. The negative correlation between silica and Sr isotope ratios in these magmas may therefore be explained by selective assimilation by turbulent ascent. In fact, the least-evolved sample (POR 14 01; 55.95 wt% SiO_2; 608 ppm Sr) has the highest $^{87}Sr/^{86}Sr$ ratios (0.70664) and extrapolating to the most differentiated sample (POR 17 04; 59.62 wt% SiO_2; 608 ppm Sr; $^{87}Sr/^{86}Sr = 0.70618$) defines a regular negative trend (Figs. 3.11 and 3.12). This is also a plausible explanation for the relatively high contents of incompatible trace elements (e.g. Rb, Ba, Th, Pb, Sr; Figs. 3.7 and 3.8), as consequence of selective incorporation of evolved components of the continental crust. In the Central Andes, similar geochemical character (e.g. enrichment of some incompatible

trace elements, scattering Sr respect to silica) linked to turbulent ascent has been documented for the Neogene mafic eruptives (MgO > 6 wt%) in the Argentinian Northern Puna (Maro and Caffe, 2016; Maro et al., 2017). Although the $^{87}Sr/^{86}Sr$ trends are not similar (Figs. 3.11 and 3.12), the ATA-like development is also supported by the low percentage of crystals, fine-grained textures and skeletal crystals observed in the Puna mafic rocks, which are due to swift transport from the mantle source to the shallow crust (Maro and Caffe, 2016; Maro et al., 2017). This interpretation agrees well with the petrography obtained for La Poruña samples (Fig. 3.3; Table 3.2), however the latter skeletal morphologies of crystals are attributed to rapid cooling after the eruption.

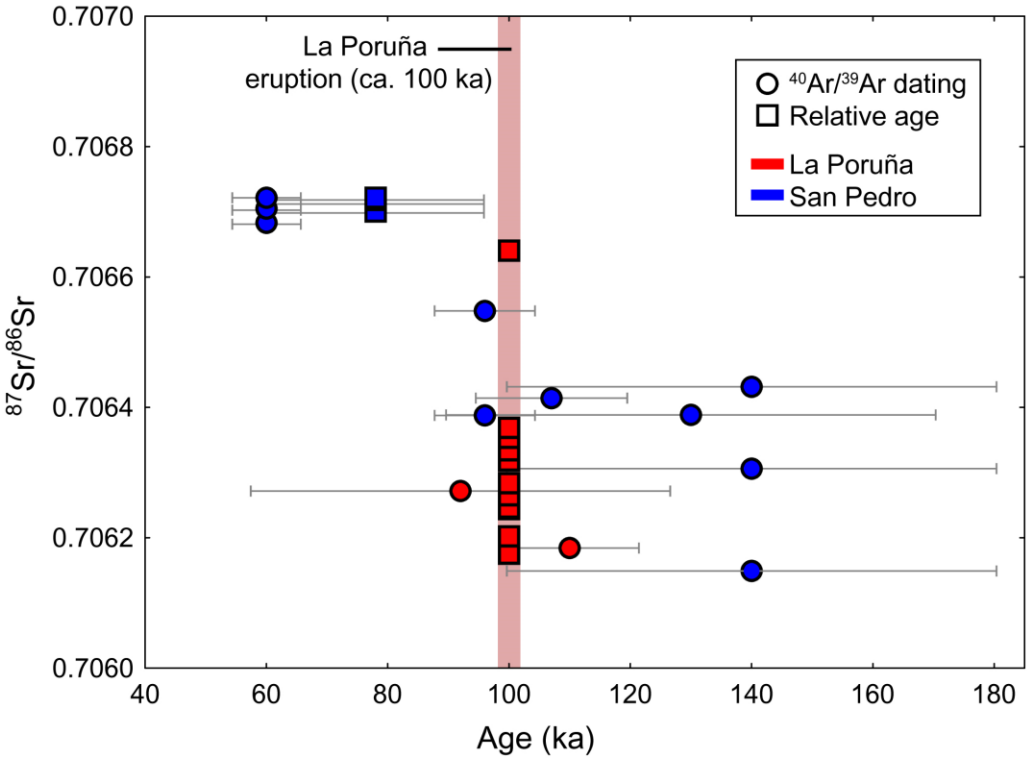

Fig. 3.10. $^{87}Sr/^{86}Sr$ vs. Age (ka) for the studied samples from La Poruña and San Pedro. Bars indicate maximum and minimum ages (2σ error) (Table 3.1; Bertin and Amigo, 2019; Delunel et al., 2016; Fig. 3.2 for reference). Relative ages are based on their distribution and stratigraphic position (Table S4 for reference).

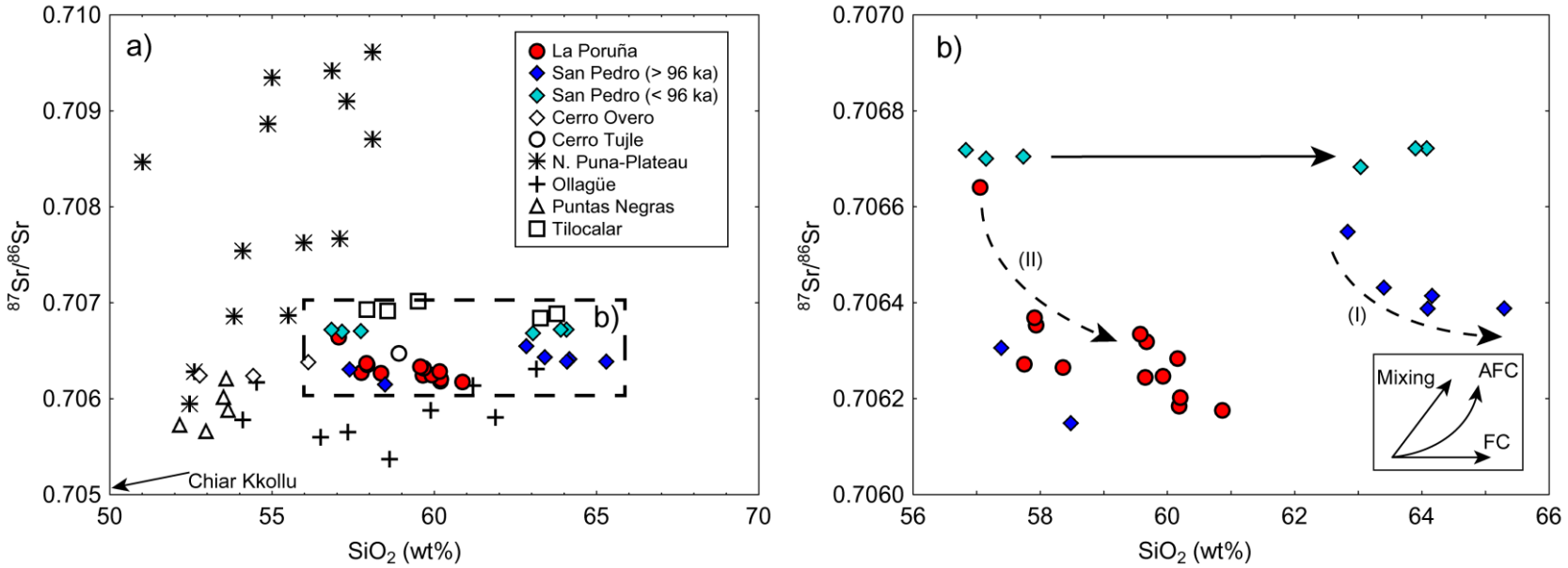

Fig. 3.11. a) $^{87}Sr/^{86}Sr$ vs. SiO_2 (wt%) diagram for La Poruña and San Pedro volcanoes, and other local mafic rocks from the northern Puna Plateau (Maro et al., 2017), Ollagüe and Chiar Kkollu regions (Davidson and de Silva, 1992; 1995), and Cerro Overo, Cerro Tujle, Puntas Negras and Tilocalar (van Alderwerelt, 2017). Arrow points to position of the Chiar Kkollu sample (Miocene; Davidson and de Silva, 1992; 1995), which lies outside the diagram ($^{87}Sr/^{86}Sr$ = 0.704; 45 wt% SiO_2). Dashed square on a) indicates the position of b); b) $^{87}Sr/^{86}Sr$ vs. SiO_2 (wt%) diagram for La Poruña and San Pedro volcanoes. Dashed arrows indicate trends of decreasing crustal contamination during differentiation for older San Pedro (I) and La Poruña (II). The younger, and most contaminated, samples from San Pedro ($^{87}Sr/^{86}Sr$ ratios > 0.7066) define a slight horizontal trend (thick black arrow). Inset shows the typical trends for mixing, assimilation and fractional crystallization (AFC), and fractional crystallization (FC) processes.

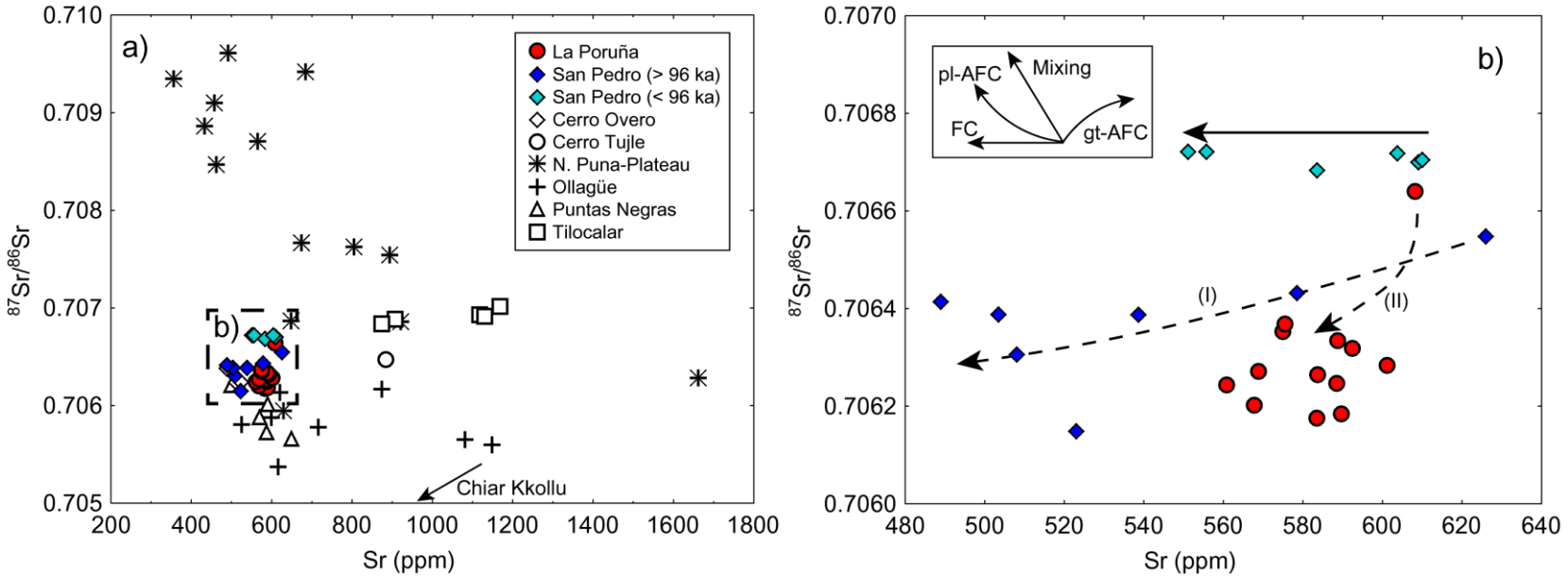

Fig. 3.12. a) $^{87}Sr/^{86}Sr$ vs. Sr (ppm) diagram for La Poruña and San Pedro volcanoes, and other local mafic rocks from the northern Puna Plateau (Maro et al., 2017), Ollagüe and Chiar Kkollu regions (Davidson and de Silva, 1992; 1995), and Cerro Overo, Cerro Tujle, Puntas Negras and Tilocalar (van Alderwerelt, 2017). Arrow points to position of the Chiar Kkollu sample (Miocene; Davidson and de Silva, 1992; 1995), which lies outside the diagram ($^{87}Sr/^{86}Sr$ = 0.704; 936 ppm Sr). Dashed square on a) indicates position of b). b) $^{87}Sr/^{86}Sr$ vs. Sr (ppm) diagram for La Poruña and San Pedro volcanoes. Dashed arrows indicate trends of decreasing crustal contamination with decreasing Sr content on samples from older San Pedro (I) and La Poruña (II). The younger, and most contaminated, samples from San Pedro ($^{87}Sr/^{86}Sr$ ratios >0.7066) define a slight horizontal trend (thick black arrow). Inset shows the typical trends for mixing, plagioclase- and garnet-dominated assimilation and fractional crystallization (pl-AFC and gt-AFC, respectively), and fractional crystallization (FC) processes.

3.5.1 Petrogenetic relation of San Pedro and La Poruña volcanoes

Rocks from San Pedro volcano define two distinct groups on major and trace elements variation diagrams (Figs. 3.5, 3.6 and 3.7), both related to low-pressure crystallization trends (Godoy et al., 2014; O'Callaghan and Francis, 1986; Fig. 3.8). Sr isotopes support significant crustal additions (Fig. 3.9), and it is noted that after ca. 96 ka the degree of crustal contamination increases for the San Pedro samples (Fig. 3.10). The Sr isotope data plots reveal two trends, with $^{87}Sr/^{86}Sr$ ratios falling below or above 0.7066 (Figs. 3.11 and 3.12). Whereas older samples (> 96 ka) with Sr isotope compositions below 0.7066 show a systematic decrease of $^{87}Sr/^{86}Sr$ ratios during differentiation, younger samples (< 96 ka) with $^{87}Sr/^{86}Sr$ ratios above 0.7066 show a regular horizontal trend (Fig. 3.11). Similar temporal trends are observed in the $^{87}Sr/^{86}Sr$ vs. Sr plot (Fig. 3.12) where the samples with $^{87}Sr/^{86}Sr$ values above 0.7066 define a horizontal trend and those with ratios below 0.7066 reveal a slight decrease in Sr isotopic compositions at lower Sr concentrations. This temporal evolution is also consistent with the petrography described (Fig. 3.4), as two main types of San Pedro samples studied were defined (Assemblage I and II; Fig. 3.4; Table 3.2). The decreases Dy/Dy* and Dy/Yb in Fig. 3.13a support the involvement of clinopyroxene or amphibole during differentiation, owing to these minerals being capable of fractionating both REE ratios (Davidson et al., 2013). The San Pedro REE data in Fig. 3.13b plot as two groups at varying silica contents (56-59 and 63-66 wt% SiO_2), however the silica-rich group can be subdivided since the younger lavas have lower Dy/Dy* ratios respect to the older volcanics, and associate with an increasing role of amphibole fractionation. Hence, three distinctly different groups of samples are defined: (i) olivine-pyroxene-bearing basaltic-andesite to andesite (plagioclase > olivine > pyroxene), (ii) pyroxene-bearing dacite (plagioclase > pyroxene > olivine ± amphibole), and (iii) amphibole-bearing dacite (plagioclase > amphibole > magnetite). Based on these petrographic, geochemical and geochronological observations, a temporal change in the differentiation regime of San Pedro volcano at ca. 96 ka is proposed, which is likely related to the eruption of the adjacent La Poruña scoria cone.

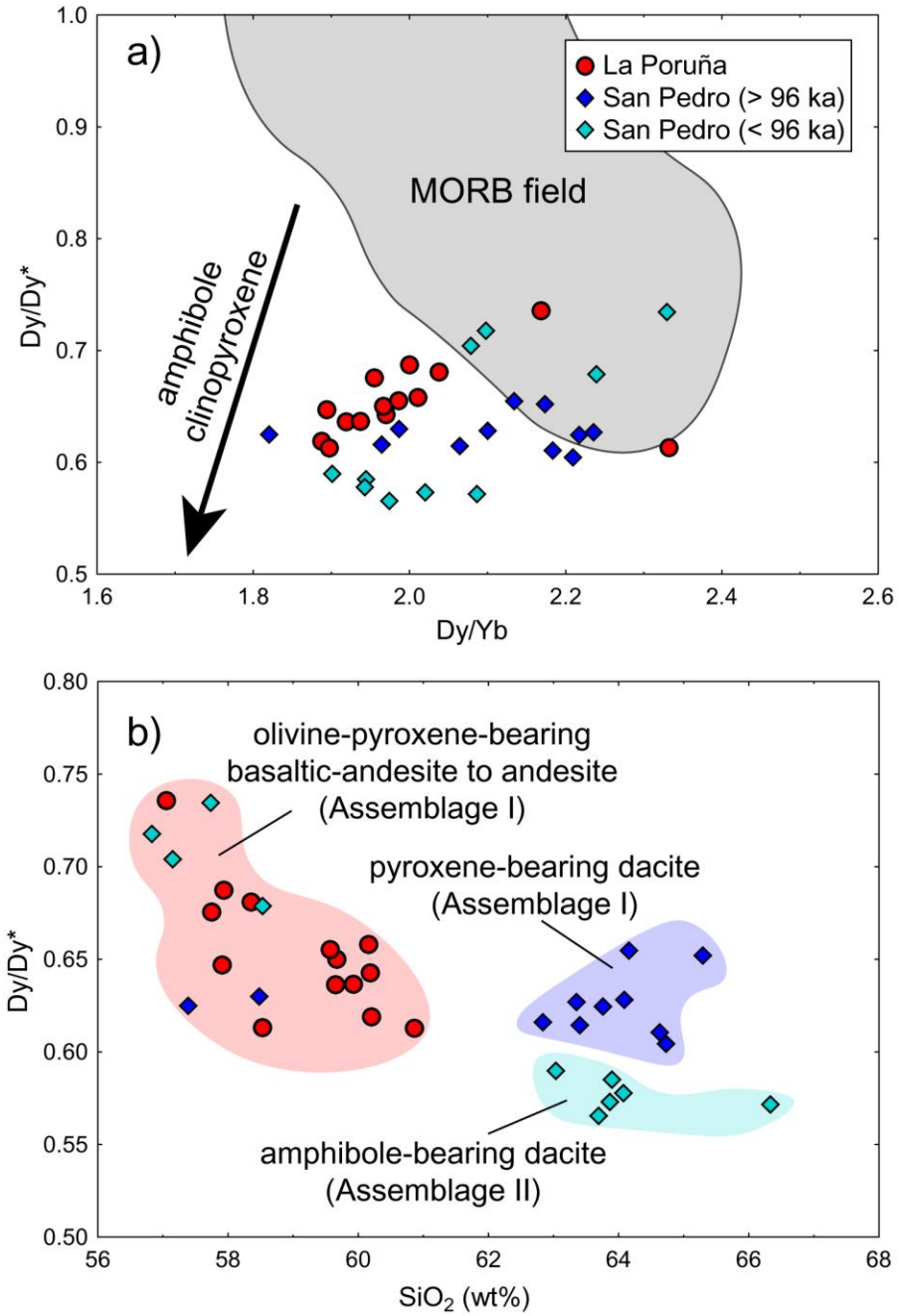

Fig. 3.13. a) Dy/Dy* vs. Dy/Yb diagram for La Poruña and San Pedro samples. The studied samples show decreased Dy/Dy* and Dy/Yb ratios, which can be attributed to significant fractionation of clinopyroxene and/or amphibole. Vector for mineral control and MORB array as references from Davidson et al. (2013). b) Plot of Dy/Dy* vs. SiO_2 for La Poruña and San Pedro volcanoes. Three distinctly different groups of samples were defined by trace element variation, which are also consistent with the petrography described (Section 3.4.2).

The older eruptions of the San Pedro occurred between 160 and ca. 96 ka (Bertin and Amigo, 2019; Delunel et al., 2016; this chapter), involving predominantly pyroxene-bearing dacitic lavas (62-64 wt% SiO_2; Fig. 3.13b), and minor olivine-pyroxene-bearing basaltic-andesites to andesites (< 59 wt% SiO_2; Fig. 3.13b). These rocks have calc-alkaline affinities and large variability in major and trace element composition (Figs. 3.5, 3.6 and 3.7), including low-pressure crystallization signatures (Fig. 3.8), and reversed isotopic behaviour for Sr isotope ratios during differentiation (Figs. 3.11 and 3.12). This suggests that the main petrogenesis of the older lavas of San Pedro most-likely involved the same two-stage model (i.e. mixing-AFC, followed by an ATA-like stage) as proposed for the La Poruña eruptives (Fig. 3.14a). The presence of mafic samples at older San Pedro may indicate an early period of mafic injections prior to the major basaltic-andesite to andesite volcanism occurred in La Poruña at ca. 100 ka. At ca. 100 ka, two different magmatic systems, sharing a common parental magma that assimilates crustal material or melts derived from the Altiplano-Puna Magma Body, started to operate. These systems are associated with the scoria cone construction, and the latest eruption stage of the San Pedro volcano (Fig. 3.14b). The mafic eruptives are likely related to an increasing input of mantle-derived magmas from deeper sources (Fig. 3.13). In a typical scenario of magma reservoirs, mafic magmas tend to accumulate in the lower part of the felsic chambers due to density differences (Huber et al., 2009). Considering that La Poruña, and San Pedro, are spatially related to the areal extent of the Altiplano Puna Magma Body (Chapter 2), ascent of the parental mafic magmas would have required an unrealistic, continuous vertical transport of melts from e.g. the mantle to easily transit through this large partially molten magma body. This implies that parental mafic magmas rather bypassed the Altiplano-Puna Magma Body to pond in the middle-upper crust and lead to evolved low-silica melts that underwent a final stage of direct ascent prior to eruption (Fig. 3.14b). Additionally, the location of the scoria cone and San Pedro could indicate that crustal faulting and pre-existing lineaments facilitated magma ascent (e.g. Giambiagi et al., 2016; Marín, 2016; Sellés and Gardeweg, 2017; Tibaldi et al., 2017), with direct ascent and therefore limited interaction between the parental magma and country rock. This, as discussed earlier, is also a plausible

petrogenetic model for the older rocks (> 96 ka) from San Pedro volcano (Fig. 3.14a), if the partially molten layer is assumed to have been relatively stationary with time. The geochemical character of the latest stage of the San Pedro (< 96 ka), i.e. the relatively high $^{87}Sr/^{86}Sr$ ratios with horizontal trends (> 0.7066; Figs. 3.11 and 3.12) and the occurrences of olivine-pyroxene-bearing to amphibole-bearing rocks (Figs. 3.4 and 3.13), argue, however, for an increasing of contamination of the parental magmas and late mineral phase crystallization at possibly shallow crustal levels (Fig. 3.14b). This therefore indicates progressively longer interaction times between successive ascending mafic magmas and crustal material, which may be attributed to changes in the thermal conditions due to the massive mafic input associated with the eruption of La Poruña.

3.6 Conclusions

La Poruña scoria cone (ca. 100 ka) was constructed during a period of increasing input of parental mafic magmas to the middle-upper crust. Some of these magmas were diverted to the margins of the Altiplano-Puna Magma Body, where they ponded in a shallow crustal magma-plumbing system and differentiated to generate basaltic-andesite to andesitic compositions before direct ascent and eruption. Therefore, parental magmas of La Poruña were generated by a two-stage evolutionary process: a stage of differentiation by magma mixing with melts derived from the APMB and/or by coupled crustal assimilation and fractional crystallization, followed by an assimilation-by-turbulent-ascent stage. The erupted fine-grained rocks are observed as olivine and pyroxene phyric with relatively larger compositional ranges in major and trace element concentrations (56.0-59.6 wt% SiO_2; 4.1-6.1 wt% MgO; 560-608 ppm Sr; 184-625 ppm Cr), and in Sr and Nd isotope ratios ($^{87}Sr/^{86}Sr$ = 0.70618-0.70664; $^{143}Nd/^{144}Nd$ = 0.51239-0.51245).

Similar, geochemical evidence from older San Pedro eruptives (> 96 ka) suggest magmatic evolution involving ATA-like processes after mixing-AFC. The small, isolated outcrops of olivine-pyroxene-

bearing rocks exposed in the San Pedro volcano appeared as earlier mafic activity before the La Poruña eruption. The younger eruptions (< 96 ka) of San Pedro, coeval with the La Poruña eruption, represent a period of more differentiated volcanism due to a higher degree of crustal assimilation and contamination of the parental magmas. This is indicated by the abrupt increase of Sr isotope ratios and significant amphibole fractionation during differentiation, interpreted here as due to a potential change in the thermal conditions close to the scoria cone.

Finally, petrogenesis of La Poruña scoria cone, revealed by $^{40}Ar/^{39}Ar$ ages, geochemistry and petrography, argues for an independent system with overall magmatic evolution controlled by the amounts of mafic melts injected through the thickened crust, and likely associated to local crustal faulting of the overlying brittle shallowest crust. This scenario appears plausible for other small mafic complexes in the Central Andes, which are usually considered as peripheral or parasitic edifices to larger stratovolcanoes.

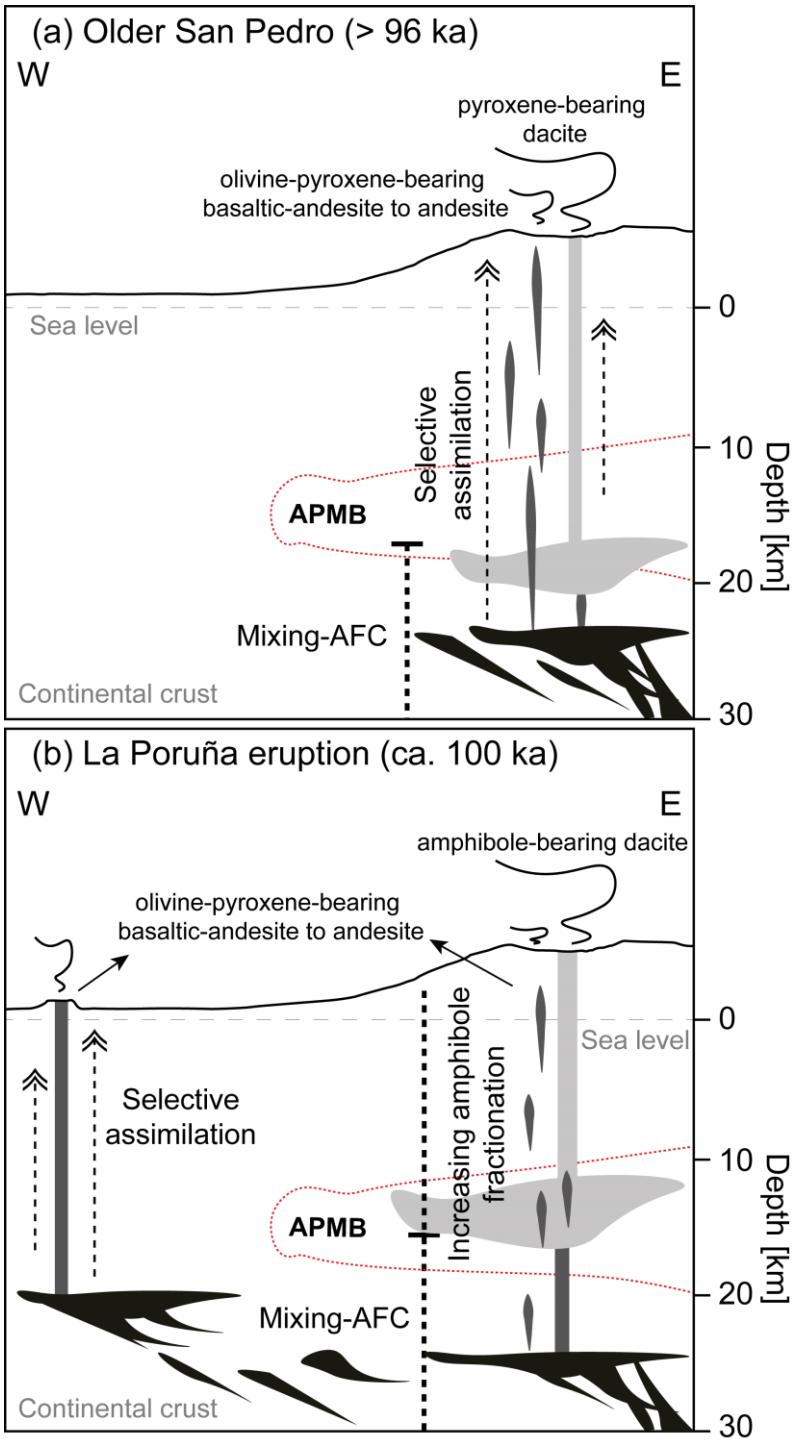

Fig. 3.14. Schematic model (not to scale) of the related petrogenesis of La Poruña and its relation with coeval eruptions from San Pedro. (a) The older San Pedro period (> 96 ka) corresponds to the eruption of pyroxene-bearing dacite, and isolated batches of olivine-pyroxene-bearing basaltic-andesite to andesite lavas, from San Pedro. Such parental magmas involved a late stage of

assimilation-by-turbulent-ascent after a magma mixing-AFC stage in the middle-upper crust. The mafic eruptives may indicate earlier injections of mafic magmas prior to construction of La Poruña. (b) La Poruña eruption (ca. 100 ka) represents a singular escape of mafic magma around the margin of the APMB as consequence of the increasing input of parental mafic magmas to the middle-upper crust. Our data suggest the same two-stage petrogenesis for the older volcanics of San Pedro and the La Poruña mafic eruptives (mixing-AFC followed by ATA-like processes). This latter eruption potentially modified the thermal conditions near to La Poruña, thus increasing the degrees of crustal assimilation and amphibole fractionation of the San Pedro plumbing system. The geochemical and isotopic data of the younger San Pedro samples (> 96 ka) suggest that the ascending mafic magmas stalling at upper crustal levels, which evolved by fractional crystallization processes after extensive crustal contamination. The depth and extent estimation of the APMB is based on Ward et al. (2014).

3.7 Examiners' non-typographic corrections and comments

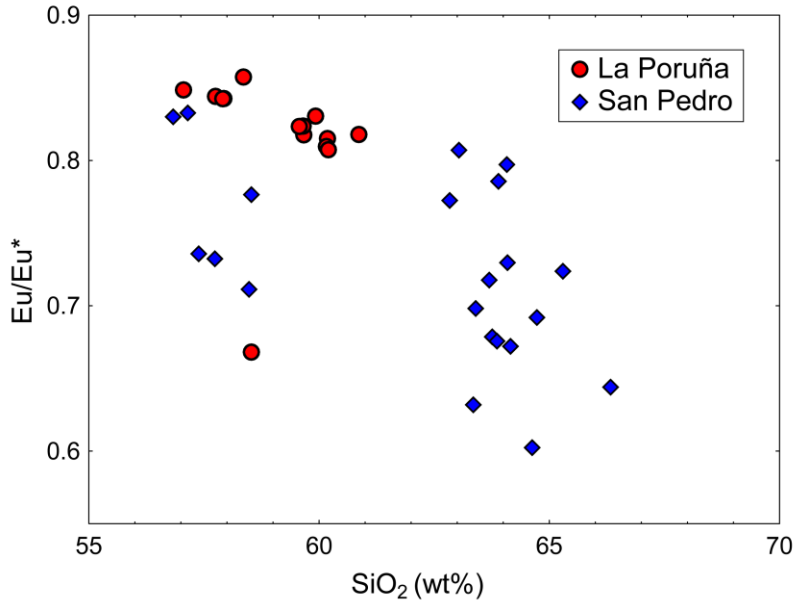

Fig. 3.15. Eu/Eu* vs. SiO_2 diagram for the studied samples from La Poruña and San Pedro. The overall negative correlation is postulated to reflect an increasing role of plagioclase fractionation during differentiation.

The mafic rocks of the Argentinian Puna frequently contain xenoliths and xenocrysts of quartz, plagioclase and/or K-feldspar, which also support the ATA process developed in the back-arc region (e.g. Guzmán et al., 2006; Maro et al., 2017). For La Poruña and San Pedro, neither xenoliths nor xenocrysts of quartz and K-feldspar were observed, however plagioclase xenocrysts are rarely found. The unusual reversed isotopic trend of decreasing Sr-isotope ratios as SiO_2 increases, on the other hand, was not observed for the Puna mafic rocks. As felsic metamorphic and plutonic complexes with highly $^{87}Sr/^{86}Sr$ isotope ratios (e.g. $^{87}Sr/^{86}Sr$ = 0.7085 to 0.7278, Lucassen et al., 2001) form the basement in the area (Damm et al., 1990), this reversed isotopic behaviour cannot be explained by assimilation of low-$^{87}Sr/^{86}Sr$ continental crust but agrees with that expected for an ATA development (See Section 3.5.1).

Chapter 4

Parental magma $\delta^{18}O$ values of the Altiplano-Puna Volcanic Complex

Section 4.1 of this chapter is based on the Laser Fluorination work published as:

González-Maurel, O., Deegan, F.M., le Roux, P., Harris, C., Troll, V.R., Godoy, B., 2020. Constraining the sub-arc, parental magma composition for the giant Altiplano-Puna Volcanic Complex, northern Chile. Scientific Reports, 10(1):1-10. https://doi.org/10.1038/s41598-020-63454-1.

Section 4.2 of this chapter is based on unpublished Secondary Ionisation Mass Spectrometry and Electron Probe Microanalysis work.

The Andean continental arc is built upon the thickest crust on Earth and the composition of most erupted materials reflect magma-crust interaction. Robust models of mass and volatile fluxes at subduction zones require that crustal "noise" is taken into consideration, and that the nature of parental magmas is constrained. Here I present new olivine and clinopyroxene oxygen isotope data obtained by single mineral Laser Fluorination (LF) analysis from the most mafic volcanic rocks erupted at the western margin of the Altiplano-Puna Volcanic Complex. Additionally, the first *in-situ* $\delta^{18}O$ values for mafic minerals from the studied mafic rocks of differing ages are presented. Lastly, pre-eruptive storage depth of these mafic magmas and the oxygen isotope composition of the parental melt are estimated. It is also worth noting that the results in Section 4.1 and 4.2 lead to slightly different conclusions, which are discussed thoroughly in Section 4.3.

The following text in Section 4.1 is reproduced verbatim from the published paper mentioned above and only reformatted to comply fully with the Doctoral Degree Board (University of Cape Town) guidelines for Doctoral Thesis.

4.1 The sub-arc, parental magma composition from single mineral oxygen isotope analysis

4.1.1 Introduction

Eruption products of frontal arc volcanoes usually exhibit heterogeneous chemical and isotopic compositions because parental magmas are compositionally modified by incorporation of continental crust either at their source via subducted sedimentary material or by crustal contamination during subsequent ascent through the crust (e.g. Davidson et al., 2005). A classic example of a volcanic arc, with near ubiquitous geochemical features of continental crust in its erupted products, is that of the Central Andes, which is associated with the thickest crust on Earth (70-74 km; Beck et al., 1996). The great thickness and compositional heterogeneity of the crust material through which magmas must pass *en route* to the surface is generally assumed to modify primitive magma compositions, yet knowledge of the primitive end-member is required in order to make robust models of subduction-related element fluxes. Oxygen isotopes allow robust modelling of crustal recycling in subduction zones as (i) they undergo minimal fractionation at mantle temperatures, (ii) there is a strong contrast between the $\delta^{18}O$ values of mantle-derived magma and crustal rocks, and (iii) the end-members involved have very similar O contents (e.g. Bindeman et al., 2005; Dallai et al., 2019; Taylor, 1968). In order to utilize oxygen isotopes to assess the magnitude of crustal material assimilated by evolved magmas along the Central Andean arc, it is necessary to know the $\delta^{18}O$ value of the parent magma, which itself may be compositionally modified by assimilation in the deep crust. However, the oxygen isotope compositions of mafic magmas in the Central Andes are poorly constrained and the existing $\delta^{18}O$ values, including those obtained on olivine and pyroxene phenocrysts (Fig. 4.1), are highly

variable (Supplementary material 5; Table S5.1). Oxygen isotope data obtained by conventional and laser fluorination analysis for olivine (Entenmann, 1994; Godoy, 2014; Kay et al., 2011) and pyroxene (Chang, 2007; Entenmann, 1994; Freymuth et al., 2015; Godoy, 2014) from Central Andean volcanoes have $\delta^{18}O$ values ranging from 5.0 to 8.3‰ (average = 6.7‰, n = 19) and 5.5 to 8.7‰ (average = 6.2‰, n = 39), respectively (see also Supplementary material 5; Tables S5.2 and S5.3). In contrast, typical mantle rocks show very limited variations in their $\delta^{18}O$ values (e.g. olivine = 5.2 ± 0.3‰; clinopyroxene = 5.6 ± 0.4‰; Mattey et al., 1994). The spread in the Central Andean literature data suggests that the oxygen isotope ratios of some of these lavas were modified by various processes post-dating the formation of the parental melt (e.g. extensive fractionation, late-stage assimilation, mixing of isotopically diverse magmas, or alteration). The challenge, therefore, is to constrain the parental melt value, before extensive fractionation or late-stage assimilation has taken place. We aim to achieve this goal by analysing the $\delta^{18}O$ values of minerals from rare, weakly differentiated lavas with low silica contents (54.6 to 57.2 wt%) and relatively low Sr and high Nd isotope ratios ($^{87}Sr/^{86}Sr$ = 0.70554 to 0.70669; $^{143}Nd/^{144}Nd$ = 0.51234 to 0.51251; see Chapter 2). The samples selected for this study are from six individual volcanoes (La Poruña, San Pedro, Paniri, La Poruñita, Palpana and Chela), which were active at different times and are all located around the western margin of the Altiplano-Puna Magma Body (APMB) melt anomaly in the Altiplano-Puna Volcanic Complex (Fig. 4.1). Based on their radiogenic isotope compositions, the selected samples have experienced limited degrees of crustal modification (e.g. assimilation) and are therefore ideally suited to obtaining the parental $\delta^{18}O$ values locked in early-formed crystals. The crystal-focused approach employed here offers critical new insights that have until now been under-explored due to the limitations inherent in whole-rock geochemical approaches (e.g. the susceptibility of whole-rock samples to secondary alteration and the fact that the $\delta^{18}O$ values of whole-rock samples represent averages of the various phases that constitute the sample, cf. Davidson et al., 2005). These results therefore contribute to filling the gaps in the knowledge of subduction related parental magma compositions feeding the largest continental magma system on Earth.

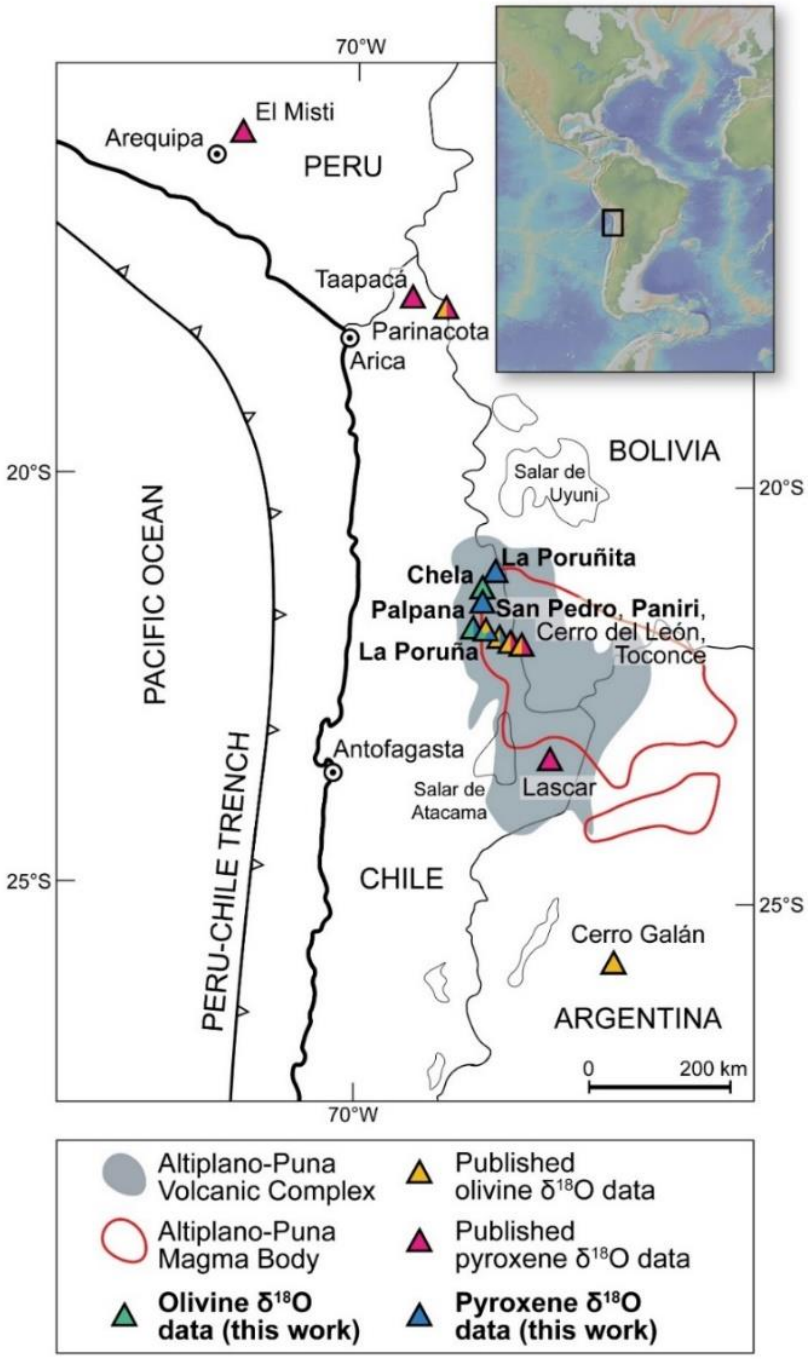

Fig. 4.1. Study area. (a) Map of the Central Andes showing the location of the volcanoes (in bold) included in this study and volcanoes with available $\delta^{18}O$ values for olivine and pyroxene. The distribution of the Altiplano-Puna Volcanic Complex and the surface projection of Altiplano-Puna Magma Body are based on Zandt et al. (2003). Inset map created using "GeoMapApp" (www.geomapapp.org; Ryan et al., 2019).

4.1.2 Study area and sample selection

Common volcanic products in the Central Andes include stratovolcanoes and extensive ignimbrite deposits, but several monogenetic volcanoes of mafic character also exist (Godoy et al., 2019; see also Chapter 2). Within the volcano-tectonic ignimbrite province of the Altiplano-Puna Volcanic Complex (de Silva, 1989), the location of mafic volcanism is largely confined to the borders of the partial melt anomaly termed the Altiplano-Puna Magma Body (APMB, Chmielowski et al., 1999; Fig. 4.1). The APMB is the largest known zone of partial melting in the continental crust throughout the world, with an estimated melt volume of 500,000 km^3 and spanning a region of ca. 200 km in diameter (Chmielowski et al., 1999; Ward et al., 2014; Fig. 4.1). Based on geophysical surveys, this anomaly, located in the upper crust, shows an increasing melt fraction from its margin (ca. 4 vol%) to its centre (up to 25 vol%) (e.g. Araya Vargas et al., 2019; Comeau et al., 2015; Ward et al., 2014). In this region, volcanoes outside the limits of the APMB are composed of lava that is more primitive than the volcanoes situated directly above the APMB (Chapter 2).

The volcanoes included in this study comprise, in order of increasing eruption age, La Poruña, San Pedro, Paniri, La Poruñita, Palpana and Chela, all of which are situated within the Altiplano-Puna Volcanic Complex but peripheral to the proposed APMB reservoir (Zandt et al., 2003; Fig. 4.1). In this region, the ascending parental basaltic-andesite magma is thought to have avoided significant contamination by evolved melts from the APMB as demonstrated by the lowest $^{87}Sr/^{86}Sr$ and highest $^{143}Nd/^{144}Nd$ being towards the borders of the large felsic body (see Fig. 2.12 in Chapter 2). The studied volcanoes (Fig. 4.1), together with the other Pliocene to Quaternary andesitic-to-dacitic stratovolcanoes, dacitic domes and monogenetic cones, overlie Miocene rhyodacitic-to-rhyolitic ignimbrite sheets (Sellés and Gardeweg, 2017).

La Poruña (21º53’S; 68º30’W) is a well-preserved 140 m high scoria cone 100 ka in age (see Chapter 3) situated on the west flank of the 6000 m San Pedro stratovolcano complex (21º53’S; 68º24’W). La

Poruña is composed of pyroclastic material and an extensive basaltic-andesite to andesite lava flow that extends up to 8 km to the south-west of the main vent, whereas San Pedro is a composite stratovolcano formed by two superimposed coalescent cones (Sellés and Gardeweg, 2017). The entire La Poruña volcano represents a monogenetic, relatively small to medium volume and short-lived singular eruption, whose magmatic evolution has been described as a two-stage evolutionary process involving minor assimilation and fractionation, followed by selective assimilation during turbulent ascent (see Fig. 3.14 in Chapter 3). In contrast, San Pedro is a >100 km^2 andesitic-to-dacitic volcanic field, with a long-lived (from ca. 510 ka to present) but episodic eruptive centre, whose recent (<160 ka) mafic activity is genetically similar to La Poruña (Chapter 3). Paniri (22º03'S; 68º14'W) is a stratovolcano constructed during four separate stages between 1.4 Ma to 100 ka, whose most primitive activity is represented by isolated basaltic-andesite to andesite lava flows erupted at ca. 400 kyr ago (Godoy et al., 2018). La Poruñita (21°17'S; 68°15'W), situated in the northernmost part of the projected APMB, is a scoria cone ca. 600 ka in age of about 700 m in diameter (Wörner et al., 2000), similar in shape and composition to La Poruña (Supplementary material 1; Table S1). Palpana (21º32'S; 68º31'W) is a conical stratovolcano built up of mafic andesite lava flows. The summit of the volcanic edifice has a crater morphology (dimensions 1.8 km by 1.3 km) that is truncated by the last-erupted dome (Sellés and Gardeweg, 2017). Chela volcano (21º24'S; 68º30'W) is very similar in shape and composition to Palpana. The shape and relatively monotonous composition have been related to rapid construction of the volcanic edifices at ca. 4.1 Ma for Chela and ca. 3.8 Ma for Palpana, followed by restricted erosion and limited duration of magmatic differentiation (Wörner et al., 2000).

Olivine- and pyroxene-phyric lava and scoria are ubiquitous at La Poruña, San Pedro, Paniri, La Poruñita, Palpana and Chela and vary from basaltic-andesite to andesite in composition, with whole-rock elemental and Sr and Nd isotope compositions that range from e.g., SiO_2 = 54.6 to 62.9 wt%, MgO = 1.6 to 6.1 wt%, Sr = 389 to 885 ppm, Cr = 5 to 625 ppm, $^{87}Sr/^{86}Sr$ = 0.705541(10) to

0.707656(10), and $^{143}Nd/^{144}Nd$ = 0.512337(12) to 0.512513(50) (see Godoy et al., 2018; Chapters 2 and 3). In this study, it was utilized whole-rock elemental and Sr and Nd isotope data to construct an evolutionary model, in which limited magmatic differentiation occurred at mid-upper crustal levels (Chapters 2 and 3). Lavas of these selected volcanoes may thus represent the composition of parental magmas feeding volcanism within the Altiplano-Puna Volcanic Complex, as the magmas feeding these mafic eruptions largely escaped assimilation of APMB felsic melts during ascent (see Fig. 2.13 in Chapter 2). In this study, I focused on sample material containing suitable mafic mineral phases for single mineral oxygen isotope analysis.

4.1.3 Methods

4.1.3.1 Sample selection and preparation

In this study, crystals from the least silicic materials identified at La Poruña, San Pedro, Paniri, La Poruñita, Palpana and Chela volcanoes were analysed. These volcanoes also had among the least evolved baseline Sr and Nd isotopic compositions thus far reported for the western boundary of the Altiplano-Puna Volcanic Complex province (Chapter 2). Pristine inclusion-free olivine and pyroxene crystals were hand-picked under a binocular microscope.

4.1.3.1 Oxygen isotope analysis by laser fluorination

Olivine and pyroxene grains visibly free of alteration or inclusions were selected by hand-picking under a binocular microscope. Laser fluorination (LF) analyses were then carried out at the Department of Geological Sciences, University of Cape Town (UCT), South Africa. The oxygen isotope results are reported in standard δ-notation relative to V-SMOW (Standard Mean Ocean Water), where $\delta = [(^{18}O/^{16}O)_{sample} / (^{18}O/^{16}O)V\text{-}SMOW - 1] * 1000$. Full analytical details of the laser fluorination method employed at UCT are given in Harris and Vogeli (2010). Measured values of the

UCT in-house standard MON GT (Monastery garnet, $\delta^{18}O = 5.38‰$) were used to normalize the raw data and correct for drift in the reference gas. The $\delta^{18}O$ value of MON GT was established by cross-calibration with the UWG-2 garnet standard of Valley et al. (1995) and San Carlos olivine. The long-term average difference in $\delta^{18}O$ values of duplicates of MON GT is 0.15‰, which corresponds to a 2σ S.D. value of 0.15‰. Laser fluorination data are given in Table 4.1. All analyses gave gas pressures of O_2 that were consistent with ~100% conversion of mineral to O_2.

4.1.4 Results

4.1.4.1 Petrography

Basaltic-andesite lavas from La Poruña contain ca. 30 vol.% phenocrysts (plagioclase > olivine > clinopyroxene > orthopyroxene) and Fe-Ti oxides set in a microlite-rich groundmass of plagioclase and pyroxene and a small percentage of remaining glass. Olivine (up to 2.5 mm in size; ≤ 12 vol.%) textures include subhedral crystals, embayments and skeletal textures. Clinopyroxene is the most common pyroxene phase and occurs as euhedral to subhedral individual crystals (up to 2 mm; ≤ 10 vol.%) or as reaction rims on orthopyroxene phenocrysts. Besides occurring individually, clinopyroxene crystals occur as glomerocrysts with plagioclase, olivine and orthopyroxene (Fig. 4.2).

Basaltic-andesites from San Pedro are porphyritic (ca. 15 vol.% phenocrysts), glassy and fine-grained, with plagioclase > olivine > clinopyroxene > orthopyroxene as phenocrysts. Olivine (up to 2 mm; ≤ 10 vol%) appears frequently embayed, resorbed, or with reaction rims of pyroxene (Fig. 4.2). Clinopyroxene appears as euhedral to subhedral phenocrysts (up to 1.5 mm; ≤ 8 vol.%). Clinopyroxene phenocrysts occur individually or as crystal clots.

Basaltic-andesites from La Poruñita are vesicular and fine-grained, containing olivine > clinopyroxene = orthopyroxene as phenocrysts (≤ 15 vol.%). These phenocrysts are set in a

hypocrystalline groundmass, which is made of microlites of plagioclase, interstitial glass, clinopyroxene and orthopyroxene. Olivine morphologies are varied, including subhedral and resorbed crystals (up to 0.5 mm in size; ≤ 7 vol.%). Most of these phenocrysts show embayments and oxide inclusions. Clinopyroxene appears as euhedral to subhedral individual phenocrysts (up to 1.5 mm; ≤ 4 vol.%).

Basaltic-andesites from Paniri are plagioclase-olivine-pyroxene-phyric lavas. These contains ca. 30 vol.% phenocrysts of plagioclase > olivine = clinopyroxene = orthopyroxene. Olivine and pyroxene frequently form glomerocrysts with plagioclase. Clinopyroxene (up to 1.5 mm in size; ≤ 8 vol.%) also appears individually as euhedral to subhedral crystals.

Andesites from Palpana contain ca. 30 vol.% phenocrysts of plagioclase > clinopyroxene > orthopyroxene and minor olivine set in a hypocrystalline groundmass of glass, plagioclase and pyroxene. Clinopyroxene (up to 2.5 mm; ≤ 15 vol.%) occurs as subhedral to euhedral tabular crystals (Fig. 4.2).

Basaltic-andesites from Chela are composed of ca. 25 vol.% phenocrysts (plagioclase > olivine >> clinopyroxene > orthopyroxene) set in a glassy groundmass. Olivine generally appears as subhedral crystals in a seriate crystal size distribution as phenocryst and microlites (up to 2 mm; ≤ 10 vol.%; Fig. 4.2). Glomerocrysts (olivine-pyroxene) and pyroxene reaction rims on olivine are common. Orthopyroxene and clinopyroxene occur only rarely as glomerocrysts and microlites.

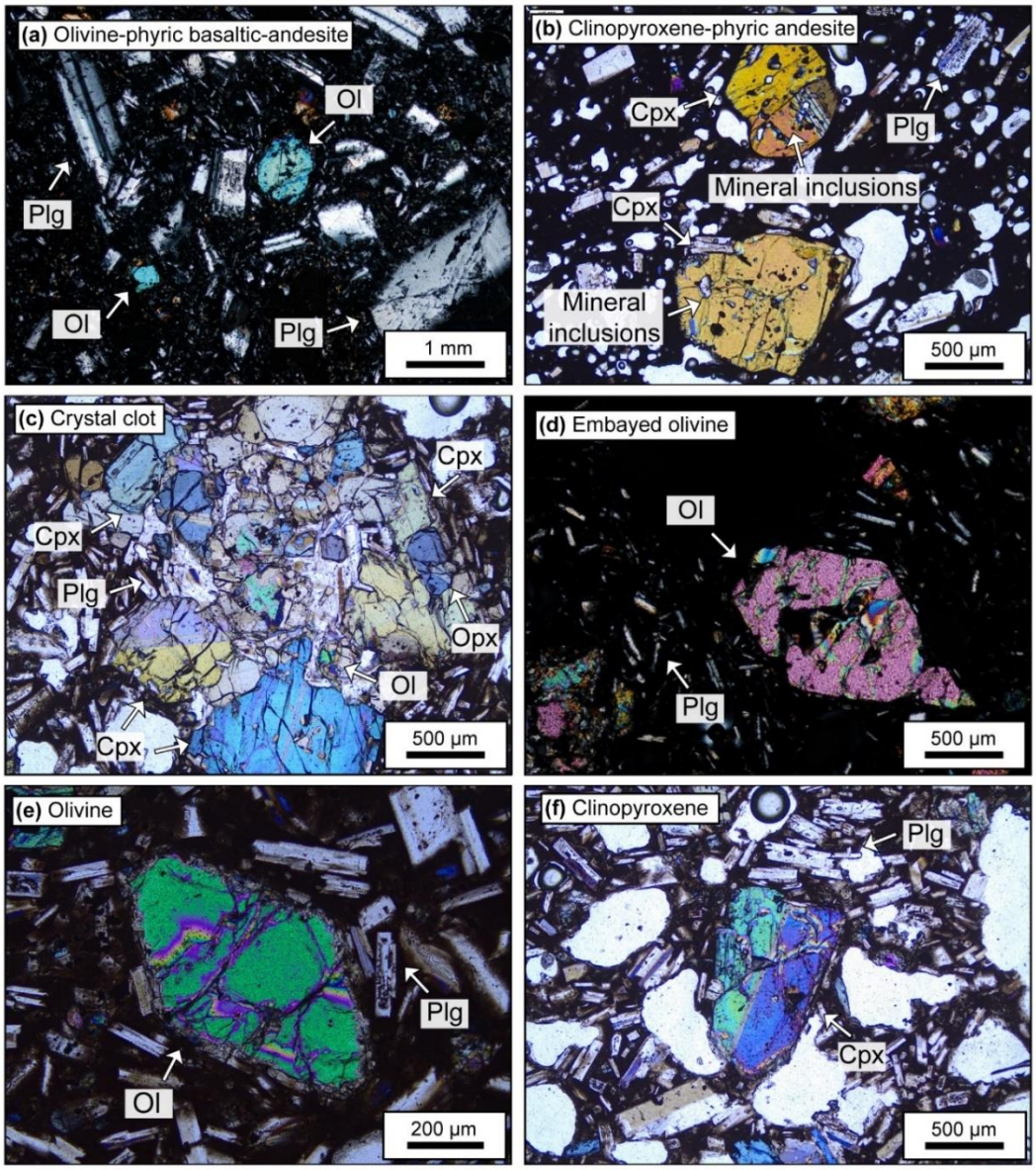

Fig. 4.2. Selected photomicrographs under cross-polarized light of the studied samples. (a) CHE-03, fine-grained seriate textured plagioclase-olivine-phyric basaltic-andesite. (b) PAL-02, glassy fine-grained plagioclase-pyroxene-phyric andesite. (c) POR-06, crystal clot of clinopyroxene, plagioclase, orthopyroxene and olivine. (d) SPE-10, embayed olivine in a glassy olivine-pyroxene basaltic-andesite (e) POR-06, euhedral olivine crystal set in a microlite-rich groundmass of plagioclase and glass. Olivine crystals usually have fractures and mineral inclusions. (f) POR-06, subhedral clinopyroxene crystal. Clinopyroxene crystals generally contain melt or mineral inclusions, and visible twinning and zoning.

4.1.4.1 Oxygen isotope data

It was determined the $\delta^{18}O$ values of olivine from lavas from three volcanoes whose erupted products contain large (≥ 2 mm) olivine phenocrysts (La Poruña, San Pedro, and Chela) and clinopyroxene from five volcanoes whose erupted products contain large (≥ 1.5 mm) pyroxene phenocrysts (La Poruña, San Pedro, Paniri, La Poruñita and Palpana) (Table 4.1). All minerals were individually selected under a binocular microscope before analysis and were visually free of inclusions or alteration. Laser Fluorination (LF, see Methods) analysis of olivine gave $\delta^{18}O$ values of 5.7 to 6.2‰ for La Poruña (n = 4), 6.2‰ for San Pedro (n = 1), and 5.8‰ for Chela (n = 1). These values overlap the higher values obtained for olivine from mantle-derived basalts (cf. up to 6.3‰, Eiler et al., 2011; Fig. 4.3). Individual clinopyroxene crystals analysed by LF for La Poruña, San Pedro, La Poruñita and Palpana volcanoes gave average $\delta^{18}O$ values of 6.4 to 7.2‰ (n = 5), 6.7 to 6.9‰ (n = 2), 7.0‰ (n = 1) and 6.3 to 7.0‰ (n = 2), respectively. The clinopyroxene crystals analysed here have higher $\delta^{18}O$ values than mantle-derived pyroxene (cf. up to 6.5‰, after Eiler et al., 2011; Fig. 4.3).

New olivine and pyroxene $\delta^{18}O$ values display substantially narrower ranges than the available data for the Central Andes (Fig. 4.3). Published olivine $\delta^{18}O$ values (Chang, 2007; Entenmann, 1994; Freymuth et al., 2015; Godoy, 2014; Kay et al., 2011) tend to have either relatively high (> 6.5‰) or mantle-like $\delta^{18}O$ values. Notably, new olivine oxygen isotope data from La Poruña, San Pedro and Chela volcanoes have among the lowest $\delta^{18}O$ values ($\delta^{18}O$ = 5.7% to 6.2‰) with respect to all olivine data reported thus far for the Central Andes (cf. Parinacota, Entenmann, 1994; Cerro Galán, Kay et al., 2011; San Pedro, Godoy, 2014; Fig. 4.4). New clinopyroxene data ($\delta^{18}O$ = 6.3% to 7.2‰) overlap with the $\delta^{18}O$ values previously obtained for pyroxene from the Central Andes (5.5‰ to 8.7‰; Chang, 2007; Entenmann, 1994; Freymuth et al., 2015; Godoy, 2014) and are at the higher end of the previously reported data range (excluding one exceptionally high value reported for Toconce volcano; Fig. 4.3).

Table 4.1. Laser fluorination analyses of olivine and clinopyroxene crystals from selected mafic volcanic rocks erupted at the western margin of the Altiplano-Puna Volcanic Complex. Whole-rock geochemical and isotope composition from Supplementary material 1 (Table S1).

Volcano (North to South)	Sample	$\delta^{18}O_{ol}$	$\delta^{18}O_{melt\text{-}ol}$	$\delta^{18}O_{cpx}$	$\delta^{18}O_{melt\text{-}cpx}$	Whole-rock geochemistry and Sr and Nd isotopes					
						SiO_2 (wt%)	*MgO (wt%)*	*Mg#*	*Sr (ppm)*	*$^{87}Sr/^{86}Sr$*	*$^{143}Nd/^{144}Nd$*
La Poruñita	PORU-01			7.0	7.7	55.49	4.28	52	484	0.706408(13)	0.512344(12)
Palpana	PAL-02			6.4 7.0	7.1 7.7	57.21	3.82	52	632	0.705730(11)	0.512426(11)
Chela	CHE-03	5.8	7.1			54.61	3.86	49	793	0.705541(10)	0.512513(50)
La Poruña	POR-05	5.7	7.0	6.4 6.6	7.1 7.3	56.28	4.09	57	452	0.706441(10)	0.512444(13)
	POR-06	5.9	7.2	6.4 6.5	7.1 7.2	55.61	6.08	61	514	0.706361(12)	0.512419(17)
	CH-AZU-010	6.0 6.2	7.3 7.5								
	POR-08			7.2	7.9	55.78	5.52	59	456	0.706679(12)	0.512385(14)
San Pedro	SPE-10	6.2	7.5	6.7 6.9	7.4 7.6	55.17	5.50	59	558	0.706672(11)	0.512374(14)
Paniri	PANI-05			6.3 7.0	7.0 7.7	56.04	4.09	53	599	0.706690(11)	0.512374(14)

The oxygen isotope data are reported in ‰ relative to the V-SMOW scale. See Methods for analytical details. *ol* olivine, *cpx* clinopyroxene. The estimations of melt $\delta^{18}O$ values (i.e. $\delta^{18}O_{melt\text{-}ol}$ and $\delta^{18}O_{melt\text{-}cpx}$) are based on an equilibrium mineral-melt fractionation factor of 1.3‰ for olivine and 0.7‰ for clinopyroxene (see text for details; mineral-melt fractionations from Bindeman et al. (2004)).

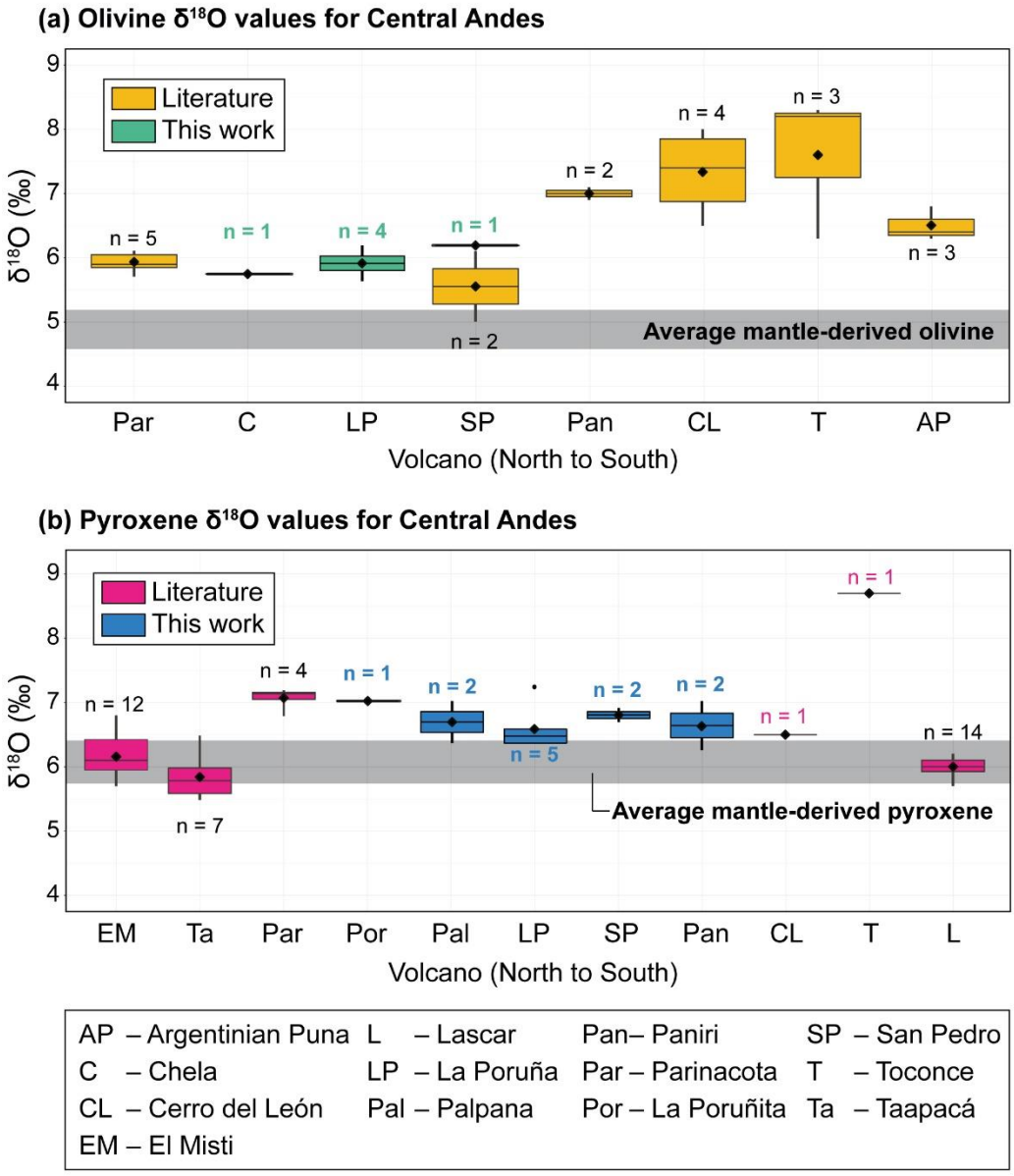

Fig. 4.3. Oxygen isotope data for the Central Andes. (a, b) Variation in new (in bold) and literature $\delta^{18}O$ values for olivine (a) and pyroxene (b) obtained by conventional (i.e. Parinacota, Entenmann, 1994) and laser fluorination and displayed as box-and-whisker plots. Note that the new olivine and clinopyroxene data have higher average $\delta^{18}O$ values for olivine and pyroxene than mantle-derived basalts (average = 4.8‰ ± 0.2, n = 104 for olivine and average = 6.1‰ ± 0.3, n = 16 for pyroxene; Eiler et al., 2011). Further details of published data are given in Supplementary material 5 (Tables S5.2 and S5.3).

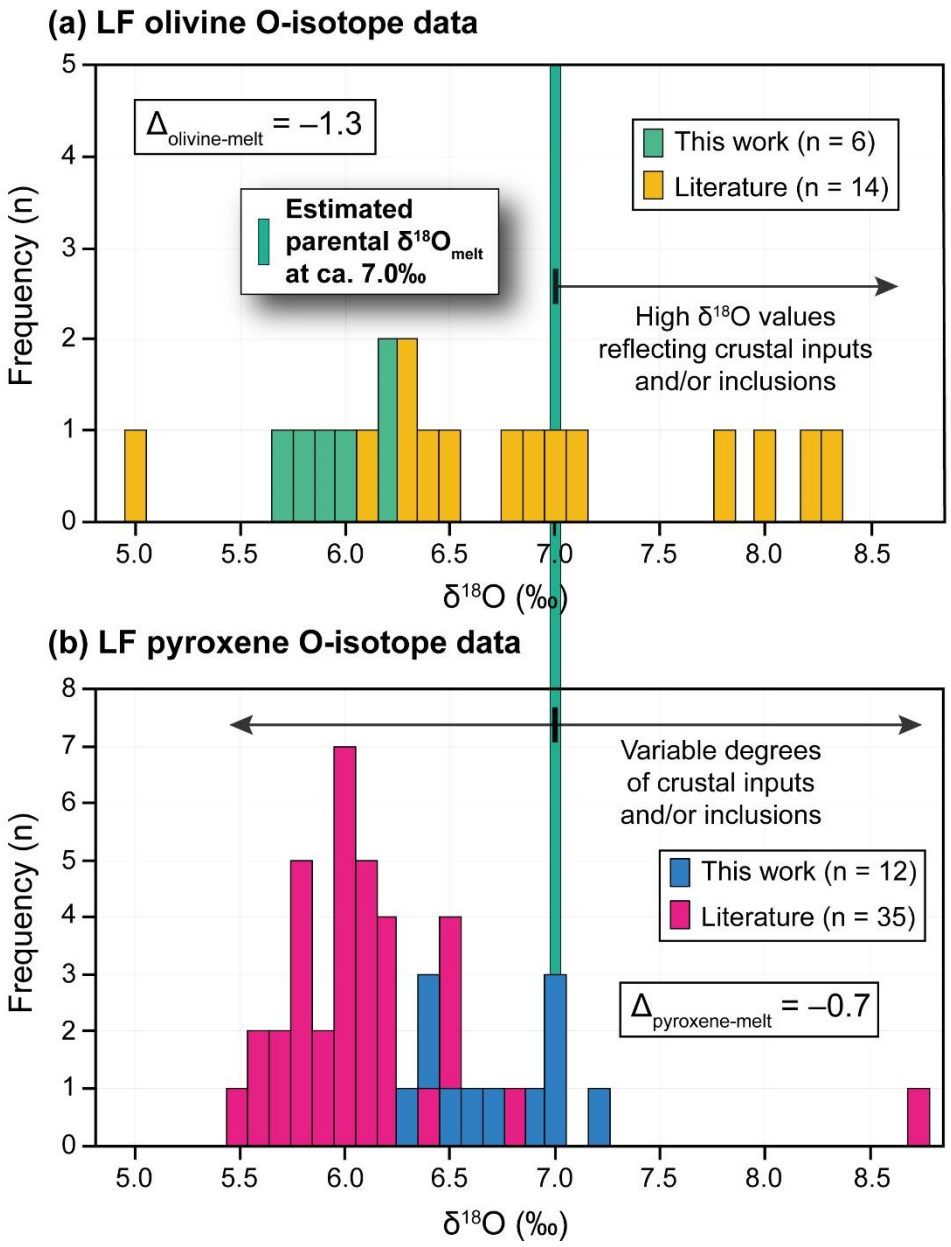

Fig. 4.4. Frequency distribution of $\delta^{18}O$ values of olivine (a) and pyroxene (b) for the new data in comparison to published data obtained by laser fluorination from the Central Andes. Note that new olivine data overlap with the lowest $\delta^{18}O$ values reported previously for the Central Andes, whereas new clinopyroxene data overlap the higher end of the $\delta^{18}O$ range. The equilibrium melt would have had a $\delta^{18}O$ value of ca. 7.0‰, based on olivine-melt and clinopyroxene-melt fractionation factors of 1.3‰ and 0.7‰, respectively (see text; mineral-melt fractionations from Bindeman et al. (2004)). Summary of previously published data are given in Supplementary material 5 (Tables S5.2 and S5.3).

4.1.5 Discussion

Available whole-rock geochemistry for the studied samples (Table 4.1) reveal that clinopyroxene-phyric (e.g. PAL-02) and olivine-pyroxene-phyric lavas (e.g. POR-06) have higher SiO_2 contents than samples that only contain olivine as phenocrysts (e.g. CHE-03). It is thus possible that pyroxene crystallized at a higher crustal level than olivine and might record late-stage crustal assimilation (cf. Burns et al., 2020; Deegan et al., 2016; Risse et al., 2013). It is also noted that arc lava pyroxenes frequently contain inclusions of plagioclase (which would have higher $\delta^{18}O$ values) and/or oxide (lower $\delta^{18}O$ values) (e.g. Fig. 4.2; see also Fig. 4 in Deegan et al., 2016). Because of the very dark appearance of pyroxene under the binocular microscope, it is both difficult to determine if inclusions are present or and what they are. The wider variation of pyroxene $\delta^{18}O$ values in this study, compared to olivine may, therefore, be due to either late-stage crustal assimilation or unavoidable inclusions of various types in the analysed material.

It is possible to estimate the $\delta^{18}O$ values of the equilibrium melt by using mineral-melt fractionation factors appropriate for basaltic-andesite (SiO_2 average 55.8 wt% among the studied samples; Table 4.1). These are calculated to be $\Delta_{olivine\text{-}melt} = -1.3$ and $\Delta_{pyroxene\text{-}melt} = -0.7$, using the silica-based equations in Bindeman et al. (2004). Olivine with $\delta^{18}O$ values of 5.7 to 6.2‰, therefore, crystallized from magma having a $\delta^{18}O$ value of 7.0 to 7.5‰ (average = 7.3‰ ± 0.17, n = 6). Clinopyroxene with $\delta^{18}O$ values between 6.3 and 7.2‰ similarly calculates to magma $\delta^{18}O$ values of 7.0 to 7.9‰ (average = 7.4‰ ± 0.29, n = 12). These magma $\delta^{18}O$ values are within error of each other but are up to 2.0‰ higher than the accepted value for normal mid-ocean ridge basalts (N-MORB) (5.4‰ to 5.8‰, Eiler, 2001) and MORB glass (5.4 to 5.8‰, Eiler et al., 2000). They are also higher than previously reported $\delta^{18}O$ values from mantle-derived rocks in subduction zones elsewhere (e.g. $\delta^{18}O \leq 6.3$‰, Dallai et al., 2019; Deegan et al., 2016; Eiler et al., 2000; Jacques et al., 2014). Given that studied samples have relatively high SiO_2 contents and Mg numbers that range from 54.6 to 57.2 wt% and 49 to 61, respectively (Table 4.1), they are unlikely to represent primary or primitive mantle-derived magmas.

Indeed, the O-isotope data presented here suggest assimilation of e.g. high-$\delta^{18}O$ felsic continental crust resulting in an ^{18}O-enriched parental magma.

The high calculated melt $\delta^{18}O$ values presented here cannot be explained by closed-system Rayleigh fractionation (see calculated curve in Fig. 4.5) as this would only increase primitive $\delta^{18}O$ values by 0.2 to 0.3‰ (e.g. Bindeman et al., 2004). Pre-Mesozoic felsic metamorphic and plutonic complexes form the Central Andean basement of northern Chile at ca. 18°S to 25°S have $\delta^{18}O$ values that range between 6.4‰ to 11.8‰ (Damm et al., 1990). If it is assumed that the mantle-derived magma had a $\delta^{18}O$ value of 5.7‰ (e.g. Ito et al., 1987), a minimum of approximately 21% assimilation of local crust with a $\delta^{18}O$ of 11.8‰ would be required to reach a magma value of 7.0‰, using simple mass balance calculations ($X = [\delta^{18}O_{final} - \delta^{18}O_{initial}] / [\delta^{18}O_{assimilant} - \delta^{18}O_{initial}]$, where X is the amount of contamination as a fraction) and assuming equal oxygen content for all end-members. This estimated degree of assimilation agrees well with the estimates based on radiogenic isotope and trace element modelling using data from the same samples, which require about 12 to 28% assimilation (discussed thoroughly in Chapter 5, Section 5.2), in broad agreement with recent findings for the studied volcanoes (cf. ~13% to 23%; Godoy et al., 2017). Binary mixing modelling shows that new data are best explained by interaction between primitive mantle-derived melt and continental crust with high $^{87}Sr/^{86}Sr$ ratios (> 0.714) and $\delta^{18}O$ values of 11.8‰ to 19.5‰ (Fig. 4.5), which is not unreasonable for felsic crust in the whole Central Andean region given that e.g. Damm et al. (1990) reported $\delta^{18}O$ values up to 15.2‰ for Precambrian basement rocks from northern Argentina. The isotope modelling so far assumes simple mixing, which probably approximates behaviour in a deep crustal hot zone, but models involving AFC would likely require greater overall assimilation for the same result, because high-$\delta^{18}O$ material is removed in the cumulates. Notably, the steady increase in SiO_2 with no change in $\delta^{18}O$ value at ca. 7.0‰ (Fig. 4.5) is consistent with parental magmas that underwent closed-system fractional crystallization after an initial stage of crustal assimilation by mantle-derived magmas.

It is proposed, therefore, a model of magmatic evolution for the Altiplano-Puna Volcanic Complex where mantle-derived (primitive) magmas are injected into the felsic continental crust. Upon stagnation, these mantle-derived magmas assimilated basement rocks with high-$\delta^{18}O$ values and highly radiogenic Sr isotope ratios to form a parental magma with a $\delta^{18}O$ value of ca. 7.0‰ (Fig. 4.5). Building on the model in Fig. 2.13 (Chapter 2) for the western boundary of the Altiplano-Puna Volcanic Complex, parental melts ascended to mid to upper crustal storage levels, where they stalled, differentiated and fractionated (Godoy et al., 2019), avoiding significant further contamination by e.g. felsic melts derived from the APMB as it by-passed the molten body. At these crustal levels, olivine and subsequent clinopyroxene crystallization occurred, which is consistent with previous thermobarometric estimations performed in Quaternary lavas from the southwestern border of the Altiplano-Puna Volcanic Complex (Burns et al., 2020). Such an injection of mafic magma possibly initiated a subsequent phase of further differentiation before final ascent and eruption (see also Chapter 2 and 3).

In conclusion, volcanic rocks from the most mafic volcanoes at the western border of the Altiplano-Puna Volcanic Complex of the Central Andes have the lowest reported $\delta^{18}O$ values of 5.7 to 6.2‰ (average = 6.0‰, n = 6) for olivine, whereas clinopyroxene yielded higher $\delta^{18}O$ values of 6.3 to 7.2‰ (average = 6.7‰, n = 12). These mineral data are consistent with crystallization from a magma of the same O-isotope composition, allowing a robust $\delta^{18}O$ estimate of 7.0‰ for the sub-arc, parental magma of the APMB and associated volcanic centres in the Altiplano-Puna Volcanic Complex. This composition may be representative of parental magmas in the wider Central Andean region.

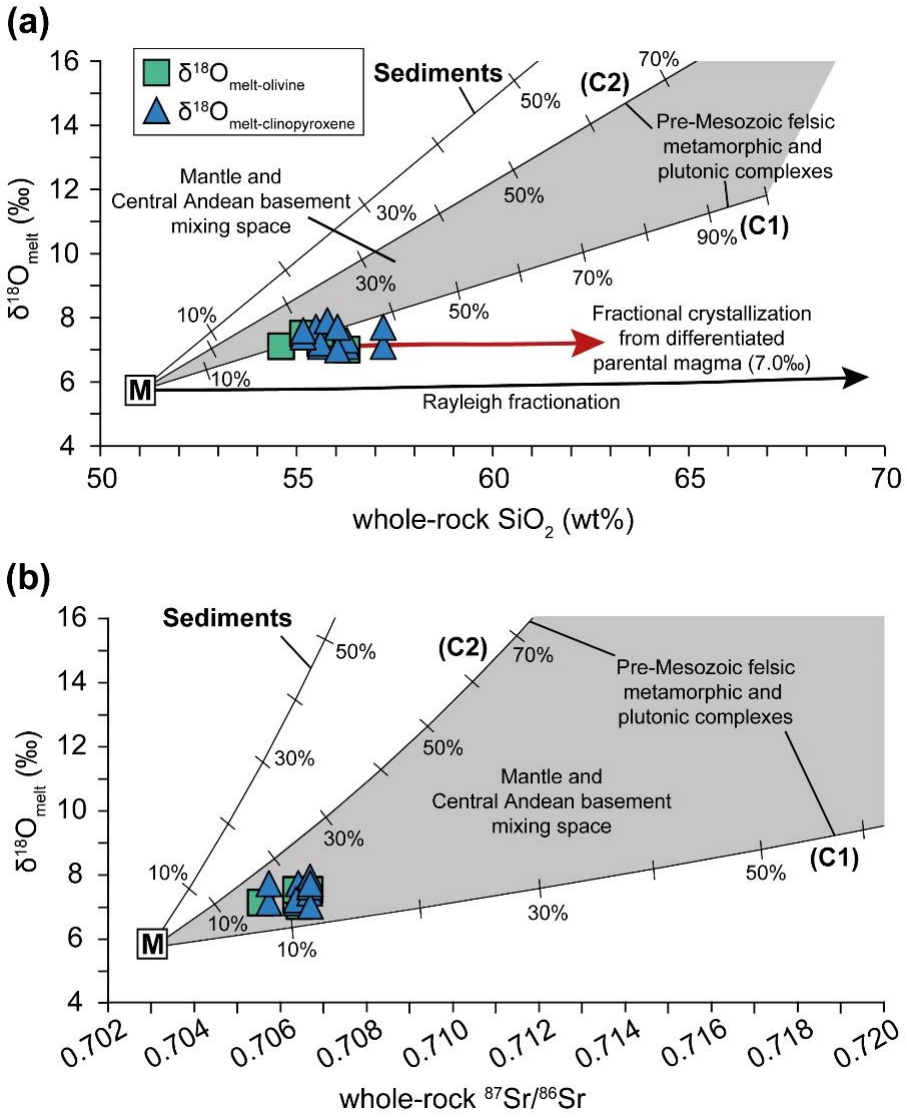

Fig. 4.5. Binary mixing models of $\delta^{18}O$ estimated melt values from analysed olivine and clinopyroxene in this work versus whole-rock (a) SiO_2 and (b) $^{87}Sr/^{86}Sr$ ratios from Supplementary material 1 (Table S1). The classical Rayleigh fractionation trend illustrates the variation in $\delta^{18}O$ values expected from closed-system fractional crystallization. Curves *C1*, *C2* and *Sediments* indicate possible types of local crustal contaminants or recycled components. The sub-arc, parental melt $\delta^{18}O$ values of 7.0‰ ± 0.2 (2σ S.D.) are postulated to reflect mantle-derived magmas (M) assimilating significant amounts of high-$\delta^{18}O$ continental crust (C1 and C2). Following crustal assimilation by M, parental magmas appear to undergo closed-system fractional crystallization, i.e. increasing magma SiO_2 at constant $\delta^{18}O$. Additional data sources are shown in Supplementary material 6.

4.2 Intra-crystal scale oxygen isotope variations in mafic minerals

In order to contrast the studied LF data in Section 4.1 and assess how representative the parental $\delta^{18}O$ values recorded in olivine and clinopyroxene are, this section adds new intra-crystal O-isotope data obtained by Secondary Ionisation Mass Spectrometry (SIMS) from the least silicic sample at La Poruña and Palpana volcanoes. The new SIMS dataset provides a first approximation of "undisturbed" clinopyroxene $\delta^{18}O$ values, since unlike in LF analysis fractures or mineral/melt inclusions can be avoided. However, disparities between LF and SIMS datasets were found. These data are reported in this study to ensure a robust parental melt $\delta^{18}O$ composition for the Altiplano-Puna Volcanic Complex.

4.2.1 Introduction

The $\delta^{18}O$ olivine and pyroxene values obtained in this work (Section 4.1) are all higher than expected in a mantle-derived magma (cf. Eiler et al., 2011; Fig. 4.3). Variability of $\delta^{18}O$ values in crustal materials, especially in arc systems, can be explained by open system processes of e.g. melting, assimilation, storage and homogenization (Hildreth and Moorbath, 1988). If parental magmas assimilate both high and low $\delta^{18}O$ crustal components, the "true" characteristics of the primary sources become obscured during magmatic evolution. Here, early-formed phases, such as olivine or pyroxene, play an important role by recording the composition of the geochemical mantle end-member or the role of crustal input into primitive magmas. The isotopic variability of Central Andean olivine and pyroxene reflect variable interactions with crustal components during storage and growth (Fig. 4.5). Mineral data are preferable to bulk-rock data which are susceptible to changes in $\delta^{18}O$ value due to secondary alteration, even in very recent lavas. However, it is also worth noting that conventional and laser fluorination analyses incorporate all parts of the rock or crystal, including not only altered or crustally contaminated crystal zones but also any inclusions present in the crystal(s) analysed. Inconspicuous but numerous mineral inclusions of e.g. plagioclase (higher $\delta^{18}O$ values) or

oxide (lower $\delta^{18}O$ values) are common in pyroxene. Olivine, by contrast, normally contains fewer inclusions than pyroxene, and any inclusions are visible under the binocular microscope.

In order to accurately model mass and volatile fluxes at subduction zones, it is imperative to see through crustal "noise" and constrain the nature of primitive (or parental) magmas. Here, clinopyroxene intra-crystal $\delta^{18}O$ values obtained by Secondary Ionisation Mass Spectrometry (SIMS) are presented in order to distinguish crystal cores from rims and thus increase the likelihood of primitive, or parental, $\delta^{18}O$ value locked in early-formed crystal cores. This is the first SIMS oxygen isotope study of mafic minerals for the Andean subduction zone which offers a statistically robust value for the oxygen isotope composition of mafic magmas of the Altiplano-Puna Volcanic Complex. Additionally, in order to gain insight into the crystallization and storage history of magmas carrying parental $\delta^{18}O$ components, clinopyroxene-melt thermobarometry is carried out on crystals from the samples that were used for $\delta^{18}O$ analysis by SIMS. Selected samples were sourced from La Poruña and Palpana, which were active at different times at the margins of the APMB melt anomaly in the Altiplano-Puna Volcanic Complex (Fig. 4.1). Further details of geological settings for the selected volcanoes are given in Section 4.1.2.

4.2.2 Methods

4.2.2.1 Sample selection and preparation

Pristine pyroxene crystals were hand-picked under a binocular microscope from the least silicic material identified at La Poruña (POR-06, Mount 1651) and Palpana (PAL-02, Mount 1652) volcanoes for micro-beam analysis, including Electron Probe Micro Analysis (EPMA) and Secondary Ionisation Mass Spectrometry analysis (SIMS), as described below. Crystals for micro-analysis were mounted in low-volatile epoxy and placed adjacent to the reference material (NRM-AG-1, see below) and at least 5 mm from the edge of the mount to avoid analytical artefacts related to sample geometry

and topography (Whitehouse and Nemchin, 2009). The sample mount was polished flat, carbon coated prior to EPMA analysis, and then cleaned and gold coated before SIMS analysis. Prior to EPMA and SIMS analysis, Back Scattered Electron (BSE) maps were constructed of each sample mount to permit accurate recording of core versus rim analyses and to facilitate positioning of the SIMS spots away from fractures or impurities. Several thin sections of the studied lavas were also prepared in order to obtain a sufficiently large amount of pyroxene compositional data to ensure statistically robust thermobarometric models.

4.2.2.2 Kernel density estimates (KDE)

Kernel density estimates (KDE) were used to evaluate the distribution of $\delta^{18}O$ values in La Poruña and Palpana. The kernel density (smoothed density estimate) plots were generated using the R programming language for statistical computing. The function geom.density{ggplot2} was utilised in this study. This function computes and draws a kernel density estimate, which is a smoothed version of the histogram. Its default method does so with the given kernel and bandwidth for univariate observations. For further information see https://www.r-project.org/.

4.2.2.3 Electron Probe Micro Analysis

Mineral compositions and backscattered electron (BSE) images of pyroxene were acquired using a JEOL JXA-8530F Hyperprobe Field Emission Gun Electron Probe Microanalyser (FEG-EPMA) at the Department of Earth Sciences, Uppsala University (UU), Sweden on polished thin sections and epoxy mounts. The run conditions were 15 kV accelerating voltage and 10 nA beam current with 10 s on peak and 5 s on lower and upper background, and a beam diameter of 2 μm for pyroxene analysis. Mineral standards employed for calibration include wollastonite for Ca and Si, pyrophanite ($MnTiO_3$) for Mn and Ti, magnesium oxide for Mg, orthoclase for K, albite for Na, aluminium oxide for Al,

fayalite for Fe, nickel oxide for Ni, and chromium oxide for Cr. Analytical precision was measured on Smithsonian Institute mineral standards. The 2σ S.D. analytical uncertainty on the standards as reported in Geiger et al. (2018) are as follows: for SiO_2, Al_2O_3, MgO and CaO ranged from ≤ 1.5%RSD, ≤ 2.2%RSD for FeO, ≤ 4.5%RSD for Na_2O, and ≤ 10%RSD for minor elements. Full mineral compositional data are presented in Supplementary material 7.

4.2.2.4 Secondary Ionisation Mass Spectrometry (SIMS) analysis

SIMS analyses were conducted at the Nordsim ion microprobe facility (NRM), Swedish Museum of Natural History in Stockholm, Sweden using a CAMECA IMS 1280 multi-collector equipped instrument. The SIMS instrumentation and methods employed here are described by Nemchin et al. (2006) and Whitehouse and Nemchin (2009), incorporating within-run beam centering in the field aperture using the transfer deflectors. A 20 keV Cs+ primary beam of ca. 2.5 nA was used in critically-focused mode together with a 5 μm raster to sputter a ca. 10 μm sample area. A normal incidence low energy electron gun provided charge compensation. The runs comprised a 90 s pre-sputter period with a raster of 20 μm, and field aperture centring using ^{16}O signal followed by 64 s (16 cycles of 4 s integrations) of data acquisition using two Faraday detectors in the multicollector system that operated at a common mass resolution of ca. 2500. The secondary magnet field was regulated at high precision using a Metrolab NMR teslameter. The data were collected over two separate analytical sessions (reference numbers 1651, POR-06 and 1652, PAL-02). Throughout the sessions, a sample-bracketing procedure was employed, where five sample analyses were bracketed before and after by two standard analyses. In sessions 1651 and 1652 an augitic standard (NRM-AG-1, Deegan et al., 2016) was employed to monitor instrumental mass fractionation (IMF) and to ensure data accuracy, and in session 1652 the widely employed JV-1 diopside standard was included as an added external check. Throughout the pyroxene analytical sessions, external reproducibility (2σ S.D. mean) ranged from 0.34 to 0.38‰. Internal precision or spot to spot reproducibility (2σ S.D.) ranged from ±0.34‰

to 0.40‰ (RSD; n = 92) and from ±0.38‰ to 0.46‰ (RSD; n = 72) on NRM-AG-1 for sessions 1651 and 1652, respectively. The average ^{16}O intensity for both pyroxene sessions was 2.8×10^9 cps. All pyroxene unknowns were compositionally close to NRM-AG-1 and thus no matrix effect was expected. The oxygen isotope results are reported in standard $\delta^{18}O$ values relative to the V-SMOW scale. All crystals were visually inspected after analysis to verify that analysis spots were not placed on fractures or foreign phases. Full clinopyroxene and standard SIMS $\delta^{18}O$ values are provided in the Supplementary material 8.

It is worth noting that olivine data from the same samples were collected over a third separate analytical session. However, the data obtained revealed large internal differences, differed from the olivine LF data obtained in this work and were significantly higher with respect to clinopyroxene SIMS data (Table 4.2). Olivine crystals were re-mounted and re-polished several times to counter the possible common relief/curvature issue due to large mineral grains (> 2 mm) but similar results were obtained. The exact reason for this inconsistency in the SIMS olivine data is unknown at present and these data are thus not presented further in this study. The focus in this study is therefore rather on the more consistent SIMS clinopyroxene data, that are assumed to be robust.

Table 4.2. Olivine and clinopyroxene oxygen isotope data from studied volcanoes in this work obtained by laser fluorination and SIMS. Further details of obtained data are given in Table 4.1 (LF) and Supplementary material 8 (SIMS).

Phase	Volcanoes (North to South)	Method	Number of analysis	$\delta^{18}O$ range	$\delta^{18}O$ average
Olivine	Chela, La Poruña, San Pedro	Laser fluorination	6	**5.7 - 6.2**	**6.0**
	Chela, La Poruña, San Pedro	SIMS*	45	**6.0 - 7.4**	**6.7**
Clinopyroxene	La Poruñita, Palpana, La Poruña, San Pedro, Paniri	Laser fluorination	12	**6.3 - 7.2**	**6.7**
	Palpana, La Poruña	SIMS	357	**4.5 - 6.9**	**5.7**

The oxygen isotope data are reported in ‰ relative to the V-SMOW scale. Typical internal two-sigma analytical errors for individual analyses were 0.15‰ for Laser Fluorination and 0.34‰ to 0.40‰ for SIMS. See sections 4.1.3 and 4.2.2 for analytical details. *Not presented in detail in this study (see text).

4.2.2.5 Clinopyroxene-melt thermobarometry

To estimate the P-T conditions and depth of clinopyroxene core crystallization (n = 269 for La Poruña; n = 246 for Palpana), the clinopyroxene-melt thermobarometric model after Putirka (2008, Eq. 30 and 33) was used that has been shown to robustly recover crystallization pressure and temperature estimates for subduction-related volcanic systems (e.g. Deegan et al., 2016; Geiger et al., 2016, 2018). A recent re-calibration of this model by Putirka (2008) was used in this study, as Eq. 30 and 33 now incorporate water (H_2O) as input parameter to be applicable to hydrous systems. This model is based on the jadeite-diopside/hedenbergite exchange between coexisting clinopyroxene-melt pairs and has a standard error of estimate (SEE) of ±33 °C and ±170 MPa for predicted temperature and pressure, respectively. Equilibrium tests were applied on EPMA data and included in Fig. 4.6 before thermobarometric calculations were carried out. The K_D(Fe-Mg) equilibrium test (after Putirka, 2008) on clinopyroxene coupled with possible melt compositions was used (Fig. 4.6, whole-rock data obtained from Supplementary material 1, Table S1). Based on this equilibrium test, only lavas from

the neighbouring, larger San Pedro stratovolcano were found as best nominal melts for La Poruña clinopyroxenes, with most of the matched data points falling within the accepted equilibrium envelope (Fig. 4.6a). In contrast, three nominal melts were tested in combination with clinopyroxene from Palpana where PAL-01 from Palpana best fits as nominal melt (Fig 4.6b). For a second equilibrium test, predicted versus observed clinopyroxene components were compared (diopside-hedenbergite, DiHd). A close match (within ± 0.10) of the predicted versus observed clinopyroxene components is needed to validate equilibrium conditions (Fig. 4.6). Only data satisfying these conditions were employed in the subsequent thermobarometric calculations.

4.2.3 Results

4.2.3.1 Mineral chemistry

The compositions of clinopyroxene phenocrysts were determined from the two selected lava samples (POR-06, and PAL-02). Clinopyroxene is the most common pyroxene phase in the selected POR-06 sample from La Poruña and occurs as individual euhedral to subhedral crystals (up to 2 mm in size; 10 vol.%) or as reaction rims on orthopyroxene phenocrysts. Besides occurring individually, clinopyroxene crystals occur as glomerocrysts with plagioclase, olivine and orthopyroxene. Augite, with a range of $Wo_{5-46}En_{39-67}Fs_{9-32}$, is the most common composition. Clinopyroxene phenocrysts have Mg# (where Mg# is defined as 100Mg / [Mg + Fe^{2+}]) between 65 to 84 (average = 76; n = 269). Andesite PAL-02 from Palpana, on the other hand, only contains clinopyroxene as ferromagnesian phenocrysts. Clinopyroxene (up to 2.5 mm; 15 vol.%) occurs as subhedral to euhedral tabular crystals and with a composition of $Wo_{6-45}En_{39-67}Fs_{11-29}$, classifying them mostly as augite. Clinopyroxene Mg# ranges from 65 to 81 (average = 74; n = 246). Further petrographic details and mineral photomicrographs can be found in Section 4.1.4.1 and Fig. 4.2, respectively. Chemical classification plots are given in Fig. 4.7.

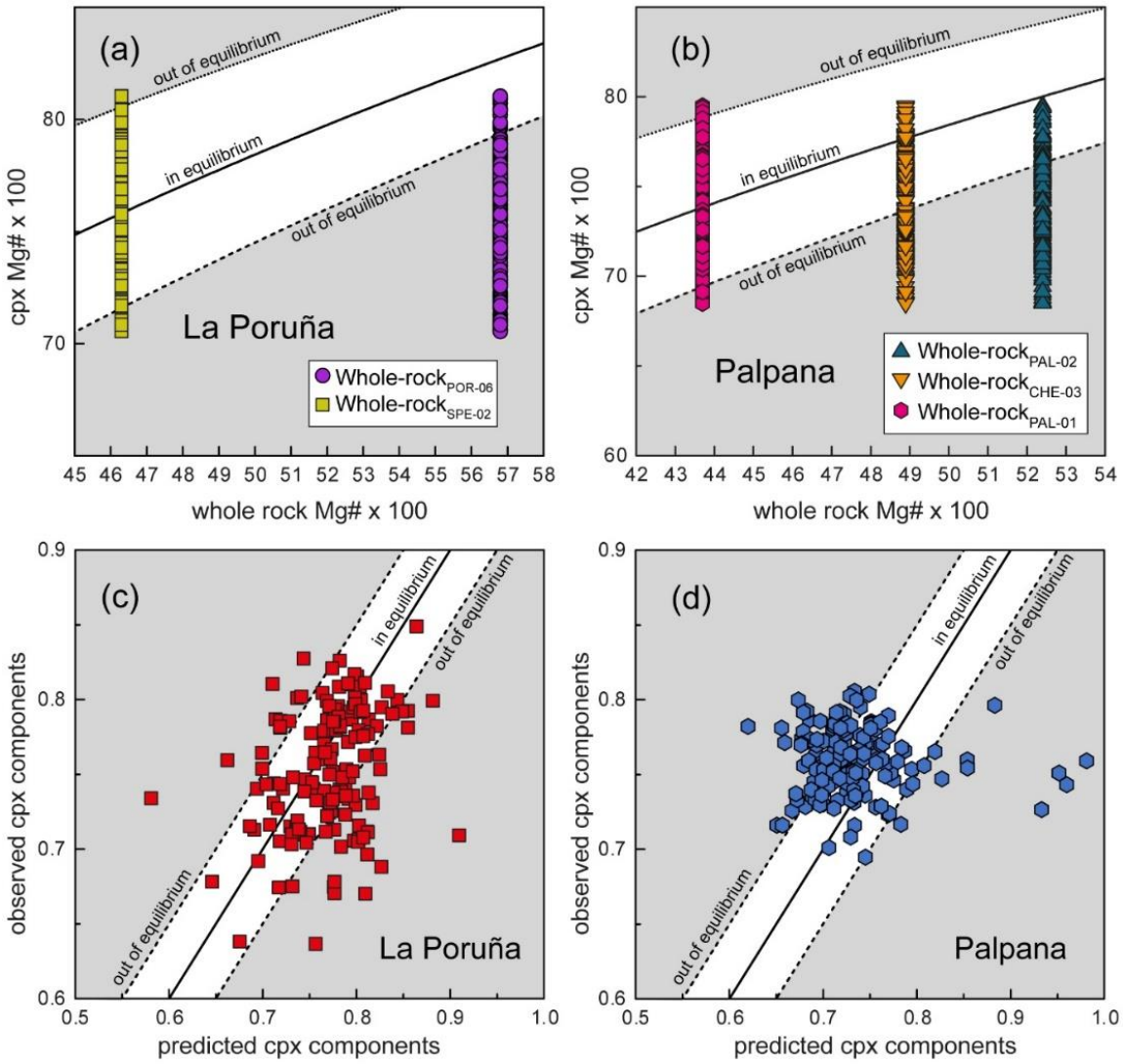

Fig. 4.6. The K_D(Fe-Mg) equilibrium test after Putirka (2008) (Eq. 30 & 33) applied to clinopyroxene from La Poruña (a) and Palpana (b) volcanoes coupled with possible nominal melts. The predicted vs. observed (diopside/hedenbergite) clinopyroxene component equilibrium test utilizing whole-rock$_{SPE-02}$ (c) and whole-rock$_{PAL-01}$ (d) from Supplementary material 1 (Table S1) as possible nominal melts for La Poruña and Palpana, respectively.

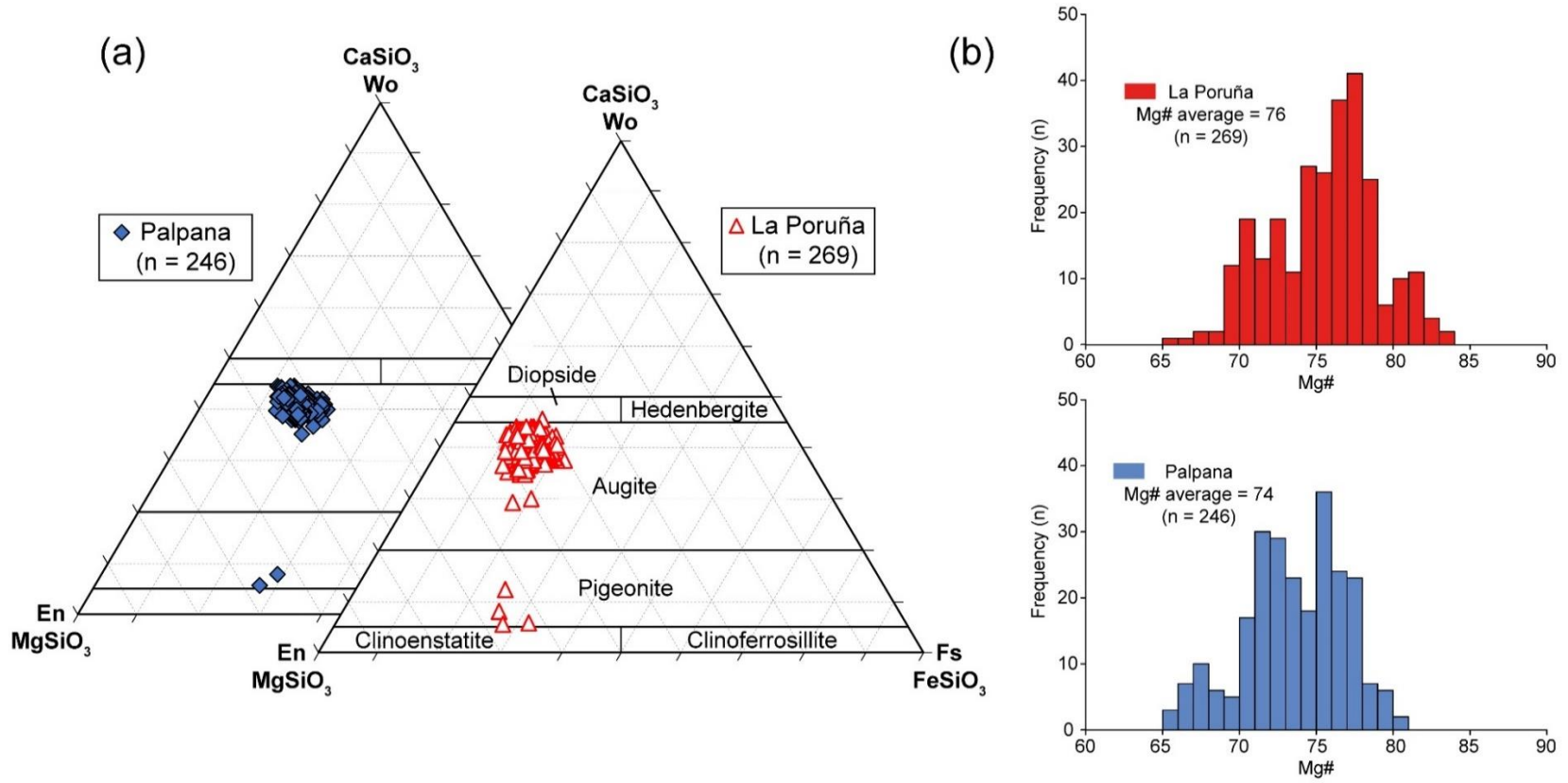

Fig. 4.7. (a) Composition of clinopyroxene (after Morimoto, 1988) from the La Poruña and Palpana volcanoes, which classify for the most part as augite. (b) Frequency distribution plots showing similar ranges and averages in Mg-number (Mg# as 100Mg / [Mg + Fe^{2+}]) for La Poruña and Palpana clinopyroxenes.

4.2.3.2 Oxygen isotope SIMS data

SIMS analysis of clinopyroxene from La Poruña (POR-06, n = 47 crystals, total of 198 individual spot analyses) and Palpana (PAL-02, n = 41 crystals, total of 159 individual spot analyses) yielded average $\delta^{18}O$ values of 5.8‰ ± 0.4 (2σ S.D.) and 5.5‰ ± 0.4 (2σ S.D.), respectively (Fig. 4.8). The frequency peaks of $\delta^{18}O$ values obtained by SIMS for each volcano overlap with the frequency peak of the literature data for Andean pyroxene, however SIMS $\delta^{18}O$ values are up to 1.8‰ lower than the LF data obtained in Section 4.1 (Table 4.2; Fig. 4.8).

A key benefit of the intra-crystal analytical approach is the ability to test for systematic differences between crystal cores and rims by visually inspecting the location of all SIMS points and flagging the data as "core" or "rim". Isotopic heterogeneity was observed within individual crystals, and some crystals show increasing (or decreasing) $\delta^{18}O$ values from their cores to rims (significant within 1σ uncertainty of the SIMS data) (Figs. 4.8, 4.9 and 4.10). Furthermore, kernel density estimation (KDE) analysis of the SIMS data reveals that crystal cores have a density peak at 5.6‰ for both La Poruña and Palpana samples (Fig. 4.11). On the other hand, crystal rims show a high degree of isotopic variability with rims offset compared to cores to relatively higher values for La Poruña and to relatively lower values for Palpana, with density peaks at 6.0‰ and 5.4‰ respectively (Fig. 4.11).

4.2.3.3 Thermobarometry

In order to determine the pressure and temperature of crystallization for these pyroxene-rich samples (La Poruña and Palpana) clinopyroxene-melt thermobarometric modelling after Putirka (2008) was performed (see Section 4.2.2.4), employing mineral data obtained by EPMA. These calculations require rigorous equilibrium testing before application, the results of which are presented in Fig. 4.6. In summary, most of the clinopyroxene from La Poruña and Palpana are in chemical equilibrium with nominal melts with Mg-numbers of 46 and 43, respectively. The equilibrium crystals from La Poruña

and Palpana range in their Mg-numbers from 71 to 81 (n = 229) and from 68 to 79 (n = 222), respectively. For La Poruña, the nominal melt composition in equilibrium with clinopyroxene (n = 125) yields a temperature range from 977 ºC to 1053 ºC and pressure from 15 MPa to 645 MPa (Fig. 4.12), corresponding to crystallization depths of about 1 to 24 km with peaks between 13 to 18 km. Applying the same formulation to the clinopyroxene-nominal melt pairs (n = 107) from Palpana yielded similar temperatures of 1003 ºC to 1067 ºC and pressures of 14 MPa to 717 MPa (1 to 26 km depth with peaks between 13 to 19 km; Fig. 4.12). Depths were calculated assuming an average crustal density of 2740 kg/m^3 (Schaller et al., 2015).

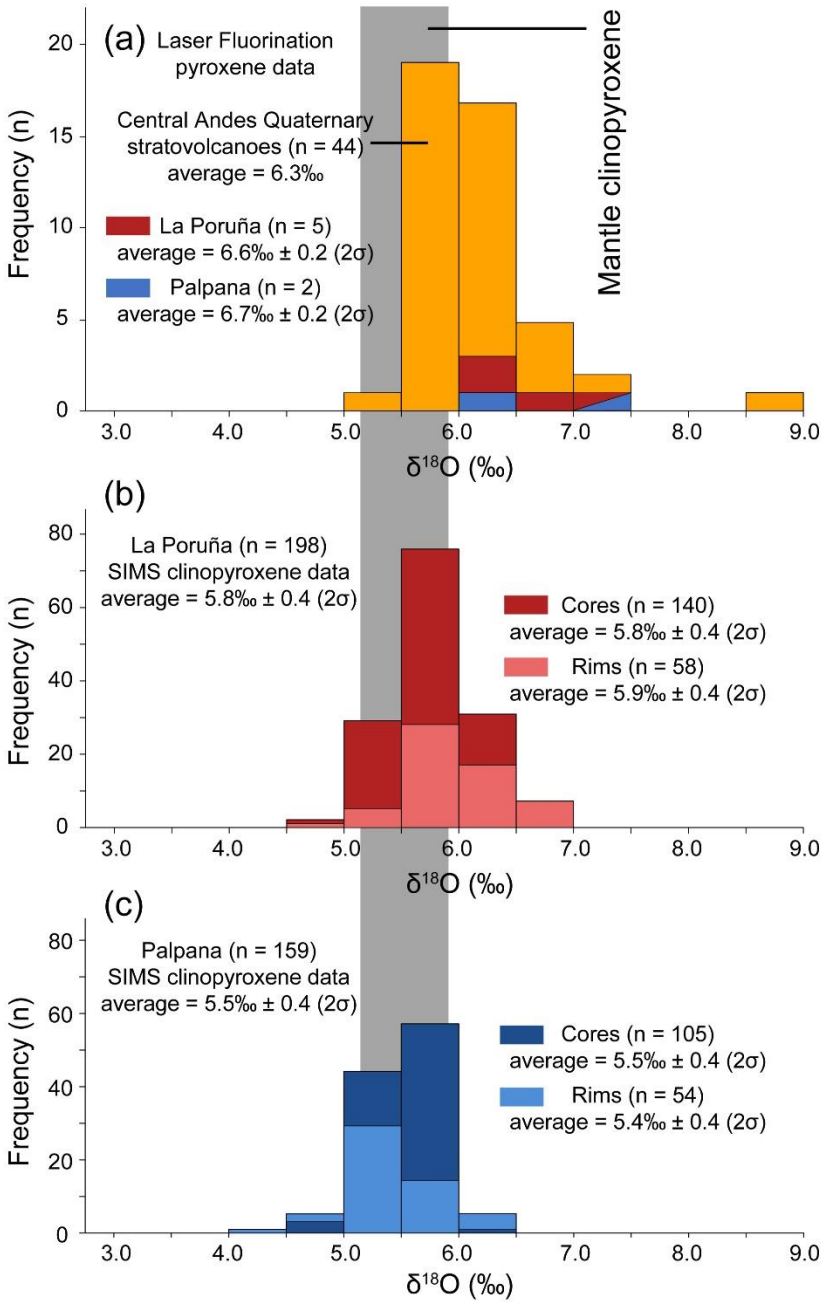

Fig. 4.8. Oxygen isotope data for La Poruña and Palpana. (a) Frequency distribution of $\delta^{18}O$ values of pyroxene from La Poruña and Palpana volcanoes obtained by laser fluorination in comparison to published data from the Central Andes (Supplementary material 5), including new LF data obtained in this work (Table 4.1). (b, c) Frequency distribution of $\delta^{18}O$ values obtained by SIMS for La Poruña (b) and Palpana (c) clinopyroxene. Note that the new SIMS data are lower than the LF data obtained in this work. Mantle clinopyroxene composition is shown for comparison (after Mattey et al., 1994).

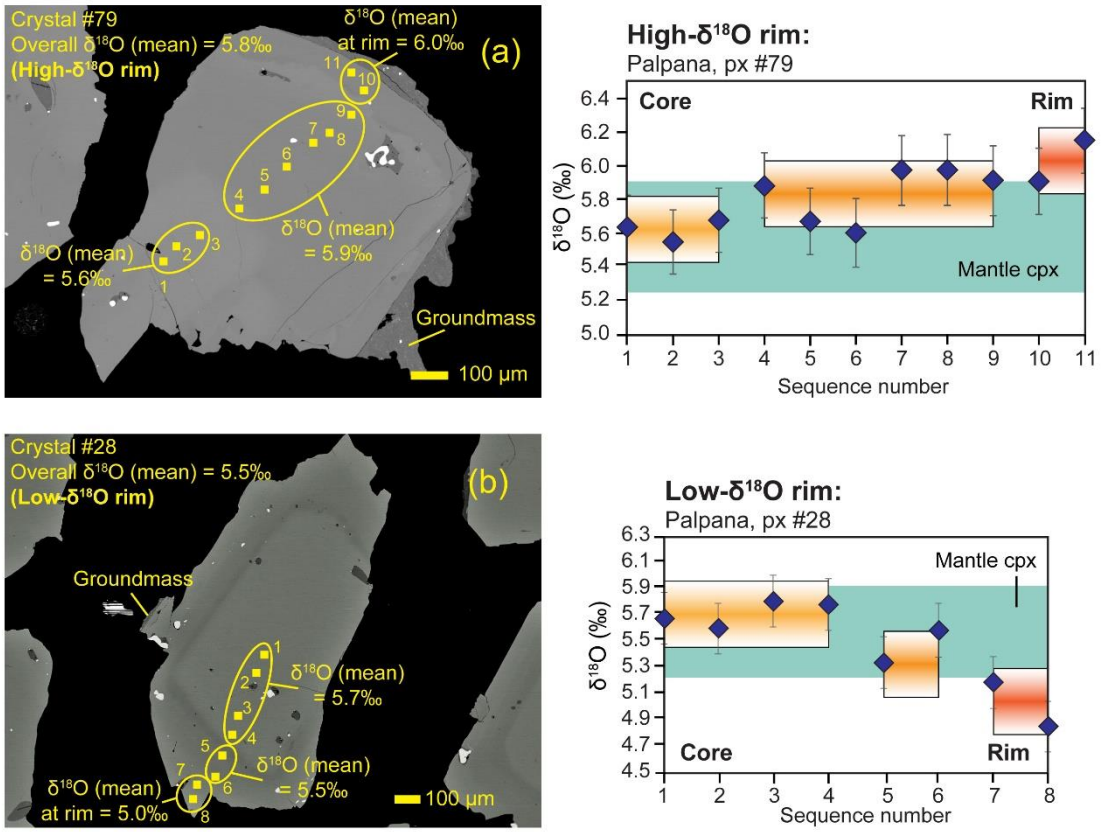

Fig. 4.9. Crystal O-isotope zoning. Oxygen isotope heterogeneity is recorded in representative augite from Palpana. Individual SIMS analysis spots are shown on the crystal SEM images to the left, whereas $\delta^{18}O$ variations are illustrated to the right. Both (a) increasing and (b) decreasing $\delta^{18}O$ values have been observed from crystal cores to rims. Relatively high or low $\delta^{18}O$ rims reflect various differentiation processes (e.g. crustal inputs) during crystal growth. The average $\delta^{18}O$ values of crystal zones are shown as orange to red bars (height of bars represents $\pm 1\sigma$ uncertainty). The range of $\delta^{18}O$ values of mantle clinopyroxene is shown for comparison (after Mattey et al., 1994). Further examples of crystal isotope zoning in Fig. 4.10**.**

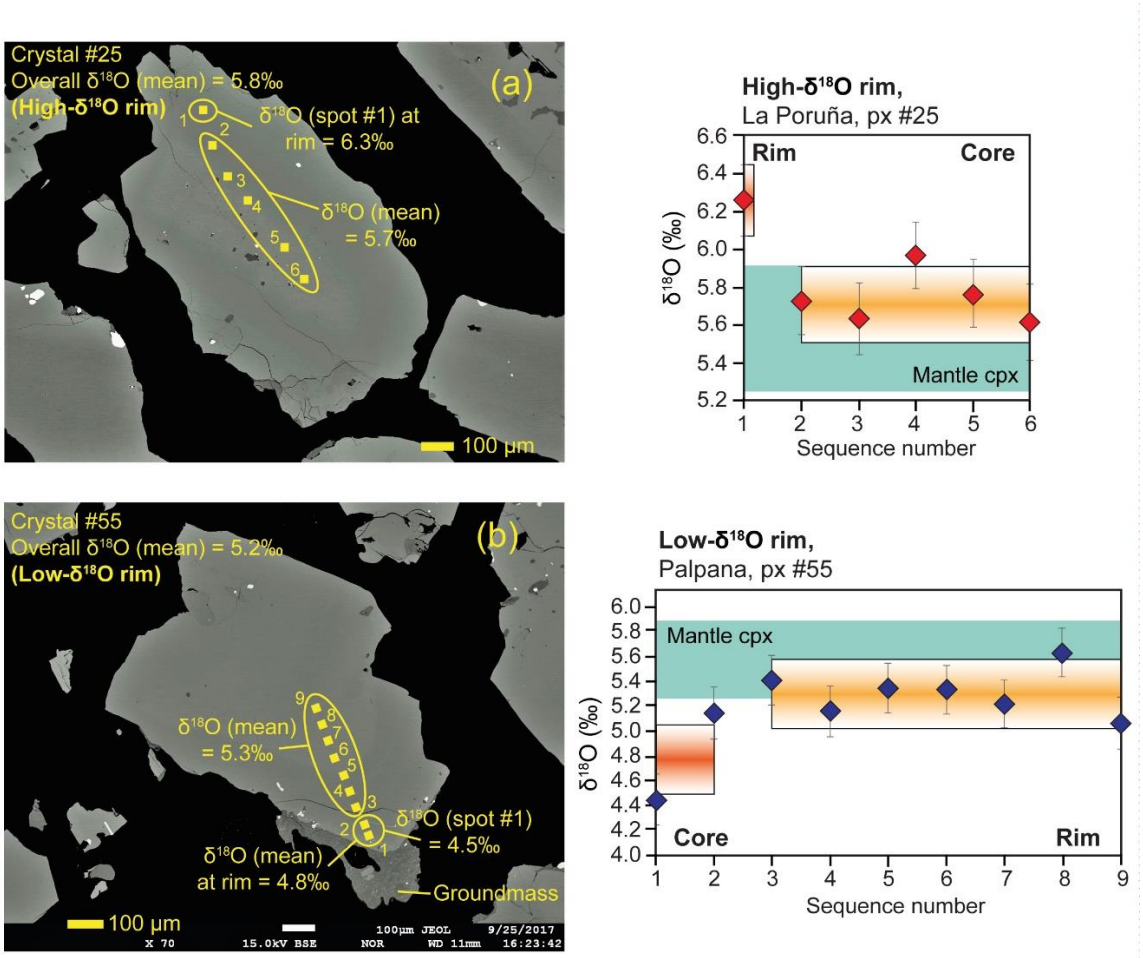

Fig. 4.10. Additional examples of $\delta^{18}O$ isotope heterogeneity observed in selected augite crystals from La Poruña (a) and Palpana (b). Residual groundmass adhered to the crystal confirms that the "true rim" has been analysed as opposed to the edge of the grain (b). Individual SIMS analysis spots are shown in the crystal sketches to the left, whereas $\delta^{18}O$ variations are illustrated to the right. Increasing and decreasing $\delta^{18}O$ values have been observed from cores to rims. The range of $\delta^{18}O$ values of crystal zones are shown in light and mid- orange bars. Red and blue bars are used to highlight the overall average $\delta^{18}O$ value for clinopyroxene from La Poruña and Palpana, respectively. The range of $\delta^{18}O$ values of mantle clinopyroxene is shown for comparison (after Mattey et al., 1994).

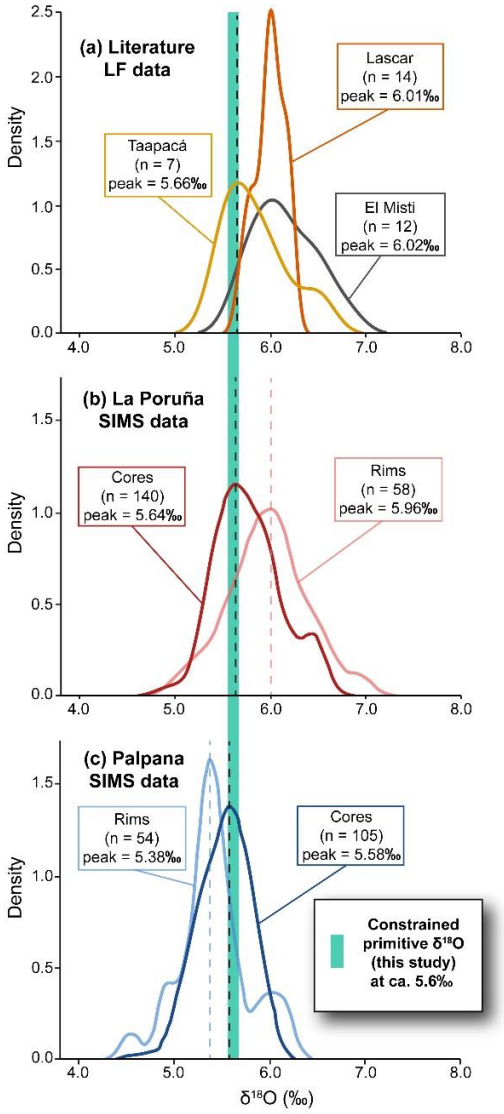

Fig. 4.11. Constraining the primitive $\delta^{18}O$ mantle value for the Central Andes. KDE plots of (a) literature data for pyroxene obtained by LF (Supplementary material 5) and SIMS clinopyroxene data from (b) La Poruña and (c) Palpana. Crystal cores from La Poruña and Palpana volcanoes both show $\delta^{18}O$ frequency peaks at 5.6‰, whereas crystal rims tend to have either relatively high (6.0‰, La Poruña) or low (5.4‰, Palpana) values. Literature data for Taapacá agree with the crystal core data obtained by SIMS, whereas data for Lascar and El Misti overlap with the high $\delta^{18}O$ rims presented here. La Poruña and Palpana crystal cores thus likely preserve the $\delta^{18}O$ value of the primitive, mantle-derived magma, which would have had a melt value of 6.3‰ ± 0.4 (2σ S.D.), based on an equilibrium clinopyroxene-melt fractionation factor of 0.7‰ (Bindeman et al., 2004).

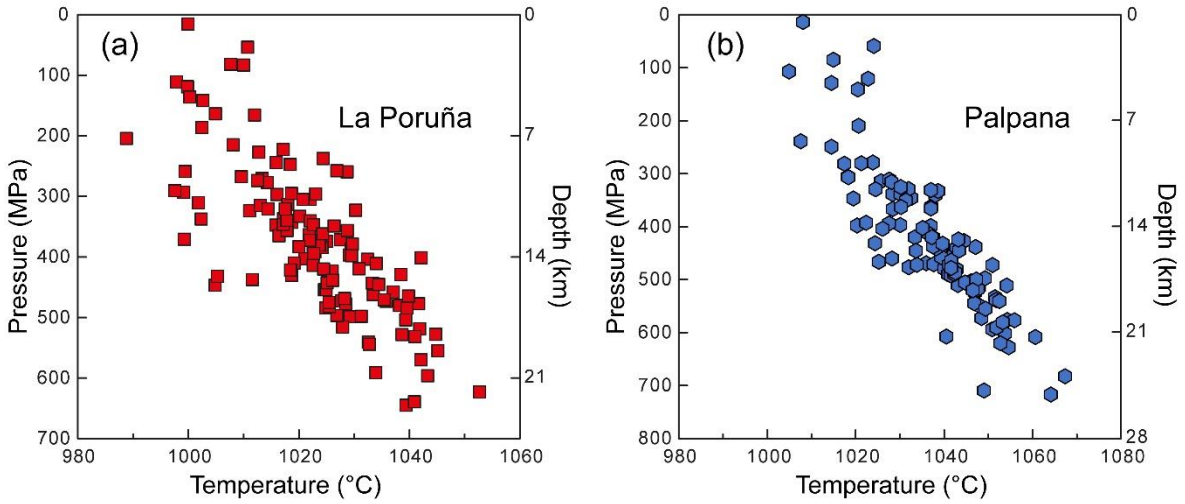

Fig. 4.12. Results from clinopyroxene-melt thermobarometry and clinopyroxene composition barometry (after Putirka, 2008) for selected nominal melts for La Poruña (a) and Palpana (b).

4.2.4 Discussion

New clinopyroxene SIMS $\delta^{18}O$ values are generally lower than those obtained by LF in Section 4.1 (Table 4.1) and are similar to primitive mantle clinopyroxene ($\delta^{18}O$ = 5.3% to 5.9‰ for mantle xenoliths, Mattey et al., 1994; Fig. 4.8), which are best preserved in the crystal cores of La Poruña and Palpana samples. Subtle zonation and heterogeneity in clinopyroxene $\delta^{18}O$ values were observed, for example recorded as a decrease or increase in $\delta^{18}O$ values from the core to the rims of individual phenocrysts (up to ± 1.1‰; Figs. 4.9 and 4.10). Furthermore, a KDE analysis reveals that La Poruña and Palpana rims have a $\delta^{18}O$ frequency peak of 6.0‰ and 5.9‰ compared to 5.6‰ ± 0.4 (2σ S.D.) for their cores, respectively (Fig. 4.11). These subtle zonal variations may record oxygen exchange with continental crust (cf. Damm et al., 1990) or hydrothermally altered components (Feeley and Sharp, 1995) during storage and crystal growth. Crystal cores, on the other hand, show a consistent $\delta^{18}O$ frequency peak at 5.6‰ for both sample populations (Fig. 4.11). Clinopyroxene core SIMS data thus appear to retain a consistent record of parental oxygen isotope compositions, whereas rim data presented here cannot be used to reconstruct parental magma signatures for the Altiplano-Puna

Volcanic Complex. Utilizing a clinopyroxene-melt fractionation factor of 0.7‰ (Bindeman et al., 2004), the $\delta^{18}O$ value of the melt in equilibrium with the crystal cores (5.6‰ ± 0.4) is 6.3‰ ± 0.4 (2σ S.D.). This value obtained from core data overlaps within error with the accepted value for mid-ocean ridge basalts (MORB) (5.7‰ ± 0.3; Ito et al., 1987), but is lower than the estimated parental $\delta^{18}O$ value of ca. 7.0‰ ± 0.2 (2σ S.D.) obtained in this study using LF data (cf. Table 4.1, discussed thoroughly in Section 4.3).

The oxygen isotope SIMS data obtained on clinopyroxene cores appear to retain mantle-like parental melt values formed at deep crustal levels, possibly near the mantle-lower crust MASH boundary (Fig. 4.13). The results of the thermobarometry modelling revealed almost identical crystallization pressure and temperature conditions for La Poruña and Palpana, independent of their distinct eruption sites and ages. Clinopyroxene crystal cores were found to have formed at temperatures of up to 1067 °C, and pressures up to 717 MPa (ca. 26 km depth) and record a major level of crystallization at ~ 13 to 19 km depth (Figs. 4.13), which corresponds to felsic metamorphic and plutonic basement levels (Damm et al., 1990). As La Poruña and Palpana volcanoes are on the periphery of the largest lateral extension of the APMB (Fig. 4.1), where the lowest portions of partial melting residing beneath the region are expected (Ward et al., 2014), the studied mafic lavas may be affected by small degrees of contamination from the felsic APMB body (Chapter 2). Based on clinopyroxene SIMS $\delta^{18}O$ data, clinopyroxene-melt thermobarometric modelling, O-isotope modelling in Section 4.1 and the model presented in Fig. 2.13 in Chapter 2, parental magmas are, therefore, entrained into a storage zone at ca. 13-19 km depth by-passing the deep underplating zone beneath the APMB, thus avoiding intense contamination with molten felsic material (Fig. 4.13). Following formation of clinopyroxene cores at ca. 13 to 19 km depth, clinopyroxene rims crystallized from melts with non-parental $\delta^{18}O$ values due to potential interaction with high-$\delta^{18}O$ felsic continental crust (e.g. Damm et al., 1990) and/or ^{18}O-depleted hydrothermally altered materials (e.g. Feeley and Sharp, 1995) (Fig. 4.13). The results from clinopyroxene-melt thermobarometry thus indicate the relative location where late differentiation

processes of the parental magma took place after crystallization of clinopyroxene cores (mostly between 13 to 19 km depth). This in turn agrees with previous petrological constraints for the studied area, as shallow crustal contamination has been inferred based on whole-rock geochemistry (e.g. Burns et al., 2015; Godoy et al., 2014; Taussi et al., 2019; Chapter 2 and 3).

To emphasize, new SIMS data for clinopyroxene cores from La Poruña and Palpana reveal a parental $\delta^{18}O$ value of 6.3‰ ± 0.4 (2σ S.D.), which is lower than the parental melt of 7.0‰ ± 0.2 (2σ S.D.) previously estimated through LF data (Section 4.1). Intra-crystal scale oxygen isotope measurements by SIMS in mafic minerals (e.g. clinopyroxene) allow the estimation of $\delta^{18}O$ parental values with greater confidence than previously possible as $\delta^{18}O$ values were obtained from uncompromised crystal areas, i.e. avoiding mineral or melt inclusions, fractures, groundmass, etc. However, a similar approach employing the SIMS method might be used to analyse the $\delta^{18}O$ values of more primitive phases (i.e. olivine), and more Central Andean volcanoes, in order to (i) fully contrast the internally consistent LF data presented in this study (Table 4.1), and (ii) ultimately to establish a statistically robust and consistent "undisturbed" sub-arc parental $\delta^{18}O$ value.

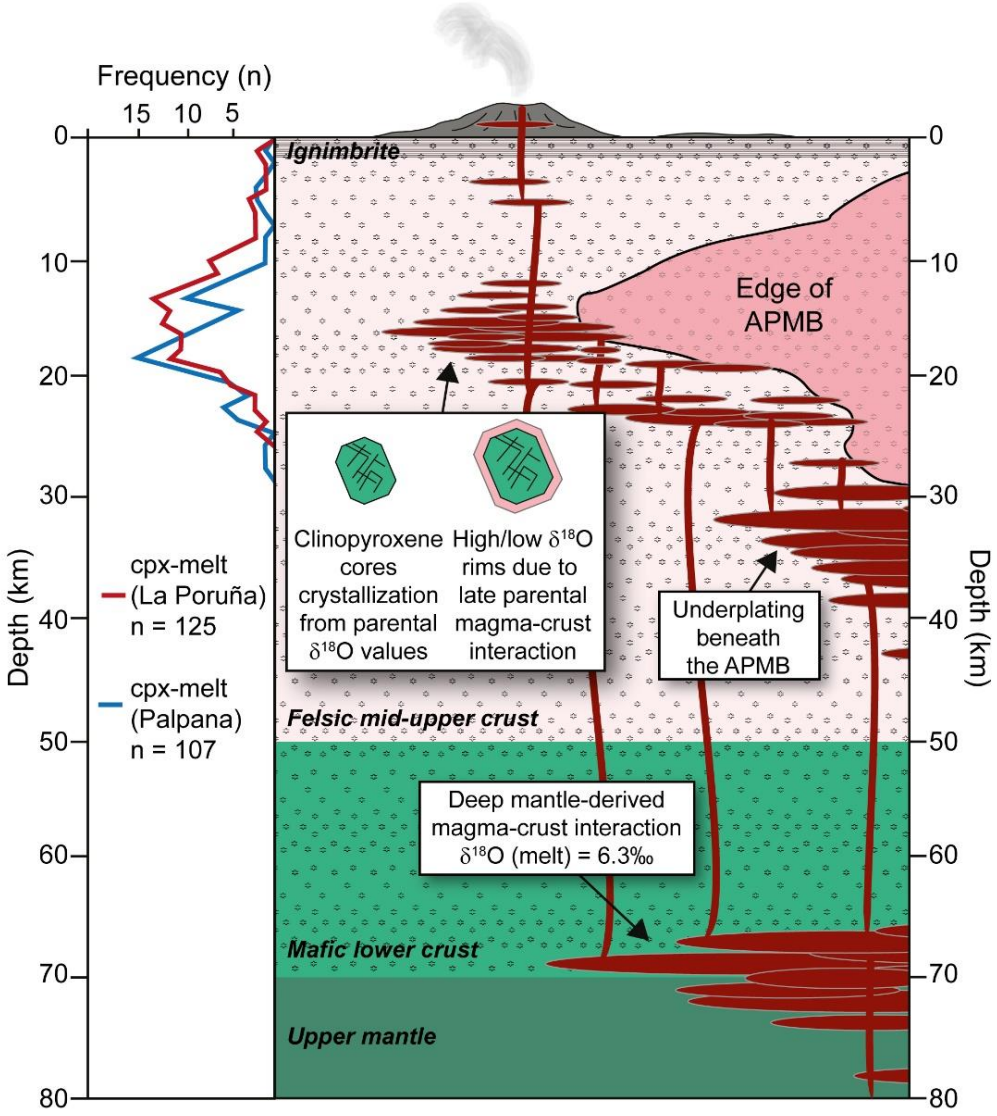

Fig. 4.13. Model. Schematic magma plumbing model for the low-silica eruptions focused at the margin of the APMB. Thermobarometry results (left) show that clinopyroxene cores from La Poruña and Palpana volcanoes crystallized at 13 to 19 km depth. The $\delta^{18}O$ values of clinopyroxene cores reflect crystallization from an equilibrium mantle-like parental melt of 6.3‰. Clinopyroxene rim SIMS data show both relatively high- and low-$\delta^{18}O$ values compared to cores and are postulated to record late-stage pyroxene crystallization from a melt with various crustal inputs (Damm et al., 1990; Feeley and Sharp, 1995). The depth of the APMB is based on the joint ambient noise-receiver function inversion S-velocity model from Ward et al. (2014), and the thickness for Central Andean crust layers and ignimbrite deposits is from Prezzi et al. (2009) and Salisbury et al. (2011), respectively.

4.3 Summarizing discussions and conclusions

New olivine (5.7 to 6.2‰; n = 6; Table 4.1) and clinopyroxene (6.3 to 7.2‰; n = 12; Table 4.1) LF $\delta^{18}O$ values of six Central Andean volcanoes presented here have narrower ranges compared to existing olivine (5.0 to 8.3‰; n = 19; Table S5.2) and clinopyroxene (5.5 to 8.7‰; n = 39; Table S5.3) O-isotope data for the Central Andes. New LF data allow a robust estimate of the $\delta^{18}O$ values of sub-arc, parental melts of ca. 7.0‰ ± 0.2 (2σ S.D.). Parental melts feeding the APMB and associated volcanic centres are postulated to form near the lower crust-mantle boundary following assimilation of up to 21% high-$\delta^{18}O$ basement rocks by mantle-derived magmas.

By employing SIMS oxygen isotope analysis, it is possible to evaluate the magmatic history recorded within the crystals by avoiding e.g. inclusions, fractures and groundmass. Clinopyroxene rim data obtained by SIMS display both lower and higher $\delta^{18}O$ values with respect to clinopyroxene cores. The intra-crystal variation, up to ± 1.1‰, toward the rims record direct oxygen exchange between parental melts and a e.g. more evolved crustal component or hydrothermally altered arc crust during storage and crystal growth. Clinopyroxene cores show consistent frequency peaks at 5.6‰ for La Poruña and Palpana, which suggest mantle-like parental melt compositions of 6.3‰ ± 0.4 (2σ S.D.) in the studied volcanoes. This $\delta^{18}O$ value is lower than the parental value of 7.0‰ ± 0.2 (2σ S.D.) robustly estimated from new olivine and clinopyroxene LF data. Analysis by LF would incorporate all parts of the crystal, including not only any unavoidable inclusions present in the analysed crystals, as suggested in Section 4.1, but also altered or crustally contaminated crystal rims (cf. Deegan et al., 2016). However, the range of variability of the clinopyroxene LF data would be similar than the SIMS data (Table 4.2) since clinopyroxene rims reveal both high- and low-$\delta^{18}O$ values compared to cores. Furthermore, the frequency distribution plots in Fig. 4.8 reveal that core and rim SIMS data are biased to lower $\delta^{18}O$ values relative to the single crystal LF data, whose mantle-like $\delta^{18}O$ values are not entirely consistent with the whole-rock geochemistry obtained in this study, e.g. SiO_2 > 53 wt%; $^{87}Sr/^{86}Sr$ > 0.7055; $^{143}Nd/^{144}Nd$ < 0.5125 (See Chapter 2 and 3). Clinopyroxene, and olivine (Table

4.2), SIMS data obtained in this study, therefore, cannot be reconciled to the LF data where olivine and clinopyroxene $\delta^{18}O$ values are internally consistent, but the exact reason for this is still unknown and is work in development. SIMS data, however, accurately reflect stages of differentiation and magmatic evolution that postdates crystal core formation.

Direct comparison of clinopyroxene mineral data from La Poruña and Palpana does not reveal significant temporal or compositional differences. Clinopyroxene-melt thermobarometry yielded crystallization depths with peaks between 13 to 19 km, within older felsic crustal lithologies levels. This allows a proposed magmatic evolution where clinopyroxene fractionated from parental melts of 7.0‰ ± 0.2 (2σ S.D.) that ascended to the storage level in the upper crust after avoiding significant magmatic differentiation with APMB derived melts.

Overall, the magmatic evolution model, based on the variability in oxygen isotope ratios, is further consistent with the combined major and trace element, and Sr and Nd radiogenic isotope compositional variations previously observed for the least silicic magmas erupted in the Altiplano-Puna Volcanic Complex. Isotope measurements by LF or SIMS in mafic minerals, on the other hand, identify and quantify pre-eruption magma changes, and ultimately, a better constrained parental composition of the deepest mafic source of the Central Andean volcanism.

Chapter 5

Consolidated discussion

New findings in relation to the overarching thesis presented in the introductory chapter were largely discussed separately in Chapter 2, 3 and 4. Chapter 5 synthesizes the relationship of the three empirical research chapters of this study and reveals the contribution and importance of the entire research in a consolidated discussion.

5.1 Mafic magmatism in the eruptive cycle of the Altiplano-Puna Volcanic Complex

Large volumes (ca. 15,000 km^3) of dacitic to rhyolitic magmas were erupted from large caldera systems in increasing major pulses at ca. 10, 8, 6 and 4 Ma with a minor ignimbrite flare-up at ca. 1 Ma, which mainly formed the ignimbritic Altiplano-Puna plateau (de Silva and Gosnold, 2007; de Silva and Kay, 2018). The ignimbrite flare-up events in the Altiplano-Puna Volcanic Complex (APVC) are directly related to a high influx of mantle derived magmas that accumulated in the Altiplano Puna Magma Body (APMB) and generate high intermediate-felsic magma flux in the pre-eruptive levels at 3-8 km depth (de Silva and Godnold, 2007; Hildreth, 1981, Taussi et al., 2019). In between the flare-up events, periods of decreased ignimbritic activity have been recognized, commonly referred to as “steady-state” periods (de Silva and Godnold, 2007; Kern et al., 2016; Salisbury et al., 2011). When the APVC entered a steady-state stage, magma production rates decreased 3 to 4 times with respect to flare-up pulses, which is attributed to a decrease in mantle heat input and more restricted mafic recharge (Godoy et al, 2019; Taussi et al., 2019). The “steady-state” thus likely represent the end of the flare-up event. However, mantle-derived supply was still high enough to build the typical Andean andesitic-to-dacitic composite stratovolcanoes and other minor mafic volcanic features, such as scoria cones or maar deposits (Burns et al., 2015; de Silva et al., 2015). Godoy et al. (2019) related the mafic eruptions between 1 and 0.2 Ma to the latest steady-state stage recognized within the APVC, which is characterized by eruption of monogenetic centers at the

borders of the APMB (e.g. La Poruñita), and isolated mafic flows towards the centre of the giant felsic body (e.g. Apacheta, Cordón Inacaliri, Licancabur). Most recent mafic eruptives (< 0.2 Ma, e.g. La Poruña, San Pedro) are suggested to represent a new phase of mantle-derived magma recharge within the area. Similar, large mafic volcanic fields in the Argentinian Northern Puna are spatially associated with 8.5-3.5 Ma APVC ignimbrites (Maro and Caffe, 2006). Thus, mafic volcanic rocks, including those investigated in this work, may be related temporally to different steady-state stages of the APVC cyclic formation, and spatially to the major ignimbrite pulses that were manifested within the APVC between ca. 8 to 0.1 Ma (Salisbury et al., 2011). This implies that following stagnation at upper crustal storage levels (Fig. 4.13 in Chapter 4), the ascend of parental mafic magmas to the surface was possibly facilitated by structures that guided the ignimbrite volcanism manifested in the western reach of the APVC (Salisbury et al., 2011; Kern et al., 2016). This direct upwelling to the surface could have favoured only minor shallow crustal interaction with the parental magma, and therefore preserving less-evolved characteristics as demonstrated by the studied samples.

5.2 Magma compositional variations in space and time within the western boundary of the Altiplano-Puna Volcanic Complex

Petrography and whole-rock geochemistry were used as discriminants to assess spatiotemporal differences between mafic eruptions concentrated in the western border of the APVC (Chapter 2). Whole-rock geochemistry reflected varied differentiation processes, such as magma mixing, coupled assimilation and fractional crystallization, and with selective assimilation varying from volcano to volcano (Chapter 2 and 3). Individual volcanoes demonstrated that contamination of parental melts generated distinctive baseline Sr and Nd isotopic values as a function of their location relative to the projected APMB reservoir. For example, Chela volcano, located just outside the northwestern border of the APMB, has basaltic-andesite lava with the lowest $^{87}Sr/^{86}Sr$ (0.705541) and highest $^{143}Nd/^{144}Nd$ (0.512513) ratios recognized in this study (i.e. sample CHE-03; Table S2.2, Supplementary material 2). In contrast, more evolved baseline values tend to appear towards the centre of the APMB (e.g.

$^{87}Sr/^{86}Sr$ = 0.71129, $^{143}Nd/^{144}Nd$ = 0.512179, sample DM58A2 from Uturuncu volcano, Michelfelder et al., 2013; see also Fig. 2.12 in Chapter 2). Variable amounts of partial melting of the Central Andean continental basement and assimilation of crustal melts derived from the APMB are therefore required to modify parental basaltic-andesite magmas during their journey to the surface. In order to constrain the amount of assimilated crust of all studied samples, the AFC-based calculation model of Aitcheson and Forrest (1994) is employed here, which has been successfully applied in recent petrological studies within the Altiplano-Puna Volcanic Complex (e.g. Godoy et al., 2017; Taussi et al., 2019). In the present model, the local basaltic-andesite end-member is represented by the sample CHE-03 from Chela volcano for modelling (see above; Table 5.1a; See also Supplementary material 2). Paleozoic felsic gneisses of the basement exposed in the northern Chilean Precordillera at 21°04'S to 22°01'S were selected as crustal contaminants (SiO_2 = 54.0 to 69.3 wt%, MgO = 1.6 to 7.1 wt%, Sr = 114 to 1091 ppm, and $^{87}Sr/^{86}Sr$ = 0.7085 to 0.7278; Lucassen et al., 2001). Note that the sample with the highest Sr isotope ratio, and associated Sr concentration, is used as the contaminant for the AFC model (Table 5.1a). The mineral assemblage is estimated based on the petrographic analysis from this work (see Tables 2.2 and 3.2 in Chapter 2 and 3, respectively). The models were generated separately for the Pliocene and Quaternary mafic magmas as they show slightly different mineral proportions (Table 5.1b). An AFC-based calculation model was used to constrain the amount of assimilated crust of the studied rocks using Eq. (5) from the RAFT model by Aitcheson and Forrest (1994) (Table 5.2). This model is particularly useful when the concentration of an element from contaminated magmas cannot be estimated since it assumes R (material assimilated/material crystallized) and D (bulk partition coefficient) to be constant during the whole AFC process (cf. Aitcheson and Forrest, 1994; DePaolo, 1981; Table 5.1). The R estimated for this study is 0.5 by taking into consideration the best fitted model and previous studies in the area (e.g. Godoy et al., 2017; Taussi et al., 2019). Results of RAFT-modelling indicate the degree of crustal assimilation to be ca. 5% to 30% for Pliocene rocks (excluding CHE-03) and up to ca. 37% for Quaternary mafic rocks (Table 5.3). Overall, the samples with low amounts (average ≤ 25%) of crustal assimilation

were collected from volcanoes located outside or within the margin of the projected areal extent of the APMB, whereas volcanoes constructed directly above the APMB are offset towards higher amounts of assimilation (average > 25%) and potentially associated with the assimilation/mixing of melts derived from the APMB.

Table 5.1 AFC model parameters (*after* DePaolo, 1981) for erupted Pliocene and Quaternary magmas at 21°10'-22°25'S. Bulk D according mineral/melt partition coefficients for basaltic and basaltic-andesite liquids from Rollinson (1993).

	Initial magma composition	**Crustal contaminant**
Location	Chela	Basement gneiss
Reference	This work	Lucassen et al. (2001)
Sample	CHE-03	4/316
*Major elements (wt%)**		
SiO_2	55.50	67.01
Al_2O_3	18.20	15.52
FeO_t	7.31	8.26
MgO	3.92	2.20
CaO	7.47	1.83
Na_2O	4.04	2.53
K_2O	1.44	3.28
Trace elements (ppm)		
Sr	793	185
Nd	18	37
Radiogenic isotopes		
$^{87}Sr/^{86}Sr$	0.705541	0.727770
$^{143}Nd/^{144}Nd$	0.512513	0.512087
	Pliocene magma	**Quaternary magma**
Mineral assemblage		
Plagioclase (vol%)	70	60
Olivine (vol%)	5	10
Orthopyroxene (vol%)	10	15
Clinopyroxene (vol%)	15	15
Bulk partition coefficient		
D_{Sr}	1.29	1.11
D_{Nd}	0.09	0.10
Conditions		
r = Ma / Mc	0.5	0.5

$_t$ = total Fe as Fe^{2+}

*Recalculated to 100% anhydrous

Table 5.2 Calculated amounts of crustal assimilation for Pliocene and Quaternary mafic magmas using Eq. (5) (Aitcheson and Forrest, 1994). Estimated remaining melt fraction (F) from AFC modelling in this work (Table 5.1).

F (%)	Pliocene magma		Quaternary magma		Assimilated crust (vol%)
	Sr (ppm)	$^{87}Sr/^{86}Sr$	Sr (ppm)	$^{87}Sr/^{86}Sr$	
100	793	0.705541	793	0.705541	0
95	740	0.705815	754	0.705812	5
90	689	0.706120	716	0.706109	9
85	640	0.706462	678	0.706436	13
80	592	0.706847	640	0.706796	17
75	546	0.707282	603	0.707195	20
70	502	0.707776	567	0.707640	23
65	459	0.708339	531	0.708137	26
60	419	0.708984	496	0.708696	29
55	380	0.709728	461	0.709328	31
50	343	0.710589	427	0.710047	33

Table 5.3 Estimated amounts of crustal assimilation for Pliocene and Quaternary studied volcanoes at 21°10′S to 22°50′S based on calculations of Table 5.2.

Volcano	Number of samples	Assimilated crust range (vol%)			Average (vol%)
Pliocene					
Chela	5	0	-	15	9
Palpana	3	12	-	17	14
Cerro Carcote	4	7	-	21	15
Araral	3	10	-	27	21
Ascotán	3	27	-	30	28
Quaternary					
Cordón Inacaliri	1		27		27
Cerro La Quebrada	1		37		37
Licancabur	1		31		31
Juriques	2	27	-	29	28
Paniri	5	19	-	33	26
Apacheta	2	11	-	16	14
La Poruñita	2	23	-	24	24
La Poruña	23	0	-	28	21
San Pedro	18	17	-	27	22

As demonstrated by the findings based on Sr and Nd baseline isotopic values (Chapter 2), and estimated proportions of assimilated crust (Table 5.3), the less contaminated mafic products were erupted peripheral to the largest lateral extension of the APMB, where low portions of partial melts were calculated (Ward et al., 2014). At this border, the studied mafic magmas, including their early-formed phases (Chapter 4), are affected by minor degrees of contamination from the felsic body as they bypassed the partially molten zone before ponding at upper crustal levels. Olivine and/or pyroxene-rich basaltic-andesites to andesites are ubiquitous in scoria cones (e.g. La Poruña) and stratovolcanoes-related mafic lava flows (e.g. Chela, Palpana, San Pedro) built around the western border of the APMB at 21°10′-22°50′S. The construction of the La Poruña scoria cone (ca. 0.1 Ma; Wörner et al., 2000; Chapter 2) and the genetically-related less evolved lavas from San Pedro stratovolcano (ca. < 0.16 Ma; Bertin and Amigo, 2019; Delunel et al., 2016; Chapter 2) represent the youngest mafic activity within the study area. Such mafic magmas involved a late stage of mechanical assimilation after a mixture of crustal and mantle components, through AFC processes in the middle-upper crust. The Pliocene mafic lava flows from Palpana and Chela (ca. 3.8 Ma and 4.1 Ma, respectively; Wörner et al., 2000), on the other hand, correspond to the oldest studied mafic eruptives. Notably, there are no significant temporal differences related to whole-rock geochemistry, mineral composition and clinopyroxene crystallization amongst the volcanoes mentioned above (See Chapter 2, 3 and 4).

New oxygen isotope data for olivine and clinopyroxene indicate a common origin for the investigated lavas, independent of age (Chapter 4). Parental magmas are postulated to form in the felsic continental crust through significant assimilation (up to 28%) of high-$\delta^{18}O$ basement rocks ($\delta^{18}O$ = 11.8 to 19.5‰; Chapter 4) into stagnated mantle-derived magmas (see Figs. 4.5 and 4.13 in Chapter 4). As clinopyroxene appeared to crystallize from these parental melts, the clinopyroxene-melt thermobarometric modelling performed in this work likely constrains the location where late differentiation of the parental magmas took place for the studied volcanoes, i.e. at ~ 13 to 19 km

depth. This is consistent with differentiation trends in a garnet-free environment at upper crustal levels revealed by whole-rock trace element data of the studied rocks (Chapter 2 and 3), which in turn agree with previous petrological constraints within the APVC (e.g. Burns et al., 2015; Godoy et al., 2014; Taussi et al., 2019) and is consistent with recent reconstructions of magmatic differentiation regimes for different types of volcanoes in the Central Andes (e.g. Wörner et al., 2018).

5.3 Thermobarometric estimations for the western Altiplano-Puna Volcanic Complex

Recent thermometric and barometric calculations based on olivine, clinopyroxene and amphibole systematics estimated storage levels and crystallization conditions of parental magmas that ascended just outside the APMB limits (Burns et al., 2020) and through the APMB (Gorini et al., 2018) within the western border of the APVC.

Burns et al. (2020) calculated olivine crystallization temperatures and clinopyroxene P-T conditions in the southwesternmost border of the APMB (at 23°S). Olivine crystallization was related to Cr-spinel growth in the mantle-lower crust MASH boundary at ca. 60 km depth. Combined Sr and Nd radiogenic isotope data and new olivine $\delta^{18}O$ values from this work indicate olivine crystallization to be deeper than clinopyroxene, however there is no geochemical or petrographic evidence to argue for olivine crystallizing at deep MASH reservoir levels (Section 4.1 in Chapter 4). As the volcanoes investigated in this work show low LREE/HREE ratios (see Chapter 2 and 3), and a garnet-free environment is proposed to be present during magma differentiation (e.g. Fig. 2.9 in Chapter 2), the involvement of an eclogitic slab/crust can be rule out. The latter indicates that neither partial melting of the slab by subduction erosion (Stern, 1991), crustal foundering during delamination (Kay et al., 1994), nor differentiation within a garnet-bearing lower crustal MASH zone (Wörner et al., 2018) are related to the enrichment of the primitive magmas. By contrast, it was interpreted that olivine crystallization occurred within the middle continental crust (see Chapter 4). Following olivine crystallization, Burns et al. (2020) suggested an adiabatic ascent for the parental magma up to 20 km

depth based on thermobarometric clinopyroxene calculations (20 to 55 km depth). The shallowest clinopyroxene population appears to be the most similar with respect to clinopyroxene crystal chemistry and thermobarometry obtained in this work. However, when using the same thermobarometric approach from this study (i.e. Eq. 30 and 33, Putirka, 2008) and the clinopyroxene data set from Burns et al. (2020) coupled with their choice of associated melt (sample 44x from Hawkesworth et al., 1982), K_D(Fe-Mg) equilibrium conditions *after* Putirka (2008) are not met. In comparison, when using the sample PAL-01 from this study (Supplementary material 1 (Table S1)) as associated melt with clinopyroxene data reported in Burns et al. (2020), ~92% of all crystals fulfil equilibrium conditions. The predicted vs. observed clinopyroxene component equilibrium test (diopside/hedenbergite; DiHd) resulted in ~99% of all clinopyroxene data points being in equilibrium. Applying clinopyroxene-melt thermobarometry (Eq. 30, Putirka, 2008) to the remaining mineral-melt pairs results in pressures of 80 to 571 MPa, which translates to depth of 3 to 21 km with frequency peaks between 9 and 14 km. These depths, in turn, are in agreement with the results from the thermobarometric calculations made in this study (cf. 13 to 19 km depth; Fig. 4.14 in Chapter 4).

Gorini et al. (2018), on the other hand, estimated a main crystallization range between 4 and 8 km, with deeper amphibole that formed at up to 20 km depth. This deep amphibole population seems to have crystallized at similar levels to that suggested by pyroxene-melt calculations in this work. Amphibole is not identified as a main phase in the less-evolved samples investigated in this study (e.g. La Poruña, San Pedro, Palpana, Chela; Chapter 2, 3 and 4; Sellés and Gardeweg, 2017), implying that more differentiated phases (e.g. amphibole) crystallize and remain stable at similar depths (cf. 13 to 19 km depth) when parental magmas involve increasing uptake of APMB-derived melts during their journey.

Therefore, these recent thermobarometric estimations (i.e. Burns et al., 2020; Gorini et al., 2018; Chapter 4) may reflect an inherent crystallization sequence of olivine → clinopyroxene → amphibole

for the APVC rocks, where olivine likely crystallize in middle-crustal magma chambers prior to clinopyroxene crystallization mostly at ca. 9 to 19 km depth, then the parental magma would evolve by e.g. AFC-type or mixing processes at shallow crustal depths before eruption with amphibole formed and, in some cases, more evolved phases such as biotite or quartz.

5.4 The significance of $\delta^{18}O$ variability in the Central Andes

As oxygen is the most abundant element in the Earth's crust and mantle, oxygen isotopic composition provides robust constraints on magma genesis (Bindeman, 2008). Oxygen isotope analysis is a well-established method used to identify the crustal contamination processes or hydrothermal alteration possible within a magmatic system feeding a volcano and have been studied in Central Andean samples previously (e.g. Davidson et al., 1990; Feeley and Sharp, 1995; Freymuth et al., 2015). In trying to see through to the source of the Central Andean volcanic rocks, it is thus necessary to identify these effects. Based on Fig. 4.5 in Chapter 4, a more pronounced influence from high-$\delta^{18}O$ continental basement, compare to recycled sediments, is required to modify mantle-derived magmas to form the parental magmas of the studied volcanoes. The influence of bulk crustal assimilation instead of e.g. sediments agrees well with previous studies in the whole Central Andes (e.g. Davidson et al., 1990; Freymuth et al., 2015; Kay et al., 2011). Most of the evolved silicic magmas in the APVC are hybrid magmas derived by a ca. 50:50 mixture of mantle and crustal components (Hildreth and Moorbath, 1988; Kay et al., 2010, 2011; Maro and Caffe, 2016). O-isotope and Sr-isotope modelling in this work allow up to about 37 vol% of assimilation of local crust to form basaltic-andesite to andesite magmas.

Because mixing of mantle-derived magmas and continental crust thus appear to be ubiquitous below the main arc, previous reported oxygen isotope values in bulk-rock and monomineralic crystal separates from various Central Andean volcanoes display very large $\delta^{18}O$ variations (2.2 to 14.6‰; Supplementary material 5; Table S5.1). The large displacements among same analysed phase can possibly be explained by local geochemical and isotopic variations due to underlying basement rocks

compositions, or even by crustal thickness differences (e.g. Mamani et al., 2010). However, regardless of the exact process at hand, the chosen material to analyse may also contribute to these large variations. Here an oxygen isotope approach of early ferromagnesian phases such as olivine and clinopyroxene from spatially related volcanoes was used to increase the likelihood of obtaining narrower $\delta^{18}O$ ranges and then be able to robustly estimate parental $\delta^{18}O$ values. Olivine and clinopyroxene oxygen isotope data obtained by laser fluorination (LF) define a robust parental arc end-member $\delta^{18}O$ value of 7.0‰ ± 0.2 (2σ S.D.). Analysis by SIMS, on the other hand, are offset to lower values with respect to LF data (Table 4.2 in Chapter 4), and clinopyroxene cores indicate a lower parental melt value of 6.3‰ ± 0.4 (2σ S.D.). All the exact reasons for these differences are unknown at present but the presence of unavoidable O-enriched melt/mineral inclusions within crystals could distort the $\delta^{18}O$ values obtained using bulk crystal LF analysis (See also Chapter 4). Finally, parental $\delta^{18}O$ values estimated by SIMS data are only based on clinopyroxene core values from two individual volcanoes and would need to be replicated in more mafic phases (e.g. olivine) and other volcanoes in the Central Andes in order to contrast the internal consistency revealed by the oxygen isotope LF data for coexisting olivine and clinopyroxene.

5.5 Origin and evolution of parental magmas associated with Pliocene-Quaternary low-silica volcanism within the western boundary of the Altiplano-Puna Volcanic Complex

The LF $\delta^{18}O$ values of olivine and clinopyroxene reflect crystallization from an equilibrium parental magma with a $\delta^{18}O$ value of 7.0 ± 0.2‰, as a consequence of mantle-derived magmas assimilating significant amounts (up to 28%) of high-$\delta^{18}O$ continental crust ($\delta^{18}O$ = 11.8 to 19.5‰, Chapter 4). Parental magmas migrated to a deep underplating zone beneath the APMB (Chapter 2) where fractional crystallization of e.g. olivine likely occurred (Fig. 4.5 in Chapter 4). The parental melts related to the mafic volcanism erupted at the western border of the Altiplano-Puna Volcanic Complex avoided extensive fractionation and/or interaction with the APMB as such mafic eruptives reveal relatively high baseline $^{143}Nd/^{144}Nd$ ratios (0.51237 to 0.51251), relatively low baseline $^{87}Sr/^{86}Sr$

ratios (0.7055 to 0.7070) and low amounts of crustal assimilation (< 28%; see also Section 5.2). These melts ascended to storage levels at ca. 13 to 19 km depth where clinopyroxene cores fractionated (Section 4.2.3.3 in Chapter 4). Late differentiation of such parental magmas also occurred, which is recorded in clinopyroxene rims (Figs. 4.9 and 4.10 in Chapter 4). On the other hand, some parental melts passed through the APMB, and their volcanic products reveal lower baseline $^{143}Nd/^{144}Nd$ ratios (< 0.5123), higher baseline $^{87}Sr/^{86}Sr$ ratios (> 0.7070) and higher amounts of crustal assimilation (up 37%) with respect to mafic lavas mentioned above. Such parental magmas ascended to upper crustal levels (< 19 km depth) where more evolved phases (e.g. amphibole) formed in addition to the observed olivine and clinopyroxene (See Section 5.3). The proposed model in this section is illustrated in Fig. 5.1.

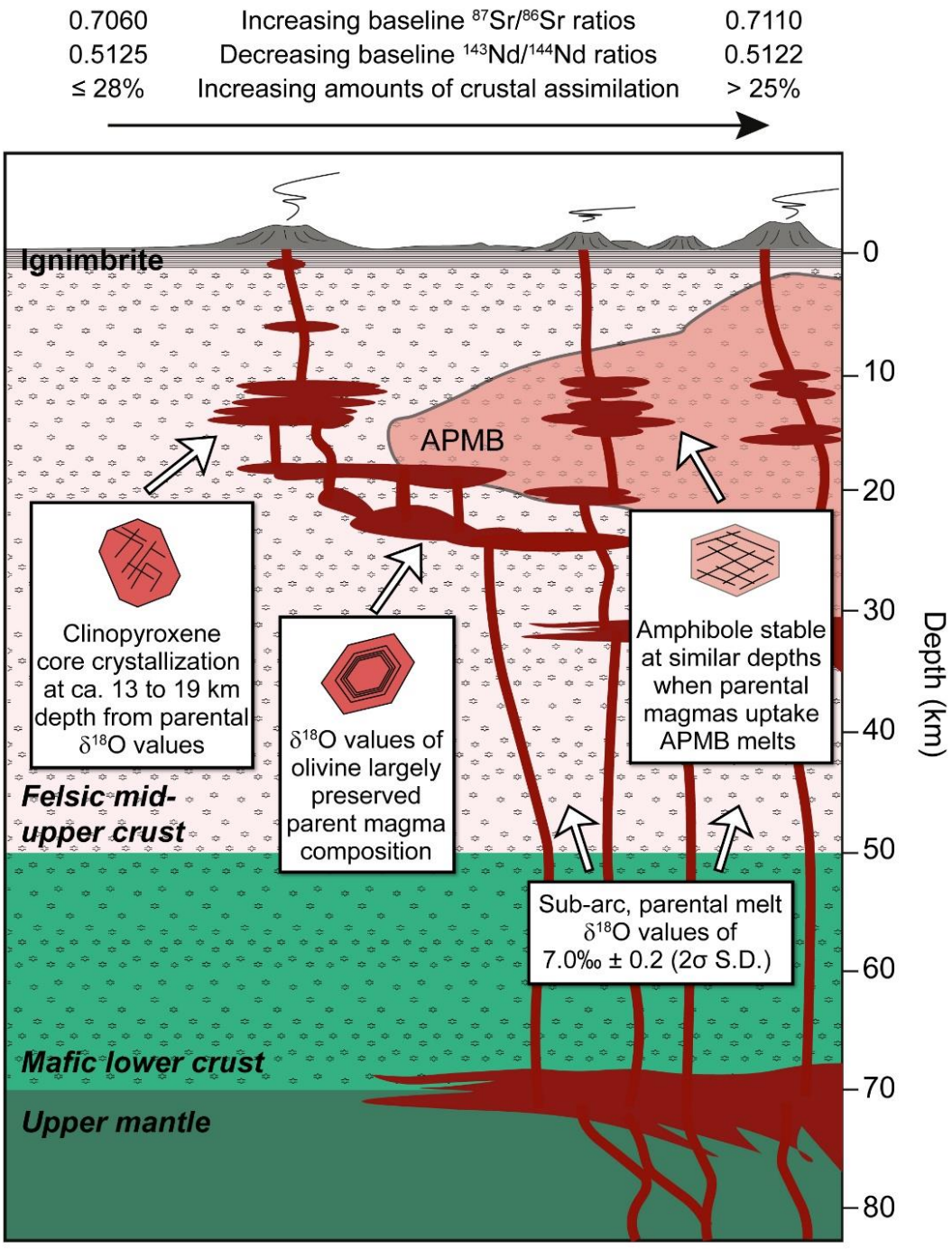

Fig. 5.1. Schematic model of the petrogenesis of low-silica eruptions focused at the western margin of the APMB. See Section 5.5 for details. The depth of the APMB is based on the joint ambient noise-receiver function inversion S-velocity model from Ward et al. (2014), and the thickness for Central Andean crust layers and ignimbrite deposits is from Prezzi et al. (2009) and Salisbury et al. (2011), respectively.

Chapter 6

Conclusions

Olivine and two-pyroxene phyric rocks form the Pliocene to Quaternary mafic lava flows from stratovolcanoes and monogenetic cones located at the western margin of the Altiplano-Puna Volcanic Complex (APVC), between 21º10’ to 22º50’S. The mafic eruptions studied in this work occur in different steady-state stages of the APVC cyclic formation as they are spatially related to large ignimbrite deposits 4 to 0.1 Ma in age. New whole-rock compositional and Sr and Nd isotope data of forty-eight mafic rock samples from fourteen volcanoes reveal a large degree of compositional heterogeneity (e.g. SiO_2 = 53.2 to 63.2 wt%, MgO = 1.74 to 6.08 wt%, Cr = 2 to 382 ppm, Sr = 304 to 885 ppm, $^{87}Sr/^{86}Sr$ = 0.7055 to 0.7088, and $^{143}Nd/^{144}Nd$ = 0.5122 to 0.5125). This compositional variability is explained by parental basaltic-andesite magmas assimilating the most fusible portions of the continental crust and various amounts of felsic melts derived from the Altiplano-Puna Magma Body (APMB) melt anomaly in the APVC. The development of differentiation processes, such as magma mixing, coupled assimilation and fractional crystallization, or selective assimilation, are spatially variable from volcano to volcano. Most of the Pliocene and Quaternary volcanoes outside or within the margin of the APMB show compositionally similar least evolved eruptions, whereas more evolved geochemical and mineralogical magma features tend to appear further towards the centre of the melt body. Results of radiogenic isotope modelling indicate that crustal contamination involving APMB melts decreases as APMB vertical mush thickness decreases for the investigated eruptives. The degree of crustal assimilation was calculated to be ≤ 25 vol% for mafic eruptions located outside or within the margin of the projected areal extent of the APMB and up to 37 vol% for mafic samples collected directly above the giant felsic body. The spatial variability in the Sr and Nd isotope compositions of the mafic volcanism also appears to be a useful indicator for evaluating the temporal evolution of the APMB, which remains thermally active due to steady replenishment of mafic melt from depth and may have slightly reduced its molten extent at least since the Pliocene.

La Poruña is one of the centers that yielded the least evolved magma characteristics in the area, with magmatic evolution related to the neighbouring, larger San Pedro stratovolcano. The whole volcanic deposit of La Poruña is classified as monogenetic, as it generated a relatively small-volume and short-lived singular eruption at ca. 100 kyr ago. Whereas the episodic mafic eruptions of San Pedro volcano occurred between 160 and ca. 96 ka. The youngest eruptions (< 96 ka) at San Pedro represent a period of increasing contamination of the parental magmas with more evolved crustal components (e.g. APMB) as a consequence of a change in the thermal conditions due to an increasing mafic input related to the construction of La Poruña. The coeval mafic lavas from La Poruña and San Pedro are similar in composition and mineralogy, therefore evidence of similar magmatic processes. A remarkable compositional feature of these rocks is the unusual reversed isotopic trend of $^{87}Sr/^{86}Sr$ decreasing as SiO_2 increases, which is related to late-stage processes of selective assimilation during turbulent magma ascent following initial minor assimilation and fractionation.

New internally consistent olivine ($\delta^{18}O$ = 5.7 to 6.2‰; n = 6) and clinopyroxene ($\delta^{18}O$ = 6.3 to 7.2‰; n = 12) data of six volcanoes (La Poruñita, Palpana, Chela, La Poruña, San Pedro and Paniri) obtained by single mineral Laser Fluorination (LF) now define a robust constraint on $\delta^{18}O$ compositions of parental magmas that supply the Altiplano-Puna Volcanic Complex, and is likely applicable as the parental magma composition that feeds Central Andean volcanoes in general. These data have a narrower range compared to existing olivine and clinopyroxene $\delta^{18}O$ values for the Central Andes. A sub-arc, parental magma $\delta^{18}O$ composition of 7.0‰ ± 0.2 (2σ S.D.) was estimated from the new LF data, which is postulated to reflect mantle-derived magmas assimilating significant amounts of high-$\delta^{18}O$ continental material at mid-upper crustal levels. Additionally, mineral oxygen isotope data from Palpana and La Poruña were obtained by *in-situ* Secondary Ionisation Mass Spectrometry (SIMS) analysis to ensure a statistically robust parental melt $\delta^{18}O$ composition for the Altiplano-Puna Volcanic Complex. The SIMS data for clinopyroxene cores ($\delta^{18}O$ = 4.7 to 6.5‰; n = 245) allow an

estimate of 6.3‰ ± 0.4 (2σ S.D.) for a parental magma $\delta^{18}O$ value, which does not reconcile with the internally consistent LF data obtained in this work. Clinopyroxene rims, on the other hand, reveal both high- and low-$\delta^{18}O$ values compared to cores ($\delta^{18}O$ = 4.5 to 6.9‰; n = 112), suggesting distinct compositional arrays reflecting stages of differentiation and magmatic evolution that postdates crystal core formation.

The parental magmas associated with the mafic volcanism within the Altiplano-Puna Volcanic Complex are proposed in the middle-upper crust. Mantle-derived magmas require significant assimilation, up to 28 vol%, of basement rocks with high-$\delta^{18}O$ values ($\delta^{18}O$ = 11.8 to 19.5‰) and highly radiogenic Sr isotope ratios (> 0.714) to produce parental basaltic-andesite magmas with $\delta^{18}O$ values of ca. 7.0‰ and $^{87}Sr/^{86}Sr$ ratios of 0.7055. Parental melts ascended to an underplating zone beneath the APMB in the middle crust that keeps the giant felsic body thermally active. At this stage, parental magmas appear to undergo closed-system fractional crystallization, consistent with potential early olivine crystallization. A fraction of parental magmas is diverted to the margins of the APMB, where it ponds, fractionates (e.g. reflected in clinopyroxene cores) and differentiates in a plumbing system at 13 to 19 km depth. Continuous injections of such parental basaltic-andesite at these upper crustal levels likely initiated subsequent phases of further differentiation as recorded by clinopyroxene rims. Finally, parental magmas that ascended peripheral to the APMB reservoir show lowest rates of magma-crust interaction (12 to 28 vol%) and tend to preserve less evolved baseline compositions (e.g. SiO_2 = 52.7 to 61.5 wt%, $^{87}Sr/^{86}Sr$ = 0.70554 to 0.70668, and $^{143}Nd/^{144}Nd$ = 0.51226 to 0.51251), whereas basaltic-andesite passing through the APMB reflects more evolved final compositional characteristics (e.g. SiO_2 = 53.2 to 62.4 wt%, $^{87}Sr/^{86}Sr$ = 0.70658 to 0.71129, and $^{143}Nd/^{144}Nd$ = 0.51218 to 0.51233) and higher amounts of crustal assimilation (> 25 vol%) due to increasing uptake of APMB material.

References

Aitcheson, S.J., Forrest, A.H., 1994. Quantification of crustal contamination in open magmatic systems. Journal of Petrology, 35(2):461-488. https://doi.org/10.1093/petrology/35.2.461.

Allmendinger, R.W., Jordan, T.E., Kay, S.M., Isacks, B.L., 1997. The evolution of the Altiplano-Puna plateau of the Central Andes. Annual review of earth and planetary sciences, 25(1):139-174. https://doi.org/10.1146/annurev.earth.25.1.139.

Annen, C., Blundy, J.D., Sparks, R.S.J., 2006. The genesis of intermediate and silicic magmas in deep crustal hot zones. Journal of Petrology, 47(3):505-539.

Annen, C., Sparks, R.S.J., 2002. Effects of repetitive emplacement of basaltic intrusions on thermal evolution and melt generation in the crust. Earth and Planetary Science Letters, 203(3-4):937-955. https://doi.org/10.1016/S0012-821X(02)00929-9.

Araya Vargas, J., Meqbel, N. M., Ritter, O., Brasse, H., Weckmann, U., Yáñez, G., Godoy, B., 2019. Fluid distribution in the Central Andes subduction zone imaged with magnetotellurics. Journal of Geophysical Research: Solid Earth, 124. https://doi.org/10.1029/2018JB016933.

Baker, M.B., Grove, T.L., Price, R., 1994. Primitive basalts and andesites from the Mt. Shasta region, N. California: products of varying melt fraction and water content. Contributions to Mineralogy and Petrology, 118(2):111-129. https://doi.org/10.1007/BF01052863.

Beck, S. L., Zandt, G., Myers, S. C., Wallace, T. C., Silver, P. G., Drake, L., 1996. Crustal-thickness variations in the central Andes. Geology, 24(5):407-410. https://doi.org/10.1130/0091-7613.

Bertin, D., Amigo, A., 2019. Geología del volcán San Pedro, Región de Antofagasta. Servicio Nacional de Geología y Minería, Carta Geológica de Chile, Serie Geología Básica, mapa escala 1:50.000. Santiago, Chile.

Best, M.G. 2003. Igneous and metamorphic petrology. John Wiley & Sons.

Bidart, N., 2014. Petrología y geoquímica de lavas recientes, al sureste del campo geotermal del Tatio. Dissertation, B. Sc. Thesis. Universidad de Chile, Santiago, Chile.

Bindeman, I.N., 2008. Oxygen isotopes in mantle and crustal magmas as revealed by single crystal analysis. Reviews in Mineralogy and Geochemistry, 69(1):445-478. https://doi.org/10.2138/rmg.2008.69.12.

Bindeman, I.N., Eiler, J.M., Yogodzinski, G.M., Tatsumi, Y., Stern, C.R., Grove, T.L., Portnyagin, M., Hoernle, K., Danyushevsky, L.V., 2005. Oxygen isotope evidence for slab melting in modern and ancient subduction zones. Earth and Planetary Science Letters, 235(3-4):480-496. https://doi.org/10.1016/j.epsl.2005.04.014.

Bindeman, I.N., Ponomareva, V.V., Bailey, J.C., Valley, J.W., 2004. Volcanic arc of Kamchatka: a province with high-$\delta^{18}O$ magma sources and large-scale 18O/16O depletion of the upper crust. Geochimica et Cosmochimica Acta, 68(4):841-865. https://doi.org/10.1016/j.gca.2003.07.009.

Blum-Oeste, M., Wörner, G., 2016. Central Andean magmatism can be constrained by three ubiquitous end-members. Terra Nova, 28(6):434-440. https://doi.org/10.1111/ter.12237.

Brasse, H., Lezaeta, P., Rath, V., Schwalenberg, K., Soyer, W., Haak, V., 2002. The Bolivian altiplano conductivity anomaly. Journal of Geophysical Research: Solid Earth, 107(B5):EPM-4. https://doi.org/10.1029/2001JB000391.

Burns, D. H., de Silva, S. L., Tepley, F. J., Schmitt, A. K., 2020. Chasing the mantle: Deciphering cryptic mantle signals through Earth's thickest continental magmatic arc. Earth and Planetary Science Letters, 531:115985. https://doi.org/10.1016/j.epsl.2019.115985.

Burns, D.H., de Silva, S.L., Tepley III, F., Schmitt, A.K., Loewen, M.W., 2015. Recording the transition from flare-up to steady-state arc magmatism at the Purico-Chascon volcanic complex, northern Chile. Earth and Planetary Science Letters, 422:75-86. https://doi.org/10.1016/j.epsl.2015.04.002.

Chang, Y-H., 2007. O-Isotopes as tracer for assimilation processes in different magmatic regimes (El Misti, S. Peru and Tapaaca, N. Chile). Dissertation, Diploma Thesis, Georg-August-Universität Göttingen, Germany.

Chiodi, A., Tassi, F., Báez, W., Filipovich, R., Bustos, E., Galli, M.G., Suzaño, N., Ahumada, M.F., Viramonte, J.G., Giordano, G., Pecoraino, G., 2019. Preliminary conceptual model of the Cerro Blanco caldera-hosted geothermal system (Southern Puna, Argentina): Inferences from geochemical investigations. Journal of South American Earth Sciences, 94:102213. https://doi.org/10.1016/j.jsames.2019.102213.

Chmielowski, J., Zandt, G., Haberland, C., 1999. The central Andean Altiplano-Puna magma body. Geophysical Research. Letters, 26(6):783-786. https://doi.org/10.1029/1999GL900078.

Coira, B., Davidson, J., Mpodozis, C., Ramos, V., 1982. Tectonic and magmatic evolution of the Andes of northern Argentina and Chile. Earth-Science Reviews, 18(3-4):303-332. https://doi.org/10.1016/0012-8252(82)90042-3.

Comeau, M.J., Unsworth, M.J., Ticona, F., Sunagua, M., 2015. Magnetotelluric images of magma distribution beneath Volcán Uturuncu, Bolivia: Implications for magma dynamics. Geology, 43(3):243-246. https://doi.org/10.1130/G36258.1.

Dallai, L., Bianchini, G., Avanzinelli, R., Natali, C., Conticelli, S., 2019. Heavy oxygen recycled into the lithospheric mantle. Scientific Reports, 9(1):8793. https://doi.org/10.1038/s41598-019-45031-3.

Damm K.-W., Pichowiak S., Harmon R. S., Todt W., Omarini R., Niemeyer H., 1990. Pre-Mesozoic Evolution of the Central Andes; The basement revisited. in Kay, S.M., Rapela, C. W., eds., Plutonism from Antarctica to Alaska. Geological Society of America Special Paper 241:101-126.

Davidson, J.P., 1996. Deciphering mantle and crustal signatures in subduction zone magmatism. Subduction: top to bottom, 96:251-262. https://doi.org/10.1029/GM096p0251.

Davidson, J.P., de Silva, S.L., 1992. Volcanic rocks from the Bolivian Altiplano: Insights into crustal structure, contamination, and magma genesis in the central Andes. Geology, 20(12):1127:1130. https://doi.org/10.1130/0091-7613(1992)020<1127:VRFTBA>2.3.CO;2.

Davidson, J.P., de Silva, S.L., 1995. Late cenozoic magmatism of the Bolivian Altiplano. Contributions to Mineralogy and Petrology, 119(4):387-408. https://doi.org/10.1007/BF00286937.

Davidson, J.P., Harmon, R., Wörner, G., 1991. The source of central Andean magmas: some considerations. Geological Society of America Special Paper, 265:233-243.

Davidson, J.P., Hora, J.M., Garrison, J.M., Dungan, M.A., 2005. Crustal forensics in arc magmas. Journal of Volcanology and Geothermal Research, 140(1-3) 157-170. https://doi.org/10.1016/j.jvolgeores.2004.07.019.

Davidson, J.P., Turner, S., Plank, T., 2013. Dy/Dy*: variations arising from mantle sources and petrogenetic processes. Journal of Petrology, 54(3): 525-537. https://doi.org/ 10.1093/petrology/egs076.

Davidson, J.P., McMillan, N.J., Moorbath, S., Wörner, G., Harmon, R.S., López-Escobar, L., 1990a. The Nevados de Payachata volcanic region (18°S/69°W, N. Chile) II. Evidence for widespread crustal involvement in Andean magmatism. Contributions to Mineralogy and Petrology, 105(4):412-432. https://doi.org/10.1007/BF00286829.

Davidson, J.P., Turner, S., Handley, H., Macpherson, C., Dosseto, A., 2007. Amphibole “sponge” in arc crust?. Geology, 35(9):787-790. https://doi.org/10.1130/G23637A.1.

Davidson, J.P., Turner, S., Plank, T., 2013. Dy/Dy*: variations arisingfrom mantle sources and petrogenetic processes. Journal of Petrology, 54(3), 525-537. https://doi.org/10.1093/petrology/egs076.

Danyushevsky, L.V., Della-Pasqua, F.N., Sokolov, S., 2000. Re-equilibration of melt inclusions trapped by magnesian olivine phenocrysts from subduction-related magmas: petrological implications. Contributions to Mineralogy and Petrology, 138(1):68-83. https://doi.org/10.1007/PL00007664.

de Silva, S.L., Zandt, G., Trumbull, R., Viramonte, J., 2006. Large-scale silicic volcanism—The result of thermal maturation of the crust. In Advances in Geosciences: Volume 1: Solid Earth (SE), 215-230.

de Silva, S.L., 1989. Altiplano-Puna volcanic complex of the central Andes. Geology, 17(12):1102-1106. https://doi.org/10.1130/0091-7613.

de Silva, S.L., Francis, P.W. 1991. Volcanoes of the Central Andes. Springer-Verlag, Heidelberg, 216 pp.

de Silva, S.L., Gosnold, W.D., 2007. Episodic construction of batholiths: Insights from the spatiotemporal development of an ignimbrite Flare-up. Journal of Volcanology and Geothermal Research, 167(1-4):320-335. https://doi.org/10.1016/j.jvolgeores.2007.07.015.

de Silva, S.L., Kay, S.M., 2018. Turning up the heat: high-flux magmatism in the Central Andes. Elements, 14(4):245-250. https://doi.org/10.2138/gselements.14.4.245.

de Silva, S.L., Riggs, N.R., Barth, A.P., 2015. Quickening the pulse: fractal tempos in continental arc magmatism. Elements, 11(2):113-118. https://doi.org/10.2113/gselements.11.2.113.

Deegan, F.M., Whitehouse, M.J., Troll, V.R., Budd, D.A., Harris, C., Geiger, H., Hålenius, U., 2016. Pyroxene standards for SIMS oxygen isotope analysis and their application to Merapi volcano, Sunda arc, Indonesia. Chemical Geology, 447:1-10. https://doi.org/10.1016/j.chemgeo.2016.10.018.

del Potro, R., Díez, M., Blundy, J., Camacho, A.G., Gottsmann, J., 2013. Diapiric ascent of silicic magma beneath the Bolivian Altiplano. Geophysical Research Letters, 40:2044-2048. https://doi.org/10.1002/grl.50493.

Delunel, R., Blard, P.H.,Martin, L.C.P., Nomade,S., Schlunegger,F., 2016. Long-term low latitude and high elevation cosmogenic ^{3}He production rate inferred from a 107 ka-old lava flow in northern Chile; 22°S-3400 m a.s.l. Geochimica et Cosmochimica Acta, 184:71-87. https://doi.org/10.1016/j.gca.2016.04.023.

DePaolo, D.J., 1981. Trace element and isotopic effects of combined wallrock assimilation and fractional crystallization. Earth and planetary science letters, 53(2):189-202. https://doi.org/10.1016/0012-821X(81)90153-9.

Drew, S.T., Ducea, M.N., Schoenbohm, L.M., 2009. Mafic volcanism on the Puna Plateau, NW Argentina: Implications for lithospheric composition and evolution with an emphasis on lithospheric foundering. Lithosphere, 1(5):305-318. https://doi.org/10.1130/L54.1.

Eiler, J.M., 2001. Oxygen isotope variations of basaltic lavas and upper mantle rocks. Reviews in mineralogy and geochemistry, 43(1):319-364.

Eiler, J.M., Schiano, P., Kitchen, N., Stolper, E.M., 2000. Oxygen-isotope evidence for recycled crust in the sources of mid-ocean-ridge basalts. Nature, 403(6769):530. https://doi.org/10.1038/35000553.

Eiler, J.M., Stolper, E.M., McCanta, M.C., 2011. Intra-and intercrystalline oxygen isotope variations in minerals from basalts and peridotites. Journal of Petrology, 52(7-8):1393-1413. https://doi.org/10.1093/petrology/egr006.

Entenmann, J., 1994. Magmatic evolution of the Nevados de Payachata complex and the petrogenesis of basaltic andesites in the Central Volcanic Zone of northern Chile. Dissertation, Ph.D. Thesis, Johannes Gutenberg-Universität Mainz, Germany.

Feeley, T.C., Davidson, J.P., 1994. Petrology of Calc-Alkaline Lavas at Volcán Ollagüe and the Origin of Compositional Diversity at Central Andean Stratovolcanoes. Journal of Petrology, 35(5):1295-1340. https://doi.org/10.1093/petrology/35.5.1295.

Feeley, T.C., Sharp, Z.D., 1995. $^{18}O^{16}O$ isotope geochemistry of silicic lava flows erupted from Volcán Ollagüe, Andean Central Volcanic Zone. Earth and Planetary Science Letters, 133(3-4):239-254. https://doi.org/10.1016/0012-821X(95)00094-S.

Feeley, T.C., Davidson, J.P., Armendia, A., 1993. The volcanic and magmatic evolution of Volcán Ollagüe, a high-K, late Quaternary stratovolcano in the Andean Central Volcanic Zone. Journal of Volcanology and Geothermal Research, 54(3-4):221-245. https://doi.org/10.1016/0377-0273(93)90065-Y.

Figueroa, O., Déruelle, B., Demaiffe, D., 2009. Genesis of adakite-like lavas of Licancabur volcano (Chile—Bolivia, Central Andes). C. R. Geoscience, 341(4):310-318. https://doi.org/10.1016/j.crte.2008.11.008.

Francis, P., Oppenheimer, C., 2004. Volcanoes 2nd ed. Oxford University Press.

Francis, P.W., Hawkesworth, C.J., 1994. Late Cenozoic rates of magmatic activity in the Central Andes and their relationships to continental crust formation and thickening. Journal of the Geological Society, 151(5):845-854. https://doi.org/10.1144/gsjgs.151.5.0845.

Francis, P.W., Roobol, M.J., Walker, G.P.L., Cobbold, P.R., Coward, M., 1974. The San Pedro and San Pablo volcanoes of northern Chile and their hot avalanche deposits. Geologische Rundschau, 63(1):357-388. https://doi.org/10.1007/BF01820994.

Freymuth, H., Brandmeier, M., Wörner, G., 2015. The origin and crust/mantle mass balance of Central Andean ignimbrite magmatism constrained by oxygen and strontium isotopes and erupted volumes. Contributions to Mineralogy and Petrology, 169(6):58. https://doi.org/10.1007/s00410-015-1152-5.

Frimmel, H.E., Zartman, R.E., Späth, A., 2001. Dating Neoproterozoic continental break-up in the Richtersveld Igneous Complex, South Africa. Journal of Geology, 109(4):493-508. https://doi.org/10.1086/320795.

Geiger, H., Barker, A.K., Troll, V.R., 2016. Locating the depth of magma supply for volcanic eruptions, insights from Mt. Cameroon. Scientific reports, 6(1):1-10. https://doi.org/10.1038/srep33629.

Geiger, H., Troll, V.R., Jolis, E.M., Deegan, F.M., Harris, C., Hilton, D.R., Freda, C., 2018. Multi-level magma plumbing at Agung and Batur volcanoes increases risk of hazardous eruptions. Scientific reports, 8(1):1-14. https://doi.org/10.1038/s41598-018-28125-2.

Giambiagi, L., Alvarez, P., Spagnotto, S., 2016. Temporal variation of the stress field during the construction of the central Andes: Constrains from the volcanic arc region (22–26° S), Western Cordillera, Chile, during the last 20 Ma. Tectonics, 35(9):2014-2033. https://doi.org/10.1002/2016TC004201.

Godoy, B., 2014. Evolución petrológica de la Cadena Volcánica San Pedro-Linzor (21º30'S-22º10'S), norte de Chile, y su relación con la geodinámica Andina. Dissertation, Ph.D. Thesis, Universidad Católica del Norte, Chile.

Godoy, B., Lazcano, J., Rodríguez, I., Martínez, P., Parada, M.A., Le Roux, P., Wilke, H.G., Polanco, E., 2018. Geological evolution of Paniri volcano, Central Andes, northern Chile. Journal of South American Earth Sciences, 84:184-200. https://doi.org/10.1016/j.jsames.2018.03.013.

Godoy, B., Taussi, M., González-Maurel, O., Renzulli, A., Hernández-Prat, L., le Roux, P., Morata, D., Menzies, A., 2019. Linking the mafic volcanism with the magmatic stages during the last 1 Ma in the main volcanic arc of the Altiplano-Puna Volcanic Complex (Central Andes). Journal of South American Earth Sciences, 95:102295. https://doi.org/10.1016/j.jsames.2019.102295.

Godoy, B., Wörner, G., Kojima, S., Aguilera, F., Simon, K., Hartmann, G., 2014. Low-pressure evolution of arc magmas in thickened crust: The San Pedro-Linzor volcanic chain, Central Andes, Northern Chile. Journal of South American Earth Sciences, 52:24-42. https://doi.org/10.1016/j.jsames.2014.02.004.

Godoy, B., Wörner, G., Le Roux, P., de Silva, S., Parada, M.A., Kojima, S., González-Maurel, O., Morata, D., Polanco, E., Martínez, P., 2017. Sr- and Nd- isotope variations along the Pleistocene San Pedro – Linzor volcanic chain, N. Chile: Tracking the influence of the upper crustal Altiplano-Puna Magma Body. Journal of Volcanology and Geothermal Research, 341:172-186. https://doi.org/10.1016/j.jvolgeores.2017.05.030.

González-Ferrán, O., 1995. Volcanes de Chile. Instituto Geográfico Militar, Santiago, Chile. 640pp.

Gorini, A., Ridolfi, F., Piscaglia, F., Taussi, M., Renzulli, A., 2018. Application and reliability of calcic amphibole thermobarometry as inferred from calc-alkaline products of active geothermal areas in the Andes. Journal of Volcanology and Geothermal Research, 358:58-76. https://doi.org/10.1016/j.jvolgeores.2018.03.018.

Goss, A.R., Kay, S.M., Mpodozis, C., 2011. The geochemistry of a dying continental arc: the Incapillo Caldera and Dome Complex of the southernmost Central Andean Volcanic Zone (~ 28 S). Contributions to Mineralogy and Petrology, 161(1):101-128. https://doi.org/10.1007/s00410-010-0523-1.

Gottlieb, P., Wilkie, G., Sutherland, D., Ho-Tun, E., Suthers, S., Perera, K., Jenkins, B., Spencer, S., Butcher, A., Rayner, J., 2000. Using quantitative electron microscopy for process mineralogy applications. JoM, 52(4):24-25. https://doi.org/10.1007/s11837-000-0126-9.

Guzmán, S.R., Petrinovic, I.A., Brod, J.A., 2006. Pleistocene mafic volcanoes in the Puna–Cordillera Oriental boundary, NW-Argentina. Journal of Volcanology and Geothermal Research, 158(1-2):51-69. https://doi.org/10.1016/j.jvolgeores.2006.04.014.

Haberland, C., Rietbrock, A., 2001. Attenuation tomography in the western central Andes: A detailed insight into the structure of a magmatic arc. Journal of Geophysical Research: Solid Earth, 106(B6):11151-11167. https://doi.org/10.1029/2000JB900472.

Harmon, R.S., Thorpe, R.S., Francis, P.W., 1981. Petrogenesis of Andean andesites from combined O–Sr isotope relationships. Nature, 290(5805):396-399. https://doi.org/10.1038/290396a0.

Harris, C., Le Roux, P., Cochrane, R., Martin, L., Duncan, A.R., Marsh, J. S., le Roex, A.P., Class, C., 2015. The oxygen isotope composition of Karoo and Etendeka picrites: High δ18. Contributions to Mineralogy and Petrology, 170(1):1-24. https://doi.org/10.1007/s00410-015-1164-1.

Harris, C., Vogeli, J., 2010. Oxygen isotope composition of garnet in the Peninsula Granite, Cape Granite Suite, South Africa: constraints on melting and emplacement mechanisms. South African Journal of Geology, 113(4):401-412. https://doi.org/10.2113/gssajg.113.4.401.

Haschke, M. R., 2002. Evolutionary geochemical patterns of Late Cretaceous to Eocene arc magmatic rocks in north Chile: Implications for Archean crustal growth. European Geosciences Union, EGU Stephan Mueller Special Publication Series, 2, 207-218.

Hawkesworth, C.J., Hammill, M., Gledhill, A.R., van Calsteren, P., Rogers, G., 1982. Isotope and trace element evidence for late-stage intra-crustal melting in the High Andes. Earth and Planetary Science Letters, 58(2):240-254. https://doi.org/10.1016/0012-821X(82)90197-2.

Hayes, G.P., Wald, D.J., Johnson, R.L., 2012. Slab1. 0: A three-dimensional model of global subduction zone geometries. Journal of Geophysical Research: Solid Earth, 117(B1). https://doi.org/10.1029/2011JB008524.

Hildreth, W., 1981. Gradients in silicic magma chambers: implications for lithospheric magmatism. Journal of Geophysical Research: solid earth, 86(B11):10153-10192. https://doi.org/10.1029/JB086iB11p10153.

Hildreth, W., Moorbath, S., 1988. Crustal contributions to arc magmatism in the Andes of central Chile. Contributions to mineralogy and petrology, 98(4):455-489. https://doi.org/10.1007/BF00372365.

Howarth, G.H., Moore, A.E., Harris, C., van der Meer, Q.H.A., le Roux, P., 2019. Crustal versus mantle origin of carbonate xenoliths from Kimberley region kimberlites using C-O-Sr-Nd-Pb isotopes and trace element abundances. Geochimica et Cosmochimica Acta, 266:258-273. https://doi.org/10.1016/j.gca.2019.03.026.

Huber, C., Bachmann, O., Manga, M., 2009. Homogenization processes in silicic magma chambers by stirring and mushification (latent heat buffering). Earth and Planetary Science Letters, 283:38-47. https://doi.org/10.1016/j.epsl.2009.03.029.

Huppert, H.E., Sparks, R.S.J., 1985. Cooling and contamination of mafic and ultramafic magmas during ascent through continental crust. Earth and Planetary Science Letters, 74(4):371-386. https://doi.org/10.1016/S0012-821X(85)80009-1.

Irvine, T.N.J., Baragar, W.R.A.F., 1971. A guide to the chemical classification of the common volcanic rocks. Canadian journal of earth sciences, 8(5):523-548. https://doi.org/10.1139/e71-055.

Ito, E., White, W.M., Göpel, C., 1987. The O, Sr, Nd and Pb isotope geochemistry of MORB. Chemical Geology, 62(3-4):157-176. https://doi.org/10.1016/0009-2541(87)90083-0.

Jacques, G., Hoernle, K., Gill, J., Wehrmann, H., Bindeman, I., Lara, L.E., 2014. Geochemical variations in the Central Southern Volcanic Zone, Chile (38–43 S): the role of fluids in generating arc magmas. Chemical Geology, 371:27-45. https://doi.org/10.1016/j.chemgeo.2014.01.015.

Kay, S.M., Coira, B., Viramonte, J., 1994. Young mafic back arc volcanic rocks as indicators of continental lithospheric delamination beneath the Argentine Puna plateau, central Andes. Journal of Geophysical Research, 99(B12):24323-24339. https://doi.org/10.1029/94JB00896.

Kay, S.M., Coira, B.L., Caffe, P.J., Chen, C.H., 2010. Regional chemical diversity, crustal and mantle sources and evolution of central Andean Puna plateau ignimbrites. Journal of Volcanology and Geothermal Research, 198(1):81-111. https://doi.org/10.1016/j.jvolgeores.2010.08.013.

Kay, S.M., Coira, B., Wörner, G., Kay, R.W., Singer, B.S., 2011. Geochemical, isotopic and single crystal $^{40}Ar/^{39}Ar$ age constraints on the evolution of the Cerro Galan ignimbrites. Bulletin of Volcanology, 73(10):1487-1511. https://doi.org/10.1007/s00445-010-0410-7.

Kay, R.W., Kay, S.M., 1993. Delamination and delamination magmatism. Tectonophysics, 219(1-3):177-189. https://doi.org/10.1016/0040-1951(93)90295-U.

Kay, S.M., Mpodozis, C., Coira, B., 1999. Neogene magmatism, tectonism, and mineral deposits of the Central Andes (22 to 33 S latitude). In Geology and ore deposits of the Central Andes (Vol. 7, pp. 27-59). Society of Economic Geologists.

Kelemen, P.B., Hanghøj, K., & Greene, A.R., 2003. One view of the geochemistry of subduction-related magmatic arcs, with an emphasis on primitive andesite and lower crust. Treatise on geochemistry, 3:593-659. https://doi.org/10.1016/B0-08-043751-6/03035-8.

Kern, J.M., de Silva, S.L., Schmitt, A.K., Kaiser, J.F., Iriarte, A.R., Economos, R., 2016. Geochronological imaging of an episodically constructed subvolcanic batholith: U-Pb in zircon chronochemistry of the Altiplano-Puna Volcanic Complex of the Central Andes. Geosphere, 12(4):1054-1077. https://doi.org/10.1130/GES01258.1.

Kerr, A. C., Kempton, P. D., Thompson, R. N., 1995. Crustal assimilation during turbulent magma ascent (ATA); new isotopic evidence from the Mull Tertiary lava succession, NW Scotland. Contributions to Mineralogy and Petrology, 119(2-3):142-154. https://doi.org/10.1007/BF00307277.

Klug, J., Singer, B., Jicha, B., Ramírez, A., 2018. Intercalibrating the SERNAGEOMIN and WiscAr $^{40}Ar/^{39}Ar$ Geochronology Laboratories for Quaternary dating. In Libro de Actas, XV Congreso Geológico Chileno “Geociencias hacia la comunidad”, Concepción, 18 a 23 de Noviembre, 2018. p. 892.

Laube, N., Springer, J., 1998. Crustal melting by ponding of mafic magmas: A numerical model. Journal of Volcanology and Geothermal Research, 81(1-2):19-35. https://doi.org/10.1016/S0377-0273(97)00072-3.

Le Maitre, R.W., Bateman, P., Dudek, A., Keller, J., Lameyre, J., Le Bas, M.J., Sabine, P.A., Schmid, R., Sorensen, H., Strekeisen, A., Woolley, A.R., Zanettin, B., 1989. A classification of igneous rocks and glossary of terms: Recommendations of the International Union of Geological Sciences, Subcommission on the Systematics of Igneous Rocks (No. 552.3 CLA). International Union of Geological Sciences, 193 pp.

Lindsay, J.M., Schmitt, A.K., Trumbull, R.B., De Silva, S.L., Siebel, W., Emmermann, R., 2001. Magmatic evolution of the La Pacana caldera system, Central Andes, Chile: Compositional variation of two cogenetic, large-volume felsic ignimbrites. Journal of Petrology, 42(3):459-486. https://doi.org/10.1093/petrology/42.3.459.

Lister, J., 2019. Petrogenesis of lavas from Volcano Azufre, Northern Chile: evidence for crustal input. Dissertation, M.Sc. Thesis, University of Cape Town, South Africa.

Mamani, M., Wörner, G., Sempere, T., 2010. Geochemical variations in igneous rocks of the Central Andean orocline (13°S to 18°S): tracking crustal thickening and magma generation through time and space. Geological Society of America Bulletin, 122(1-2):162-182. https://doi.org/10.1130/B26538.1.

Marín, C., 2016. Petrología del volcán La Poruña, Región de Antofagasta, Chile. Dissertation, B. Sc. Thesis, Universidad Católica del Norte, Antofagasta, Chile.

Marinovic, N., Lahsen, A., 1984. Hoja Calama. Servicio Nacional de Geología y Minería, Carta Geológica de Chile, Serie Geología Básica 58, 1 mapa escala 1:250.000. Santiago, Chile.

Maro, G., Caffe, P.J., 2016. The Cerro Bitiche Andesitic Field: petrological diversity and implications for magmatic evolution of mafic volcanic centers from the northern Puna. Bulletin of Volcanology, 78(7): 51. https://doi.org/10.1007/s00445-016-1039-y.

Maro, G., Caffe, P.J., Romer, R.L., Trumbull, R.B., 2017. Neogene Mafic Magmatism in the Northern Puna Plateau, Argentina: Generation and Evolution of a Back-arc Volcanic Suite. Journal of Petrology, 58(8):1591-1617. https://doi.org/10.1093/petrology/egx066.

Matteini, M., Mazzuoli, R., Omarini, R., Cas, R., Maas, R., 2002. The geochemical variations of the upper cenozoic volcanism along the Calama–Olacapato–El Toro transversal fault system in central Andes (~ 24 S): petrogenetic and geodynamic implications. Tectonophysics, 345(1-4):211-227. https://doi.org/10.1016/S0040-1951(01)00214-1.

Mattey, D., Lowry, D., Macpherson, C., 1994. Oxygen isotope composition of mantle peridotite. Earth and Planetary Science Letters, 128(3-4):231-241. https://doi.org/10.1016/0012-821X(94)90147-3.

Mattioli, M., Renzulli, A., Menna, M., Holm, P.M., 2006. Rapid ascent and contamination of magmas through the thick crust of the CVZ (Andes, Ollagüe region): Evidence from a nearly aphyric high-K andesite with skeletal olivines. Journal of Volcanology and Geothermal Research, 158(1-2): 87-105. https://doi.org/10.1016/j.jvolgeores.2006.04.019.

Mazzuoli, R., Vezzoli, L., Omarini, R., Acocella, V., Gioncada, A., Matteini, M., Dini, A., Guillou, H., Hauser, N., Uttini, A., Scaillet, S., 2008. Miocene magmatism and tectonics of the easternmost sector of the Calama–Olacapato–El Toro fault system in Central Andes at ~ 24°S: Insights into the evolution of the Eastern Cordillera. Geological Society of America Bulletin, 120(11-12):1493-1517. https://doi.org/10.1130/B26109.1.

McDonough, W.F., Sun, S.S., 1995. The composition of the Earth. Chemical geology, 120(3-4):223-253. https://doi.org/10.1016/0009-2541(94)00140-4.

McKay, G.A., 1989. Partitioning of rare earth elements between major silicate minerals and basaltic melts. Reviews in Mineralogy and Geochemistry, 21(1):45-77.

Meade, F.C., Troll, V.R., Ellam, R.M., Freda, C., Font, L., Donaldson, C.H., Klonowska, I., 2014. Bimodal magmatism produced by progressively inhibited crustal assimilation. Nature communications, 5:4199. https://doi.org/10.1038/ncomms5199.

Métois, M., Vigny, C., Socquet, A., Delorme, A., Morvan, S., Ortega, I., Valderas-Bermejo, C.M., 2014. GPS-derived interseismic coupling on the subduction and seismic hazards in the Atacama region, Chile. Geophysical Journal International, 196(2):644-655. https://doi.org/10.1093/gji/ggt418.

Michelfelder, G.S., Feeley, T.C., Wilder, A.D., Klemetti, E.W., 2013. Modification of the Continental Crust by Subduction Zone Magmatism and Vice-Versa: Across-Strike Geochemical Variations of Silicic Lavas from Individual Eruptive Centers in the Andean Central Volcanic Zone. Geosciences 3(4): 633-667. https://doi.org/10.3390/geosciences3040633.

Moorbath, S., Thompson, R. N. 1980. Strontium Isotope Geochemistry and Petrogenesis of the Early Tertiary Lava Pile of the Isle of Skye, Scotland, and other Basic Rocks of the British Tertiary Province: an Example of Magma—Crust Interaction. Journal of Petrology, 21(2), 295-321. https://doi.org/101093/petrology/212295.

Morimoto, N., 1988. Nomenclature of pyroxenes. Mineralogy and Petrology, 39(1):55-76. https://doi.org/10.1007/BF01226262.

Mpodozis, C., Kay, S.M., 1990. Provincias magmáticas ácidas y evolución tectónica de Gondwana: Andes chilenos (28-31°S). Andean Geology, 17(2):153-180. http://doi.org/10.5027/andgeoV17n2-a03.

Murray, K.E., Ducea, M.N., Schoenbohm, L., 2015. Foundering-driven lithospheric melting: The source of central Andean mafic lavas on the Puna Plateau (22°S–27°S). Geodynamics of a Cordilleran Orogenic System: The Central Andes of Argentina and Northern Chile: Geological Society of America Memoir, 212:139-166.

Nemchin, A.A., Pidgeon, R.T., Whitehouse, M.J., 2006. Re-evaluation of the origin and evolution of > 4.2 Ga zircons from the Jack Hills metasedimentary rocks. Earth and Planetary Science Letters, 244(1-2):218-233. https://doi.org/10.1016/j.epsl.2006.01.054.

Norini, G., Baez, W., Becchio, R., Viramonte, J., Giordano, G., Arnosio, M., Pinton, A., Groppelli, G., 2013. The Calama–Olacapato–El Toro fault system in the Puna Plateau, Central Andes: geodynamic implications and stratovolcanoes emplacement. Tectonophysics, 608:1280-1297. https://doi.org/10.1016/j.tecto.2013.06.013.

O'Callaghan, L.J., Francis, P.W., 1986. Volcanological and petrological evolution of San Pedro volcano, Provincia El Loa, North Chile. Journal of the Geological Society of London, 143:275-286. https://doi.org/10.1144/gsjgs.143.2.0275.

Peccerillo, A., Dallai, L., Frezzotti, M.L., Kempton, P.D., 2004. Sr-Nd-Pb-O isotopic evidence for decreasing crustal contamination with ongoing magma evolution at Alicudi volcano (Aeolian arc, Italy): implications for style of magma-drust interaction and for mantle source compositions. Lithos, 78(1-2):217-233. https://doi.org/10.1016/j.lithos.2004.01.040.

Peccerillo, A., Taylor, S.R., 1976. Geochemistry of Eocene calc-alkaline volcanic rocks from the Kastamonu area, northern Turkey. Contributions to mineralogy and petrology, 58(1):63-81. https://doi.org/10.1007/BF00384745.

Perkins, J.P., Ward, K.M., de Silva, S.L., Zandt, G., Beck, S.L., Finnegan, N.J., 2016. Surface uplift in the Central Andes driven by growth of the Altiplano Puna Magma Body. Nature Communications, 7:13185. https://doi.org/10.1038/ncomms13185.

Pichowiak, S., Buchelt, M., Damm, K.W., 1990. Magmatic activity and tectonic setting of the early stages of the Andean cycle in northern Chile. In Plutonism from Antarctica to Alaska (Vol. 241, pp. 127-144). Geological Society of America.

Pirrie, D., Butcher, A. R., Power, M. R., Gottlieb, P., Miller, G. L., 2004. Rapid quantitative mineral and phase analysis using automated scanning electron microscopy (QemSCAN); potential applications in forensic geoscience. Geological Society, London, Special Publications, 232(1):123-136. https://doi.org/10.1144/GSL.SP.2004.232.01.12.

Portnyagin, M., Almeev, R., Matveev, S., Holtz, F., 2008. Experimental evidence for rapid water exchange between melt inclusions in olivine and host magma. Earth and Planetary Science Letters, 272(3-4):541-552. https://doi.org/10.1016/j.epsl.2008.05.020.

Prezzi, C.B., Götze, H.J., Schmidt, S., 2009. 3D density model of the Central Andes. Physics of the Earth and Planetary Interiors, 177(3-4):217-234. https://doi.org/10.1016/j.pepi.2009.09.004.

Putirka, K.D., 2008. Thermometers and barometers for volcanic systems. Reviews in mineralogy and geochemistry, 69(1):61-120. https://doi.org/10.2138/rmg.2008.69.3.

R Core Team, 2008. The R project for statistical computing. http://www.r-project.org.

Ramírez, C., Huete, C., 1981. Hoja Ollagüe. Servicio Nacional de Geología y Minería, Carta Geológica de Chile, Serie Geología Básica, nº40, 1 mapa escala 1:250000, Santiago, Chile.

Richards, J.P., Boyce, A.J., Pringle, M.S., 2001. Geologic evolution of the Escondida area, northern Chile: A model for spatial and temporal localization of porphyry Cu mineralization. Economic Geology, 96(2):271-305. https://doi.org/10.2113/gsecongeo.96.2.271.

Richards, J.P., Villeneuve, M., 2002. Characteristics of late Cenozoic volcanism along the Archibarca lineament from Cerro Llullaillaco to Corrida de Cori, northwest Argentina. Journal of Volcanology and Geothermal Research, 116(3-4):161-200. https://doi.org/10.1016/S0377-0273(01)00329-8.

Rickwood, P.C., 1989. Boundary lines within petrologic diagrams which use oxides of major and minor elements. Lithos 22 (4):247–263. https://doi.org/10.1016/0024-4937(89)90028-5.

Riller, U., Petrinovic, I., Ramelow, J., Strecker, M., Oncken, O., 2001. Late Cenozoic tectonism, collapse caldera and plateau formation in the central Andes. Earth and Planetary Science Letters, 188(3-4):299-311. https://doi.org/10.1016/S0012-821X(01)00333-8.

Risse, A., Trumbull, R.B., Kay, S.M., Coira, B., Romer, R.L., 2013. Multi-stage evolution of late Neogene mantle-derived magmas from the central Andes back-arc in the Southern Puna Plateau of Argentina. Journal of Petrology, 54(10):1963-1995. https://doi.org/10.1093/petrology/egt038.

Rollinson, H.R., 1993. Using Geochemical Data: Evaluation, Presentation, Interpretation. Longman Scientific and Technical (352 pp.).

Ryan, W.B., Carbotte, S.M., Coplan, J.O., O'Hara, S., Melkonian, A., Arko, R., Weissel, R.A., Ferrini, V., Goodwillie, A., Nitsche, F., Bonczkowski, J., 2009. Global multi-resolution topography synthesis. Geochemistry, Geophysics, Geosystems, 10(3). https://doi.org/10.1029/2008GC002332.

Salazar, J.S., Madriaza, E., Fonseca, E., 2018. Mejoras en la preparación de rocas volcánicas cálcicas jóvenes (<1 Ma) para datación Ar/Ar en masa fundamental, en el laboratorio del SERNAGEOMIN. In Libro de Actas, XV Congreso Geológico Chileno "Geociencias hacia la comunidad", Concepción, 18 a 23 de Noviembre, 2018. p. 906.

Salfity, J.A., 1985. Lineamentos transversales al rumbo andino en el Noroeste Argentino. IV Congreso Geológico Chileno, Universidad Católica del Norte. Antofagasta, Chile, p. 119-137

Salisbury, M.J., Jicha, B.R., de Silva, S.L., Singer, B.S., Jiménez, N.C., Ort, M.H., 2011. $^{40}Ar/^{39}Ar$ chronostratigraphy of Altiplano-Puna volcanic complex ignimbrites reveals the development of a major magmatic province. GSA Bulletin, 123(5-6):821-840. https://doi.org/10.1130/B30280.1.

Schaller, T., Andersen, J., Götze, H.J., Koproch, N., Schmidt, S., Sobiesiak, M., Splettstößer, S., 2015. Segmentation of the Andean margin by isostatic models and gradients. Journal of South American Earth Sciences, 59:69-85. https://doi.org/10.1016/j.jsames.2015.01.008.

Schilling, F. R., Partzsch, G. M., 2001. Quantifying partial melt fraction in the crust beneath the central Andes and the Tibetan Plateau. Physics and Chemistry of the Earth, Part A: Solid Earth and Geodesy, 26(4-5), 239-246. https://doi.org/10.1016/S1464-1895(01)00051-5.

Schilling, F.R., Partzsch, G.M., Brasse, H., Schwarz, G., 1997. Partial melting below the magmatic arc in the central Andes deduced from geoelectromagnetic field experiments and laboratory data. Physics of the Earth and Planetary Interiors, 103(1-2):17-31. https://doi.org/10.1016/S0031-9201(97)00011-3.

Schmitt, A., de Silva, S., Trumbull, R., Emmermann, R., 2001. Magma evolution in the Purico ignimbrite complex, northern Chile: evidence for zoning of a dacitic magma by injection of rhyolitic melts following mafic recharge. Contributions to Mineralogy and Petrology, 140(6):680-700. https://doi.org/10.1007/s004100000214.

Schnurr, W.B.W., Trumbull, R.B., Clavero, J., Hahne, K., Siebel, W., Gardeweg, M., 2007. Twenty-five million years of silicic volcanism in the southern central volcanic zone of the Andes: geochemistry and magma genesis of ignimbrites from 25 to 27 S, 67 to 72 W. Journal of Volcanology and Geothermal Research, 166(1):17-46. https://doi.org/10.1016/j.jvolgeores.2007.06.005.

Scott, E.M., Allen, M.B., Macpherson, C.G., McCaffrey, K.J., Davidson, J.P., Saville, C., Ducea, M.N., 2018. Andean surface uplift constrained by radiogenic isotopes of arc lavas. Nature communications, 9(1):969. https://doi.org/10.1038/s41467-018-03173-4.

Seelenfreund, A., Fonseca, E., Llona, F., Lera, L., Sinclaire, C., Rees, C., 2009. Geochemical analysis of vitreous rocks exploited during the formative period in the Atacama region, northern Chile. Archaeometry, 51 (1):1-25. https://doi.org/10.1111/j.1475-4754.2008.00386.x.

Sellés, D., Gardeweg, M., 2017. Geología del área Ascotán-Cerro Inacaliri, Región de Antofagasta. Servicio Nacional de Geología y Minería, Carta Geológica de Chile, Serie Geología Básica 190:73 p., 1 mapa escala 1:100.000. Santiago, Chile.

Sellés, D., Gardeweg, M., 2017. Geología del área Ascotán-Cerro Inacaliri, Región de Antofagasta. Servicio Nacional de Geología y Minería, Carta Geológica de Chile, Serie Geología Básica 190:73p., 1 mapa escala 1:100.000. Santiago, Chile.

Stern, C.R., 1991. Role of subduction erosion in the generation of Andean magmas. Geology, 19(1):78-81. https://doi.org/10.1130/0091-7613(1991)019<0078:ROSEIT>2.3.CO;2.

Stern, C. R., 2004. Active Andean volcanism: its geologic and tectonic setting. Revista geológica de Chile, 31(2):161-206. https://doi.org/10.4067/S0716-02082004000200001.

Streck, M.J., 2008. Mineral textures and zoning as evidence for open system processes. Reviews in Mineralogy and Geochemistry, 69:595-622. https://doi.org/10.2138/rmg.2008.69.15.

Sun, S.-S., McDonough, W.F., 1989. Chemical and isotopic systematics of oceanic basalts: implications for mantle composition and processes. Geological Society, London, Special Publications, 42(1):313-345. https://doi.org/10.1144/GSL.SP.1989.042.01.19.

Taussi, M., Godoy, B., Piscaglia, F., Morata, D., Agostini, S., le Roux, P., González-Maurel, O., Gallmeyer, G., Menzies, A., Renzulli, A., 2019. The upper crustal magma plumbing system of the Pleistocene Apacheta-Aguilucho Volcanic Complex area (Altiplano-Puna, northern Chile) as inferred from the erupted lavas and their enclaves. Journal of Volcanology and Geothermal Research, 373:179-198. https://doi.org/10.1016/j.jvolgeores.2019.01.021.

Taylor, H.P., 1968. The oxygen isotope geochemistry of igneous rocks. Contributions to mineralogy and Petrology, 19(1):1-71. https://doi.org/10.1007/BF00371729.

Taylor, S.R., McLennan, S.M., 1988. The significance of the rare earths in geochemistry and cosmochemistry. Handbook on the physics and chemistry of rare earths, 11:485-578. https://doi.org/10.1016/S0168-1273(88)11011-8.

Tibaldi, A., Bistacchi, A., Pasquare, F.A., Vezzoli, L., 2006. Extensional tectonics and volcano lateral collapses: insights from Ollagüe volcano (Chile-Bolivia) and analogue modelling. Terra Nova, 18(4):282-289. https://doi.org/10.1111/j.1365-3121.2006.00691.x.

Tibaldi, A., Bonali, F.L., Corazzato, C., 2017. Structural control on volcanoes and magma paths from local-to orogen-scale: the Central Andes case. Tectonophysics 699:16-41. https://doi.org/10.1016/j.tecto.2017.01.005.

Tierney, C.R., Schmitt, A.K., Lovera, O.M., de Silva, S.L., 2016. Voluminous plutonism during volcanic quiescence revealed by thermochemical modeling of zircon. Geology, 44(8):683-686. https://doi.org/10.1130/G37968.1.

Troll, V.R., Chadwick, J.P., Ellam, R.M., Mc Donnell, S., Emeleus, C.H., Meighan, I.G., 2005. Sr and Nd isotope evidence for successive crustal contamination of Slieve Gullion ring-dyke magmas, Co. Armagh, Ireland. Geological Magazine, 142(6):659-668. https://doi.org/10.1017/S0016756805001068.

Trumbull, R.B., Riller, U., Oncken, O., Scheuber, E., Munier, K., Hongn, F., 2006. The time-space distribution of Cenozoic volcanism in the South-Central Andes: a new data compilation and some tectonic implications. In The Andes (pp. 29-43). Springer, Berlin, Heidelberg.

Valley, J.W., Kitchen, N., Kohn, M.J., Niendorf, C.R., Spicuzza, M.J., 1995. UWG-2, a garnet standard for oxygen isotope ratios: strategies for high precision and accuracy with laser heating. Geochimica et Cosmochimica Acta, 59(24):5223-5231. https://doi.org/10.1016/0016-7037(95)00386-X.

van Alderwerelt, B.M.E.D., 2017. Diverse monogenetic volcanism across the main arc of the Central Andes, northern Chile. Dissertation, Ph.D. Thesis, The University of Iowa (Iowa), U.S.A.

Wallace, P.J., Carmichael, I.S., 1999. Quaternary volcanism near the Valley of Mexico: implications for subduction zone magmatism and the effects of crustal thickness variations on primitive magma compositions. Contributions to Mineralogy and Petrology, 135(4):291-314. https://doi.org/10.1007/s004100050513.

Ward, K.M., Zandt, G., Beck, S.L., Christensen, D.H., McFarlin, H., 2014. Seismic imaging of the magmatic underpinnings beneath the Altiplano-Puna volcanic complex from the joint inversion of surface wave dispersion and receiver functions. Earth and Planetary Science Letters, 404:43-53. https://doi.org/10.1016/j.epsl.2014.07.022.

Watts, R.B., de Silva, S.L., de Rios, G.J., Croudace, I., 1999. Effusive eruption of viscous silicic magma triggered and driven by recharge: a case study of the Cerro Chascon-Runtu Jarita Dome Complex in Southwest Bolivia. Bulletin of Volcanology, 61(4):241-264. https://doi.org/10.1007/s004450050274.

Whitehouse, M.J., Nemchin, A.A., 2009. High precision, high accuracy measurement of oxygen isotopes in a large lunar zircon by SIMS. Chemical Geology, 261(1-2):32-42. https://doi.org/10.1016/j.chemgeo.2008.09.009.

Wörner, G., Hammerschmidt, K., Henjes-Kunst, F., Lezaun, J., Wilke, H., 2000. Geochronology (40Ar/39Ar, K-Ar and He-exposure ages) of Cenozoic magmatic rocks from northern Chile (18-22°S): Implications for magmatism and tectonic evolution of the central Andes. Revista Geologica de Chile, 27(2):205-240. https://doi.org/10.4067/S0716-02082000000200004.

Wörner, G., Mamani, M., Blum-Oeste, M., 2018. Magmatism in the Central Andes. Elements, 14(4):237-244. https://doi.org/10.2138/gselements.14.4.237.

Wörner, G., Moorbath, S., Horn, S., Entenmann, J., Harmon, R. S., Davidson, J. P., Lopez-Escobar, L. 1994. Large-and fine-scale geochemical variations along the Andean arc of northern Chile (17.5–22 S). In Tectonics of the southern Central Andes (pp. 77-92). Springer, Berlin, Heidelberg. https://doi.org/101007/978-3-642-77353-2_5

Zandt, G., Leidig, M., Chmielowski, J., Baumont, D., Yuan, X., 2003. Seismic detection and characterization of the Altiplano-Puna magma body, Central Andes. Pure and Applied Geophysics, 160(3):789-807. https://doi.org/10.1007/PL00012557.

Zen, E.A., 1986. Aluminum enrichment in silicate melts by fractional crystallization: some mineralogic and petrographic constraints. Journal of Petrology, 27 (5):1095-1117. https://doi.org/10.1093/petrology/27.5.1095.

Appendix A. Supplementary data

Supplementary material 1: Geochemical and isotopic data

Table S1. New whole-rock major and trace element data, and Sr and Nd isotope ratios of the volcanic rocks from the studied volcanoes.

	Pliocene							
Volcano	Chela					Palpana		
Sample	CHE-01	CHE-02	CHE-03	CHE-04	CHE-05	PAL-01	PAL-02	PAL-03
Latitude	21º 24' 17"	21º 24' 18"	21º 24' 17"	21º 22' 37"	21º 22' 30"	21º 30' 56"	21º 30' 55"	21º 30' 47"
Longitude	68º 26' 58"	68º 26' 58"	68º 26' 59"	68º 26' 54"	68º 26' 52"	68º 28' 23"	68º 28' 21"	68º 28' 15"
Major oxides (wt%)								
SiO_2	56.65	55.81	54.61	56.49	57.83	61.57	57.21	58.79
TiO_2	0.85	0.85	0.90	0.81	0.85	0.84	0.86	0.83
Al_2O_3	17.07	17.59	17.91	17.07	16.79	16.81	16.77	17.16
Fe_2O_3	6.80	7.27	8.00	7.48	6.54	5.67	6.87	6.20
MnO	0.10	0.11	0.11	0.11	0.09	0.07	0.09	0.08
MgO	3.83	3.97	3.86	4.11	3.90	2.23	3.82	3.24
CaO	6.56	6.97	7.35	6.54	6.34	4.88	6.32	6.05
Na_2O	3.72	3.88	3.97	3.87	4.02	4.36	4.02	4.23
K_2O	1.98	1.75	1.41	1.84	1.74	2.60	1.76	1.96
P_2O_5	0.24	0.25	0.26	0.24	0.25	0.24	0.25	0.26
SO_3	b.d.	b.d.	0.01	b.d.	0.04	b.d.	0.03	0.01
Cr_2O_3	0.01	0.01	b.d.	0.01	0.01	b.d.	0.01	0.01
NiO	0.01	0.01	0.01	0.01	0.01	0.01	0.01	0.01
H_2O-	0.16	0.14	0.15	0.15	0.16	0.09	0.16	0.06
LOI	0.95	0.42	0.47	0.35	0.76	0.37	0.91	0.35
Total	98.92	99.04	99.00	99.09	99.36	99.73	99.10	99.25
FeO*[a]	6.12	6.54	7.20	6.73	5.89	5.10	6.18	5.58
Mg#[b]	53	52	49	52	54	44	52	51
Trace elements (ppm)								
Li	12.1	9.28	13.0	10.7	11.3	14.7	12.2	12.2
Sc	16.1	17.3	15.4	15.2	11.7	7.62	12.3	11.0
V	163	174	235	159	145	125	158	98
Cr	83	97	34	73	94	37	101	83
Co	27	29	28	31	29	23	29	28
Ni	18.8	23	13.1	24	42	14.7	35	29
Cu	71	67	69	60	62	57	64	70
Zn	94	100	93	93	95	94	98	86
Rb	45	40	25	39	35	78	40	47
Sr	728	666	793	593	614	570	632	615
Y	13.3	14.5	15.6	14.2	11.6	13.6	13.3	12.5
Zr	129	118	118	135	131	180	132	137
Nb	5.21	4.70	4.71	5.00	5.58	7.82	5.50	5.83
Ba	712	628	858	662	966	905	760	764
La	18.7	17.0	15.5	17.4	17.8	27	18.8	21
Ce	38	35	33	36	39	57	40	46
Pr	4.76	4.50	4.25	4.58	4.63	6.39	4.82	5.12
Nd	19.2	18.6	18.2	18.8	19.4	26	20	21
Sm	3.75	3.74	3.80	3.78	3.95	4.93	3.91	4.05
Eu	1.02	1.05	1.06	1.02	0.950	1.06	1.02	0.986
Gd	3.09	3.32	3.57	3.34	3.07	3.57	3.45	3.08
Tb	0.454	0.479	0.522	0.478	0.418	0.480	0.474	0.422
Dy	2.51	2.77	2.96	2.79	2.26	2.58	2.57	2.35
Ho	0.480	0.532	0.576	0.538	0.403	0.463	0.474	0.430
Er	1.34	1.48	1.59	1.48	1.06	1.23	1.26	1.15
Tm	0.191	0.207	0.214	0.210	0.145	0.168	0.174	0.157
Yb	1.19	1.33	1.34	1.33	0.904	1.11	1.11	1.01
Lu	0.192	0.224	0.214	0.220	0.139	0.171	0.172	0.155
Hf	3.09	2.93	2.95	3.29	3.47	4.68	3.48	3.63
Ta	0.319	0.285	0.284	0.305	0.332	0.494	0.326	0.345
Pb	9.29	8.25	6.99	8.38	7.98	11.7	8.19	6.94
Th	3.43	2.51	1.88	3.03	3.03	7.33	3.59	4.39
U	0.721	0.532	0.460	0.641	0.587	1.60	0.777	0.773
$^{87}Sr/^{86}Sr$	0.705698	0.705553	0.705541	0.705681	0.705948	0.706085	0.705730	0.705708
$\pm 2\sigma$ (10^{-6})	13	11	10	16	12	13	11	10
$^{143}Nd/^{144}Nd$	0.512445	0.512465	0.512513	0.512476	0.512408	0.512389	0.512426	0.512434
$\pm 2\sigma$ (10^{-6})	14	19	50	16	20	12	11	24

Table S1. Continued.

	Pliocene						
Volcano	Cerro Carcote				Araral		
Sample	CAR-01	CAR-02	CAR-03	CAR-04	ARA-01	ARA-04	ARA-10
Latitude	21º 26' 23"	21º 26' 21"	21º 26' 19"	21º 26' 20"	21º 39' 18"	21º 35' 3"	21º 38' 9"
Longitude	68º 23' 15"	68º 23' 13"	68º 23' 22"	68º 23' 23"	68º 12' 21"	68º 13' 54"	68º 14' 35"
Major oxides (wt%)							
SiO_2	56.05	59.23	58.60	55.14	61.64	58.80	61.12
TiO_2	1.06	0.99	0.97	0.98	0.70	0.62	0.70
Al_2O_3	16.72	16.87	16.75	16.45	15.74	14.72	15.93
Fe_2O_3	7.43	6.55	6.64	7.60	5.35	4.87	5.50
MnO	0.11	0.08	0.09	0.11	0.08	0.08	0.08
MgO	4.17	3.04	3.05	4.99	2.59	2.70	2.94
CaO	6.59	5.57	5.69	7.11	4.89	6.83	5.04
Na_2O	3.76	4.28	4.08	3.48	3.49	3.27	3.62
K_2O	1.92	2.41	2.44	2.29	3.07	2.88	2.97
P_2O_5	0.31	0.26	0.26	0.22	0.19	0.18	0.19
SO_3	0.07	0.01	0.02	0.01	0.02	1.18	0.01
Cr_2O_3	0.02	0.01	0.01	0.03	0.01	0.01	0.01
NiO	0.01	0.01	0.01	0.01	0.01	0.01	0.01
H_2O-	0.19	0.03	0.17	0.15	0.24	0.60	0.22
LOI	0.78	-0.13	0.52	0.68	1.09	2.38	0.70
Total	99.20	99.20	99.30	99.24	99.11	99.14	99.04
FeO*[a]	6.69	5.90	5.98	6.84	4.81	4.38	4.95
Mg#[b]	53	48	48	57	49	52	51
Trace elements (ppm)							
Li	10.9	13.9	11.0	12.3	31	24	22
Sc	12.9	9.30	9.97	19.2	15.6	10.4	10.7
V	163	141	149	178	115	113	129
Cr	130	51	74	217	57	70	92
Co	26	28	24	28	19.4	14.3	22
Ni	24	9.36	18.9	39	14.6	17.2	22
Cu	44	45	43	41	21	24	22
Zn	106	111	105	93	118	78	82
Rb	35	57	66	54	233	103	109
Sr	718	603	595	503	725	458	418
Y	14.3	12.4	13.5	16.9	27	14.7	15.8
Zr	148	182	173	153	140	140	146
Nb	6.78	7.85	7.87	6.84	7.89	8.10	8.35
Ba	2705	796	850	688	1016	720	679
La	22	28	28	23	50	27	27
Ce	46	58	57	47	79	54	54
Pr	5.86	6.89	6.81	5.73	10.7	6.24	6.19
Nd	24	27	27	23	40	24	24
Sm	4.71	5.03	4.97	4.47	7.16	4.43	4.50
Eu	1.17	1.26	1.25	1.18	1.45	0.937	0.988
Gd	4.07	4.02	4.01	3.92	5.82	3.60	3.73
Tb	0.552	0.525	0.540	0.561	0.854	0.527	0.569
Dy	2.90	2.64	2.75	3.22	4.58	2.83	3.04
Ho	0.533	0.473	0.515	0.642	0.886	0.567	0.618
Er	1.38	1.20	1.31	1.76	2.53	1.61	1.69
Tm	0.202	0.170	0.175	0.253	0.358	0.232	0.240
Yb	1.19	0.986	1.06	1.61	2.24	1.46	1.57
Lu	0.190	0.161	0.167	0.256	0.350	0.230	0.244
Hf	3.64	4.36	4.16	3.73	3.92	3.88	4.03
Ta	0.453	0.520	0.526	0.480	0.732	0.725	0.795
Pb	7.18	9.48	9.95	6.66	17.8	13.9	14.4
Th	3.11	5.13	5.41	4.70	30	14.0	15.6
U	0.976	1.27	1.38	1.21	8.27	7.11	5.65
$^{87}Sr/^{86}Sr$	0.706280	0.706434	0.706444	0.706104	0.707597	0.707490	0.707111
$\pm 2\sigma$ (10^{-6})	12	9	10	11	11	10	10
$^{143}Nd/^{144}Nd$	0.512376	0.512314	0.512368	0.512407	0.512325	0.512322	0.512366
$\pm 2\sigma$ (10^{-6})	19	37	18	15	22	25	20

Table S1. Continued.

	Pliocene			*Quaternary*				
Volcano	Ascotán			Cordón Inacaliri	Cerro La Quebrada	Licancabur	Juriques	
Sample	ASC-01	ASC-04	ASC-06	INA-01	QUE-01	LIC-01	JUR-01	JUR-05
Latitude	21º 41' 25"	21º 41' 49"	21º 41' 32"	21º 55' 2"	22º 24' 52"	22º 52' 35"	22º 53' 7"	22º 52' 51"
Longitude	68º 10' 6"	68º 9' 54"	68º 9' 59"	68º 5' 32"	67º 57' 10"	68º 1' 33"	67º 48' 45"	67º 48' 33"
Major oxides (wt%)								
SiO_2	63.24	63.21	61.67	62.54	57.75	58.99	55.45	53.16
TiO_2	0.65	0.64	0.74	0.70	0.71	1.11	1.09	1.11
Al_2O_3	15.79	15.46	16.01	15.99	14.80	17.16	18.37	17.60
Fe_2O_3	4.77	4.78	5.45	5.06	7.24	6.50	7.96	8.94
MnO	0.07	0.07	0.08	0.08	0.12	0.09	0.13	0.14
MgO	2.38	2.32	2.80	2.73	5.82	1.74	3.10	4.95
CaO	4.30	4.15	4.83	4.64	6.92	6.27	8.12	8.50
Na_2O	3.31	3.11	3.49	3.86	2.48	3.35	3.22	3.00
K_2O	3.40	3.63	2.81	2.99	2.05	2.55	1.55	1.31
P_2O_5	0.19	0.18	0.19	0.21	0.14	0.27	0.28	0.26
SO_3	0.01	0.00	b.d.	b.d.	0.01	0.01	b.d.	b.d.
Cr_2O_3	b.d.	b.d.	0.01	0.01	0.06	b.d.	b.d.	0.01
NiO	0.01	0.01	0.01	0.01	0.01	0.01	0.01	0.01
H_2O-	0.24	0.28	0.18	0.06	0.35	0.22	0.13	0.03
LOI	1.06	1.10	0.99	0.00	0.82	0.79	0.11	-0.16
Total	99.40	98.95	99.24	98.86	99.26	99.07	99.50	98.85
FeO*[a]	4.29	4.30	4.90	4.55	6.51	5.85	7.16	8.05
Mg#[b]	50	49	50	52	61	35	44	52
Trace elements (ppm)								
Li	21	22	17.1	28	16.7	15.5	11.7	9.13
Sc	8.90	9.25	9.95	9.23	25	13.3	23	25
V	115	120	135	112	174	175	224	232
Cr	52	51	68	93	383	1.62	21	72
Co	20	18.7	21	28	50	29	25	48
Ni	11.0	9.72	15.0	26	30	17.5	2.90	12.2
Cu	27	21	41	37	19.2	20	13.9	17.2
Zn	96	98	95	83	87	93	95	107
Rb	128	135	98	137	86	87	49	39
Sr	426	390	435	482	304	436	498	465
Y	16.4	16.8	14.6	16.4	22	30	32	27
Zr	154	151	151	177	94	201	134	126
Nb	8.29	8.48	7.87	10.0	7.02	11.1	8.07	8.01
Ba	797	782	676	742	452	614	409	361
La	30	31	26	30	20	29	18.8	17.9
Ce	61	61	56	67	45	63	42	41
Pr	7.24	7.38	6.41	7.04	4.94	7.26	5.02	4.85
Nd	28	28	25	27	20	30	22	21
Sm	5.22	5.28	4.77	4.99	4.08	6.42	5.09	4.95
Eu	1.02	1.01	1.02	0.910	0.893	1.29	1.20	1.15
Gd	4.18	4.21	3.82	3.62	3.94	5.29	4.78	4.47
Tb	0.603	0.621	0.559	0.516	0.596	0.809	0.769	0.703
Dy	3.23	3.31	2.95	2.95	3.52	4.87	4.97	4.39
Ho	0.611	0.643	0.566	0.553	0.712	0.949	1.03	0.891
Er	1.74	1.75	1.55	1.55	2.01	2.67	3.06	2.58
Tm	0.246	0.247	0.220	0.221	0.295	0.377	0.446	0.370
Yb	1.45	1.53	1.35	1.47	1.98	2.48	2.98	2.44
Lu	0.229	0.234	0.203	0.232	0.311	0.384	0.477	0.385
Hf	4.30	4.23	4.17	4.78	2.81	5.38	3.63	3.40
Ta	0.717	0.747	0.646	0.932	0.627	0.778	0.553	0.512
Pb	19.0	19.4	15.3	15.3	12.7	14.2	10.3	7.89
Th	11.8	12.5	9.80	20	11.0	9.20	4.50	3.89
U	3.84	4.06	3.09	5.73	2.75	2.24	1.09	0.803
$^{87}Sr/^{86}Sr$	0.708409	0.708746	0.707796	0.706583	0.708329	0.707843	0.707563	0.707893
$\pm 2\sigma$ (10^{-6})	13	10	11	14	11	16	12	11
$^{143}Nd/^{144}Nd$	0.512242	0.512208	0.512276	0.512337	0.512306	0.512311	0.512318	0.512332
$\pm 2\sigma$ (10^{-6})	17	16	13	13	16	10	16	12

Table S1. Continued.

	Quaternary								
Volcano	Paniri					Apacheta		La Poruñita	
Sample	PANI-01	PANI-03	PANI-05	PANI-14	PANI-15	APA-01	APA-02	PORU-01	PORU-02
Latitude	21º 59' 50"	22º 1' 27"	22º 2' 31"	21º 59' 56"	22º 0' 32"	21º 50' 42"	21º 50' 45"	21º 19' 15"	21º 19' 18"
Longitude	68º 17' 37"	68º 17' 18"	68º 15' 26"	68º 17' 41"	68º 10' 49"	68º 11' 8"	68º 7' 27"	68º 17' 39"	68º 17' 38"
Major oxides (wt%)									
SiO_2	57.96	56.64	56.04	56.94	56.14	54.78	59.49	55.49	55.56
TiO_2	0.83	0.82	0.86	0.80	0.95	0.77	0.78	1.14	1.11
Al_2O_3	16.54	17.90	16.87	16.01	17.58	17.59	16.82	16.69	16.82
Fe_2O_3	6.19	6.80	7.06	5.92	7.50	6.32	5.72	7.77	7.63
MnO	0.09	0.11	0.11	0.09	0.11	0.13	0.10	0.11	0.11
MgO	3.01	3.03	4.09	3.03	3.50	3.09	2.21	4.28	4.14
CaO	5.99	6.60	7.37	7.23	6.92	7.00	5.36	6.66	6.63
Na_2O	3.49	3.97	3.49	3.26	3.33	3.24	3.17	3.73	3.72
K_2O	2.44	2.00	1.91	2.38	1.96	2.27	3.12	1.97	1.98
P_2O_5	0.22	0.21	0.21	0.26	0.22	0.22	0.29	0.25	0.24
SO_3	0.02	0.01	0.22	0.04	0.02	0.18	0.03	0.01	0.00
Cr_2O_3	0.01	b.d.	0.01	0.01	0.01	b.d.	b.d.	0.01	0.01
NiO	0.01	0.01	0.01	0.01	0.02	0.01	0.01	0.01	0.01
H_2O-	0.23	0.11	0.23	0.23	0.15	0.82	-0.05	0.18	0.21
LOI	1.95	0.46	1.02	2.53	0.65	2.59	2.17	0.85	0.83
Total	98.96	98.66	99.51	98.73	99.05	99.02	99.21	99.14	99.00
FeO*[a]	5.57	6.12	6.35	5.32	6.75	5.69	5.14	6.99	6.86
Mg#[b]	49	47	53	50	48	49	43	52	52
Trace elements (ppm)									
Li	30	17.6	17.5	31	16.6	11.8	10.7	13.4	16.3
Sc	15.3	11.2	19.6	10.8	17.9	18.7	13.0	12.8	12.1
V	150	169	179	134	198	164	130	187	182
Cr	51	15.1	55	73	39	32	6.87	86	90
Co	17.1	20	23	13.9	22	21	20	25	23
Ni	11.0	17.6	18.7	14.0	12.3	15.1	6.99	10.2	12.8
Cu	31	29	42	29	47	34	22	30	43
Zn	95	86	92	86	88	87	109	114	116
Rb	103	49	56	64	65	123	203	32	31
Sr	569	499	599	389	436	643	720	484	478
Y	21	13.8	17.3	16.3	23	22	29	17.2	16.5
Zr	174	133	131	169	163	129	169	157	162
Nb	9.58	7.30	7.28	9.34	9.23	6.82	10.3	8.75	8.79
Ba	702	518	579	597	564	624	939	763	796
La	30	17.9	20	24	24	22	43	23	24
Ce	61	40	42	52	50	42	76	50	53
Pr	7.38	4.58	5.38	5.83	6.05	5.21	9.84	6.25	6.43
Nd	29	18.2	22	23	24	21	37	25	26
Sm	5.51	3.62	4.36	4.55	4.93	4.17	6.88	5.28	5.27
Eu	1.30	0.968	1.15	1.03	1.11	1.05	1.45	1.39	1.33
Gd	4.62	3.08	3.75	3.86	4.53	3.91	6.03	4.52	4.42
Tb	0.704	0.481	0.572	0.537	0.671	0.630	0.904	0.628	0.632
Dy	3.86	2.71	3.22	3.17	4.11	3.76	4.97	3.55	3.43
Ho	0.761	0.554	0.650	0.584	0.816	0.831	1.01	0.647	0.631
Er	2.09	1.55	1.78	1.68	2.32	2.47	2.88	1.77	1.65
Tm	0.301	0.223	0.248	0.224	0.331	0.372	0.411	0.233	0.218
Yb	1.95	1.45	1.64	1.54	2.19	2.37	2.58	1.48	1.34
Lu	0.305	0.226	0.261	0.229	0.344	0.382	0.403	0.234	0.220
Hf	4.81	3.69	3.59	4.48	4.32	3.41	4.60	4.17	4.15
Ta	0.654	0.509	0.483	0.621	0.624	0.519	0.937	0.715	0.626
Pb	14.4	10.4	10.3	11.0	9.56	9.93	19.0	8.00	10.8
Th	10.1	4.86	5.00	8.50	8.51	5.70	21	3.13	3.30
U	2.35	1.24	1.09	3.28	2.30	1.18	5.51	0.864	0.835
$^{87}Sr/^{86}Sr$	0.707539	0.706229	0.706690	0.707656	0.707348	0.706574	0.707097	0.706408	0.706481
$\pm 2\sigma$ (10^{-6})	13	14	11	10	10	11	11	13	11
$^{143}Nd/^{144}Nd$	0.512337	0.512406	0.512374	0.512338	0.512359	0.512413	0.512359	0.512344	0.512341
$\pm 2\sigma$ (10^{-6})	12	14	14	13	15	17	18	12	9

Table S1. Continued.

	Quaternary							
Volcano	San Pedro					La Poruña		
Sample	SPE-01	SPE-02	SPE-07	SPE-09	SPE-10	POR-01	POR-02	POR-03
Latitude	21º 54' 22"	21º 56' 5"	21º 51' 51"	21º 53' 13"	21º 53' 11"	21º 53' 10"	21º 53' 28"	21º 53' 32"
Longitude	68º 30' 3"	68º 30' 38"	68º 29' 58"	68º 27' 28"	68º 27' 39"	68º 30' 3"	68º 30' 1"	68º 29' 58"
Major oxides (wt%)								
SiO_2	57.59	62.84	55.28	55.75	55.17	56.41	56.66	56.52
TiO_2	0.75	0.80	0.97	0.89	0.88	0.78	0.78	0.76
Al_2O_3	15.94	15.49	17.16	16.18	16.20	16.16	16.09	15.72
Fe_2O_3	6.97	5.17	7.54	7.51	7.58	7.21	7.15	7.12
MnO	0.11	0.08	0.11	0.11	0.11	0.12	0.11	0.11
MgO	5.32	2.25	4.30	5.52	5.50	5.48	5.42	5.84
CaO	6.28	4.34	7.12	6.99	7.10	6.55	6.72	6.60
Na_2O	3.49	4.03	3.54	3.59	3.57	3.49	3.61	3.61
K_2O	1.98	3.11	1.77	1.67	1.55	1.61	1.76	1.77
P_2O_5	0.24	0.25	0.24	0.24	0.23	0.22	0.22	0.19
SO_3	0.04	0.05	0.01	0.01	0.07	0.04	0.03	0.02
Cr_2O_3	0.04	0.01	0.01	0.03	0.03	0.05	0.04	0.05
NiO	0.01	0.01	0.01	0.01	0.01	0.02	0.01	0.02
H_2O-	0.17	0.11	0.15	0.07	0.11	0.20	0.15	0.09
LOI	0.73	0.77	0.53	0.59	0.67	0.72	0.48	0.31
Total	99.67	99.31	98.73	99.15	98.80	99.08	99.22	98.73
FeO*[a]	6.27	4.66	6.78	6.75	6.82	6.49	6.44	6.41
Mg#[b]	60	46	53	59	59	60	60	62
Trace elements (ppm)								
Li	16.3	23	11.5	7.24	11.6	14.1	31	13.0
Sc	16.8	9.06	16.2	17.1	18.3	18.1	30	16.3
V	158	132	187	181	184	168	176	166
Cr	276	63	68	251	267	341	358	380
Co	28	12.4	21	25	27	26	29	30
Ni	70	12.8	23	54	57	71	68	80
Cu	77	48	34	35	37	49	71	39
Zn	92	85	104	101	101	97	140	91
Rb	50	94	36	30	31	39	96	39
Sr	494	469	615	541	558	531	885	465
Y	15.7	17.9	17.6	15.2	15.4	15.1	23	14.0
Zr	143	189	132	123	121	129	135	126
Nb	6.51	9.90	7.24	6.64	6.53	6.27	6.46	5.98
Ba	635	843	650	557	550	586	725	564
La	19.2	28	19.4	16.9	16.9	17.5	24	16.4
Ce	40	58	41	36	36	38	44	36
Pr	4.96	7.03	5.19	4.65	4.68	4.63	5.88	4.36
Nd	20.0	27	21	19.5	19.6	19.0	24	17.8
Sm	4.04	5.26	4.58	4.13	4.15	3.95	4.78	3.71
Eu	0.993	1.10	1.22	1.08	1.09	1.01	1.22	0.964
Gd	3.46	4.16	4.02	3.48	3.52	3.29	4.04	3.10
Tb	0.529	0.625	0.617	0.531	0.536	0.509	0.634	0.473
Dy	2.98	3.40	3.38	2.92	2.97	2.83	3.65	2.65
Ho	0.609	0.673	0.671	0.586	0.598	0.586	0.771	0.546
Er	1.69	1.86	1.80	1.61	1.64	1.64	2.22	1.54
Tm	0.244	0.266	0.247	0.225	0.232	0.239	0.326	0.223
Yb	1.60	1.74	1.57	1.45	1.49	1.54	2.19	1.45
Lu	0.251	0.273	0.243	0.227	0.232	0.252	0.360	0.230
Hf	4.00	5.36	3.66	3.41	3.37	3.40	3.65	3.36
Ta	0.414	0.667	0.433	0.390	0.388	0.463	0.428	0.425
Pb	11.7	17.8	9.85	8.82	8.97	11.4	21	9.46
Th	3.93	7.62	2.76	2.26	2.17	3.39	5.05	3.39
U	0.992	1.86	0.628	0.487	0.455	0.728	0.791	0.712
$^{87}Sr/^{86}Sr$	0.706181	0.706464	0.706662	0.706693	0.706672	0.706492	0.706418	0.706223
$\pm 2\sigma$ (10^{-6})	11	10	10	10	11	13	12	13
$^{143}Nd/^{144}Nd$	0.512431	0.512378	0.512372	0.512370	0.512374	0.512414	0.512420	0.512419
$\pm 2\sigma$ (10^{-6})	18	20	18	20	14	12	9	9

Table S1. Continued.

	Quaternary						
Volcano	La Poruña						
Sample	POR-04	POR-05	POR-06	POR-07	POR-08	POR-09	POR-10
Latitude	21º 55' 30"	21º 53' 42"	21º 53' 38"	21º 53' 27"	21º 53' 27"	21º 53' 22"	21º 53' 20"
Longitude	68º 28' 14"	68º 30' 31"	68º 30' 15"	68º 30' 39"	68º 30' 38"	68º 29' 56"	68º 29' 55"
Major oxides (wt%)							
SiO_2	59.03	56.28	55.61	55.87	55.78	56.80	57.06
TiO_2	0.68	0.71	0.75	0.86	0.87	0.79	0.78
Al_2O_3	16.01	15.63	15.98	16.14	16.33	16.14	16.00
Fe_2O_3	6.17	6.17	7.59	7.35	7.52	7.16	7.04
MnO	0.10	0.09	0.12	0.11	0.11	0.11	0.11
MgO	4.41	4.09	6.08	5.48	5.52	5.39	5.19
CaO	5.89	5.85	7.10	6.91	6.97	6.77	6.39
Na_2O	4.01	3.91	3.54	3.54	3.51	3.59	3.40
K_2O	2.07	2.04	1.69	1.70	1.55	1.71	1.67
P_2O_5	0.20	0.21	0.19	0.23	0.25	0.21	0.27
SO_3	0.02	0.02	0.06	0.03	0.02	0.03	0.03
Cr_2O_3	0.04	0.03	0.05	0.03	0.03	0.04	0.04
NiO	0.01	0.01	0.01	0.01	0.02	0.02	0.01
H_2O-	0.08	0.12	0.15	0.15	0.26	0.17	0.34
LOI	0.71	0.72	0.66	0.67	0.91	0.33	1.08
Total	99.42	95.88	99.59	99.09	99.65	99.27	99.41
FeO*[a]	5.56	5.56	6.83	6.61	6.76	6.44	6.33
Mg#[b]	59	57	61	60	59	60	59
Trace elements (ppm)							
Li	19.5	13.3	14.6	13.6	13.3	13.4	18.5
Sc	17.0	12.5	22	17.9	15.6	16.5	17.1
V	145	150	185	185	173	165	161
Cr	270	182	341	239	221	322	299
Co	25	24	29	28	26	26	27
Ni	43	36	62	58	52	67	62
Cu	50	40	41	37	46	43	81
Zn	91	85	94	101	100	91	99
Rb	67	38	41	32	24	35	41
Sr	655	452	514	539	456	456	496
Y	14.7	13.3	15.9	14.8	14.8	14.6	16.4
Zr	138	140	120	126	127	127	128
Nb	6.27	6.55	5.67	6.79	6.78	6.08	6.23
Ba	690	612	545	566	592	581	668
La	21	17.8	15.8	16.6	16.3	16.4	18.9
Ce	41	38	33	36	37	36	40
Pr	5.12	4.57	4.18	4.58	4.64	4.39	5.03
Nd	20	18.4	17.2	19.2	19.2	17.8	20
Sm	3.93	3.72	3.63	4.05	4.10	3.73	4.14
Eu	0.991	0.948	0.963	1.07	1.04	0.961	1.01
Gd	3.16	3.05	3.19	3.45	3.57	3.33	3.73
Tb	0.485	0.468	0.498	0.524	0.505	0.482	0.521
Dy	2.70	2.59	2.91	2.90	2.89	2.79	3.02
Ho	0.547	0.526	0.611	0.581	0.559	0.542	0.589
Er	1.53	1.46	1.77	1.60	1.50	1.52	1.69
Tm	0.227	0.210	0.257	0.225	0.211	0.219	0.243
Yb	1.49	1.37	1.71	1.46	1.36	1.45	1.54
Lu	0.236	0.214	0.277	0.228	0.209	0.224	0.244
Hf	3.70	3.75	3.32	3.38	3.41	3.35	3.41
Ta	0.400	0.403	0.361	0.393	0.444	0.410	0.408
Pb	17.0	9.59	9.32	9.18	8.83	8.88	11.8
Th	5.24	4.04	3.56	2.38	2.68	3.51	4.15
U	1.01	0.796	0.713	0.506	0.659	0.769	0.973
$^{87}Sr/^{86}Sr$	0.706036	0.706441	0.706361	0.706626	0.706679	0.706380	0.706422
$\pm 2\sigma$ (10^{-6})	17	10	12	17	12	11	11
$^{143}Nd/^{144}Nd$	0.512423	0.512444	0.512419	0.512395	0.512385	0.512423	0.512397
$\pm 2\sigma$ (10^{-6})	12	13	17	22	14	14	11

[a] Total Fe as Fe^{2+}.

[b] Mg# = 100*((MgO/40.30)/((MgO/40.30) + (FeO*/71.84))).

b.d., below detection limit.

LOI, loss on ignition. Negative values of LOI represent weight gain by oxidation.

Supplementary material 2: Baseline isotopic values

Table S2.1. Compilation of silica contents and Sr and Nd radiogenic isotope compositions of Pliocene and Quaternary lavas erupted at the western border of the Altiplano-Puna Magma Body. New data presented in bold.

Sample	Volcano	SiO_2	$^{87}Sr/^{86}Sr$	± 2σ (10^{-6})	$^{143}Nd/^{144}Nd$	± 2σ (10^{-6})	Reference
Pliocene							
ARA-04	**Araral**	**58.80**	**0.707490**	**10**	**0.512322**	**25**	**this work, Chapter 2**
ARA-10	**Araral**	**61.12**	**0.707111**	**10**	**0.512366**	**20**	**this work, Chapter 2**
ARA-01	**Araral**	**61.64**	**0.707597**	**11**	**0.512325**	**22**	**this work, Chapter 2**
ASC-06	**Ascotán**	**61.67**	**0.707796**	**11**	**0.512276**	**13**	**this work, Chapter 2**
ASC-04	**Ascotán**	**63.21**	**0.708746**	**10**	**0.512208**	**16**	**this work, Chapter 2**
ASC-01	**Ascotán**	**63.24**	**0.708409**	**13**	**0.512242**	**17**	**this work, Chapter 2**
CEB5	Cebollar	61.57	0.705724				Mamani et al. (2008)
CAR-04	**Cerro Carcote**	**55.14**	**0.706104**	**11**	**0.512407**	**15**	**this work, Chapter 2**
CAR-01	**Cerro Carcote**	**56.05**	**0.706280**	**12**	**0.512376**	**19**	**this work, Chapter 2**
CAR-03	**Cerro Carcote**	**58.60**	**0.706444**	**10**	**0.512368**	**18**	**this work, Chapter 2**
CAR-02	**Cerro Carcote**	**59.23**	**0.706434**	**9**	**0.512314**	**37**	**this work, Chapter 2**
PUN1	Cerro Carcote	56.54	0.705560				Wörner et al. (1994)
CAR1	Cerro Carcote	58.06	0.706240				Wörner et al. (1994)
CHE8	Chela	57.08	0.705610				Mamani et al. (2008)
CHE-03	**Chela**	**54.61**	**0.705541**	**10**	**0.512513**	**50**	**this work, Chapter 2**
CHE-02	**Chela**	**55.81**	**0.705553**	**11**	**0.512465**	**19**	**this work, Chapter 2**
CHE-04	**Chela**	**56.49**	**0.705681**	**16**	**0.512476**	**16**	**this work, Chapter 2**
CHE-01	**Chela**	**56.65**	**0.705698**	**13**	**0.512445**	**14**	**this work, Chapter 2**
CHE-05	**Chela**	**57.83**	**0.705948**	**12**	**0.512408**	**20**	**this work, Chapter 2**
CUEV1	Cerro de las Cuevas	52.95	0.705585				Mamani et al. (2008)
CUEV4	Cerro de las Cuevas	59.74	0.705912				Mamani et al. (2008)
VM99-16	Miño	57.01	0.705543	8	0.512408	2	Walker (2011)
PAL4	Palpana	58.07	0.705537				Mamani et al. (2008)
PAL-02	**Palpana**	**57.21**	**0.705730**	**11**	**0.512426**	**11**	**this work, Chapter 2**
PAL-03	**Palpana**	**58.79**	**0.705708**	**10**	**0.512434**	**24**	**this work, Chapter 2**
PAL-01	**Palpana**	**61.57**	**0.706085**	**13**	**0.512389**	**12**	**this work, Chapter 2**
Quaternary							
AA-047	Apacheta	56.22	0.706579	8	0.512392	19	Taussi et al. (2019)
APA-01	**Apacheta**	**54.78**	**0.706574**	**11**	**0.512413**	**17**	**this work, Chapter 2**
APA-02	**Apacheta**	**59.49**	**0.707097**	**11**	**0.512359**	**18**	**this work, Chapter 2**
AP2-00-71	Aucanquilcha	59.03	0.706212	8	0.512261	28	Walker (2011)
AP2-00-77	Aucanquilcha	60.21	0.706793	15	0.512277	2	Walker (2011)
AP2-00-75	Aucanquilcha	63.70	0.706405	23	0.512345	13	Walker (2011)
Cda_1_4	Cerro del Azufre	58.10	0.706510		0.512440		Trumbull et al. (1999)
CO33	Cerro Overo	52.69	0.706242	12			van Alderwerelt (2017)
CO06	Cerro Overo	54.34	0.706239	16			van Alderwerelt (2017)
CO23	Cerro Overo	56.04	0.706382	1			van Alderwerelt (2017)
COR-98-72	Colorado	62.40	0.708019		0.512225		Mamani et al. (2008)
COR-98-87	Colorado	63.10	0.708249		0.512256		Mamani et al. (2008)
INA-01	**Cordón Inacaliri**	**62.54**	**0.706583**	**14**	**0.512337**	**13**	**this work, Chapter 2**
JUR-05	**Juriques**	**53.16**	**0.707893**	**11**	**0.512332**	**12**	**this work, Chapter 2**
JUR-01	**Juriques**	**55.45**	**0.707563**	**12**	**0.512318**	**16**	**this work, Chapter 2**
64	La Poruña	58.10	0.706450				Francis et al. (1974)
POR 14 01	La Poruña	55.95	0.706640	8	0.512393	12	Godoy et al. (2017)
POR 15 04	La Poruña	56.79	0.706272	12	0.512450	12	Godoy et al. (2017)
POR 15 03	La Poruña	57.23	0.706353	13	0.512421	13	Godoy et al. (2017)
POR 15 02	La Poruña	57.85	0.706265	11	0.512427	11	Godoy et al. (2017)
POR 16 02	La Poruña	58.35	0.706244	8	0.512436	8	Godoy et al. (2017)
POR 15 06	La Poruña	58.74	0.706318	14	0.512425	12	Godoy et al. (2017)
POR 15 05	La Poruña	58.74	0.706184	10	0.512437	12	Godoy et al. (2017)
POR 16 01	La Poruña	58.90	0.706284	13	0.512412	9	Godoy et al. (2017)
POR 17 01	**La Poruña**	**57.07**	**0.706369**	**9**	**0.512413**	**11**	**This work, Chapter 3**
POR 17 02	**La Poruña**	**58.61**	**0.706334**	**12**	**0.512405**	**16**	**This work, Chapter 3**
POR 17 05	**La Poruña**	**58.75**	**0.706247**	**13**	**0.512432**	**16**	**This work, Chapter 3**
POR 17 03	**La Poruña**	**58.89**	**0.706202**	**11**	**0.512435**	**11**	**This work, Chapter 3**

Table S2.1. Continued.

Sample	Volcano	SiO_2	$^{87}Sr/^{86}Sr$	± 2σ (10^{-6})	$^{143}Nd/^{144}Nd$	± 2σ (10^{-6})	Reference
Quaternary							
POR-06	**La Poruña**	**55.61**	**0.706441**	**10**	**0.512444**	**13**	**this work, Chapter 2**
POR-08	**La Poruña**	**55.78**	**0.706679**	**12**	**0.512385**	**14**	**this work, Chapter 2**
POR-07	**La Poruña**	**55.87**	**0.706626**	**17**	**0.512395**	**22**	**this work, Chapter 2**
POR-05	**La Poruña**	**56.28**	**0.706361**	**12**	**0.512419**	**17**	**this work, Chapter 2**
POR-01	**La Poruña**	**56.41**	**0.706492**	**13**	**0.512414**	**12**	**this work, Chapter 2**
POR-03	**La Poruña**	**56.52**	**0.706223**	**13**	**0.512419**	**9**	**this work, Chapter 2**
POR-02	**La Poruña**	**56.66**	**0.706418**	**12**	**0.512420**	**9**	**this work, Chapter 2**
POR-09	**La Poruña**	**56.80**	**0.706380**	**11**	**0.512423**	**14**	**this work, Chapter 2**
POR-10	**La Poruña**	**57.06**	**0.706422**	**11**	**0.512397**	**11**	**this work, Chapter 2**
POR-04	**La Poruña**	**59.03**	**0.706036**	**17**	**0.512423**	**12**	**this work, Chapter 2**
SP-001	La Poruña	56.42	0.706630				Wörner et al. (1994)
PORU2	La Poruñita	60.52	0.706710		0.512269		Mamani et al. (2008)
PORU-01	**La Poruñita**	**55.49**	**0.706408**	**13**	**0.512344**	**12**	**this work, Chapter 2**
PORU-02	**La Poruñita**	**55.56**	**0.706481**	**11**	**0.512341**	**9**	**this work, Chapter 2**
QUE-01	**Cerro La Quebrada**	**57.75**	**0.708329**	**11**	**0.512306**	**16**	**this work, Chapter 2**
LAS-98-48	Lascar	57.50	0.7071	13	0.51244	29	Mamani et al. (2008)
LAS-98-49	Lascar	58.70	0.7064	1	0.51241	5	Mamani et al. (2008)
LAS 07-12	Lascar	55.29	0.7061	11			Mamani et al. (2010)
LAS 07-16	Lascar	56.86	0.7066	12			Mamani et al. (2010)
LAS 07-08	Lascar	57.39	0.7057	11			Mamani et al. (2010)
LAS 07-22	Lascar	57.73	0.7057	18			Mamani et al. (2010)
LAS 07-07	Lascar	58.02	0.7057	12			Mamani et al. (2010)
LAS 07-23	Lascar	58.43	0.7063	11			Mamani et al. (2010)
LAS 07-26	Lascar	58.46	0.7063	12			Mamani et al. (2010)
LA143	Lascar	55.52	0.705981				Matthews et al. (1994)
LA124	Lascar	56.19	0.706242		0.512468		Matthews et al. (1994)
LA141	Lascar	57.17	0.705947		0.512436		Matthews et al. (1994)
LA123	Lascar	57.32	0.705765		0.51247		Matthews et al. (1994)
LA136	Lascar	58	0.706148				Matthews et al. (1994)
LA102	Lascar	58.3	0.706352				Matthews et al. (1994)
L31	Licancabur	55.69	0.707916		0.512318		Figueroa et al. (2009)
L4	Licancabur	56.74	0.707599		0.512321		Figueroa et al. (2009)
L24	Licancabur	58.74	0.707756				Figueroa et al. (2009)
LIC-98-12	Licancabur	60.40	0.707729		0.512270		Mamani et al. (2008)
LIC-98-37	Licancabur	60.80	0.707859		0.512264		Mamani et al. (2008)
LIC-98-11	Licancabur	60.90	0.707999		0.512428		Mamani et al. (2008)
LIC-01	**Licancabur**	**58.99**	**0.707843**	**16**	**0.512311**	**10**	**this work, Chapter 2**
OLA9017	Ollagüe	52.90	0.706321				Feeley and Davidson (1994)
BA1	Ollagüe	52.90	0.706321				Feeley and Davidson (1994)
OLA9019	Ollagüe	54.50	0.706279		0.512335		Feeley and Davidson (1994)
BA2	Ollagüe	54.50	0.706279		0.512335		Feeley and Davidson (1994)
OLA9031	Ollagüe	58.60			0.512246		Feeley and Davidson (1994)
OLA32	Ollagüe	53.09	0.707130				Mamani et al. (2008)
OLA14	Ollagüe	56.38	0.706690				Mamani et al. (2008)
OLA23	Ollagüe	60.41	0.707420				Mamani et al. (2008)
OLA3	Ollagüe	61.57	0.707330				Mamani et al. (2008)
OLA29	Ollagüe	61.65	0.707759				Mamani et al. (2008)
OLA25	Ollagüe	62.08	0.707739				Mamani et al. (2008)
OLA21	Ollagüe	62.12	0.707320				Mamani et al. (2008)
OLA13	Ollagüe	62.15	0.706910		0.512263		Mamani et al. (2008)
OLA1	Ollagüe	62.41	0.707059				Mamani et al. (2008)
OLA17	Ollagüe	62.70	0.707440				Mamani et al. (2008)
OLA26	Ollagüe	63.23	0.708099				Mamani et al. (2008)
OLA24	Ollagüe	63.37	0.707459				Mamani et al. (2008)
OLA19	Ollagüe	63.46	0.707640				Mamani et al. (2008)
OLA11	Ollagüe	63.79	0.707660				Mamani et al. (2008)
SC2	Ollagüe	58.08	0.706826		0.512300		Mattioli et al. (2006)

Table S2.1. Continued.

Sample	Volcano	SiO_2	$^{87}Sr/^{86}Sr$	± 2σ (10^{-6})	$^{143}Nd/^{144}Nd$	± 2σ (10^{-6})	Reference
Quaternary							
BG SPL 022	Paniri	55.45	0.706676	6	0.512279	6	Godoy et al. (2018)
MJL-103-M1	Paniri	56.16	0.706675	12	0.512392	15	Godoy et al. (2018)
PANI 16 01	Paniri	56.43	0.706699	11	0.512374	11	Godoy et al. (2018)
PANI-05	**Paniri**	**56.04**	**0.706690**	**11**	**0.512374**	**14**	**this work, Chapter 2**
PANI-15	**Paniri**	**56.14**	**0.707348**	**10**	**0.512359**	**15**	**this work, Chapter 2**
PANI-03	**Paniri**	**56.64**	**0.706229**	**14**	**0.512406**	**14**	**this work, Chapter 2**
PANI-14	**Paniri**	**56.94**	**0.707656**	**10**	**0.512338**	**13**	**this work, Chapter 2**
PANI-01	**Paniri**	**57.96**	**0.707539**	**13**	**0.512337**	**12**	**this work, Chapter 2**
PUT-98-44-2	Putana	59.80	0.708209		0.512271		Mamani et al. (2008)
N3L	Sairecabur	56.67	0.708000				Deruelle (1982)
N3M	Sairecabur	58.76	0.708000				Deruelle (1982)
N3K	Sairecabur	58.87	0.708000				Deruelle (1982)
N3H	Sairecabur	59.41	0.708010				Deruelle (1982)
SAI-98-42-B	Sairecabur	61.50	0.708099		0.512256		Mamani et al. (2008)
SAI-98-40	Sairecabur	62.60	0.708239		0.512220		Mamani et al. (2008)
SAI-98-42	Sairecabur	63.00	0.708299		0.512215		Mamani et al. (2008)
186	San Pedro	56.20	0.706900				Francis et al. (1974)
184	San Pedro	62.50	0.706260				Francis et al. (1974)
61	San Pedro	63.00	0.706530				Francis et al. (1974)
284	San Pedro	63.10	0.706400				Francis et al. (1974)
166	San Pedro	63.90	0.706500				Francis et al. (1974)
SPSP 16 07	San Pedro	55.89	0.706718	11	0.512383	8	Godoy et al. (2017)
BG SPL 015	San Pedro	55.94	0.706306	9	0.512404	3	Godoy et al. (2017)
SPSP 16 06	San Pedro	56.16	0.706700	15	0.512383	13	Godoy et al. (2017)
BG SPL 010	San Pedro	56.29	0.706705	5			Godoy et al. (2017)
BG SPL 004	San Pedro	57.79	0.706149	4			Godoy et al. (2017)
SPSP 16 07	**San Pedro**	**55.89**	**0.706718**	**11**	**0.512383**	**9**	**This work, Chapter 3**
SPSP 16 06	**San Pedro**	**56.16**	**0.706700**	**15**	**0.512383**	**13**	**This work, Chapter 3**
SPSP 16 02	**San Pedro**	**61.89**	**0.706548**	**11**	**0.512431**	**14**	**This work, Chapter 3**
SPSP 16 08	**San Pedro**	**62.25**	**0.706432**	**13**	**0.512388**	**9**	**This work, Chapter 3**
SPSP 16 04	**San Pedro**	**62.71**	**0.706722**	**13**	**0.512362**	**11**	**This work, Chapter 3**
SPSP 16 01	**San Pedro**	**62.94**	**0.706388**	**12**	**0.512386**	**13**	**This work, Chapter 3**
SPSP 16 05	**San Pedro**	**63.46**	**0.706722**	**11**	**0.512372**	**13**	**This work, Chapter 3**
SPSP 16 03	**San Pedro**	**63.83**	**0.706388**	**11**	**0.512387**	**19**	**This work, Chapter 3**
SPP-98-56	San Pedro	62.90	0.705709		0.512346		Mamani et al. (2008)
SPP-98-54	San Pedro	63.00	0.706659		0.512351		Mamani et al. (2008)
SP1	San Pedro	56.42	0.706630		0.512378		Mamani et al. (2010)
7901	San Pedro	55.62	0.706444		0.512345		Rogers and Hawkesworth (1989)
176	San Pedro	57.60	0.705958		0.512429		Rogers and Hawkesworth (1989)
170	San Pedro	59.30	0.706296		0.512352		Rogers and Hawkesworth (1989)
172	San Pedro	63.40	0.706198		0.512351		Rogers and Hawkesworth (1989)
SPE-10	**San Pedro**	**55.17**	**0.706672**	**11**	**0.512374**	**14**	**this work, Chapter 2**
SPE-07	**San Pedro**	**55.28**	**0.706662**	**10**	**0.512372**	**18**	**this work, Chapter 2**
SPE-09	**San Pedro**	**55.75**	**0.706693**	**10**	**0.512370**	**20**	**this work, Chapter 2**
SPE-01	**San Pedro**	**57.59**	**0.706181**	**11**	**0.512431**	**18**	**this work, Chapter 2**
SPE-02	**San Pedro**	**62.84**	**0.706464**	**10**	**0.512378**	**20**	**this work, Chapter 2**
BG SPL 048	Toconce	57.31	0.707693	4	0.512296	1	Godoy et al. (2017)
TOC 14 001	Toconce	57.72	0.707771	11	0.512294	14	Godoy et al. (2017)

Table S2.2. Baseline isotopic value of each volcano in our compilation (Table S2.1). It was considered the least silicic sample and its Sr and Nd isotope ratios as baseline isotope composition. New data presented in bold.

	Sample	Volcano	SiO_2	$^{87}Sr/^{86}Sr$	± 2σ (10^{-6})	$^{143}Nd/^{144}Nd$	± 2σ (10^{-6})	Reference
	Pliocene							
1	VM99-16	Miño	57.01	0.705543	8	0.512408	2	Walker (2011)
2	**CHE-03**	**Chela**	**54.61**	**0.705541**	**10**	**0.512513**	**50**	**this work, Chapter 2**
3	**CAR-04**	**Cerro Carcote**	**55.14**	**0.706104**	**11**	**0.512407**	**15**	**this work, Chapter 2**
4	**PAL-02**	**Palpana**	**57.21**	**0.705730**	**11**	**0.512426**	**11**	**this work, Chapter 2**
5	**ARA-04**	**Araral**	**58.80**	**0.707490**	**10**	**0.512322**	**25**	**this work, Chapter 2**
6	CUEV1	Cerro de las Cuevas	52.95	0.705585				Mamani et al. (2008)
7	CEB5	Cebollar	61.57	0.705724				Mamani et al. (2008)
8	**ASC-06**	**Ascotán**	**61.67**	**0.707796**	**11**	**0.512276**	**13**	**this work, Chapter 2**
	Quaternary							
9	AP2-00-71	Aucanquilcha	59.03	0.706212	8	0.512261	28	Walker (2011)
10	OLA9017	Ollagüe	52.90	0.70632				Feeley and Davidson (1994)
11	**PORU-01**	**La Poruñita**	**55.49**	**0.706408**	**13**	**0.512344**	**12**	**this work, Chapter 2**
12	Cda_1_4	Cerro del Azufre	58.10	0.70651		0.512440		Trumbull et al. (1999)
13	**POR-06**	**La Poruña**	**55.61**	**0.706361**	**12**	**0.512419**	**17**	**this work, Chapter 2**
14	**SPE-10**	**San Pedro**	**55.17**	**0.706672**	**11**	**0.512374**	**14**	**this work, Chapter 2**
15	**APA-01**	**Apacheta**	**54.78**	**0.706574**	**11**	**0.512413**	**17**	**this work, Chapter 2**
16	**INA-01**	**Cordón Inacaliri**	**62.54**	**0.706583**	**14**	**0.512337**	**13**	**this work, Chapter 2**
17	BG SPL 022	Paniri	55.45	0.706676	6	0.512279	6	Godoy et al. (2018)
18	BG SPL 048	Toconce	57.31	0.707693	4	0.512296	1	Godoy et al. (2017)
19	DM58A2	Uturuncu	62.30	0.71129		0.512179		Michelfelder et al. (2013)
20	**QUE-01**	**Cerro La Quebrada**	**57.75**	**0.708329**	**11**	**0.512306**	**16**	**this work, Chapter 2**
21	PUT-98-44-2	Putana	59.80	0.70821		0.512271		Mamani et al. (2008)
22	COR-98-72	Colorado	62.40	0.70802		0.512225		Mamani et al. (2008)
23	N3L	Sairecabur	56.67	0.70800				Deruelle (1982)
24	L31	Licancabur	55.69	0.70792		0.512318		Figueroa et al. (2009)
25	**JUR-05**	**Juriques**	**53.16**	**0.707893**	**11**	**0.512332**	**12**	**this work, Chapter 2**
26	LAS 07-12	Lascar	55.29	0.7061	11			Mamani et al. (2010)
27	CO33	Cerro Overo	52.69	0.706242	12			van Alderwerelt (2017)

Supplementary material 3: Geochemical and isotopic data from La Poruña and San Pedro volcanoes

Table S3. New and published (Godoy et al., 2014, 2017) whole-rock major and trace element data, and Sr and Nd isotope ratios of the studied samples from La Poruña and San Pedro.

Volcano	La Poruña							
Sample	POR 10 01[a]	POR 14 01[b]	POR 15 02[b]	POR 15 03[b]	POR 15 04[b]	POR 15 05[b]	POR 15 06	POR 16 01
Latitude (S)	21° 53' 33"	21º 53' 27"	21º 53' 29"	21º 53' 32"	21º 53' 35"	21º 55' 32"	21º 53' 42"	21º 53' 38"
Longitude (W)	68° 29' 42"	68º 30' 39"	68º 29' 47"	68º 29' 58"	68º 30' 19"	68º 34' 2"	68º 30 39"	68º 30' 15"
Major oxides (wt%)								
SiO_2	57.52	55.95	57.85	57.23	56.79	58.74	58.74	58.90
TiO_2	0.78	0.86	0.75	0.78	0.75	0.68	0.75	0.73
FeO*[c]	6.24	6.70	6.32	6.48	6.52	5.59	5.73	5.58
Al_2O_3	16.21	16.35	16.16	16.26	15.89	15.93	16.39	16.42
MnO	0.11	0.11	0.10	0.11	0.11	0.09	0.10	0.10
MgO	5.29	5.49	5.74	5.57	6.11	4.51	4.39	4.12
CaO	6.39	6.98	6.46	6.77	6.66	5.91	6.11	5.96
Na_2O	3.75	3.70	3.72	3.63	3.55	3.87	3.97	3.89
K_2O	1.79	1.69	1.83	1.76	1.76	2.08	2.05	2.01
P_2O_5	0.19	0.22	0.19	0.20	0.19	0.19	0.21	0.20
SUM	98.27	98.06	99.13	98.79	98.34	97.61	98.44	97.90
Mg#[d]	60.19	59.36	61.82	60.50	62.55	59.00	57.75	56.81
Trace elements (ppm)								
XRF								
Ba	601	619	622	602	602	676	674	689
Cr	289	227	493	356	501	322	219	185
Ni	69	43	99	62	102	53	39	29
Rb	46	37	47	44	44	60	53	53
Sr	560	608	584	575	569	590	592	601
Zr	137	157	161	160	156	169	171	175
ICP-MS								
Nb	13.0	6.71	6.03	6.09	5.81	6.23	6.47	6.56
Cs	5.05							
Th	13.9	2.73	3.93	3.70	3.59	4.87	4.45	4.69
U	3.72	0.607	0.809	0.780	0.770	1.08	0.920	0.958
Ta	0.796	0.412	0.358	0.365	0.364	0.411	0.424	0.415
Pb	16.8	8.49	9.35	9.69	9.03	10.4	10.3	11.3
Hf	4.05	3.33	3.34	3.32	3.25	3.57	3.55	3.69
Y	16.9	15.4	14.2	15.0	13.6	12.4	12.8	12.9
La	37	16.6	16.5	16.5	15.1	16.6	18.3	18.8
Ce	58	36	35	36	33	37	38	40
Pr	7.11	4.55	4.27	4.35	4.04	4.24	4.59	4.71
Nd	27	18.9	17.3	17.8	16.6	16.9	18.2	18.8
Sm	5.00	3.85	3.45	3.64	3.38	3.30	3.64	3.71
Eu	1.02	1.04	0.939	0.973	0.888	0.830	0.926	0.934
Gd	4.30	0.488	0.455	0.478	0.445	0.418	0.478	0.482
Tb	0.556	3.64	3.23	3.40	3.05	2.92	3.27	3.34
Dy	3.19	3.04	2.69	2.90	2.64	2.44	2.79	2.84
Ho	0.569	0.556	0.512	0.541	0.504	0.467	0.530	0.540
Er	1.72	1.58	1.45	1.54	1.48	1.31	1.48	1.50
Tm	0.206	0.206	0.202	0.216	0.205	0.190	0.221	0.213
Yb	1.37	1.40	1.32	1.45	1.35	1.24	1.42	1.41
Lu	0.191	0.219	0.210	0.219	0.217	0.194	0.221	0.225
$^{87}Sr/^{86}Sr$	-	0.706640	0.706265	0.706353	0.706272	0.706184	0.706318	0.706284
$\pm 2\sigma$ (10^{-6})	-	0.000008	0.000110	0.000013	0.000012	0.000010	0.000014	0.000013
$^{143}Nd/^{144}Nd$	-	0.512393	0.512427	0.512421	0.512450	0.512437	0.512425	0.512412
$\pm 2\sigma$ (10^{-6})	-	0.000012	0.000011	0.000013	0.000012	0.000011	0.000012	0.000008

Table S3. Continued.

Volcano	La Poruña						San Pedro	
Sample	POR 16 02	POR 17 01	POR 17 02	POR 17 03	POR 17 04	POR 17 05	BG SPL 002A[a]	BG SPL 004[a]
Latitude (S)	21º 54' 26"	21º 53' 38"	21º 53' 47"	21º 53' 28"	21º 54' 55"	21º 54' 38"	21° 56' 5"	21° 54 '22"
Longitude (W)	68º 31' 22"	68º 29' 49"	68º 30' 28"	68º 31' 26"	68º 32' 25"	68º 33' 9"	68° 30' 38"	68° 30' 3"
Major oxides (wt%)								
SiO_2	58.35	57.07	58.61	58.89	59.62	58.75	62.61	57.79
TiO_2	0.68	0.79	0.73	0.66	0.65	0.73	0.71	0.76
FeO*[c]	5.73	6.41	5.75	5.50	5.42	5.69	3.74	6.38
Al_2O_3	15.92	16.20	16.27	16.01	16.06	16.11	17.18	15.75
MnO	0.10	0.11	0.10	0.09	0.10	0.10	0.06	0.11
MgO	4.81	5.49	4.57	4.59	4.34	4.52	1.67	5.87
CaO	6.26	6.75	6.32	5.89	5.60	5.97	4.97	6.44
Na_2O	3.76	3.75	3.81	3.79	3.86	3.95	4.27	3.63
K_2O	2.01	1.77	2.02	2.19	2.12	2.01	2.73	1.89
P_2O_5	0.18	0.21	0.20	0.19	0.20	0.20	0.26	0.20
SUM	97.81	98.55	98.39	97.82	97.97	98.04	98.20	98.82
Mg#[d]	59.94	60.43	58.62	59.80	58.78	58.57	44.30	62.12
Trace elements (ppm)								
XRF								
Ba	639	597	650	661	690	648	871	634
Cr	263	625	223	239	258	440	77	326
Ni	35	1078	35	32	45	792	18.0	90
Rb	57	45	52	60	63	55	84	51
Sr	561	575	589	568	583	588	567	523
Zr	165	162	167	168	174	172	209	146
ICP-MS								
Nb	5.99	6.24	6.20	6.06	6.20	6.33	10.1	7.27
Cs							2.33	1.32
Th	5.03	4.19	4.46	5.33	5.83	4.74	7.75	4.06
U	1.05	0.833	0.921	1.12	1.22	0.979	1.87	0.990
Ta	0.405	0.520	0.425	0.417	0.418	0.394	0.590	0.400
Pb	10.7	10.5	11.2	11.4	12.0	11.1	23	12.2
Hf	3.47	3.37	3.54	3.54	3.71	3.56	4.97	4.19
Y	12.9	15.6	13.1	12.3	12.5	12.9	16.7	14.9
La	18.2	19.1	18.6	18.4	19.6	18.8	33	22
Ce	38	39	39	38	40	40	56	38
Pr	4.50	4.82	4.63	4.49	4.73	4.68	6.76	4.62
Nd	17.9	19.4	18.4	17.8	18.4	18.7	27	19.5
Sm	3.56	4.02	3.69	3.46	3.52	3.69	5.29	3.97
Eu	0.917	1.05	0.952	0.862	0.895	0.955	1.11	0.910
Gd	0.464	0.542	0.478	0.451	0.459	0.481	4.70	3.83
Tb	3.23	3.57	3.37	3.06	3.16	3.33	0.580	0.490
Dy	2.73	3.13	2.84	2.62	2.68	2.78	3.37	2.96
Ho	0.539	0.605	0.549	0.515	0.512	0.539	0.620	0.580
Er	1.53	1.77	1.53	1.44	1.45	1.54	1.86	1.73
Tm	0.223	0.256	0.222	0.207	0.211	0.215	0.230	0.220
Yb	1.42	1.65	1.43	1.39	1.41	1.43	1.52	1.49
Lu	0.224	0.262	0.228	0.214	0.219	0.228	0.220	0.220
$^{87}Sr/^{86}Sr$	0.706244	0.706369	0.706334	0.706202	0.706176	0.706247	-	0.706149
$\pm 2\sigma$ (10^{-6})	0.000009	0.000009	0.000012	0.000011	0.000011	0.000014	-	0.000004
$^{143}Nd/^{144}Nd$	0.512436	0.512413	0.512405	0.512435	0.512417	0.512432	-	-
$\pm 2\sigma$ (10^{-6})	0.000008	0.000011	0.000016	0.000011	0.000011	0.000016	-	-

Table S3. Continued.

Volcano	San Pedro						
Sample	BG SPL 009[a]	BG SPL 010[a]	BG SPL 012[a]	BG SPL 015[a]	BG SPL 016[a]	SPSP 10 01[a]	SPSP 10 02[a]
Latitude (S)	21° 52' 12"	21° 50' 1"	21° 49' 55"	21° 53' 25"	21° 54' 2"	21° 49 '5"	21° 49' 52"
Longitude (W)	68° 30' 0"	68° 30' 1"	68° 28' 50"	68° 29' 33"	68° 28' 5"	68° 28' 0"	68° 29' 47"
Major oxides (wt%)							
SiO_2	60.99	56.29	63.57	55.94	58.97	63.15	62.00
TiO_2	0.67	0.95	0.68	0.75	0.72	0.63	0.69
FeO*[c]	4.18	6.54	4.18	6.60	4.41	4.00	4.34
Al_2O_3	16.52	16.90	15.82	15.83	15.26	16.12	16.84
MnO	0.08	0.10	0.07	0.11	0.07	0.07	0.09
MgO	1.62	4.28	2.39	6.03	2.61	2.14	1.72
CaO	4.27	7.00	4.17	6.72	4.42	4.36	4.47
Na_2O	4.26	3.57	4.26	3.60	3.83	4.15	4.36
K_2O	2.69	1.63	3.04	1.73	2.60	2.78	2.62
P_2O_5	0.22	0.23	0.19	0.17	0.20	0.17	0.22
SUM	95.50	97.50	98.36	97.48	93.08	97.56	97.34
Mg#[d]	40.83	53.84	50.50	61.97	51.34	48.84	41.41
Trace elements (ppm)							
XRF							
Ba	804	610	861	536	766	829	804
Cr	5.00	84	79	349	81	45	7.00
Ni	4.00	32	22	70	21	14.0	5.00
Rb	75	37	98	46	79	90	75
Sr	523	610	498	508	533	541	538
Zr	198	137	216	129	185	181	196
ICP-MS							
Nb	9.80	7.96	9.54	6.31	9.17	8.68	9.81
Cs	1.74	0.808	2.55	1.24	2.17	2.59	1.72
Th	6.97	3.00	8.38	4.35	7.29	8.17	6.86
U	1.65	0.664	2.06	0.892	1.79	1.99	1.64
Ta	0.557	0.421	0.574	0.343	0.563	0.537	0.545
Pb	14.6	9.32	15.1	8.86	15.0	14.9	14.4
Hf	5.19	3.59	4.84	3.42	4.57	3.31	5.27
Y	14.8	16.3	14.6	15.1	14.1	12.9	15.4
La	29	21	28	18.3	28	27	30
Ce	49	36	48	32	48	45	50
Pr	5.84	4.64	5.74	3.94	5.78	5.30	5.94
Nd	23	19.9	23	16.6	23	21	24
Sm	4.24	4.13	4.20	3.46	4.43	3.80	4.29
Eu	0.892	1.01	0.802	0.836	0.882	0.795	0.939
Gd	3.82	4.28	3.92	3.46	4.08	3.22	3.71
Tb	0.448	0.528	0.454	0.454	0.480	0.412	0.464
Dy	2.81	3.24	2.79	2.91	2.83	2.48	2.86
Ho	0.524	0.595	0.501	0.571	0.513	0.447	0.536
Er	1.59	1.71	1.50	1.74	1.52	1.35	1.63
Tm	0.205	0.216	0.188	0.236	0.193	0.168	0.211
Yb	1.39	1.39	1.28	1.60	1.27	1.12	1.45
Lu	0.203	0.199	0.181	0.232	0.184	0.157	0.209
$^{87}Sr/^{86}Sr$	-	0.706705	-	0.706306	-	-	-
$\pm 2\sigma$ (10^{-6})	-	0.000005	-	0.000009	-	-	-
$^{143}Nd/^{144}Nd$	-	-	-	0.512404	-	-	-
$\pm 2\sigma$ (10^{-6})	-	-	-	0.000003	-	-	-

Table S3. Continued.

Volcano	San Pedro						
Sample	SPSP 10 03[a]	SPSP 10 04[a]	SPSP 14 01[b]	SPSP 14 02[b]	SPSP 16 01	SPSP 16 02	SPSP 16 03
Latitude (S)	21° 50' 9"	21° 52' 21"	21º 49' 55"	21º 56' 3"	21º 51' 13"	21º 50' 58"	21° 49' 55"
Longitude (W)	68° 30' 6"	68° 29' 59"	68º 29' 48"	68º 30' 36"	68º 27' 12"	68º 27' 41"	68° 28' 50"
Major oxides (wt%)							
SiO_2	57.22	62.39	62.28	63.18	62.94	61.89	63.83
TiO_2	0.96	0.68	0.70	0.80	0.68	0.68	0.64
FeO*[c]	6.13	4.14	4.56	4.75	4.36	4.73	4.03
Al_2O_3	17.39	15.81	17.26	15.50	15.93	17.18	15.57
MnO	0.10	0.06	0.09	0.08	0.08	0.08	0.07
MgO	3.51	2.09	1.83	2.37	2.57	1.96	2.32
CaO	6.68	3.49	4.81	4.40	4.46	4.73	4.12
Na_2O	3.76	2.35	4.37	3.99	4.08	4.21	3.96
K_2O	1.77	2.86	2.66	3.16	2.90	2.74	3.02
P_2O_5	0.25	0.18	0.23	0.25	0.20	0.28	0.19
SUM	97.76	94.06	98.79	98.48	98.21	98.49	97.76
Mg#[d]	50.52	47.37	41.71	47.05	51.27	42.52	50.61
Trace elements (ppm)							
XRF							
Ba	641	769	836	894	878	826	865
Cr	47	43	59	119	103	35	87
Ni	24	15.0	5.50	19.6	13.8	1.63	11.6
Rb	44	93	75	103	92	71	99
Sr	638	433	584	489	539	626	503
Zr	158	179	223	247	232	225	229
ICP-MS							
Nb	8.52	8.92	8.63	10.2	8.31	8.36	8.69
Cs	0.787	2.72					
Th	3.98	9.26	5.96	8.61	6.55	5.05	6.14
U	0.721	2.31	1.47	2.19	1.62	1.03	1.55
Ta	0.418	0.582	0.662	0.649	0.638	0.579	0.612
Pb	10.5	15.9	13.6	16.2	15.2	12.6	15.2
Hf	4.19	4.86	4.73	5.12	4.70	4.69	4.45
Y	15.3	13.0	14.6	18.2	13.2	13.9	13.0
La	23	28	23	27	25	23	23
Ce	41	47	50	58	50	46	47
Pr	5.10	5.50	5.83	6.89	5.85	5.38	5.58
Nd	21	22	22	27	24	22	23
Sm	4.31	3.91	4.20	5.17	4.39	4.14	4.40
Eu	1.05	0.773	1.00	1.04	0.959	0.974	0.964
Gd	3.95	3.43	0.485	0.611	0.512	0.517	0.518
Tb	0.515	0.398	3.40	4.34	3.66	3.57	3.75
Dy	3.07	2.45	2.80	3.52	2.94	2.94	2.88
Ho	0.561	0.448	0.538	0.646	0.542	0.561	0.527
Er	1.66	1.35	1.52	1.80	1.50	1.59	1.44
Tm	0.204	0.173	0.223	0.258	0.210	0.229	0.202
Yb	1.37	1.17	1.47	1.65	1.40	1.50	1.33
Lu	0.188	0.171	0.236	0.253	0.213	0.242	0.212
$^{87}Sr/^{86}Sr$	-	-	0.706683	0.706414	0.706388	0.706548	0.706388
$\pm 2\sigma$ (10^{-6})	-	-	0.000011	0.000013	0.000012	0.000011	0.000011
$^{143}Nd/^{144}Nd$	-	-	0.512392	0.512384	0.512386	0.512431	0.512387
$\pm 2\sigma$ (10^{-6})	-	-	0.000011	0.000012	0.000013	0.000014	0.000019

Table S3. Continued.

Volcano	San Pedro				
Sample	SPSP 16 04	SPSP 16 05	SPSP 16 06	SPSP 16 07	SPSP 16 08
Latitude (S)	21º 50' 52"	21º 53' 10"	21º 53' 13"	21º 53' 11"	21° 54' 2"
Longitude (W)	68º 29' 07"	68º 27' 25"	68º 27' 28"	68º 27' 39"	68° 28' 5"
Major oxides (wt%)					
SiO_2	62.71	63.46	56.16	55.89	62.25
TiO_2	0.66	0.67	0.87	0.88	0.73
FeO*[c]	4.19	4.27	6.67	6.83	4.64
Al_2O_3	17.10	17.04	16.32	16.36	16.15
MnO	0.08	0.09	0.11	0.11	0.08
MgO	1.64	1.64	5.60	5.64	2.68
CaO	4.39	4.41	7.05	7.16	4.70
Na_2O	4.46	4.51	3.59	3.56	4.02
K_2O	2.69	2.72	1.67	1.67	2.71
P_2O_5	0.23	0.22	0.23	0.23	0.22
SUM	98.15	99.04	98.27	98.34	98.18
Mg#[d]	41.07	40.56	59.92	59.55	50.73
Trace elements (ppm)					
XRF					
Ba	845	837	610	596	838
Cr	14.5	35	259	269	120
Ni	<5	<5	49	47	18.2
Rb	77	79	35	35	85
Sr	556	551	609	604	578
Zr	231	229	157	155	219
ICP-MS					
Nb	8.93	8.86	6.85	6.84	8.46
Cs					
Th	5.81	6.26	2.40	2.20	6.59
U	1.56	1.63	0.480	0.441	1.66
Ta	0.587	0.561	0.429	0.419	0.559
Pb	15.9	16.2	9.52	8.68	14.7
Hf	4.93	4.86	3.24	3.23	4.53
Y	14.1	14.4	14.0	14.0	12.6
La	27	28	17.4	17.0	24
Ce	52	55	35	34	48
Pr	6.06	6.31	4.47	4.41	5.56
Nd	24	25	19.5	19.2	22
Sm	4.32	4.47	4.03	4.00	4.15
Eu	1.02	1.07	1.05	1.05	0.859
Gd	0.507	0.523	0.520	0.528	0.485
Tb	3.60	3.73	3.66	3.71	3.39
Dy	2.99	3.03	3.05	3.09	2.73
Ho	0.556	0.583	0.574	0.582	0.511
Er	1.59	1.61	1.61	1.64	1.41
Tm	0.228	0.234	0.224	0.229	0.198
Yb	1.54	1.56	1.47	1.47	1.32
Lu	0.247	0.243	0.229	0.231	0.203
$^{87}Sr/^{86}Sr$	0.706722	0.706722	0.706700	0.706718	0.706432
$\pm 2\sigma$ (10^{-6})	0.000013	0.000011	0.000015	0.000011	0.000013
$^{143}Nd/^{144}Nd$	0.512362	0.512372	0.512383	0.512383	0.512388
$\pm 2\sigma$ (10^{-6})	0.000011	0.000013	0.000013	0.000009	0.000009

[a] Data from Godoy et al. (2014). [b] Data from Godoy et al. (2017). [c] Total Fe as Fe^{2+}. [d] Mg# = 100*((MgO/40.51)/((MgO/40.51)+(FeO/71.85))).

Supplementary material 4: $^{40}Ar/^{39}Ar$ Analysis

Table S4.1. $^{40}Ar/^{39}Ar$ Step heating, and Isochron data for analyzed samples.

Sample: **POR 15 04** J= 0.0012637±0.0000002 (σ)

Step	Power (Watt)	^{40}Ar (mol)	^{40}Ar (fA)	±σ(fA)	^{39}Ar (mol)	^{39}Ar (fA)	±σ(fA)	^{38}Ar (fA)	±σ(fA)	^{37}Ar (fA)	±σ(fA)
A	0.4	6.94E-15	184.95	0.06	3.64E-16	9.71	0.03	0.27	0.02	0.12	0.03
B	0.5	2.61E-14	694.46	0.08	1.42E-15	37.97	0.04	1.20	0.02	0.52	0.03
C	0.6	6.51E-15	173.54	0.05	1.63E-15	43.31	0.03	1.05	0.02	0.79	0.03
D	0.8	4.61E-14	1228.33	0.11	2.27E-15	60.59	0.03	2.03	0.02	1.50	0.03
G	1.2	4.78E-14	1273.17	0.11	2.58E-15	68.75	0.04	2.15	0.02	2.01	0.03
F	1.5	2.95E-14	785.60	0.08	2.31E-15	61.69	0.04	1.67	0.02	2.01	0.03
G	1.9	2.48E-14	660.81	0.08	1.11E-15	29.58	0.03	0.98	0.02	1.31	0.03

Table S4.1. Continued.

Sample: **POR 15 04**

^{36}Ar (fA)	± σ(fA)	Age (ka)	±σ	Ca/K	±σ	Cl/K	±σ	(39/40)isoch	±%	(36/40)isoch	±%
0.628	0.001	-56	101	1.00	0.20	0.010	0.007	0.05256	0.35	0.003388	0.2
2.352	0.004	87	55	1.05	0.05	0.023	0.002	0.05472	0.1	0.003377	0.2
0.591	0.001	101	22	1.40	0.05	0.028	0.002	0.25046	0.08	0.003347	0.2
4.173	0.006	35	68	1.91	0.03	0.024	0.001	0.04936	0.06	0.003382	0.1
4.326	0.006	87	61	2.25	0.03	0.021	0.001	0.05403	0.06	0.003377	0.1
2.675	0.004	102	45	2.52	0.03	0.020	0.001	0.07856	0.06	0.003372	0.2
2.251	0.004	40	84	3.41	0.07	0.020	0.002	0.04476	0.12	0.003382	0.2

Table S4.1. Continued.

Sample: **POR 15 05** J= 0.0012608±0.0000002 (σ)

Step	Power (Watt)	^{40}Ar (mol)	^{40}Ar (fA)	±σ(fA)	^{39}Ar (mol)	^{39}Ar (fA)	±σ(fA)	^{38}Ar (fA)	±σ(fA)	^{37}Ar (fA)	±σ(fA)
A	0.4	5.34E-15	142.40	0.05	5.55E-16	14.78	0.03	0.41	0.02	0.24	0.03
B	0.5	5.93E-15	158.08	0.05	1.76E-15	46.94	0.03	1.19	0.02	0.54	0.03
C	0.6	3.89E-15	103.69	0.05	2.42E-15	64.51	0.04	1.51	0.02	0.91	0.03
D	0.8	3.48E-15	92.68	0.05	3.07E-15	81.74	0.03	2.05	0.02	1.37	0.02
E	1.2	6.88E-15	183.40	0.05	3.89E-15	103.81	0.04	2.57	0.02	2.43	0.02
F	1.5	1.80E-15	47.87	0.05	5.91E-16	15.75	0.03	0.45	0.02	0.58	0.03
G	1.9	1.14E-15	30.39	0.05	4.89E-16	13.03	0.03	0.38	0.02	0.69	0.02

Table S4.1. Continued.

Sample: **POR 15 05**

^{36}Ar (fA)	± σ(fA)	Age (ka)	±σ	Ca/K	±σ	Cl/K	±σ	(39/40)isoch	±%	(36/40)isoch	±%
0.482	0.001	124	58	1.23	0.14	0.028	0.004	0.10389	0.21	0.003365	0.3
0.534	0.001	117	21	0.89	0.04	0.032	0.001	0.2974	0.08	0.003333	0.3
0.351	0.001	119	12	1.09	0.03	0.029	0.001	0.62334	0.08	0.003275	0.3
0.320	0.001	97	9	1.31	0.02	0.035	0.001	0.88398	0.07	0.003259	0.3
0.635	0.001	113	10	1.83	0.02	0.033	0.001	0.56691	0.05	0.00329	0.2
0.166	0.001	143	35	2.88	0.13	0.043	0.004	0.32929	0.22	0.003315	0.5
0.109	0.001	164	48	4.13	0.15	0.440	0.005	0.42893	0.27	0.003281	0.9

Table S4.1. Continued.

Sample: **SPSP 16 01** J= 0.0013873±0.0000003 (σ)

Step	Power (Watt)	^{40}Ar (mol)	^{40}Ar (fA)	±σ(fA)	^{39}Ar (mol)	^{39}Ar (fA)	±σ(fA)	^{38}Ar (fA)	±σ(fA)	^{37}Ar (fA)	±σ(fA)
A	0.3	3.10E-15	82.50	0.05	4.24E-16	11.30	0.03	0.28	0.02	0.08	0.03
B	0.5	3.01E-15	80.12	0.05	1.09E-15	29.07	0.03	0.54	0.02	0.14	0.03
C	0.7	3.47E-15	92.49	0.05	1.66E-15	44.31	0.04	0.78	0.02	0.27	0.03
D	0.9	6.08E-15	162.01	0.05	1.57E-15	41.82	0.03	0.76	0.02	0.29	0.03
E	1.2	7.47E-15	198.94	0.06	3.25E-15	86.58	0.04	1.49	0.02	0.66	0.03
F	1.5	8.46E-15	225.51	0.06	3.20E-15	85.20	0.04	1.47	0.02	0.66	0.03
G	1.9	2.04E-15	54.44	0.05	4.32E-15	115.20	0.04	1.86	0.02	1.02	0.03
H	2.3	1.34E-15	35.64	0.05	4.91E-15	130.74	0.04	2.14	0.02	1.18	0.03
I	2.8	6.06E-16	16.15	0.05	1.98E-15	52.86	0.03	0.84	0.02	0.50	0.02

Table S4.1. Continued.

Sample: **SPSP 16 01**

^{36}Ar (fA)	± σ(fA)	Age (ka)	±σ	Ca/K	±σ	Cl/K	±σ	(39/40)isoch	±%	(36/40)isoch	±%
0.285	0.001	-281	77	0.60	0.20	0.024	0.006	0.13712	0.29	0.003436	0.4
0.273	0.001	-2	30	0.44	0.08	0.013	0.003	0.36348	0.13	0.003395	0.4
0.317	0.001	-9	22	0.55	0.06	0.012	0.002	0.48002	0.1	0.00339	0.4
0.553	0.002	-13	40	0.62	0.06	0.010	0.002	0.25856	0.09	0.003389	0.4
0.677	0.002	47	18	0.69	0.03	0.010	0.001	0.43599	0.05	0.003356	0.3
0.761	0.003	103	24	0.70	0.03	0.001	0.001	0.37844	0.05	0.003331	0.4
0.184	0.001	98	6.3	0.79	0.02	0.011	0.001	2.12565	0.1	0.003102	0.6
0.123	0.001	92.1	6.3	0.86	0.02	0.012	0.001	3.69449	0.15	0.002924	1.1
0.055	0.001	100	10	0.90	0.05	0.010	0.001	3.29513	0.32	0.002938	1.5

Table S4.2. $^{40}Ar/^{39}Ar$ Age Plateau results from Step Heating, and results of Inverse Isochron ages of analyzed samples by groundmass at SERNAGEOMIN Geochronological Laboratory (Chile).

Sample	Latitude (S)	Longitude (W)	Sample description	Age Plateau				
				Age (ka)	Error (2σ)	^{39}Ar (%)	n##	MSWD
POR 15 04	21º 53' 35"	68º 30' 19"	Western lava flow at the base of the scoria cone	**92**	**34**	**97**	**6/7**	**0.26**
POR 15 05	21º 55' 32"	68º 34' 2"	Western flank of the 8 km lava flow	**110**	**11**	**100**	**7/7**	**0.84**
SPSP 16 01	21º 51' 13"	68º 27' 12"	Upper north-western flank of San Pedro	**96**	**8**	**64**	**4/9**	**0.24**

Table S4.2. Continued

Inverse Isochron Analyses					
Age (ka)	Error (2σ)	n##	$^{40}Ar/^{36}Ar$ intercept	Error (2σ)	MSWD
111	56	6/7	295.2	0.5	0.27
94	22	7/7	296.6	1.5	0.90
94	12	4/9	296.0	2.6	0.28

Preferred ages are in bold.

Number of data points used in plateau and isochron calculations; each step heating represents one data point.

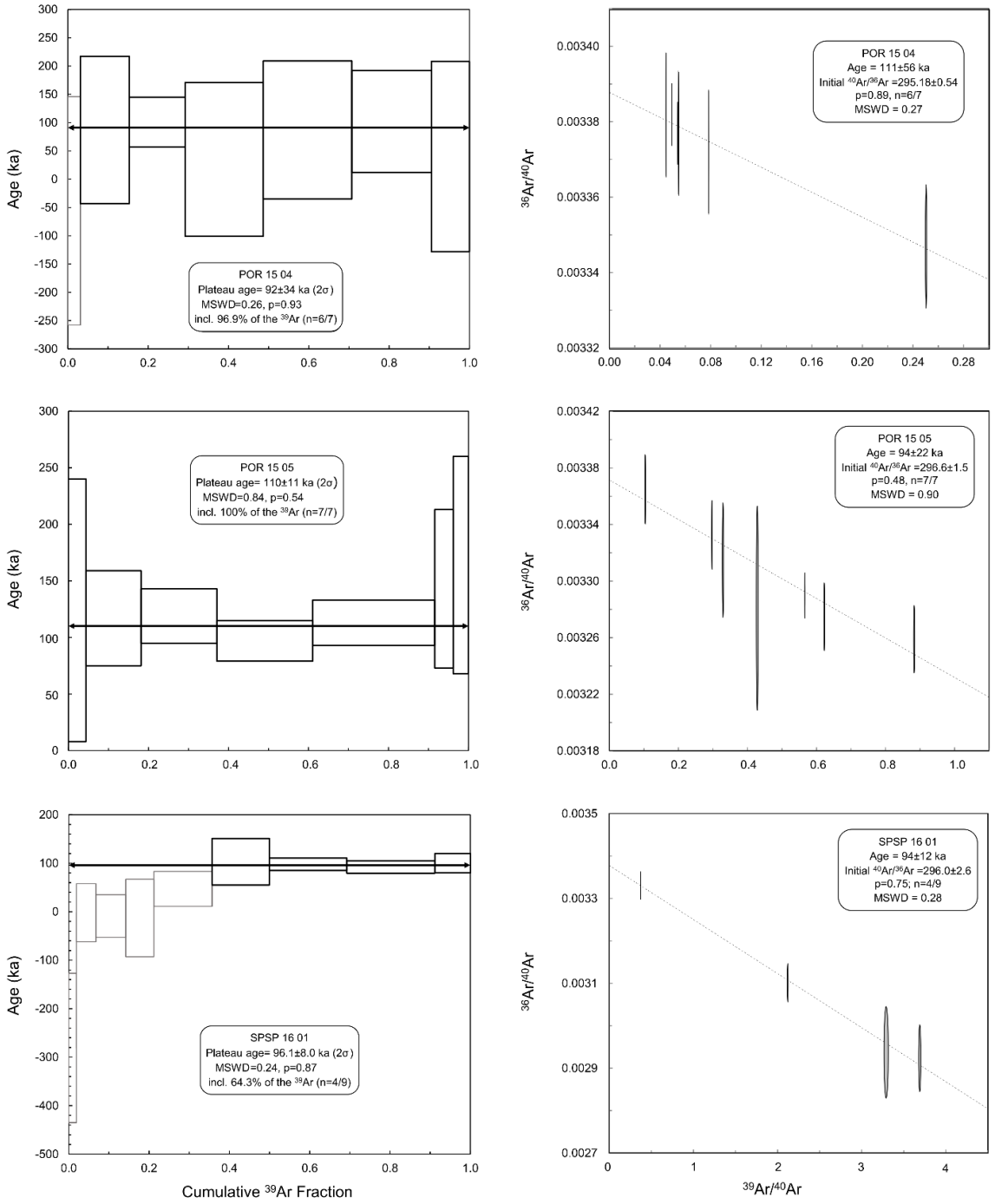

Figure S4. Age spectra and inverse isochron diagrams for analyzed samples. Box heights are 2σ error. Analytical error ellipses in isochron diagrams and initial $^{40}Ar/^{39}Ar$ ($^{40}Ar/^{39}Ar_i$) are at 2σ level. Light grey data in Plateau Ages indicate rejected analyses. MSWD = mean standard weighted deviates.

Supplementary material 5: Oxygen isotope data for the Central Andes

Table S5.1: Published mineral oxygen isotope data from Central Andean volcanoes obtained by SIMS, and conventional and laser fluorination analysis.

Phase	Method	Number of analysis	$\delta^{18}O‰$ range	$\delta^{18}O‰$ average	Reference
Olivine	Conventional fluorination	5	**5.7 - 6.1**	**5.9**	Entenmann (1994)
	Laser fluorination	14	**5.0 - 8.3**	**6.9**	Godoy (2014); Kay et al. (2011)
Pyroxene	Conventional fluorination	4	**6.8 - 7.2**	**7.1**	Entenmann (1994)
	Laser fluorination	35	**5.5 - 8.7**	**6.1**	Godoy (2014); Chang (2007); Freymuth et al. (2015)
Amphibole	Laser fluorination	28	**5.1 - 6.3**	**5.8**	Chang (2007); Freymuth et al. (2015)
Biotite	Conventional fluorination	1	**6.7**	**6.7**	Entenmann (1994)
Plagioclase	Conventional fluorination	4	**7.4 - 8.3**	**8.0**	Entenmann (1994)
	Laser fluorination	56	**6.5 - 8.1**	**7.4**	Chang (2007); Freymuth et al. (2015); Feeley and Sharp (1995)
Quartz	Conventional fluorination	5	**8.4 - 9.7**	**9.0**	Entenmann (1994)
	Laser fluorination	41	**7.8 - 14.6**	**9.1**	Kay et al. (2010; 2011); Chang (2007); Grocke et al. (2017); Lister (2019)
Zircon	SIMS	78	**5.9 - 9.7**	**6.5**	Kaiser (2014)
Magnetite	Conventional fluorination	4	**2.3 - 5.9**	**4.7**	Entenmann (1994)
	Laser fluorination	35	**2.2 - 4.8**	**3.8**	Chang (2007); Freymuth et al. (2015)
Groundmass	Conventional fluorination	7	**7.1 - 7.6**	**7.4**	Entenmann (1994)
Whole-rock	Conventional fluorination	93	**6.7 - 14.0**	**8.3**	Entenmann (1994); Davidson et al. (1990); Francis et al. (1989); Harmon et al. (1984); Longstaffe et al. (1983)
	Laser fluorination	15	**7.1 - 10.6**	**8.6**	Chang (2007); Freymuth et al. (2015); Feeley and Sharp (1995); Kay et al. (2010)

Table S5.2: Published oxygen isotope data in olivine from Central Andean volcanoes obtained by conventional and laser fluorination analysis.

Volcano	Sample	Rock type	$\delta^{18}O$‰	Reference
Conventional fluorination				
Parinacota	PAR-011	Basaltic andesite	5.9	Entenmann (1994)
	PAR-201	Andesite	5.7	Entenmann (1994)
	PAR-220	Mafic andesite	6.1	Entenmann (1994)
	PAR-223	Mafic andesite	6.1	Entenmann (1994)
	PAR-86	Andesite	5.9	Entenmann (1994)
Laser fluorination				
San Pedro	BG-SPL-004	Andesite	6.1	Godoy (2014)
	BG-SPL-010	Basaltic andesite	5.0	Godoy (2014)
Paniri	PANI-10-15	Andesite	6.9	Godoy (2014)
	BG-SPL-022	Basaltic andesite	7.1	Godoy (2014)
Cerro del León	BG-SPL-040	Andesite	6.5	Godoy (2014)
	LEO-10-01	Andesite	8.0	Godoy (2014)
	LEO-10-02	Andesite	7.0	Godoy (2014)
	LEO-10-07	Andesite	7.8	Godoy (2014)
Toconce	TOC-10-02	Andesite	8.3	Godoy (2014)
	TOC-10-04	Andesite	8.2	Godoy (2014)
	TOC-10-08	Dacite	6.3	Godoy (2014)
Cerro Galán	SAF32	Mafic lava	6.4	Kay et al. (2011)
	SAF24	Mafic lava	6.8	Kay et al. (2011)
	SAF76	Mafic lava	6.3	Kay et al. (2011)

Table S5.3: Published oxygen isotope data in pyroxene from Central Andean volcanoes obtained by conventional and laser fluorination analysis.

Volcano	Sample	Rock type	$\delta^{18}O$‰	Reference
Conventional fluorination				
Parinacota	PAR-011	Basaltic andesite	7.1	Entenmann (1994)
	PAR-201	Andesite	7.2	Entenmann (1994)
	PAR-223	Mafic andesite	7.2	Entenmann (1994)
	PAR-86	Andesite	6.8	Entenmann (1994)
Laser fluorination				
El Misti	MIS-02-02 PAS	Andesite	6.0	Chang (2007)
	MIS-02-05	Andesite	6.4	Chang (2007)
	MIS-02-06	Andesite	6.0	Chang (2007)
	MIS-02-10 a	Andesite	6.5	Chang (2007)
	MIS-02-107	Andesite	5.8	Chang (2007)
	MIS-02-109 plug	Andesite	6.1	Chang (2007)
	MIS-02-116	Andesite	6.2	Chang (2007)
	MIS-02-118	Andesite	5.7	Chang (2007)
	MIS-02-12	Andesite	6.8	Chang (2007)
	MIS-02-13	Andesite	6.1	Chang (2007)
	MIS-99-10A	Andesite	5.8	Chang (2007)
	MIS-99-10B	Andesite	6.5	Chang (2007)
Taapacá	TAP 97-29/1	Mafic inclusion	6.5	Chang (2007)
	TAP-87-002	Dacite	5.9	Chang (2007)
	TAP-97-06	Andesite	5.8	Chang (2007)
	TAP-97-22	Andesite	5.6	Chang (2007)
	TAP-97-28	Dacite	5.5	Chang (2007)
	TAP-97-29	Dacite	5.6	Chang (2007)
	TAP-97-34	Dacite	6.1	Chang (2007)
Cerro del León	LEO-10-01	Andesite	6.5	Godoy (2014)
Toconce	TOC-10-04	Andesite	8.7	Godoy (2014)
Lascar	LAS 07-01	Andesite	6.0	Freymuth et al. (2015)
	LAS 07-02	Andesite	6.2	Freymuth et al. (2015)
	LAS 07-05	Andesite	6.0	Freymuth et al. (2015)
	LAS 07-07	Andesite	6.1	Freymuth et al. (2015)
	LAS 07-08	Andesite	6.2	Freymuth et al. (2015)
	LAS 07-12	Andesite	5.8	Freymuth et al. (2015)
	LAS 07-16	Andesite	6.0	Freymuth et al. (2015)
	LAS 07-18A	Andesite	6.0	Freymuth et al. (2015)
	LAS 07-18B	Andesite	5.9	Freymuth et al. (2015)
	LAS 07-20	Andesite	6.2	Freymuth et al. (2015)
	LAS 07-22	Andesite	6.1	Freymuth et al. (2015)
	LAS 07-23	Andesite	5.7	Freymuth et al. (2015)
	LAS 07-26	Andesite	5.8	Freymuth et al. (2015)
	LAS 07-28	Andesite	6.0	Freymuth et al. (2015)

Supplementary material 6: O-isotope modelling

Supplementary Table S6: Mixing components for the end-member compositions of hypothetical mantle (M) (SiO_2 = 51 wt%; Sr = 113 ppm; $^{87}Sr/^{86}Sr$ = 0.703; $\delta^{18}O$ = 5.7‰; *after* Harmon et al., 1981; Ito et al., 1987; Hoffmann, 1988; Davidson et al., 1990; Harmon and Hoefs, 1995).

Component	SiO_2 (wt%)	Sr (ppm)	$^{87}Sr/^{86}Sr$	$\delta^{18}O$	Reference
C1	67	185	0.72777	11.8	Damm et al. (1990); Lucassen et al. (2001)
C2	70	200	0.71400	19.5	Davidson et al. (1990)
Sediments	70	300	0.71000	25	Eiler et al. (1997)

Supplementary material 7: Mineral compositional data

Table S7.1. Clinopyroxene core compositional data for La Poruña (Sample POR-06 and Mount 1651).

Sample	Major Oxides (wt%)													Wo	En	Fs
	SiO_2	TiO_2	Al_2O_3	FeO	MnO	MgO	CaO	Na_2O	K_2O	Cr_2O_3	NiO	V_2O_3	Total			
1651_X2_p3	50.73	0.73	2.97	8.20	0.21	15.27	20.91	0.32	0.00	0.02	0.04	0.04	99.44	43%	44%	13%
1651_X2_p4	50.14	0.74	3.21	8.03	0.22	14.74	20.95	0.37	0.01	0.05	0.04	0.07	98.58	44%	43%	13%
1651_X3_p5	50.56	0.57	3.34	6.37	0.22	16.29	20.74	0.30	0.01	0.47	0.01	0.01	98.89	43%	47%	10%
1651_X3_p6	50.42	0.78	3.18	8.09	0.18	15.13	21.26	0.36	0.00	0.01	0.00	0.00	99.43	44%	43%	13%
1651_X4_p7	52.19	0.41	2.36	6.25	0.17	15.80	21.85	0.31	0.00	0.38	0.04	0.00	99.77	45%	45%	10%
1651_X4_p8	50.86	0.59	2.43	7.79	0.22	15.39	21.04	0.31	0.00	0.05	0.05	0.03	98.76	43%	44%	13%
1651_X6_p11	50.47	0.73	3.07	8.20	0.22	14.89	21.31	0.30	0.01	0.04	0.01	0.03	99.28	44%	43%	13%
1651_X6_p12	51.41	0.50	1.99	8.08	0.21	15.55	20.68	0.24	0.00	0.03	0.00	0.03	98.70	43%	44%	13%
1651_X7_p13	51.66	0.41	1.75	7.77	0.27	15.69	21.13	0.28	0.00	0.00	0.01	0.02	98.99	43%	45%	12%
1651_X7_p14	51.66	0.38	1.63	7.54	0.28	15.82	20.86	0.31	0.00	0.00	0.00	0.02	98.51	43%	45%	12%
1651_X8_p15	51.36	0.45	2.04	7.85	0.19	15.60	20.67	0.33	0.00	0.00	0.01	0.02	98.52	43%	45%	13%
1651_X8_p16	51.55	0.50	2.13	8.00	0.26	15.78	20.80	0.29	0.01	0.01	0.05	0.02	99.41	42%	45%	13%
1651_X10_p20	50.78	0.42	3.03	6.48	0.20	15.54	21.33	0.47	0.01	0.47	0.07	0.06	98.86	44%	45%	11%
1651_X12_p23	50.32	0.61	2.94	8.41	0.26	13.83	22.28	0.35	0.00	0.01	0.00	0.02	99.04	46%	40%	14%
1651_X12_p24	51.29	0.56	2.38	7.78	0.29	14.79	21.55	0.34	0.00	0.02	0.08	0.03	99.12	45%	43%	13%
1651_X13_p25	50.43	0.71	2.46	9.98	0.31	14.34	19.94	0.48	0.01	0.18	0.03	0.06	98.93	42%	42%	16%
1651_X13_p26	50.06	0.84	2.97	10.17	0.30	14.17	19.95	0.42	0.00	0.35	0.00	0.10	99.33	42%	41%	17%
1651_X16_p31	51.96	0.51	1.87	8.10	0.31	15.87	20.78	0.29	0.01	0.00	0.08	0.02	99.81	42%	45%	13%
1651_X16_p32	51.64	0.46	1.85	7.78	0.31	15.85	20.80	0.33	0.01	0.00	0.02	0.02	99.07	43%	45%	12%
1651_X20_p39	50.68	0.84	3.40	8.66	0.14	14.78	21.24	0.36	0.00	0.03	0.04	0.08	100.24	44%	42%	14%
1651_X21_p41	51.33	0.50	2.29	8.27	0.27	15.71	20.20	0.30	0.00	0.01	0.05	0.02	98.96	42%	45%	13%
1651_X21_p42	51.36	0.51	2.38	8.13	0.17	15.78	20.69	0.33	0.00	0.00	0.00	0.07	99.44	42%	45%	13%
1651_X22_p44	51.85	0.44	1.91	7.83	0.22	15.60	21.21	0.29	0.00	0.02	0.07	0.02	99.46	43%	44%	12%
1651_X23_p45	50.81	0.72	2.97	8.03	0.22	14.77	21.83	0.34	0.00	0.00	0.06	0.01	99.76	45%	42%	13%
1651_X23_p46	52.11	0.43	1.87	7.45	0.16	15.48	21.47	0.29	0.00	0.00	0.00	0.02	99.28	44%	44%	12%
1651_X25_p49	51.91	0.33	1.25	10.45	0.35	14.08	20.46	0.41	0.00	0.04	0.03	0.06	99.37	42%	41%	17%
1651_X25_p50	50.20	0.84	3.38	8.27	0.20	14.88	21.37	0.32	0.01	0.04	0.02	0.02	99.54	44%	43%	13%
1651_X26_p51	51.01	0.70	2.99	7.85	0.21	14.97	21.52	0.33	0.00	0.05	0.00	0.06	99.70	44%	43%	13%
1651_X26_p52	50.81	0.80	3.01	8.11	0.20	14.55	21.20	0.39	0.01	0.01	0.02	0.12	99.21	44%	42%	13%
1651_X27_p53	52.32	0.47	2.00	8.00	0.19	15.70	20.45	0.28	0.00	0.00	0.01	0.06	99.47	42%	45%	13%
1651_X27_p54	50.75	0.68	3.07	8.14	0.17	15.04	20.92	0.36	0.00	0.05	0.04	0.03	99.25	43%	43%	13%
1651_X28_p55	52.30	0.48	1.96	8.11	0.20	15.82	20.50	0.31	0.00	0.02	0.02	0.00	99.74	42%	45%	13%
1651_X28_p56	52.45	0.46	2.16	6.62	0.18	16.03	20.86	0.20	0.00	0.19	0.09	0.07	99.30	43%	46%	11%
1651_X29_p57	51.65	0.59	2.42	7.25	0.18	15.50	21.05	0.35	0.00	0.00	0.03	0.03	99.05	44%	45%	12%
1651_X29_p58	52.30	0.39	1.80	7.00	0.23	16.64	20.17	0.24	0.00	0.20	0.01	0.05	99.03	41%	47%	11%
1651_X30_p59	51.09	0.63	2.67	7.66	0.19	14.67	21.52	0.38	0.01	0.03	0.03	0.03	98.91	45%	43%	12%
1651_X30_p60	51.19	0.70	2.39	9.16	0.25	15.17	19.95	0.38	0.01	0.09	0.03	0.08	99.40	41%	44%	15%
1651_X31_p61	52.07	0.54	2.37	7.70	0.22	15.66	20.36	0.22	0.02	0.06	0.01	0.04	99.27	42%	45%	12%
1651_X31_p62	50.77	0.74	3.19	7.70	0.17	14.72	21.28	0.43	0.01	0.04	0.05	0.05	99.15	45%	43%	13%
1651_X33_p65	51.71	0.61	2.16	9.71	0.27	14.49	19.62	0.43	0.01	0.23	0.00	0.02	99.25	41%	43%	16%

1651_X33_p66	51.77	0.49	2.82	6.65	0.17	15.39	21.28	0.37	0.02	0.38	0.10	0.01	99.45	44%	45%	11%
1651_X34_p67	51.72	0.57	2.26	8.08	0.23	15.65	20.56	0.30	0.01	0.02	0.09	0.00	99.50	42%	45%	13%
1651_X34_p68	52.26	0.54	2.12	7.92	0.29	15.65	20.69	0.30	0.00	0.00	0.00	0.07	99.84	43%	45%	13%
1651_X35_p69	50.94	0.64	3.01	9.34	0.34	14.04	20.41	0.50	0.00	0.12	0.04	0.07	99.45	43%	41%	15%
1651_X35_p70	51.09	0.60	2.55	11.60	0.33	13.81	19.47	0.52	0.00	0.09	0.00	0.06	100.12	41%	40%	19%
1651_X36_p71	52.57	0.50	1.82	8.02	0.20	15.90	20.73	0.31	0.00	0.04	0.04	0.06	100.18	42%	45%	13%
1651_X36_p72	50.94	0.84	2.59	10.45	0.24	14.59	19.54	0.45	0.00	0.06	0.00	0.03	99.73	41%	42%	17%
1651_X37_p73	52.99	0.39	2.06	5.80	0.19	16.71	21.29	0.25	0.00	0.51	0.02	0.00	100.19	43%	47%	9%
1651_X37_p74	53.07	0.37	1.93	5.93	0.19	16.28	21.33	0.30	0.00	0.28	0.05	0.07	99.80	44%	47%	10%
1651_X38_p75	51.11	0.80	3.37	8.19	0.20	14.53	21.25	0.38	0.00	0.02	0.01	0.05	99.90	44%	42%	13%
1651_X38_p76	51.02	0.76	3.14	8.18	0.20	14.57	21.08	0.30	0.01	0.03	0.05	0.00	99.33	44%	42%	13%
1651_X39_p77	52.40	0.45	2.36	7.04	0.15	15.42	21.60	0.38	0.00	0.41	0.03	0.04	100.28	44%	44%	11%
1651_X39_p78	50.43	0.93	3.32	8.19	0.20	14.73	20.94	0.33	0.00	0.06	0.01	0.03	99.15	44%	43%	13%
1651_X40_p79	52.15	0.59	2.06	9.10	0.28	14.56	20.29	0.37	0.00	0.07	0.04	0.05	99.57	43%	43%	15%
1651_X40_p80	51.19	0.82	3.24	8.00	0.19	14.80	21.10	0.28	0.00	0.06	0.05	0.03	99.77	44%	43%	13%
1651_X41_p81	51.85	0.55	1.99	7.79	0.19	15.44	21.10	0.23	0.00	0.02	0.01	0.04	99.22	43%	44%	12%
1651_X41_p82	52.26	0.48	1.92	7.92	0.25	15.58	21.09	0.32	0.00	0.00	0.00	0.01	99.83	43%	44%	13%
1651_X43_p85	52.48	0.47	1.91	8.02	0.23	15.50	20.96	0.31	0.00	0.00	0.00	0.00	99.88	43%	44%	13%
1651_X43_p86	51.20	0.70	2.80	8.02	0.19	14.54	21.34	0.34	0.01	0.07	0.04	0.04	99.29	45%	42%	13%
1651_X44_p87	52.41	0.54	2.03	7.80	0.27	15.80	20.42	0.27	0.00	0.00	0.04	0.02	99.61	42%	45%	13%
1651_X44_p88	52.29	0.51	2.02	7.80	0.22	15.47	21.18	0.30	0.01	0.02	0.06	0.06	99.94	43%	44%	12%
1651_X45_p89	52.51	0.49	1.87	7.84	0.23	15.62	21.07	0.29	0.00	0.00	0.00	0.04	99.97	43%	44%	13%
1651_X45_p90	51.04	0.78	2.99	8.56	0.22	15.06	21.14	0.29	0.01	0.04	0.05	0.02	100.21	43%	43%	14%
1651_X49_p97	52.83	0.38	1.71	7.74	0.24	15.66	20.63	0.30	0.00	0.00	0.06	0.06	99.60	43%	45%	12%
1651_X49_p98	51.09	0.66	2.87	8.10	0.17	14.90	21.46	0.37	0.00	0.00	0.05	0.00	99.67	44%	43%	13%
1651_X50_p99	51.09	0.77	2.95	8.19	0.19	14.87	21.15	0.35	0.00	0.08	0.07	0.01	99.72	44%	43%	13%
1651_X50_p100	52.72	0.45	1.91	7.38	0.25	15.46	21.25	0.26	0.01	0.04	0.01	0.04	99.78	44%	44%	12%
1651_X51_p101	51.17	0.84	3.13	8.52	0.16	14.75	21.01	0.34	0.00	0.00	0.02	0.00	99.95	44%	43%	14%
1651_X51_p102	50.74	0.81	3.31	8.23	0.24	14.75	21.12	0.40	0.01	0.04	0.02	0.08	99.76	44%	43%	13%
1651_X52_p103	52.73	0.47	1.90	7.88	0.28	15.88	20.90	0.33	0.00	0.00	0.07	0.01	100.46	43%	45%	13%
1651_X52_p104	52.81	0.53	1.83	8.10	0.24	15.75	20.43	0.28	0.00	0.00	0.03	0.06	100.06	42%	45%	13%
1651_X53_p105	51.79	0.54	1.70	9.52	0.31	14.81	20.33	0.37	0.02	0.04	0.00	0.07	99.50	42%	43%	15%
1651_X53_p106	50.96	0.79	3.29	8.14	0.15	14.51	20.95	0.42	0.00	0.01	0.03	0.06	99.30	44%	43%	13%
1651_X54_p107	52.60	0.51	2.27	8.31	0.27	15.59	20.31	0.29	0.00	0.00	0.06	0.02	100.23	42%	45%	13%
1651_X54_p108	52.45	0.48	2.22	8.36	0.28	15.69	20.61	0.28	0.00	0.00	0.00	0.00	100.38	42%	45%	13%
1651_X55_p109	52.74	0.51	1.86	7.85	0.24	15.98	20.81	0.31	0.00	0.04	0.00	0.04	100.39	42%	45%	12%
1651_X55_p110	51.65	0.72	2.74	8.11	0.21	14.95	20.59	0.27	0.00	0.04	0.05	0.04	99.37	43%	44%	13%
1651_X56_p111	51.37	0.68	2.66	9.55	0.33	13.97	20.71	0.46	0.00	0.00	0.00	0.08	99.81	44%	41%	16%
1651_X56_p112	52.38	0.48	2.16	7.61	0.22	15.27	21.48	0.33	0.01	0.01	0.02	0.04	100.02	44%	44%	12%
1651_X58_p115	51.69	0.74	2.95	7.94	0.20	15.00	21.35	0.37	0.01	0.04	0.06	0.09	100.42	44%	43%	13%
1651_X58_p116	51.03	0.76	3.11	8.41	0.17	14.59	20.71	0.34	0.01	0.00	0.08	0.02	99.23	44%	43%	14%
1651_X61_p121	52.25	0.50	2.01	8.22	0.27	15.42	20.29	0.26	0.00	0.02	0.00	0.02	99.27	42%	45%	13%
1651_X61_p122	52.35	0.53	2.05	7.41	0.18	15.31	21.19	0.32	0.00	0.00	0.00	0.03	99.37	44%	44%	12%
1651_X63_p125	51.00	0.67	2.78	8.16	0.22	14.88	21.25	0.28	0.01	0.02	0.08	0.05	99.39	44%	43%	13%
1651_X63_p126	52.53	0.43	2.04	8.11	0.21	15.69	20.71	0.34	0.01	0.06	0.00	0.00	100.13	42%	45%	13%
1651_X64_p127	52.22	0.55	2.27	7.90	0.20	15.43	20.86	0.25	0.00	0.03	0.10	0.06	99.89	43%	44%	13%
1651_X64_p128	52.44	0.52	2.47	8.37	0.23	15.52	20.01	0.29	0.00	0.00	0.04	0.03	99.92	42%	45%	14%
1651_X66_p131	52.40	0.54	2.06	7.91	0.21	15.52	21.01	0.32	0.00	0.00	0.00	0.04	100.01	43%	44%	13%

1651_X66_p132	52.24	0.51	1.93	8.01	0.29	15.65	20.82	0.31	0.00	0.01	0.02	0.04	99.83	43%	45%	13%
1651_X70_p139	51.35	0.71	2.59	8.48	0.18	15.02	20.79	0.33	0.01	0.09	0.03	0.04	99.62	43%	43%	14%
1651_X70_p140	51.17	0.76	2.14	9.65	0.29	15.49	19.27	0.30	0.00	0.09	0.08	0.09	99.33	40%	45%	16%
1651_X73_p145	52.08	0.50	2.23	8.32	0.17	14.60	20.73	0.36	0.00	0.23	0.06	0.06	99.35	44%	43%	14%
1651_X73_p146	51.57	0.62	2.51	8.02	0.19	15.06	20.74	0.30	0.00	0.07	0.03	0.07	99.18	43%	44%	13%
POR-006_px5	49.76	0.78	3.58	10.28	0.31	13.01	19.93	0.60	0.02	0.55	0.05	0.06	98.94	43%	39%	17%
POR-006_px6	51.26	0.72	1.91	11.05	0.32	14.33	18.87	0.46	0.00	0.05	0.03	0.08	99.08	40%	42%	18%
POR-006_px7	50.81	0.59	2.83	8.79	0.26	15.44	19.76	0.30	0.00	0.20	0.03	0.11	99.12	41%	45%	14%
POR-006_px8	50.34	0.73	2.80	9.07	0.22	15.30	19.65	0.30	0.02	0.24	0.00	0.05	98.73	41%	44%	15%
POR-006_px9	50.68	0.68	2.96	9.26	0.24	15.85	19.03	0.34	0.01	0.32	0.00	0.06	99.43	39%	46%	15%
POR-006_px11	51.43	0.44	1.97	9.04	0.32	16.85	18.23	0.32	0.01	0.08	0.00	0.07	98.77	37%	48%	14%
POR-006_px12	51.93	0.51	1.41	12.19	0.38	17.27	14.94	0.27	0.03	0.04	0.03	0.06	99.06	31%	50%	20%
POR-006_px14	51.11	0.77	2.29	11.13	0.35	14.69	19.30	0.55	0.01	0.00	0.05	0.04	100.29	40%	42%	18%
POR-006_px19	49.62	0.75	3.44	9.97	0.30	14.91	19.83	0.35	0.01	0.02	0.00	0.07	99.26	41%	43%	16%
POR-006_px20	50.33	0.57	3.47	7.57	0.12	15.65	20.38	0.29	0.01	0.34	0.01	0.10	98.84	42%	45%	12%
POR-006_px33	52.09	0.44	1.65	9.71	0.28	16.82	18.44	0.29	0.01	0.10	0.00	0.03	99.86	37%	47%	15%
POR-006_px34	50.10	0.88	3.42	9.97	0.22	14.83	19.07	0.47	0.01	0.01	0.00	0.08	99.05	40%	43%	16%
POR-006_px37	52.51	0.44	1.59	8.76	0.24	17.89	17.90	0.19	0.01	0.26	0.01	0.01	99.81	36%	50%	14%
POR-006_px38	51.72	0.51	1.67	9.34	0.21	16.58	18.38	0.33	0.01	0.10	0.04	0.00	98.90	38%	47%	15%
POR-006_px43	51.31	0.52	1.51	13.25	0.35	14.09	18.57	0.44	0.01	0.00	0.04	0.04	100.13	38%	40%	21%
POR-006_px44	51.10	0.80	2.44	10.25	0.24	15.26	19.60	0.42	0.03	0.02	0.06	0.04	100.25	40%	43%	16%
POR-006_px45	50.46	0.74	4.23	7.38	0.14	17.01	19.46	0.32	0.02	0.77	0.06	0.07	100.66	40%	48%	12%
POR-006_px46	50.74	0.67	2.66	8.97	0.28	15.68	19.36	0.40	0.04	0.11	0.00	0.13	99.03	40%	45%	15%
POR-006_px49	51.28	0.54	2.54	8.13	0.25	15.47	21.07	0.48	0.02	0.10	0.01	0.03	99.92	43%	44%	13%
POR-006_px50	51.29	0.67	2.00	10.48	0.26	14.35	19.82	0.49	0.02	0.00	0.04	0.04	99.46	41%	42%	17%
POR-006_px53	50.46	0.66	3.20	8.41	0.20	14.77	21.28	0.40	0.00	0.01	0.02	0.07	99.48	44%	42%	14%
POR-006_px54	50.99	0.76	2.18	9.06	0.28	14.72	20.56	0.41	0.00	0.00	0.05	0.04	99.05	43%	43%	15%
POR-006_px59	49.81	0.82	4.11	7.78	0.18	15.98	19.78	0.31	0.01	0.48	0.02	0.05	99.33	41%	46%	13%
POR-006_px62	51.25	0.60	2.08	10.51	0.29	15.30	19.43	0.38	0.01	0.01	0.00	0.05	99.91	40%	44%	17%
POR-006_px63	51.91	0.43	2.22	6.73	0.25	16.38	21.32	0.21	0.02	0.27	0.00	0.01	99.75	43%	46%	11%
POR-006_px64	52.15	0.41	2.24	7.22	0.21	16.59	20.64	0.26	0.01	0.16	0.00	0.00	99.89	42%	47%	11%
POR-006_px67	51.29	0.67	1.76	11.51	0.29	14.38	19.22	0.46	0.00	0.01	0.00	0.03	99.62	40%	41%	19%
POR-006_px68	50.40	0.84	4.00	9.38	0.16	14.47	20.21	0.40	0.02	0.20	0.03	0.11	100.23	42%	42%	15%
POR-006_px69	51.36	0.73	3.05	9.27	0.25	15.51	19.66	0.37	0.02	0.18	0.05	0.06	100.51	41%	45%	15%
POR-006_px70	51.12	0.58	3.80	6.99	0.17	16.77	19.45	0.37	0.02	0.71	0.00	0.06	100.04	40%	48%	11%
POR-006_px77	52.27	0.32	1.96	7.89	0.21	16.60	19.80	0.29	0.00	0.20	0.00	0.01	99.55	40%	47%	13%
POR-006_px79	52.54	0.47	1.72	8.97	0.36	16.84	18.49	0.27	0.02	0.08	0.02	0.03	99.80	38%	48%	14%
POR-006_px80	51.06	0.82	2.60	9.57	0.27	15.14	19.90	0.41	0.05	0.06	0.06	0.06	99.98	41%	43%	15%
POR-006_px81	51.06	0.67	1.81	10.44	0.22	15.02	18.96	0.41	0.02	0.12	0.06	0.11	98.90	39%	44%	17%
POR-006_px82	51.02	0.84	2.18	11.06	0.30	14.27	19.21	0.55	0.03	0.00	0.03	0.03	99.52	40%	42%	18%
POR-006_px87	51.89	0.49	1.69	8.20	0.23	15.51	21.07	0.41	0.01	0.04	0.00	0.08	99.62	43%	44%	13%
POR-006_px88	50.84	0.87	2.50	10.27	0.30	15.03	19.56	0.32	0.02	0.00	0.04	0.07	99.83	40%	43%	17%
POR-006_px89	51.24	0.64	1.80	10.75	0.29	14.42	19.74	0.44	0.01	0.04	0.00	0.08	99.44	41%	42%	17%
POR-006_px90	51.48	0.56	2.16	9.05	0.26	15.40	20.20	0.35	0.03	0.11	0.10	0.00	99.71	41%	44%	15%
POR-006_px93	51.38	0.51	2.62	7.74	0.25	16.19	19.86	0.27	0.00	0.56	0.00	0.03	99.41	41%	47%	12%
POR-006_px94	50.88	0.66	3.06	8.49	0.18	15.51	19.93	0.32	0.02	0.14	0.01	0.13	99.32	41%	45%	14%
POR-006_px97	50.91	0.59	2.49	10.62	0.29	14.25	19.74	0.50	0.01	0.17	0.00	0.07	99.63	41%	41%	17%
POR-006_px98	51.49	0.70	1.71	12.30	0.38	14.36	18.43	0.47	0.03	0.00	0.03	0.07	99.96	38%	42%	20%

POR-006_px99	53.05	0.57	1.95	9.62	0.23	17.32	17.46	0.30	0.01	0.18	0.00	0.03	100.72	36%	49%	15%
POR-006_px100	51.28	0.55	3.87	6.49	0.09	16.01	20.48	0.36	0.02	0.67	0.08	0.04	99.93	43%	47%	11%
POR-006_px101	51.74	0.52	2.70	7.57	0.21	16.67	19.34	0.31	0.02	0.47	0.04	0.06	99.66	40%	48%	12%
POR-006_px102	52.07	0.35	2.11	7.50	0.18	17.62	19.44	0.36	0.00	0.26	0.01	0.09	100.00	39%	49%	12%
POR-006_px103	52.91	0.41	1.52	8.20	0.22	18.19	17.98	0.22	0.01	0.28	0.06	0.01	100.01	36%	51%	13%
POR-006_px104	51.30	0.68	2.37	10.68	0.19	14.76	18.86	0.43	0.02	0.06	0.08	0.08	99.52	40%	43%	17%
POR-006_px106	51.22	0.57	3.69	7.19	0.15	16.34	18.79	0.33	0.04	0.58	0.05	0.09	99.03	40%	48%	12%
POR-006_px107	50.77	0.74	2.53	10.73	0.33	14.49	19.34	0.49	0.01	0.30	0.02	0.05	99.78	40%	42%	17%
POR-006_px108	51.76	0.70	1.98	10.20	0.29	14.42	19.64	0.53	0.02	0.11	0.00	0.06	99.72	41%	42%	17%
POR-006_px111	51.48	0.43	2.47	10.24	0.25	16.50	18.38	0.15	0.03	0.00	0.00	0.06	100.00	37%	47%	16%
POR-006_px112	51.13	0.91	2.72	10.27	0.23	14.73	19.82	0.34	0.02	0.00	0.01	0.00	100.18	41%	42%	17%
POR-006_px113	51.25	0.72	2.34	11.21	0.28	14.40	19.10	0.47	0.00	0.07	0.01	0.09	99.94	40%	42%	18%
POR-006_px114	51.79	0.69	2.02	11.05	0.31	14.67	18.66	0.53	0.01	0.13	0.03	0.05	99.95	39%	43%	18%
POR-006_px117	51.43	0.59	3.35	7.59	0.24	15.92	20.55	0.23	0.00	0.16	0.00	0.05	100.13	42%	46%	12%
POR-006_px118	50.92	0.73	3.05	8.81	0.20	15.46	19.98	0.33	0.02	0.20	0.04	0.03	99.78	41%	44%	14%
POR-006_px119	52.16	0.37	1.64	9.46	0.30	17.15	17.63	0.29	0.01	0.18	0.04	0.00	99.23	36%	49%	15%
POR-006_px121	50.97	0.67	3.41	8.32	0.25	15.78	20.18	0.31	0.00	0.27	0.02	0.06	100.24	41%	45%	13%
POR-006_px122	51.24	0.75	2.51	9.32	0.31	15.25	19.83	0.36	0.01	0.06	0.00	0.04	99.68	41%	44%	15%
POR-006_px123	52.66	0.44	1.94	8.06	0.20	15.61	20.80	0.35	0.01	0.02	0.01	0.00	100.10	43%	44%	13%
POR-006_px124	51.76	0.62	1.76	11.24	0.37	14.58	19.16	0.55	0.00	0.00	0.00	0.07	100.11	40%	42%	18%
POR-006_px127	51.45	0.59	2.03	10.69	0.31	14.42	19.49	0.52	0.00	0.04	0.00	0.13	99.66	41%	42%	17%
POR-006_px128	51.76	0.64	2.38	8.15	0.19	15.54	20.65	0.36	0.02	0.13	0.00	0.05	99.86	42%	44%	13%
POR-006_px132	51.95	0.64	2.46	9.58	0.23	15.43	19.31	0.34	0.02	0.09	0.03	0.04	100.12	40%	44%	15%
POR-006_px133	51.21	0.76	2.22	10.56	0.30	13.89	20.16	0.48	0.00	0.00	0.02	0.07	99.66	42%	40%	17%
POR-006_px134	51.57	0.78	1.75	11.98	0.36	14.49	18.79	0.42	0.00	0.06	0.03	0.08	100.32	39%	42%	19%
POR-006_px135	52.01	0.75	2.72	9.54	0.27	16.73	18.27	0.24	0.00	0.06	0.03	0.07	100.68	37%	48%	15%
POR-006_px136	51.91	0.51	3.80	6.31	0.17	16.01	20.40	0.29	0.03	0.76	0.05	0.06	100.30	43%	47%	10%
POR-006_px137	50.55	0.82	2.89	9.44	0.28	14.65	20.58	0.46	0.00	0.16	0.00	0.05	99.88	43%	42%	15%
POR-006_px139	50.98	0.63	3.71	6.24	0.18	15.72	21.45	0.31	0.02	0.49	0.00	0.01	99.74	45%	45%	10%
POR-006_px140	51.56	0.64	2.47	9.31	0.23	15.30	19.53	0.33	0.03	0.18	0.07	0.11	99.75	41%	44%	15%
POR-006_px141	52.87	0.39	1.88	7.29	0.23	18.15	18.43	0.22	0.01	0.36	0.00	0.03	99.86	37%	51%	12%
POR-006_px142	51.08	0.79	2.35	9.81	0.24	15.37	19.44	0.37	0.02	0.00	0.03	0.04	99.54	40%	44%	16%
POR-006_px145	51.69	0.56	1.93	8.48	0.29	14.74	21.13	0.47	0.10	0.03	0.00	0.04	99.46	44%	42%	14%
POR-006_px146	51.66	0.69	2.26	8.71	0.24	15.24	20.83	0.42	0.02	0.09	0.02	0.04	100.21	43%	43%	14%
POR-006_px147	51.55	0.74	2.46	10.49	0.23	14.13	20.07	0.43	0.00	0.24	0.01	0.04	100.39	42%	41%	17%
POR-006_px148	52.98	0.29	1.20	10.38	0.22	13.89	20.69	0.49	0.01	0.00	0.02	0.06	100.23	43%	40%	17%
POR-006_px149	51.89	0.60	2.22	8.19	0.24	15.81	19.76	0.27	0.01	0.22	0.01	0.06	99.28	41%	46%	13%
POR-006_px150	51.40	0.71	2.55	9.90	0.30	15.17	19.14	0.29	0.04	0.04	0.04	0.07	99.64	40%	44%	16%
POR-006_px151	51.75	0.73	2.21	11.55	0.23	14.50	19.10	0.43	0.01	0.14	0.01	0.05	100.71	40%	42%	19%
POR-006_px152	53.07	0.44	1.29	10.50	0.27	14.49	20.44	0.45	0.02	0.03	0.04	0.10	101.14	42%	41%	17%
POR-006_px155	52.25	0.60	1.58	10.14	0.20	15.03	19.67	0.53	0.01	0.05	0.04	0.03	100.13	41%	43%	16%
POR-006_px157	51.49	0.63	1.93	11.65	0.30	14.62	18.47	0.44	0.01	0.00	0.00	0.03	99.57	39%	42%	19%
POR-006_px158	51.57	0.79	2.38	9.66	0.26	15.12	19.79	0.47	0.04	0.02	0.00	0.01	100.11	41%	43%	16%
POR-006_px159	51.20	0.63	2.80	8.17	0.25	15.75	19.75	0.38	0.00	0.24	0.00	0.04	99.22	41%	46%	13%
POR-006_px160	51.27	0.66	2.57	10.02	0.26	14.91	19.19	0.39	0.02	0.07	0.10	0.01	99.46	40%	43%	16%
POR-006_px165	52.97	0.34	1.23	7.78	0.25	14.97	21.56	0.28	0.02	0.00	0.04	0.04	99.47	44%	43%	13%
POR-006_px166	51.80	0.67	1.98	9.43	0.27	15.56	19.74	0.40	0.04	0.00	0.00	0.03	99.93	40%	44%	15%
POR-006_px167	51.73	0.57	2.33	9.85	0.30	16.46	18.46	0.38	0.00	0.09	0.05	0.03	100.26	38%	47%	16%

POR-006_px168	52.21	0.57	1.79	9.83	0.26	15.91	19.13	0.35	0.00	0.04	0.02	0.01	100.11	39%	45%	16%
POR-006_px169	51.86	0.70	2.00	11.27	0.39	14.77	18.72	0.49	0.01	0.07	0.00	0.11	100.40	39%	43%	18%
POR-006_px170	53.09	0.51	1.34	9.94	0.37	15.98	19.01	0.21	0.02	0.01	0.07	0.05	100.59	39%	45%	16%
POR-006_px171	53.23	0.45	1.90	15.62	0.34	22.70	6.50	0.21	0.01	0.24	0.00	0.04	101.25	13%	63%	24%
POR-006_px172	50.93	0.76	2.84	10.13	0.23	14.65	19.40	0.55	0.00	0.00	0.04	0.07	99.62	41%	43%	17%
POR-006_px173	52.32	0.35	1.64	8.82	0.29	16.86	18.89	0.27	0.01	0.13	0.02	0.04	99.64	38%	48%	14%
POR-006_px174	51.43	0.73	2.44	9.58	0.23	15.01	19.93	0.40	0.05	0.03	0.00	0.07	99.90	41%	43%	15%
POR-006_px177	51.38	0.80	2.37	11.11	0.30	14.51	19.46	0.42	0.01	0.03	0.10	0.09	100.58	40%	42%	18%
POR-006_px178	51.39	0.73	2.39	11.22	0.30	14.24	19.16	0.50	0.00	0.01	0.00	0.05	99.99	40%	42%	18%
POR-006_px179	52.69	0.45	1.58	8.52	0.25	16.93	19.38	0.26	0.01	0.07	0.09	0.04	100.28	39%	48%	13%
POR-006_px180	52.50	0.50	1.45	9.71	0.34	16.52	18.57	0.31	0.01	0.03	0.02	0.07	100.04	38%	47%	15%
POR-006_px184	50.45	0.72	3.99	7.97	0.21	14.54	20.69	0.37	0.04	0.34	0.00	0.10	99.41	44%	43%	13%
POR-006_px185	51.83	0.62	2.59	9.45	0.27	15.75	19.19	0.32	0.01	0.13	0.02	0.14	100.32	40%	45%	15%
POR-006_px186	52.45	0.61	3.31	7.81	0.18	16.09	19.93	0.36	0.02	0.32	0.00	0.08	101.15	41%	46%	13%
POR-006_px199	52.38	0.31	1.25	8.77	0.25	14.60	21.95	0.45	0.01	0.03	0.00	0.02	100.00	45%	41%	14%
POR-006_px200	51.93	0.56	2.16	8.68	0.19	15.60	20.08	0.35	0.01	0.17	0.00	0.07	99.79	41%	45%	14%
POR-006-I_px6	53.13	0.32	0.82	20.31	0.64	22.56	2.74	0.12	0.06	0.05	0.03	0.02	100.80	5%	63%	32%
POR-006-I_px8	54.05	0.56	1.83	15.69	0.35	22.81	3.66	0.11	0.03	0.00	0.05	0.02	99.17	8%	67%	26%
POR-006-I_px17	51.40	0.78	2.13	11.07	0.24	14.41	18.89	0.47	0.02	0.02	0.00	0.10	99.53	40%	42%	18%
POR-006-I_px18	52.75	0.55	1.37	10.03	0.27	16.03	18.22	0.24	0.02	0.04	0.05	0.05	99.62	38%	46%	16%
POR-006-I_px19	51.55	0.72	2.30	10.16	0.29	15.31	18.83	0.33	0.01	0.00	0.00	0.08	99.59	39%	44%	17%
POR-006-I_px20	52.86	0.54	1.40	9.65	0.27	16.25	18.43	0.29	0.05	0.00	0.00	0.03	99.77	38%	47%	16%
POR-006-I_px29	51.67	0.69	2.18	11.06	0.27	14.65	18.66	0.50	0.00	0.00	0.00	0.06	99.73	39%	43%	18%
POR-006-I_px30	51.30	0.67	3.91	7.43	0.16	16.53	19.44	0.36	0.02	0.41	0.00	0.00	100.23	40%	48%	12%
POR-006-I_px31	52.17	0.60	1.76	10.39	0.31	15.03	19.38	0.47	0.00	0.07	0.05	0.01	100.25	40%	43%	17%
POR-006-I_px32	52.55	0.47	3.28	6.24	0.16	16.72	20.26	0.34	0.01	0.59	0.01	0.06	100.70	42%	48%	10%
POR-006-I_px41	50.69	0.71	3.40	8.87	0.24	15.43	20.22	0.30	0.01	0.19	0.00	0.06	100.12	42%	44%	14%
POR-006-I_px42	51.36	0.85	2.38	9.62	0.25	14.82	19.51	0.33	0.03	0.01	0.00	0.07	99.24	41%	43%	16%
POR-006-I_px45	50.65	0.85	3.21	10.91	0.27	13.71	19.65	0.54	0.01	0.14	0.03	0.01	99.98	42%	40%	18%
POR-006-I_px46	52.39	0.61	2.52	8.85	0.19	16.39	19.18	0.29	0.03	0.11	0.00	0.07	100.63	39%	47%	14%
POR-006-I_px49	50.91	0.67	3.73	8.32	0.18	15.72	19.93	0.31	0.00	0.33	0.01	0.06	100.18	41%	45%	13%
POR-006-I_px50	51.50	0.76	2.59	9.06	0.18	15.43	19.97	0.34	0.07	0.10	0.02	0.04	100.05	41%	44%	15%
POR-006-I_px51	52.38	0.60	2.43	9.79	0.32	16.25	18.82	0.34	0.01	0.17	0.04	0.03	101.16	38%	46%	16%
POR-006-I_px52	51.58	0.83	2.96	9.58	0.24	15.56	19.25	0.34	0.02	0.12	0.07	0.05	100.60	40%	45%	15%
POR-006-I_px53	52.43	0.60	1.92	11.07	0.31	15.20	18.56	0.49	0.00	0.06	0.03	0.09	100.75	38%	44%	18%
POR-006-I_px54	52.14	0.69	2.18	11.04	0.32	14.52	19.05	0.51	0.01	0.02	0.06	0.11	100.65	40%	42%	18%
POR-006-I_px55	51.95	0.48	3.14	6.67	0.21	16.00	20.99	0.25	0.00	0.51	0.04	0.05	100.29	43%	46%	11%
POR-006-I_px56	51.85	0.70	2.30	9.57	0.22	15.42	19.72	0.39	0.02	0.00	0.04	0.04	100.27	41%	44%	15%
POR-006-I_px57	52.03	0.52	3.34	6.64	0.18	15.84	20.87	0.29	0.00	0.54	0.00	0.01	100.26	43%	46%	11%
POR-006-I_px59	52.31	0.61	2.53	10.01	0.28	16.65	17.89	0.31	0.00	0.12	0.01	0.07	100.80	37%	47%	16%
POR-006-I_px63	52.27	0.50	2.03	9.88	0.19	14.78	20.04	0.42	0.01	0.24	0.00	0.10	100.47	41%	43%	16%
POR-006-I_px67	51.84	0.60	3.76	7.49	0.18	15.71	20.74	0.33	0.01	0.34	0.04	0.00	101.04	43%	45%	12%
POR-006-I_px68	51.91	0.70	2.82	9.53	0.28	15.93	18.40	0.30	0.00	0.10	0.01	0.04	100.03	38%	46%	15%
POR-006-I_px69	52.57	0.66	2.61	8.99	0.31	15.38	19.78	0.52	0.00	0.04	0.01	0.11	100.98	41%	44%	15%
POR-006-I_px70	51.93	0.60	2.40	10.85	0.32	14.92	19.07	0.45	0.01	0.00	0.02	0.10	100.66	39%	43%	18%
POR-006-I_px77	52.20	0.69	2.37	10.41	0.26	14.97	18.90	0.43	0.02	0.04	0.04	0.08	100.42	39%	44%	17%
POR-006-I_px78	52.73	0.58	2.46	10.10	0.28	16.97	17.38	0.29	0.00	0.10	0.00	0.05	100.94	36%	48%	16%
POR-006-I_px79	54.47	0.37	1.66	10.45	0.25	18.33	14.38	0.26	0.00	0.10	0.00	0.02	100.30	30%	53%	17%

POR-006-I_px81	52.65	0.55	2.75	8.18	0.19	15.76	20.40	0.38	0.01	0.06	0.06	0.05	101.04	42%	45%	13%
POR-006-I_px82	51.93	0.84	2.56	10.66	0.18	14.50	18.81	0.49	0.01	0.05	0.00	0.09	100.11	40%	43%	18%
POR-006-I_px93	53.21	0.51	1.97	7.96	0.23	15.83	20.84	0.30	0.01	0.04	0.00	0.00	100.91	42%	45%	13%
POR-006-I_px99	53.30	0.73	1.75	11.37	0.27	15.29	18.26	0.34	0.00	0.08	0.00	0.01	101.40	38%	44%	18%
POR-006-I_px100	53.44	0.36	1.17	11.42	0.34	13.87	19.87	0.47	0.04	0.03	0.00	0.00	101.01	41%	40%	19%
POR-006-I_px101	52.47	0.74	2.92	9.24	0.19	15.48	19.49	0.32	0.00	0.18	0.00	0.10	101.14	40%	45%	15%
POR-006-I_px102	53.90	0.37	2.23	7.14	0.14	17.00	19.29	0.29	0.00	0.30	0.00	0.03	100.70	40%	49%	11%
POR-006-I_px105	53.49	0.40	1.64	9.02	0.29	17.10	17.74	0.25	0.01	0.13	0.05	0.01	100.12	37%	49%	14%
POR-006-I_px106	52.87	0.62	2.75	9.63	0.24	14.59	19.38	0.42	0.04	0.09	0.03	0.00	100.66	41%	43%	16%
POR-006-I_px113	51.71	0.71	3.06	8.50	0.20	15.69	19.50	0.33	0.00	0.23	0.00	0.03	99.96	41%	46%	14%
POR-006-I_px114	53.15	0.60	1.88	9.91	0.32	15.77	18.56	0.37	0.02	0.04	0.00	0.00	100.64	38%	45%	16%
POR-006-I_px120	54.17	0.36	1.26	17.85	0.44	24.34	2.64	0.06	0.01	0.00	0.00	0.04	101.18	5%	67%	28%
POR-006-I_px121	53.75	0.33	1.88	7.13	0.21	16.93	19.60	0.21	0.02	0.21	0.00	0.02	100.30	40%	48%	11%
POR-006-I_px122	52.56	0.66	3.54	7.62	0.18	15.96	19.96	0.30	0.01	0.26	0.02	0.06	101.12	41%	46%	12%
POR-006-I_px130	53.27	0.70	2.63	9.74	0.25	16.47	17.48	0.31	0.03	0.12	0.04	0.04	101.08	36%	48%	16%
POR-006-I_px131	52.96	0.63	2.36	9.04	0.25	16.38	18.58	0.29	0.01	0.21	0.03	0.04	100.77	38%	47%	15%
POR-006-I_px132	52.08	0.71	2.80	9.25	0.20	15.13	19.60	0.39	0.01	0.09	0.04	0.09	100.39	41%	44%	15%
POR-006-I_px134	53.55	0.46	2.00	9.29	0.21	14.88	20.14	0.39	0.01	0.06	0.04	0.01	101.05	42%	43%	15%
POR-006-I_px141	50.17	1.27	4.38	7.90	0.12	14.78	20.76	0.34	0.00	0.00	0.05	0.09	99.86	44%	43%	13%
POR-006-I_px142	52.34	0.80	2.69	9.68	0.18	14.70	19.96	0.36	0.04	0.02	0.00	0.04	100.82	42%	43%	16%
POR-006-I_px145	53.81	0.43	1.47	9.11	0.27	17.01	17.84	0.25	0.00	0.02	0.04	0.02	100.26	37%	49%	15%
POR-006-I_px146	52.32	0.54	3.80	5.91	0.08	16.14	20.73	0.35	0.02	0.74	0.11	0.07	100.80	43%	47%	10%
POR-006-I_px149	52.49	0.60	2.20	8.86	0.24	16.14	18.77	0.31	0.02	0.26	0.00	0.00	99.90	39%	47%	14%
POR-006-I_px150	52.00	0.59	3.83	6.51	0.13	15.60	20.68	0.31	0.04	0.57	0.03	0.07	100.35	44%	46%	11%
POR-006-I_px167	53.38	0.54	2.46	7.75	0.22	16.48	19.33	0.28	0.01	0.45	0.07	0.06	101.02	40%	47%	13%
POR-006-I_px168	53.75	0.35	2.22	6.67	0.13	17.34	19.66	0.28	0.02	0.33	0.03	0.02	100.80	40%	49%	11%
POR-006-I_px169	51.95	0.69	3.06	9.47	0.27	15.35	19.47	0.27	0.00	0.11	0.06	0.08	100.78	40%	44%	15%
POR-006-I_px170	51.64	0.64	4.37	7.46	0.18	15.72	20.28	0.37	0.00	0.34	0.02	0.08	101.11	42%	46%	12%
POR-006-I_px181	53.22	0.52	1.98	8.35	0.22	15.59	20.81	0.23	0.02	0.04	0.00	0.04	101.01	42%	44%	13%
POR-006-I_px182	52.27	0.72	2.16	10.70	0.21	14.59	19.13	0.52	0.00	0.04	0.00	0.03	100.38	40%	42%	17%
POR-006-I_px185	53.60	0.57	2.38	8.26	0.26	16.22	19.43	0.30	0.01	0.23	0.04	0.05	101.36	40%	47%	13%
POR-006-I_px186	52.46	0.80	2.43	9.85	0.18	14.86	20.08	0.34	0.02	0.00	0.00	0.03	101.04	41%	43%	16%
POR-006-I_px188	52.81	0.55	2.36	10.23	0.30	14.65	19.61	0.38	0.00	0.08	0.01	0.09	101.08	41%	42%	17%
POR-006-I_px192	51.65	0.85	2.58	10.05	0.24	14.93	19.95	0.32	0.03	0.00	0.01	0.05	100.65	41%	43%	16%
POR-006-I_px194	52.51	0.58	2.42	10.29	0.25	14.63	19.31	0.41	0.00	0.08	0.03	0.05	100.57	40%	43%	17%
POR-006-I_px197	51.77	0.63	3.96	7.17	0.16	15.01	21.56	0.31	0.01	0.45	0.03	0.03	101.09	45%	43%	12%
POR-006-I_px198	52.39	0.62	4.02	6.85	0.19	15.79	20.64	0.35	0.02	0.35	0.00	0.06	101.28	43%	46%	11%

Table S7.2. Clinopyroxene core compositional data for Palpana (Sample PAL-02 and Mount 1652).

Sample	Major Oxides (wt%)													Wo	En	Fs
	SiO_2	TiO_2	Al_2O_3	FeO	MnO	MgO	CaO	Na_2O	K_2O	Cr_2O_3	NiO	V_2O_3	Total			
1652_X1_p1	49.62	0.79	4.70	10.23	0.21	13.79	20.03	0.59	0.00	0.31	0.05	0.06	100.38	42%	41%	17%
1652_X1_p2	51.28	0.51	2.19	9.90	0.16	15.19	20.17	0.45	0.00	0.12	0.06	0.04	100.07	41%	43%	16%
1652_X10_p17	50.95	0.65	2.57	8.70	0.23	15.28	21.24	0.41	0.00	0.11	0.05	0.07	100.27	43%	43%	14%
1652_X10_p18	49.92	0.84	3.82	10.32	0.24	14.33	19.92	0.49	0.00	0.05	0.08	0.05	100.07	42%	42%	17%
1652_X11_p19	50.81	0.77	2.65	11.85	0.32	13.93	19.45	0.55	0.00	0.04	0.05	0.06	100.48	40%	40%	19%
1652_X11_p20	51.48	0.65	2.96	8.85	0.24	15.12	20.82	0.44	0.00	0.12	0.05	0.09	100.80	43%	43%	14%
1652_X12_p21	51.81	0.45	2.02	9.35	0.30	15.45	20.14	0.43	0.01	0.15	0.00	0.04	100.15	41%	44%	15%
1652_X12_p22	50.80	0.69	2.68	10.35	0.25	14.29	20.01	0.46	0.01	0.02	0.00	0.00	99.56	42%	41%	17%
1652_X13_p23	50.67	0.76	2.51	11.06	0.30	14.40	19.70	0.48	0.00	0.04	0.01	0.07	99.99	41%	41%	18%
1652_X13_p24	49.98	0.75	2.95	12.19	0.30	13.59	18.75	0.61	0.00	0.07	0.00	0.03	99.22	40%	40%	20%
1652_X14_p25	49.81	0.79	4.94	8.42	0.16	14.42	21.02	0.38	0.01	0.25	0.00	0.01	100.22	44%	42%	14%
1652_X14_p26	50.28	0.72	3.55	7.87	0.17	15.53	21.09	0.37	0.01	0.25	0.08	0.10	100.01	43%	44%	13%
1652_X15_p27	50.84	0.68	2.46	9.90	0.30	14.91	19.46	0.45	0.00	0.01	0.00	0.02	99.03	41%	43%	16%
1652_X15_p28	51.49	0.78	2.81	8.61	0.19	14.85	20.76	0.47	0.00	0.06	0.11	0.08	100.21	43%	43%	14%
1652_X16_p29	51.08	0.75	2.66	11.05	0.20	14.47	19.56	0.51	0.00	0.00	0.04	0.08	100.40	40%	42%	18%
1652_X16_p30	51.66	0.64	2.67	8.38	0.25	15.76	20.27	0.35	0.01	0.02	0.00	0.06	100.06	42%	45%	13%
1652_X17_p31	51.15	0.84	3.23	8.84	0.17	15.10	21.49	0.33	0.00	0.08	0.07	0.10	101.40	44%	43%	14%
1652_X17_p32	51.15	0.79	2.33	10.35	0.24	14.77	19.79	0.52	0.00	0.04	0.06	0.01	100.04	41%	42%	17%
1652_X18_p33	51.25	0.75	2.14	10.86	0.28	14.56	19.74	0.48	0.00	0.00	0.00	0.06	100.12	41%	42%	17%
1652_X18_p34	50.62	0.85	3.25	8.94	0.22	15.21	20.46	0.39	0.00	0.07	0.01	0.00	100.01	42%	44%	14%
1652_X19_p35	50.53	0.74	3.80	8.62	0.19	15.16	21.10	0.43	0.01	0.17	0.00	0.09	100.84	43%	43%	14%
1652_X19_p36	50.66	0.62	3.58	11.66	0.28	13.68	19.01	0.66	0.00	0.07	0.03	0.06	100.31	40%	40%	19%
1652_X20_p37	51.48	0.71	2.77	9.25	0.23	14.41	20.61	0.48	0.00	0.01	0.08	0.10	100.14	43%	42%	15%
1652_X20_p38	51.15	0.72	2.96	9.04	0.20	14.88	21.11	0.48	0.00	0.15	0.07	0.02	100.77	43%	42%	14%
1652_X21_p39	51.13	0.79	2.65	12.75	0.38	13.77	18.01	0.63	0.00	0.01	0.09	0.05	100.26	38%	41%	21%
1652_X21_p40	51.21	0.67	3.39	8.35	0.17	15.35	20.94	0.34	0.00	0.02	0.00	0.05	100.49	43%	44%	13%
1652_X22_p41	50.59	0.86	3.51	10.31	0.26	14.12	20.37	0.53	0.00	0.00	0.04	0.05	100.65	42%	41%	17%
1652_X22_p42	51.57	0.80	2.58	10.09	0.33	14.62	20.05	0.51	0.00	0.00	0.04	0.06	100.65	42%	42%	16%
1652_X23_p43	50.81	0.69	3.48	8.40	0.19	14.56	21.26	0.50	0.00	0.11	0.00	0.03	100.04	44%	42%	14%
1652_X23_p44	52.22	0.60	2.06	8.51	0.16	15.60	20.57	0.39	0.00	0.03	0.00	0.02	100.15	42%	44%	14%
1652_X24_p45	50.21	0.78	4.32	7.89	0.22	14.42	20.91	0.43	0.01	0.32	0.02	0.05	99.58	44%	43%	13%
1652_X24_p46	50.57	0.64	3.73	7.75	0.24	15.03	21.15	0.50	0.01	0.35	0.00	0.07	100.04	44%	43%	13%
1652_X25_p47	50.97	0.87	2.88	10.81	0.31	14.60	19.80	0.52	0.00	0.05	0.00	0.06	100.88	41%	42%	17%
1652_X25_p48	50.32	0.80	3.56	8.62	0.18	14.92	21.01	0.45	0.00	0.10	0.02	0.03	100.00	43%	43%	14%
1652_X26_p49	51.56	0.60	2.32	10.42	0.24	14.48	20.33	0.53	0.00	0.05	0.00	0.06	100.59	42%	41%	17%
1652_X26_p50	52.00	0.50	2.21	10.37	0.28	14.12	20.39	0.55	0.00	0.08	0.05	0.12	100.67	42%	41%	17%
1652_X27_p51	51.55	0.75	2.60	11.30	0.27	14.39	19.36	0.60	0.00	0.08	0.01	0.04	100.95	40%	42%	18%
1652_X27_p52	50.64	0.84	3.47	8.67	0.17	14.69	20.92	0.38	0.00	0.13	0.02	0.00	99.93	43%	42%	14%
1652_X28_p53	50.19	0.74	3.03	11.64	0.22	13.41	18.80	0.58	0.00	0.05	0.04	0.05	98.75	40%	40%	20%
1652_X28_p54	51.34	0.67	2.35	10.15	0.22	15.05	19.23	0.46	0.01	0.00	0.07	0.05	99.60	40%	44%	16%
1652_X29_p55	51.98	0.36	1.75	11.55	0.34	13.74	20.46	0.49	0.00	0.04	0.03	0.02	100.76	42%	39%	19%
1652_X29_p56	51.99	0.39	1.89	11.74	0.32	13.33	20.32	0.54	0.01	0.00	0.05	0.05	100.62	42%	39%	19%
1652_X3_p3	51.05	0.74	2.42	11.75	0.27	14.75	18.57	0.61	0.00	0.08	0.00	0.02	100.26	38%	43%	19%

1652_X3_p4	50.77	0.71	3.04	10.11	0.21	14.28	20.54	0.49	0.00	0.10	0.00	0.06	100.32	43%	41%	16%
1652_X30_p57	50.94	0.54	3.33	12.17	0.22	13.20	19.49	0.57	0.00	0.19	0.10	0.06	100.81	41%	39%	20%
1652_X30_p58	51.27	0.76	3.81	8.44	0.13	14.72	20.79	0.41	0.00	0.24	0.04	0.11	100.72	43%	43%	14%
1652_X32_p61	51.17	0.80	2.99	8.67	0.16	14.77	21.50	0.42	0.00	0.04	0.09	0.04	100.67	44%	42%	14%
1652_X32_p62	50.88	0.77	2.98	8.27	0.23	14.69	21.50	0.37	0.00	0.06	0.00	0.03	99.78	44%	42%	13%
1652_X33_p63	50.56	0.68	2.75	12.83	0.25	13.47	19.28	0.53	0.00	0.05	0.00	0.06	100.46	40%	39%	21%
1652_X33_p64	50.53	0.89	3.51	8.85	0.17	14.45	21.12	0.48	0.00	0.04	0.03	0.07	100.14	44%	42%	14%
1652_X34_p65	51.79	0.49	3.70	6.54	0.14	15.37	21.52	0.47	0.02	0.53	0.00	0.10	100.66	45%	45%	11%
1652_X34_p66	50.85	0.49	3.21	10.29	0.21	14.00	20.45	0.52	0.00	0.58	0.01	0.04	100.65	43%	41%	17%
1652_X35_p67	50.88	0.72	3.21	11.25	0.18	13.78	19.57	0.56	0.01	0.12	0.00	0.01	100.29	41%	40%	18%
1652_X35_p68	51.59	0.69	2.27	12.24	0.28	13.85	18.79	0.51	0.01	0.00	0.06	0.07	100.35	39%	40%	20%
1652_X36_p69	51.73	0.42	3.11	7.79	0.14	15.03	21.20	0.51	0.01	0.29	0.03	0.04	100.29	44%	43%	13%
1652_X36_p70	51.47	0.36	2.90	8.55	0.25	14.75	20.84	0.49	0.00	0.31	0.05	0.00	99.97	43%	43%	14%
1652_X37_p71	51.89	0.61	2.53	9.36	0.23	14.80	20.94	0.40	0.00	0.07	0.07	0.02	100.93	43%	42%	15%
1652_X37_p72	51.24	0.65	2.53	11.65	0.27	14.01	19.13	0.60	0.00	0.03	0.06	0.03	100.19	40%	41%	19%
1652_X38_p73	50.86	0.83	3.22	7.73	0.16	14.81	21.20	0.38	0.01	0.42	0.00	0.05	99.67	44%	43%	13%
1652_X38_p74	50.63	0.70	3.61	8.44	0.16	14.76	20.86	0.43	0.00	0.21	0.00	0.04	99.83	43%	43%	14%
1652_X39_p75	50.32	0.72	5.14	8.16	0.12	14.18	20.65	0.62	0.01	0.17	0.03	0.05	100.16	44%	42%	14%
1652_X39_p76	51.20	0.63	3.38	7.84	0.17	14.96	21.06	0.34	0.00	0.31	0.00	0.12	100.00	44%	43%	13%
1652_X4_p5	50.13	0.69	5.19	7.50	0.12	14.82	20.83	0.58	0.00	0.46	0.02	0.02	100.38	44%	44%	12%
1652_X4_p6	50.58	0.59	4.23	8.50	0.22	15.01	20.06	0.57	0.01	0.21	0.07	0.02	100.06	42%	44%	14%
1652_X40_p77	50.52	0.77	3.31	11.63	0.28	13.63	19.47	0.58	0.00	0.06	0.07	0.08	100.40	41%	40%	19%
1652_X40_p78	51.78	0.57	2.04	12.33	0.26	13.64	19.16	0.51	0.00	0.05	0.00	0.07	100.41	40%	40%	20%
1652_X42_p81	51.62	0.80	2.73	10.47	0.26	14.40	19.53	0.43	0.01	0.10	0.00	0.07	100.42	41%	42%	17%
1652_X42_p82	51.64	0.65	2.35	10.23	0.30	14.48	20.26	0.40	0.00	0.03	0.00	0.05	100.40	42%	42%	17%
1652_X43_p83	50.58	0.82	3.83	9.80	0.20	13.66	20.33	0.49	0.00	0.07	0.00	0.06	99.85	43%	40%	16%
1652_X43_p84	50.65	0.78	3.65	11.01	0.13	13.45	19.90	0.46	0.02	0.10	0.00	0.06	100.20	42%	40%	18%
1652_X44_p85	51.07	0.44	4.26	7.90	0.16	14.49	20.89	0.58	0.01	0.71	0.10	0.06	100.65	44%	43%	13%
1652_X44_p86	50.88	0.42	3.63	8.94	0.11	14.09	20.59	0.54	0.00	0.64	0.11	0.05	99.99	44%	42%	15%
1652_X45_p87	52.06	0.54	2.48	10.27	0.17	14.20	20.13	0.43	0.00	0.05	0.06	0.04	100.43	42%	41%	17%
1652_X45_p88	51.94	0.69	2.43	10.76	0.14	14.23	20.01	0.45	0.01	0.03	0.05	0.08	100.81	42%	41%	17%
1652_X46_p89	52.19	0.63	2.65	11.74	0.28	13.76	19.14	0.53	0.00	0.01	0.01	0.07	101.01	40%	40%	19%
1652_X46_p90	51.83	0.82	3.01	8.88	0.19	15.01	20.14	0.39	0.00	0.08	0.02	0.11	100.48	42%	44%	14%
1652_X47_p91	51.75	0.65	3.19	9.10	0.27	14.68	20.74	0.40	0.00	0.16	0.01	0.04	101.00	43%	42%	15%
1652_X47_p92	51.92	0.60	2.80	9.22	0.17	14.61	20.28	0.44	0.00	0.18	0.02	0.04	100.28	42%	43%	15%
1652_X48_p93	52.29	0.57	2.90	7.91	0.17	15.07	21.34	0.42	0.00	0.14	0.06	0.05	100.92	44%	43%	13%
1652_X48_p94	51.93	0.61	2.32	8.20	0.15	15.34	21.32	0.33	0.01	0.10	0.00	0.08	100.40	43%	44%	13%
1652_X49_p95	51.93	0.59	2.08	11.60	0.24	13.56	19.89	0.46	0.00	0.05	0.06	0.05	100.49	42%	39%	19%
1652_X49_p96	51.46	0.84	3.34	8.66	0.17	14.67	20.87	0.37	0.00	0.15	0.00	0.06	100.60	43%	42%	14%
1652_X5_p7	50.47	0.75	3.45	10.58	0.25	14.30	19.80	0.55	0.00	0.09	0.05	0.09	100.38	41%	41%	17%
1652_X5_p8	50.09	0.80	3.38	9.88	0.23	14.46	20.33	0.48	0.02	0.06	0.00	0.06	99.78	42%	42%	16%
1652_X50_p97	52.08	0.71	2.83	8.47	0.15	14.69	21.57	0.40	0.00	0.04	0.02	0.02	100.98	44%	42%	14%
1652_X50_p98	53.11	0.37	2.50	7.95	0.17	16.53	19.54	0.32	0.01	0.41	0.01	0.06	100.98	40%	47%	13%
1652_X51_p100	51.12	0.83	3.03	10.45	0.28	14.18	19.86	0.53	0.00	0.12	0.03	0.02	100.46	42%	41%	17%
1652_X51_p99	51.46	0.65	3.20	10.08	0.21	14.29	20.48	0.50	0.00	0.05	0.03	0.04	100.99	42%	41%	16%
1652_X52_p101	52.20	0.63	2.65	8.44	0.17	15.37	20.46	0.34	0.00	0.05	0.03	0.03	100.37	42%	44%	14%
1652_X52_p102	50.41	0.71	4.58	7.57	0.15	14.61	20.74	0.51	0.00	0.45	0.00	0.02	99.76	44%	43%	13%
1652_X53_p103	51.77	0.68	3.02	9.37	0.18	14.51	20.76	0.38	0.00	0.06	0.07	0.02	100.83	43%	42%	15%

1652_X53_p104	51.33	0.74	3.23	8.42	0.20	14.75	21.14	0.42	0.00	0.08	0.03	0.08	100.43	44%	43%	14%
1652_X54_p105	51.97	0.71	2.92	9.36	0.25	15.24	20.46	0.35	0.00	0.00	0.05	0.07	101.39	42%	43%	15%
1652_X54_p105	52.34	0.58	2.55	8.99	0.24	15.20	20.01	0.39	0.00	0.02	0.01	0.02	100.35	42%	44%	15%
1652_X54_p106	51.12	0.73	2.56	10.26	0.31	14.23	19.87	0.52	0.01	0.07	0.00	0.07	99.75	42%	42%	17%
1652_X55_p107	52.43	0.63	2.56	9.38	0.21	15.36	19.83	0.38	0.01	0.04	0.03	0.01	100.86	41%	44%	15%
1652_X55_p108	51.09	0.74	3.28	8.47	0.21	14.76	21.25	0.43	0.00	0.15	0.00	0.05	100.43	44%	42%	14%
1652_X56_p109	50.85	0.69	3.01	10.50	0.24	14.02	19.36	0.47	0.00	0.12	0.05	0.01	99.33	41%	41%	17%
1652_X56_p110	51.99	0.76	2.71	9.76	0.23	14.73	20.18	0.45	0.00	0.05	0.10	0.02	100.99	42%	42%	16%
1652_X57_p111	50.31	1.00	4.07	10.19	0.16	13.92	20.26	0.50	0.01	0.02	0.00	0.07	100.51	43%	41%	17%
1652_X57_p112	52.11	0.66	2.77	8.81	0.26	15.03	20.80	0.41	0.01	0.11	0.03	0.06	101.07	43%	43%	14%
1652_X57_p112	51.84	0.65	2.68	8.32	0.23	14.98	20.62	0.32	0.02	0.11	0.02	0.13	99.93	43%	43%	14%
1652_X58_p113	51.95	0.44	3.14	8.11	0.15	15.12	20.97	0.48	0.00	0.31	0.00	0.09	100.76	43%	44%	13%
1652_X58_p114	52.03	0.30	2.75	7.81	0.17	15.37	20.54	0.56	0.00	0.75	0.12	0.04	100.44	43%	45%	13%
1652_X59_p115	50.64	0.66	4.24	8.33	0.15	14.82	20.42	0.47	0.00	0.70	0.02	0.05	100.50	43%	43%	14%
1652_X59_p116	50.53	0.81	3.35	8.93	0.16	14.45	21.02	0.43	0.00	0.11	0.00	0.07	99.86	44%	42%	14%
1652_X6_p10	50.40	0.75	3.35	8.54	0.16	14.93	21.30	0.41	0.00	0.06	0.00	0.09	99.99	44%	43%	14%
1652_X6_p9	50.65	0.76	3.16	10.60	0.19	14.16	20.20	0.50	0.00	0.18	0.00	0.05	100.45	42%	41%	17%
1652_X60_p117	51.46	0.82	3.09	9.98	0.26	14.42	20.20	0.47	0.01	0.01	0.03	0.07	100.81	42%	42%	16%
1652_X60_p118	51.08	0.77	3.29	8.58	0.21	14.78	20.93	0.41	0.01	0.03	0.04	0.08	100.22	43%	43%	14%
1652_X61_p119	51.33	0.86	2.65	11.39	0.28	14.20	19.32	0.54	0.00	0.02	0.11	0.04	100.73	40%	41%	19%
1652_X61_p120	51.68	0.56	2.73	8.08	0.21	15.26	20.96	0.40	0.00	0.14	0.00	0.06	100.07	43%	44%	13%
1652_X62_p121	50.65	0.74	5.58	7.93	0.16	14.00	20.88	0.50	0.01	0.28	0.03	0.07	100.83	45%	42%	13%
1652_X62_p122	52.43	0.63	2.96	7.26	0.15	15.46	21.26	0.31	0.00	0.24	0.00	0.03	100.74	44%	44%	12%
1652_X63_p123	51.16	0.80	3.26	10.35	0.25	14.25	20.03	0.48	0.00	0.08	0.13	0.05	100.83	42%	41%	17%
1652_X63_p124	51.37	0.82	3.22	10.17	0.20	14.17	20.26	0.51	0.01	0.02	0.03	0.06	100.84	42%	41%	17%
1652_X64_p125	51.45	0.82	2.95	10.50	0.19	14.21	19.77	0.45	0.00	0.01	0.01	0.07	100.42	41%	41%	17%
1652_X64_p126	52.35	0.77	2.19	10.35	0.27	14.59	19.36	0.48	0.01	0.00	0.02	0.01	100.40	41%	43%	17%
1652_X65_p127	51.94	0.81	2.20	9.76	0.21	14.92	20.39	0.38	0.00	0.00	0.06	0.05	100.72	42%	43%	16%
1652_X65_p128	51.36	0.86	3.44	8.50	0.24	14.65	21.04	0.43	0.00	0.04	0.10	0.07	100.72	44%	42%	14%
1652_X66_p129	51.10	0.91	3.66	8.57	0.19	14.73	21.18	0.39	0.00	0.11	0.00	0.05	100.90	44%	42%	14%
1652_X66_p130	50.65	0.82	3.13	9.48	0.17	14.51	20.59	0.48	0.00	0.14	0.00	0.03	100.00	43%	42%	15%
1652_X67_p131	50.82	0.77	4.17	9.42	0.20	14.12	20.23	0.55	0.00	0.13	0.01	0.09	100.51	43%	42%	16%
1652_X67_p132	52.46	0.40	2.94	7.95	0.17	15.25	20.58	0.46	0.01	0.24	0.02	0.08	100.57	43%	44%	13%
1652_X68_p133	52.07	0.71	2.64	9.60	0.25	14.46	20.58	0.41	0.00	0.07	0.09	0.02	100.90	43%	42%	16%
1652_X68_p134	52.17	0.64	2.48	8.88	0.20	14.77	21.28	0.37	0.00	0.08	0.01	0.04	100.93	44%	42%	14%
1652_X69_p135	51.14	0.69	3.30	11.98	0.29	13.24	19.29	0.73	0.01	0.05	0.01	0.04	100.76	41%	39%	20%
1652_X69_p136	51.26	0.78	3.26	8.38	0.17	14.44	21.07	0.43	0.00	0.03	0.03	0.00	99.85	44%	42%	14%
1652_X7_p11	50.36	0.74	3.26	10.38	0.22	14.20	19.94	0.56	0.00	0.11	0.00	0.09	99.86	42%	41%	17%
1652_X7_p12	50.77	0.74	3.99	7.66	0.21	15.09	21.01	0.43	0.00	0.16	0.03	0.00	100.10	44%	44%	12%
1652_X70_p137	52.20	0.64	2.45	8.55	0.18	15.25	21.19	0.31	0.00	0.00	0.02	0.03	100.83	43%	43%	14%
1652_X70_p138	51.54	0.72	2.97	8.82	0.16	14.69	20.68	0.38	0.01	0.14	0.05	0.05	100.21	43%	43%	14%
1652_X71_p139	51.58	0.84	2.26	9.51	0.24	14.94	20.55	0.43	0.00	0.04	0.04	0.03	100.46	42%	43%	15%
1652_X71_p140	51.83	0.70	2.03	9.47	0.19	14.92	19.92	0.43	0.01	0.00	0.00	0.04	99.53	41%	43%	15%
1652_X72_p141	51.42	0.65	2.60	9.54	0.31	14.66	20.48	0.40	0.00	0.05	0.00	0.06	100.18	42%	42%	15%
1652_X72_p142	51.99	0.52	2.61	8.61	0.20	15.67	20.16	0.43	0.01	0.09	0.07	0.04	100.39	41%	45%	14%
1652_X74_p145	52.25	0.65	2.05	9.39	0.25	15.13	20.48	0.33	0.00	0.00	0.09	0.04	100.67	42%	43%	15%
1652_X74_p146	51.72	0.71	2.77	7.93	0.12	15.51	20.99	0.34	0.01	0.07	0.03	0.06	100.26	43%	44%	13%
1652_X75_p147	52.48	0.62	1.89	9.77	0.19	15.17	19.86	0.45	0.00	0.00	0.00	0.00	100.43	41%	43%	16%

1652_X75_p148	50.92	0.82	3.54	8.02	0.20	14.54	21.19	0.44	0.00	0.19	0.02	0.13	100.01	44%	42%	13%
1652_X76_p149	52.23	0.53	3.48	6.72	0.17	15.37	21.33	0.44	0.01	0.23	0.09	0.08	100.69	44%	45%	11%
1652_X76_p150	51.44	0.58	3.95	6.97	0.15	15.11	21.34	0.50	0.01	0.25	0.04	0.01	100.35	45%	44%	11%
1652_X77_p151	52.14	0.45	2.41	8.63	0.25	15.00	20.69	0.33	0.01	0.07	0.08	0.01	100.07	43%	43%	14%
1652_X77_p152	51.46	0.74	3.56	8.40	0.13	14.84	20.59	0.40	0.01	0.13	0.06	0.04	100.36	43%	43%	14%
1652_X78_p153	51.51	0.69	2.59	8.75	0.26	15.18	21.03	0.35	0.00	0.00	0.05	0.00	100.40	43%	43%	14%
1652_X78_p154	50.83	0.86	3.35	9.17	0.19	14.47	20.87	0.50	0.00	0.07	0.00	0.05	100.36	43%	42%	15%
1652_X79_p155	51.85	0.58	2.41	8.38	0.15	15.19	21.20	0.36	0.00	0.03	0.02	0.08	100.24	43%	43%	13%
1652_X79_p156	51.87	0.62	2.64	8.41	0.17	15.03	20.86	0.43	0.02	0.09	0.01	0.03	100.18	43%	43%	14%
1652_X8_p13	51.38	0.78	2.49	10.03	0.28	15.09	19.70	0.47	0.00	0.06	0.00	0.05	100.33	41%	43%	16%
1652_X8_p14	51.28	0.77	2.27	10.56	0.23	15.07	19.89	0.45	0.00	0.04	0.08	0.02	100.66	41%	43%	17%
1652_X80_p157	51.57	0.74	3.03	9.68	0.16	14.44	20.50	0.44	0.01	0.00	0.03	0.02	100.62	43%	42%	16%
1652_X81_p159	51.42	0.65	2.67	10.91	0.26	14.13	19.33	0.46	0.00	0.04	0.09	0.04	100.01	41%	41%	18%
1652_X81_p160	50.55	0.86	3.81	8.67	0.25	14.13	20.84	0.41	0.00	0.31	0.03	0.05	99.92	44%	42%	14%
1652_X82_p161	51.68	0.50	2.38	8.49	0.20	15.25	20.86	0.41	0.00	0.13	0.05	0.06	100.02	43%	44%	14%
1652_X82_p162	51.08	0.64	3.21	8.57	0.21	14.69	20.93	0.46	0.00	0.17	0.04	0.06	100.06	44%	43%	14%
1652_X83_p163	51.53	0.73	2.60	8.87	0.21	14.86	20.98	0.42	0.01	0.07	0.09	0.05	100.42	43%	43%	14%
1652_X83_p164	50.94	0.73	3.24	7.85	0.20	14.69	21.45	0.40	0.00	0.07	0.02	0.08	99.68	45%	43%	13%
1652_X84_p165	51.62	0.74	2.46	11.57	0.24	14.30	18.24	0.56	0.01	0.21	0.01	0.07	100.02	39%	42%	19%
1652_X84_p165	51.12	0.67	2.41	12.37	0.29	14.61	17.51	0.51	0.00	0.17	0.00	0.06	99.71	37%	43%	20%
1652_X84_p166	50.90	0.81	3.52	8.86	0.12	14.67	20.85	0.47	0.00	0.10	0.06	0.10	100.46	43%	42%	14%
1652_X85_p167	51.35	0.78	3.59	8.93	0.21	14.53	20.93	0.42	0.00	0.09	0.04	0.11	100.98	43%	42%	14%
1652_X85_p168	51.59	0.72	3.21	8.80	0.18	14.74	20.56	0.37	0.00	0.11	0.02	0.06	100.35	43%	43%	14%
1652_X86_p169	50.78	0.69	3.37	8.79	0.16	14.75	21.13	0.42	0.01	0.11	0.03	0.06	100.30	44%	42%	14%
1652_X86_p170	51.96	0.63	2.40	10.41	0.20	15.20	20.03	0.33	0.00	0.00	0.01	0.10	101.27	41%	43%	16%
1652_X9_p15	50.46	0.62	2.71	12.33	0.27	13.72	19.72	0.50	0.00	0.05	0.00	0.03	100.41	41%	39%	20%
1652_X9_p16	50.05	0.65	2.81	11.97	0.29	13.59	19.75	0.52	0.01	0.04	0.00	0.04	99.71	41%	39%	19%
PAL-002-I_px23	51.13	0.73	1.86	12.33	0.30	14.19	18.96	0.44	0.00	0.05	0.00	0.02	100.01	39%	41%	20%
PAL-002-I_px24	51.06	0.78	1.66	10.29	0.28	14.79	19.68	0.37	0.02	0.01	0.00	0.06	98.99	41%	43%	17%
PAL-002-I_px25	51.37	0.49	1.21	18.31	0.48	22.32	4.07	0.15	0.06	0.02	0.05	0.04	98.57	8%	63%	29%
PAL-002-I_px31	51.09	0.55	1.65	11.98	0.29	14.02	19.19	0.47	0.01	0.03	0.00	0.03	99.31	40%	41%	19%
PAL-002-I_px35	50.36	0.63	4.38	7.92	0.12	15.25	20.75	0.42	0.01	0.30	0.00	0.04	100.18	43%	44%	13%
PAL-002-I_px36	51.27	0.69	2.09	10.24	0.22	16.08	18.69	0.32	0.02	0.02	0.04	0.02	99.69	38%	46%	16%
PAL-002-I_px39	50.88	0.60	3.23	7.85	0.15	15.53	20.99	0.33	0.01	0.18	0.00	0.05	99.80	43%	44%	13%
PAL-002-I_px40	50.29	0.69	3.63	7.70	0.18	15.17	20.60	0.38	0.00	0.24	0.01	0.10	98.99	43%	44%	13%
PAL-002-I_px41	50.59	0.73	3.65	7.69	0.11	15.19	20.82	0.44	0.00	0.34	0.02	0.08	99.67	43%	44%	13%
PAL-002-I_px42	51.04	0.62	3.51	7.54	0.14	15.56	20.68	0.48	0.00	0.33	0.01	0.00	99.92	43%	45%	12%
PAL-002-I_px45	52.25	0.62	1.24	10.48	0.28	15.86	18.62	0.25	0.00	0.01	0.03	0.04	99.71	38%	45%	17%
PAL-002-I_px57	51.70	0.52	1.40	10.25	0.32	15.48	18.54	0.30	0.00	0.00	0.02	0.09	98.62	39%	45%	17%
PAL-002-I_px58	51.71	0.58	1.45	10.33	0.26	15.48	19.26	0.32	0.00	0.05	0.00	0.04	99.48	39%	44%	17%
PAL-002-I_px60	51.61	0.59	1.51	10.66	0.21	15.59	18.94	0.31	0.02	0.00	0.02	0.05	99.51	39%	44%	17%
PAL-002-I_px62	52.01	0.62	1.26	11.10	0.34	15.82	18.68	0.38	0.01	0.03	0.02	0.04	100.33	38%	45%	18%
PAL-002-I_px65	50.81	0.62	2.52	8.03	0.21	15.54	20.99	0.37	0.01	0.08	0.00	0.03	99.20	43%	44%	13%
PAL-002-I_px66	51.41	0.68	2.56	7.20	0.11	15.16	21.11	0.33	0.02	0.13	0.00	0.05	98.76	44%	44%	12%
PAL-002-I_px71	52.45	0.62	1.21	11.85	0.37	15.81	17.15	0.32	0.00	0.03	0.00	0.16	99.96	35%	45%	19%
PAL-002-I_px72	51.87	0.66	1.36	11.11	0.34	15.02	19.18	0.33	0.01	0.00	0.10	0.06	100.04	39%	43%	18%
PAL-002-I_px84	52.01	0.66	1.50	10.23	0.35	14.94	19.45	0.35	0.01	0.00	0.01	0.02	99.52	40%	43%	17%
PAL-002-I_px85	51.50	0.61	2.95	7.75	0.20	15.38	20.82	0.37	0.02	0.18	0.01	0.01	99.80	43%	44%	13%

PAL-002-I_px86	50.76	0.71	3.30	7.80	0.17	15.34	21.40	0.26	0.00	0.21	0.01	0.12	100.09	44%	44%	12%
PAL-002-I_px87	50.81	0.68	3.26	7.71	0.19	15.08	21.22	0.34	0.00	0.18	0.00	0.07	99.53	44%	44%	12%
PAL-002-I_px88	51.90	0.57	2.62	7.33	0.15	15.94	20.75	0.30	0.01	0.24	0.01	0.07	99.90	43%	46%	12%
PAL-002-I_px89	50.28	0.73	3.33	8.56	0.23	14.85	20.57	0.43	0.00	0.16	0.02	0.05	99.22	43%	43%	14%
PAL-002-I_px90	50.66	0.74	3.62	8.39	0.18	15.06	20.76	0.42	0.01	0.24	0.09	0.00	100.16	43%	43%	14%
PAL-002-I_px95	51.18	0.60	1.54	10.94	0.33	15.29	18.89	0.34	0.01	0.04	0.00	0.07	99.23	39%	44%	18%
PAL-002-I_px96	51.47	0.76	1.76	10.19	0.26	15.02	19.40	0.32	0.02	0.04	0.06	0.01	99.31	40%	43%	16%
PAL-002-I_px97	51.28	0.65	1.58	10.37	0.23	14.99	19.16	0.41	0.00	0.02	0.00	0.10	98.79	40%	43%	17%
PAL-002-I_px98	51.94	0.61	1.55	9.74	0.25	15.77	19.03	0.33	0.02	0.05	0.00	0.04	99.34	39%	45%	16%
PAL-002-I_px101	51.32	0.67	1.74	10.68	0.26	15.07	19.50	0.38	0.00	0.03	0.02	0.08	99.75	40%	43%	17%
PAL-002-I_px102	51.95	0.58	1.50	9.59	0.27	15.46	19.51	0.35	0.00	0.10	0.03	0.02	99.37	40%	44%	15%
PAL-002-I_px104	52.32	0.58	1.33	11.59	0.37	14.56	19.03	0.34	0.01	0.00	0.11	0.04	100.28	39%	42%	19%
PAL-002-I_px107	51.04	0.84	2.27	10.72	0.23	14.91	19.23	0.34	0.01	0.02	0.06	0.04	99.71	40%	43%	17%
PAL-002-I_px108	51.72	0.58	1.39	10.03	0.25	15.18	19.26	0.32	0.00	0.00	0.00	0.05	98.78	40%	44%	16%
PAL-002-I_px127	52.50	0.67	1.30	10.59	0.30	15.74	18.89	0.38	0.01	0.00	0.01	0.03	100.42	39%	45%	17%
PAL-002-I_px128	52.59	0.65	1.44	9.82	0.31	15.42	19.15	0.31	0.02	0.01	0.07	0.07	99.86	40%	44%	16%
PAL-002-I_px129	52.34	0.59	1.51	10.44	0.25	15.72	19.01	0.29	0.00	0.06	0.01	0.06	100.29	39%	45%	17%
PAL-002-I_px130	51.39	0.88	2.16	10.03	0.34	15.14	19.47	0.34	0.02	0.00	0.10	0.07	99.95	40%	44%	16%
PAL-002-I_px131	51.68	0.75	1.67	10.73	0.35	15.26	18.93	0.35	0.01	0.00	0.00	0.07	99.79	39%	44%	17%
PAL-002-I_px132	52.09	0.89	1.88	10.70	0.26	14.98	19.28	0.41	0.05	0.00	0.04	0.03	100.62	40%	43%	17%
PAL-002-I_px133	51.59	0.78	1.74	10.39	0.27	14.88	19.28	0.30	0.01	0.00	0.03	0.02	99.29	40%	43%	17%
PAL-002-I_px134	51.60	0.71	1.65	10.42	0.38	14.98	19.29	0.32	0.00	0.05	0.00	0.03	99.43	40%	43%	17%
PAL-002-I_px137	51.88	0.64	1.48	10.64	0.20	14.99	18.84	0.36	0.02	0.02	0.05	0.02	99.13	39%	43%	17%
PAL-002-I_px138	51.95	0.69	1.64	10.26	0.25	15.12	19.56	0.37	0.01	0.01	0.10	0.02	99.98	40%	43%	16%
PAL-002-I_px149	51.14	0.72	1.81	9.81	0.27	15.04	19.74	0.37	0.00	0.00	0.02	0.07	98.98	41%	43%	16%
PAL-002-I_px150	51.94	0.79	1.74	10.16	0.22	15.04	19.35	0.38	0.03	0.00	0.00	0.03	99.68	40%	43%	16%
PAL-002-I_px159	52.09	0.58	1.45	10.35	0.30	15.45	18.93	0.36	0.00	0.06	0.00	0.04	99.62	39%	44%	17%
PAL-002-I_px160	51.35	0.82	1.81	10.77	0.23	15.09	18.53	0.38	0.03	0.00	0.00	0.04	99.04	39%	44%	18%
PAL-002-I_px189	51.78	0.68	1.44	10.76	0.29	15.05	19.02	0.35	0.00	0.01	0.02	0.06	99.46	39%	43%	17%
PAL-002-I_px191	52.22	0.61	1.49	9.87	0.29	15.09	19.22	0.33	0.01	0.00	0.00	0.05	99.18	40%	44%	16%
PAL-002-I_px192	51.46	0.77	1.87	9.82	0.28	15.14	19.78	0.32	0.02	0.03	0.00	0.08	99.57	41%	43%	16%
PAL-002-I_px193	51.04	0.76	2.99	7.58	0.17	15.27	20.91	0.29	0.01	0.14	0.00	0.02	99.18	43%	44%	12%
PAL-002-I_px194	50.98	0.69	3.48	8.34	0.19	14.80	20.18	0.47	0.01	0.20	0.07	0.02	99.43	43%	44%	14%
PAL-002-I_px197	51.95	0.59	1.42	10.34	0.26	14.71	20.09	0.31	0.00	0.05	0.05	0.07	99.83	41%	42%	17%
PAL-002-I_px198	51.96	0.66	1.52	10.38	0.28	15.20	19.44	0.35	0.02	0.02	0.00	0.02	99.84	40%	43%	17%
PAL-002-II_px1	51.25	0.69	3.79	7.92	0.20	14.84	19.98	0.42	0.01	0.17	0.12	0.04	99.43	43%	44%	13%
PAL-002-II_px2	51.30	0.63	3.66	7.33	0.18	15.06	19.72	0.44	0.00	0.24	0.04	0.10	98.69	43%	45%	12%
PAL-002-II_px9	52.82	0.58	1.25	10.20	0.30	15.00	18.67	0.34	0.00	0.01	0.02	0.08	99.28	39%	44%	17%
PAL-002-II_px13	54.57	0.51	1.18	17.16	0.40	23.71	2.74	0.09	0.02	0.04	0.00	0.04	100.46	6%	67%	27%
PAL-002-II_px15	50.80	0.57	4.92	7.63	0.08	14.11	19.52	0.57	0.01	0.31	0.05	0.00	98.57	43%	44%	13%
PAL-002-II_px29	52.15	0.58	2.48	7.35	0.13	15.87	19.93	0.27	0.00	0.18	0.00	0.00	98.95	42%	46%	12%
PAL-002-II_px30	51.99	0.72	1.64	10.18	0.27	15.03	18.39	0.30	0.01	0.04	0.04	0.04	98.66	39%	44%	17%
PAL-002-II_px35	51.74	0.80	1.81	9.86	0.24	15.06	19.06	0.33	0.00	0.04	0.00	0.05	99.00	40%	44%	16%
PAL-002-II_px37	51.81	0.59	2.78	7.15	0.19	15.22	20.28	0.34	0.02	0.27	0.00	0.08	98.73	43%	45%	12%
PAL-002-II_px38	51.04	0.72	3.69	7.88	0.14	14.53	19.98	0.49	0.01	0.28	0.08	0.01	98.85	43%	44%	13%
PAL-002-II_px39	50.66	0.58	5.20	7.08	0.15	14.74	19.85	0.64	0.01	0.32	0.01	0.04	99.27	43%	45%	12%
PAL-002-II_px40	50.97	0.64	3.56	7.44	0.14	15.00	20.04	0.41	0.01	0.31	0.00	0.06	98.59	43%	45%	12%
PAL-002-II_px43	50.99	0.69	3.41	8.17	0.18	15.01	20.09	0.41	0.01	0.10	0.00	0.02	99.08	42%	44%	13%

PAL-002-II_px44	52.51	0.73	2.02	9.81	0.28	14.89	19.11	0.40	0.01	0.03	0.00	0.12	99.89	40%	44%	16%
PAL-002-II_px54	51.91	0.60	2.96	8.22	0.21	15.08	19.42	0.36	0.02	0.03	0.08	0.03	98.91	41%	45%	14%
PAL-002-II_px57	51.33	0.76	3.34	9.15	0.17	14.11	19.50	0.56	0.00	0.26	0.02	0.07	99.28	42%	42%	15%
PAL-002-II_px63	53.16	0.41	1.75	9.26	0.35	14.35	20.52	0.39	0.02	0.02	0.01	0.00	100.24	43%	42%	15%
PAL-002-II_px64	51.44	0.78	2.11	9.67	0.25	14.91	19.09	0.38	0.03	0.00	0.00	0.08	98.74	40%	44%	16%
PAL-002-II_px74	51.56	0.57	2.91	7.10	0.20	15.48	20.27	0.32	0.01	0.19	0.00	0.11	98.72	43%	45%	12%
PAL-002-II_px75	52.26	0.64	1.44	10.62	0.26	15.07	18.20	0.32	0.01	0.02	0.00	0.12	98.96	38%	44%	17%
PAL-002-II_px80	52.08	0.60	1.63	10.14	0.27	15.06	18.61	0.34	0.00	0.06	0.00	0.07	98.85	39%	44%	17%
PAL-002-II_px82	51.84	0.58	1.97	8.81	0.22	16.22	18.74	0.32	0.01	0.00	0.00	0.00	98.70	39%	47%	14%
PAL-002-II_px85	50.75	0.70	3.72	8.07	0.15	14.75	19.66	0.41	0.01	0.25	0.04	0.01	98.53	42%	44%	14%
PAL-002-II_px86	51.14	0.69	3.17	7.76	0.14	15.20	20.05	0.32	0.01	0.17	0.00	0.00	98.65	42%	45%	13%

Supplementary material 8: SIMS O-isotope data

Table S8.1. Clinopyroxene (1651) and standard (NRM-AG-1) SIMS $\delta^{18}O$ values for La Poruña.

Sample ID	18O/16O drift corrected	± absolute	δ18O‰	± ‰	Stage position (µm)		Field ap. (digits)	
					x	y	x	y
NRM-AG-1_20171002_@2	0.00202305	0.00000019	5.47	0.18	-4465	-1493	-4	-18
NRM-AG-1_20171002_@3	0.00202275	0.00000019	5.33	0.18	-4465	-1423	-5	-19
NRM-AG-1_20171002_@4	0.00202344	0.00000012	5.67	0.17	-4465	-1353	-6	-19
NRM-AG-1_20171002_@5	0.00202300	0.00000012	5.45	0.17	-4465	-1283	-6	-19
NRM-AG-1_20171002_@6	0.00202277	0.00000019	5.33	0.18	-4465	-1213	-6	-19
NRM-AG-1_20171002_@7	0.00202310	0.00000024	5.50	0.20	-4465	-1143	-6	-19
NRM-AG-1_20171002_@8	0.00202319	0.00000017	5.54	0.18	-4465	-1073	-7	-19
NRM-AG-1_20171002_@9	0.00202302	0.00000021	5.46	0.19	-4465	-1003	-6	-18
1651_20171002_@2a	0.00202319	0.00000022	5.55	0.19	261	-5189	17	-25
1651_20171002_@2b	0.00202362	0.00000016	5.76	0.17	384	-5114	17	-23
1651_20171002_@30a	0.00202323	0.00000019	5.56	0.18	6335	-747	41	-6
1651_20171002_@30b	0.00202314	0.00000019	5.52	0.18	6436	-665	41	-7
NRM-AG-1_20171002_@10	0.00202295	0.00000012	5.43	0.17	-4465	-933	-7	-19
NRM-AG-1_20171002_@11	0.00202239	0.00000016	5.15	0.18	-4465	-863	-7	-18
NRM-AG-1_20171002_@13	0.00202296	0.00000012	5.43	0.17	-4475	-713	0	-15
1651_20171002_@3a	0.00202380	0.00000018	5.85	0.18	-324	-4425	20	-20
1651_20171002_@3b	0.00202412	0.00000015	6.01	0.17	-241	-4403	19	-20
1651_20171002_@3c	0.00202400	0.00000019	5.95	0.18	-105	-4419	17	-20
1651_20171002_@3d	0.00202388	0.00000020	5.89	0.18	-20	-4421	16	-21
1651_20171002_@3e	0.00202335	0.00000015	5.62	0.17	97	-4406	16	-21
NRM-AG-1_20171002_@14	0.00202323	0.00000013	5.56	0.17	-4475	-643	-6	-17
NRM-AG-1_20171002_@15	0.00202292	0.00000012	5.41	0.17	-4475	-573	-6	-17
1651_20171002_@4a	0.00202358	0.00000021	5.74	0.19	569	-4180	17	-18
1651_20171002_@4b	0.00202378	0.00000015	5.84	0.17	952	-4432	19	-21
1651_20171002_@4c	0.00202333	0.00000012	5.61	0.17	1325	-4264	23	-18
1651_20171002_@6a	0.00202405	0.00000017	5.97	0.18	2784	-3927	27	-19
1651_20171002_@6b	0.00202333	0.00000026	5.61	0.20	2907	-3865	27	-19
NRM-AG-1_20171002_@16	0.00202301	0.00000013	5.45	0.17	-4476	-484	-7	-17
NRM-AG-1_20171002_@17	0.00202298	0.00000017	5.44	0.18	-4476	-414	-7	-18
1651_20171002_@6c	0.00202275	0.00000017	5.33	0.18	3078	-3944	29	-19
1651_20171002_@7a	0.00202419	0.00000019	6.04	0.18	-649	-3418	14	-19
1651_20171002_@7b	0.00202317	0.00000014	5.54	0.17	-439	-3416	12	-19
1651_20171002_@7c	0.00202329	0.00000019	5.59	0.18	-193	-3731	13	-22
1651_20171002_@7d	0.00202300	0.00000012	5.45	0.17	69	-3729	13	-21
NRM-AG-1_20171002_@18	0.00202310	0.00000012	5.50	0.17	-4476	-344	-6	-17
NRM-AG-1_20171002_@19	0.00202266	0.00000013	5.28	0.17	-4476	-274	-5	-18
1651_20171002_@8a	0.00202345	0.00000013	5.67	0.17	662	-3635	17	-21
1651_20171002_@8b	0.00202266	0.00000015	5.28	0.17	918	-3581	17	-22
1651_20171002_@8c	0.00202266	0.00000014	5.28	0.17	1278	-3623	19	-22
1651_20171002_@8d	0.00202312	0.00000015	5.51	0.17	1461	-3392	20	-18

1651_20171002_@12a	0.00202314	0.00000019	5.52	0.18	4358	-2126	33	-9
NRM-AG-1_20171002_@20	0.00202292	0.00000016	5.41	0.18	-4476	-204	-8	-18
NRM-AG-1_20171002_@21	0.00202328	0.00000012	5.59	0.17	-4476	-134	-5	-18
1651_20171002_@12b	0.00202274	0.00000013	5.32	0.17	4455	-2628	37	-12
1651_20171002_@13a	0.00202321	0.00000020	5.55	0.18	4824	-3078	41	-12
1651_20171002_@13b	0.00202263	0.00000017	5.27	0.18	4838	-3377	42	-13
1651_20171002_@16a	0.00202441	0.00000020	6.15	0.19	-505	-2481	16	-15
1651_20171002_@16b	0.00202407	0.00000022	5.98	0.19	-396	-2444	18	-16
NRM-AG-1_20171002_@22	0.00202318	0.00000012	5.54	0.17	-4476	-64	-4	-17
NRM-AG-1_20171002_@23	0.00202359	0.00000016	5.74	0.17	-4476	6	-4	-17
1651_20171002_@16c	0.00202332	0.00000017	5.61	0.18	-282	-2424	17	-16
1651_20171002_@16d	0.00202348	0.00000017	5.69	0.18	-179	-2390	16	-17
1651_20171002_@16e	0.00202283	0.00000024	5.37	0.19	-52	-2354	16	-16
1651_20171002_@20a	0.00202311	0.00000012	5.51	0.17	3427	-1924	30	-12
1651_20171002_@20b	0.00202306	0.00000016	5.48	0.17	3377	-1650	30	-10
NRM-AG-1_20171002_@24	0.00202302	0.00000021	5.46	0.19	-4476	76	-4	-17
NRM-AG-1_20171002_@25	0.00202278	0.00000012	5.34	0.17	-4476	146	-4	-17
1651_20171002_@20c	0.00202304	0.00000019	5.47	0.18	3676	-1476	30	-10
1651_20171002_@21a	0.00202247	0.00000014	5.19	0.17	4786	-1381	37	-7
1651_20171002_@21b	0.00202246	0.00000017	5.18	0.18	4869	-1305	37	-7
1651_20171002_@21c	0.00202242	0.00000021	5.16	0.19	4948	-1200	38	-7
NRM-AG-1_20171002_@26	0.00202290	0.00000020	5.40	0.18	-4476	216	-4	-16
NRM-AG-1_20171002_@27	0.00202316	0.00000017	5.53	0.18	-4476	286	-5	-17
1651_20171002_@22b	0.00202287	0.00000019	5.39	0.18	5151	-1973	42	-9
1651_20171002_@22c	0.00202289	0.00000016	5.39	0.18	5383	-1827	42	-8
1651_20171002_@23a	0.00202421	0.00000019	6.05	0.18	-1151	-1712	15	-14
1651_20171002_@23b	0.00202340	0.00000012	5.65	0.17	-968	-1872	14	-17
1651_20171002_@23c	0.00202343	0.00000014	5.67	0.17	-686	-1583	13	-14
NRM-AG-1_20171002_@28	0.00202252	0.00000014	5.21	0.17	-4476	356	-3	-16
NRM-AG-1_20171002_@29	0.00202262	0.00000015	5.26	0.17	-4477	461	-4	-17
1651_20171002_@25a	0.00202463	0.00000021	6.26	0.19	955	-1349	18	-10
1651_20171002_@25b	0.00202356	0.00000017	5.73	0.18	851	-1449	17	-12
1651_20171002_@25c	0.00202337	0.00000022	5.64	0.19	742	-1573	16	-13
1651_20171002_@25d	0.00202405	0.00000016	5.97	0.18	635	-1683	17	-13
1651_20171002_@25e	0.00202364	0.00000017	5.77	0.18	496	-1867	17	-14
NRM-AG-1_20171002_@30	0.00202299	0.00000012	5.44	0.17	-4477	531	-3	-16
NRM-AG-1_20171002_@31	0.00202289	0.00000021	5.40	0.19	-4477	601	-4	-16
1651_20171002_@25f	0.00202332	0.00000027	5.61	0.21	377	-2020	17	-15
1651_20171002_@26a	0.00202428	0.00000024	6.09	0.20	1564	-1376	21	-11
1651_20171002_@26b	0.00202321	0.00000013	5.55	0.17	1726	-1390	22	-12
1651_20171002_@26c	0.00202401	0.00000017	5.95	0.18	1907	-1379	21	-12
1651_20171002_@26d	0.00202331	0.00000014	5.61	0.17	2168	-1374	22	-13
NRM-AG-1_20171002_@32	0.00202335	0.00000016	5.62	0.17	-4652	776	-3	-16
NRM-AG-1_20171002_@33	0.00202311	0.00000018	5.51	0.18	-4652	846	-4	-16
1651_20171002_@27a	0.00202356	0.00000024	5.73	0.19	2675	-1229	26	-11
1651_20171002_@27b	0.00202333	0.00000016	5.61	0.18	2745	-1119	25	-10
1651_20171002_@27c	0.00202394	0.00000021	5.92	0.19	2893	-1073	24	-10

1651_20171002_@27d	0.00202325	0.00000017	5.57	0.18	3016	-1052	25	-10
1651_20171002_@27e	0.00202238	0.00000017	5.14	0.18	3162	-992	26	-8
NRM-AG-1_20171002_@34	0.00202282	0.00000023	5.36	0.19	-4652	916	-4	-16
1651_20171002_@28a	0.00202326	0.00000013	5.58	0.17	3920	-745	30	-8
1651_20171002_@28b	0.00202336	0.00000012	5.63	0.17	4111	-529	30	-6
1651_20171002_@28c	0.00202355	0.00000026	5.73	0.20	3923	-451	30	-4
1651_20171002_@29a	0.00202336	0.00000012	5.63	0.17	5348	-639	40	-6
1651_20171002_@29b	0.00202285	0.00000015	5.38	0.17	5462	-629	42	-6
NRM-AG-1_20171002_@36	0.00202353	0.00000015	5.72	0.17	-4652	1056	-5	-16
NRM-AG-1_20171002_@37	0.00202358	0.00000015	5.74	0.17	-4652	1126	-5	-16
1651_20171002_@29c	0.00202294	0.00000015	5.42	0.17	5592	-608	42	-5
1651_20171002_@30c	0.00202290	0.00000015	5.40	0.17	6303	-424	47	-5
1651_20171002_@30d	0.00202208	0.00000016	5.00	0.17	6337	-1002	46	-7
1651_20171002_@31a	0.00202472	0.00000016	6.31	0.18	-1451	-751	11	-12
1651_20171002_@31b	0.00202502	0.00000019	6.45	0.18	-1296	-821	11	-12
NRM-AG-1_20171002_@38	0.00202339	0.00000016	5.64	0.17	-4844	1267	-4	-16
NRM-AG-1_20171002_@39	0.00202248	0.00000016	5.19	0.17	-4844	1267	-3	-16
1651_20171002_@31c	0.00202406	0.00000020	5.98	0.18	-1120	-867	11	-14
1651_20171002_@31d	0.00202345	0.00000012	5.67	0.17	-962	-918	10	-14
1651_20171002_@33a	0.00202516	0.00000023	6.53	0.19	131	-204	26	1
1651_20171002_@33b	0.00202407	0.00000015	5.98	0.17	248	-526	16	-11
1651_20171002_@33c	0.00202387	0.00000017	5.88	0.18	483	-677	16	-12
NRM-AG-1_20171002_@40	0.00202341	0.00000012	5.66	0.17	-4844	1337	-4	-16
NRM-AG-1_20171002_@41	0.00202288	0.00000012	5.39	0.17	-4914	1337	-4	-16
1651_20171002_@33d	0.00202308	0.00000017	5.49	0.18	753	-616	15	-11
1651_20171002_@34a	0.00202403	0.00000015	5.96	0.17	806	90	16	-10
1651_20171002_@34b	0.00202429	0.00000013	6.09	0.17	1023	130	16	-9
1651_20171002_@34c	0.00202306	0.00000018	5.48	0.18	1498	102	16	-9
1651_20171002_@34d	0.00202342	0.00000017	5.66	0.18	1773	129	17	-8
NRM-AG-1_20171002_@42	0.00202286	0.00000019	5.38	0.18	-4914	1267	-4	-16
NRM-AG-1_20171002_@43	0.00202278	0.00000021	5.34	0.19	-4914	1197	-4	-16
1651_20171002_@35a	0.00202364	0.00000019	5.77	0.18	1698	-524	20	-10
1651_20171002_@35b	0.00202416	0.00000016	6.03	0.18	1872	-476	21	-10
1651_20171002_@35c	0.00202361	0.00000013	5.75	0.17	2131	-468	21	-10
1651_20171002_@35d	0.00202351	0.00000014	5.70	0.17	2379	-344	21	-9
1651_20171002_@35e	0.00202321	0.00000017	5.55	0.18	2640	-204	22	-8
NRM-AG-1_20171002_@44	0.00202339	0.00000017	5.64	0.18	-4914	1127	-3	-16
NRM-AG-1_20171002_@45	0.00202257	0.00000019	5.24	0.18	-4914	1057	-2	-16
1651_20171002_@36a	0.00202296	0.00000014	5.43	0.17	3376	-111	25	-7
1651_20171002_@36b	0.00202371	0.00000019	5.81	0.18	3440	48	25	-5
1651_20171002_@36c	0.00202321	0.00000022	5.55	0.19	3475	217	25	-3
1651_20171002_@36d	0.00202377	0.00000022	5.83	0.19	3500	459	21	-1
1651_20171002_@36e	0.00202281	0.00000012	5.36	0.17	3547	645	18	-2
NRM-AG-1_20171002_@47	0.00202262	0.00000021	5.26	0.19	-4914	917	-1	-16
1651_20171002_@37a	0.00202386	0.00000021	5.88	0.19	4349	89	38	-6
1651_20171002_@37b	0.00202376	0.00000019	5.83	0.18	4469	94	39	-8
1651_20171002_@37c	0.00202377	0.00000019	5.83	0.18	4607	112	39	-9

1651_20171002_@37d	0.00202325	0.00000015	5.57	0.17	4781	244	41	-9
1651_20171002_@38a	0.00202348	0.00000020	5.69	0.19	5203	387	44	-13
NRM-AG-1_20171002_@49	0.00202258	0.00000013	5.24	0.17	-4914	777	-3	-25
1651_20171002_@38b	0.00202273	0.00000012	5.32	0.17	5447	509	43	-14
1651_20171002_@38c	0.00202283	0.00000015	5.37	0.17	5650	762	43	-14
1651_20171002_@38d	0.00202265	0.00000019	5.28	0.18	5679	960	44	-13
1651_20171002_@38e	0.00202366	0.00000021	5.78	0.19	5544	1102	45	-12
1651_20171002_@39a	0.00202517	0.00000018	6.53	0.18	-1229	1084	10	-16
NRM-AG-1_20171002_@50	0.00202336	0.00000013	5.63	0.17	-4917	516	-2	-25
1651_20171002_@39b	0.00202475	0.00000020	6.32	0.18	-1196	982	10	-16
1651_20171002_@39c	0.00202455	0.00000016	6.22	0.18	-1161	893	10	-17
1651_20171002_@39d	0.00202431	0.00000012	6.10	0.17	-1097	740	9	-18
1651_20171002_@39e	0.00202388	0.00000012	5.89	0.17	-1072	428	9	-20
1651_20171002_@39f	0.00202398	0.00000014	5.94	0.17	-1002	260	9	-21
NRM-AG-1_20171002_@52	0.00202283	0.00000017	5.37	0.18	-4921	343	-1	-25
NRM-AG-1_20171002_@53	0.00202290	0.00000018	5.40	0.18	-4921	273	0	-25
1651_20171002_@40a	0.00202433	0.00000017	6.11	0.18	-169	1170	13	-14
1651_20171002_@40b	0.00202413	0.00000016	6.01	0.18	-240	944	13	-15
1651_20171002_@40c	0.00202426	0.00000015	6.08	0.17	-12	962	12	-15
1651_20171002_@40d	0.00202367	0.00000012	5.78	0.17	-105	491	13	-19
1651_20171002_@41a	0.00202400	0.00000023	5.95	0.19	565	849	16	-15
NRM-AG-1_20171002_@54	0.00202299	0.00000017	5.45	0.18	-4921	203	-1	-25
NRM-AG-1_20171002_@55	0.00202289	0.00000019	5.39	0.18	-4921	133	0	-25
1651_20171002_@41b	0.00202409	0.00000014	5.99	0.17	756	1006	16	-15
1651_20171002_@41c	0.00202365	0.00000017	5.77	0.18	866	1081	16	-15
1651_20171002_@41d	0.00202372	0.00000015	5.81	0.17	1019	1189	16	-15
1651_20171002_@41e	0.00202351	0.00000016	5.71	0.17	1266	1315	17	-13
1651_20171002_@41f	0.00202351	0.00000012	5.70	0.17	1504	1551	18	-13
NRM-AG-1_20171002_@56	0.00202278	0.00000023	5.34	0.19	-4921	133	0	-25
NRM-AG-1_20171002_@57	0.00202308	0.00000012	5.49	0.17	-4921	-7	1	-25
1651_20171002_@43a	0.00202431	0.00000016	6.10	0.18	2883	2216	27	-9
1651_20171002_@43b	0.00202388	0.00000015	5.89	0.17	2839	2039	26	-9
1651_20171002_@43c	0.00202365	0.00000018	5.77	0.18	2817	1869	25	-11
1651_20171002_@43d	0.00202292	0.00000016	5.41	0.18	3003	1625	24	-13
1651_20171002_@43e	0.00202270	0.00000018	5.30	0.18	2753	1345	23	-14
NRM-AG-1_20171002_@58	0.00202249	0.00000012	5.20	0.17	-4921	-217	1	-26
NRM-AG-1_20171002_@59	0.00202247	0.00000015	5.19	0.17	-4921	-287	0	-26
1651_20171002_@44a	0.00202382	0.00000016	5.86	0.18	3684	2192	31	-11
1651_20171002_@44b	0.00202309	0.00000017	5.49	0.18	3697	2057	30	-12
1651_20171002_@44c	0.00202290	0.00000012	5.40	0.17	3666	1907	30	-13
1651_20171002_@44d	0.00202283	0.00000023	5.37	0.19	3724	1659	28	-15
1651_20171002_@44e	0.00202201	0.00000017	4.96	0.18	3750	1384	24	-20
NRM-AG-1_20171002_@60	0.00202344	0.00000025	5.67	0.20	-4921	-357	0	-26
NRM-AG-1_20171002_@61	0.00202322	0.00000018	5.56	0.18	-4921	-427	1	-25
1651_20171002_@44f	0.00202194	0.00000023	4.92	0.19	3655	1099	16	-23
1651_20171002_@45a	0.00202391	0.00000017	5.90	0.18	4520	1042	58	-27
1651_20171002_@45b	0.00202325	0.00000015	5.58	0.17	4662	1100	52	-20

1651_20171002_@45c	0.00202348	0.00000024	5.69	0.20	4829	1185	47	-17
1651_20171002_@45d	0.00202283	0.00000015	5.36	0.17	4997	1311	44	-15
NRM-AG-1_20171002_@62	0.00202332	0.00000015	5.61	0.17	-4921	-497	1	-26
NRM-AG-1_20171002_@63	0.00202296	0.00000015	5.43	0.17	-4921	-567	2	-26
1651_20171002_@45e	0.00202286	0.00000013	5.38	0.17	5131	1404	45	-13
1651_20171002_@49a	0.00202374	0.00000017	5.82	0.18	130	1677	15	-12
1651_20171002_@49b	0.00202364	0.00000022	5.77	0.19	315	1708	14	-13
1651_20171002_@49c	0.00202360	0.00000015	5.75	0.17	569	1911	14	-10
1651_20171002_@50a	0.00202362	0.00000018	5.76	0.18	1484	1923	19	-11
NRM-AG-1_20171002_@64	0.00202322	0.00000021	5.56	0.19	-4921	-637	1	-26
NRM-AG-1_20171002_@65	0.00202348	0.00000024	5.69	0.20	-4921	-707	2	-26
1651_20171002_@50b	0.00202381	0.00000020	5.85	0.18	1679	1974	19	-11
1651_20171002_@50c	0.00202400	0.00000018	5.95	0.18	1930	2033	20	-10
1651_20171002_@50d	0.00202366	0.00000017	5.78	0.18	2245	2060	22	-9
1651_20171002_@51a	0.00202342	0.00000015	5.66	0.17	4429	2757	40	-8
1651_20171002_@51b	0.00202343	0.00000014	5.67	0.17	4432	2463	38	-11
NRM-AG-1_20171002_@66	0.00202329	0.00000016	5.60	0.17	-4921	-777	2	-26
NRM-AG-1_20171002_@67	0.00202295	0.00000014	5.42	0.17	-4921	-847	2	-26
1651_20171002_@51c	0.00202292	0.00000012	5.41	0.17	4390	2286	38	-12
1651_20171002_@51d	0.00202333	0.00000017	5.61	0.18	4560	2075	38	-14
1651_20171002_@52a	0.00202315	0.00000019	5.53	0.18	5028	2218	44	-12
1651_20171002_@52b	0.00202312	0.00000016	5.51	0.18	5119	2275	44	-12
1651_20171002_@52c	0.00202314	0.00000022	5.52	0.19	5200	2313	44	-12
NRM-AG-1_20171002_@68	0.00202309	0.00000019	5.49	0.18	-4921	-917	2	-26
NRM-AG-1_20171002_@69	0.00202266	0.00000017	5.28	0.18	-4921	-987	3	-26
1651_20171002_@52d	0.00202336	0.00000015	5.63	0.17	5292	2353	46	-12
1651_20171002_@52e	0.00202272	0.00000012	5.31	0.17	5410	2395	46	-11
1651_20171002_@53a	0.00202596	0.00000016	6.92	0.17	-1592	3272	6	-9
1651_20171002_@53b	0.00202516	0.00000013	6.52	0.17	-1593	3112	7	-10
1651_20171002_@53c	0.00202441	0.00000020	6.15	0.19	-1614	2933	7	-12
NRM-AG-1_20171002_@70	0.00202263	0.00000012	5.27	0.17	-4921	-1057	2	-27
NRM-AG-1_20171002_@71	0.00202336	0.00000015	5.63	0.17	-4921	-1197	2	-27
1651_20171002_@53d	0.00202503	0.00000028	6.46	0.21	-1620	2787	7	-13
1651_20171002_@53e	0.00202416	0.00000013	6.03	0.17	-1539	2695	7	-14
1651_20171002_@54a	0.00202527	0.00000012	6.58	0.17	-476	3226	9	-8
1651_20171002_@54b	0.00202506	0.00000020	6.48	0.18	-593	3070	8	-10
1651_20171002_@54c	0.00202455	0.00000012	6.22	0.17	-653	2887	7	-12
NRM-AG-1_20171002_@72	0.00202298	0.00000018	5.44	0.18	-4921	-1267	3	-27
NRM-AG-1_20171002_@73	0.00202300	0.00000012	5.45	0.17	-4921	-1337	3	-27
1651_20171002_@54d	0.00202383	0.00000022	5.87	0.19	-746	2712	8	-12
1651_20171002_@54e	0.00202460	0.00000021	6.25	0.19	-861	2555	7	-14
1651_20171002_@55a	0.00202379	0.00000014	5.84	0.17	218	3656	13	-7
1651_20171002_@55b	0.00202394	0.00000015	5.92	0.17	194	3502	13	-7
1651_20171002_@55c	0.00202503	0.00000012	6.46	0.17	172	3361	13	-7
NRM-AG-1_20171002_@74	0.00202279	0.00000015	5.35	0.17	-4921	-1407	3	-28
1651_20171002_@55d	0.00202418	0.00000023	6.04	0.19	145	3221	12	-9
1651_20171002_@55e	0.00202418	0.00000012	6.04	0.17	297	3096	12	-9

1651_20171002_@55f	0.00202464	0.00000016	6.27	0.18	376	2935	11	-11
1651_20171002_@56a	0.00202394	0.00000016	5.92	0.18	1195	2472	17	-11
1651_20171002_@56b	0.00202426	0.00000012	6.08	0.17	1312	2523	16	-12
NRM-AG-1_20171002_@76	0.00202296	0.00000016	5.43	0.17	-4921	-1547	3	-28
NRM-AG-1_20171002_@77	0.00202238	0.00000012	5.14	0.17	-4921	-1617	3	-29
1651_20171002_@56c	0.00202379	0.00000018	5.84	0.18	1470	2636	17	-11
1651_20171002_@56d	0.00202415	0.00000018	6.02	0.18	1726	2900	19	-8
1651_20171002_@58a	0.00202351	0.00000026	5.70	0.20	3470	2626	30	-10
1651_20171002_@58b	0.00202388	0.00000012	5.89	0.17	3538	2703	32	-9
1651_20171002_@58c	0.00202334	0.00000015	5.62	0.17	3718	2911	34	-8
NRM-AG-1_20171002_@78	0.00202279	0.00000017	5.34	0.18	-4991	-1617	3	-28
NRM-AG-1_20171002_@79	0.00202354	0.00000019	5.72	0.18	-4991	-1547	3	-28
1651_20171002_@58d	0.00202406	0.00000012	5.98	0.17	3737	3094	35	-8
1651_20171002_@61a	0.00202463	0.00000020	6.26	0.19	-226	4175	11	-5
1651_20171002_@61b	0.00202514	0.00000019	6.51	0.18	-119	4229	11	-4
1651_20171002_@61c	0.00202486	0.00000017	6.38	0.18	34	4226	12	-4
1651_20171002_@61d	0.00202494	0.00000022	6.42	0.19	192	4276	14	-4
NRM-AG-1_20171002_@80	0.00202311	0.00000020	5.51	0.18	-4991	-1477	2	-28
NRM-AG-1_20171002_@81	0.00202286	0.00000015	5.38	0.17	-4991	-1407	2	-28
1651_20171002_@61e	0.00202503	0.00000023	6.46	0.19	360	4297	13	-4
1651_20171002_@63a	0.00202401	0.00000016	5.95	0.17	1876	3355	21	-9
1651_20171002_@63b	0.00202482	0.00000019	6.36	0.18	1808	3501	22	-7
1651_20171002_@63c	0.00202427	0.00000017	6.08	0.18	1811	3665	22	-6
1651_20171002_@63d	0.00202388	0.00000022	5.89	0.19	2042	3759	22	-6
NRM-AG-1_20171002_@82	0.00202334	0.00000021	5.62	0.19	-4991	-1337	2	-27
NRM-AG-1_20171002_@83	0.00202258	0.00000013	5.24	0.17	-4991	-1267	2	-28
1651_20171002_@63e	0.00202419	0.00000016	6.04	0.17	2063	3990	24	-4
1651_20171002_@63f	0.00202438	0.00000018	6.14	0.18	2351	4165	26	-3
1651_20171002_@64a	0.00202417	0.00000012	6.03	0.17	2981	4364	33	-2
1651_20171002_@64b	0.00202407	0.00000018	5.98	0.18	2842	4020	29	-5
1651_20171002_@64c	0.00202354	0.00000014	5.72	0.17	3093	3933	30	-7
NRM-AG-1_20171002_@84	0.00202358	0.00000019	5.74	0.18	-4991	-1197	2	-27
NRM-AG-1_20171002_@85	0.00202340	0.00000012	5.65	0.17	-4991	-1127	2	-26
1651_20171002_@64d	0.00202332	0.00000019	5.61	0.18	3351	4082	33	-6
1651_20171002_@66a	0.00202501	0.00000012	6.45	0.17	-1090	4592	8	-3
1651_20171002_@66b	0.00202445	0.00000024	6.17	0.20	-951	4528	8	-4
1651_20171002_@66c	0.00202495	0.00000021	6.42	0.19	-792	4521	8	-4
1651_20171002_@66d	0.00202491	0.00000018	6.40	0.18	-628	4520	8	-4
NRM-AG-1_20171002_@86	0.00202288	0.00000013	5.39	0.17	-4991	-1057	1	-27
NRM-AG-1_20171002_@87	0.00202267	0.00000015	5.29	0.17	-4991	-987	1	-27
1651_20171002_@66e	0.00202503	0.00000015	6.46	0.17	-818	4724	8	-2
1651_20171002_@66f	0.00202475	0.00000017	6.32	0.18	-861	4362	7	-5
1651_20171002_@70a	0.00202531	0.00000012	6.60	0.17	-2027	4852	1	-6
1651_20171002_@70b	0.00202446	0.00000017	6.18	0.18	-1898	4894	1	-5
1651_20171002_@70c	0.00202438	0.00000020	6.14	0.18	-1634	4895	1	-5
NRM-AG-1_20171002_@88	0.00202329	0.00000018	5.60	0.18	-4991	-917	1	-26
NRM-AG-1_20171002_@89	0.00202300	0.00000012	5.45	0.17	-4991	-847	1	-26

1651_20171002_@70d	0.00202448	0.00000020	6.19	0.18	-1607	5051	2	-2
1651_20171002_@70e	0.00202512	0.00000022	6.51	0.19	-1506	5107	3	-1
1651_20171002_@73a	0.00202404	0.00000019	5.97	0.18	122	5414	15	2
1651_20171002_@73b	0.00202466	0.00000013	6.28	0.17	362	5718	16	6
1651_20171002_@73c	0.00202593	0.00000012	6.91	0.17	460	5729	17	6
NRM-AG-1_20171002_@90	0.00202336	0.00000014	5.63	0.17	-4991	-777	1	-26
NRM-AG-1_20171002_@91	0.00202330	0.00000023	5.60	0.19	-4991	-707	0	-26
NRM-AG-1_20171002_@92	0.00202264	0.00000012	5.27	0.17	-4991	-637	0	-26
NRM-AG-1_20171002_@93	0.00202230	0.00000015	5.10	0.17	-4991	-567	1	-26

Table S8.2. Clinopyroxene (1652) and standard (NRM-AG-1 and JV-1) SIMS $\delta^{18}O$ values for Palpana.

Sample ID	18O/16O drift corrected	± absolute	δ18O‰	± ‰	Stage position (µm)		Field ap. (digits)	
					x	y	x	y
NRM-AG-1_20181015_@02	0.00201683	0.00000023	5.46	0.22	-4194	-736	-14	3
NRM-AG-1_20181015_@03	0.00201680	0.00000022	5.44	0.21	-4194	-796	-13	3
NRM-AG-1_20181015_@04	0.00201723	0.00000013	5.65	0.19	-4194	-856	-14	3
JV1_20181005_@1	0.00204796	0.00000014	20.97	0.20	-4222	-3623	-10	-9
1652_20181005_@12a	0.00201651	0.00000022	5.29	0.21	-1083	-4418	3	-16
1652_20181005_@12b	0.00201797	0.00000018	6.02	0.20	-1289	-4500	3	-17
1652_20181005_@18a	0.00201726	0.00000029	5.67	0.23	-929	-3817	2	-12
1652_20181005_@18b	0.00201714	0.00000016	5.61	0.20	-881	-3971	3	-13
1652_20181005_@26a	0.00201720	0.00000015	5.64	0.20	14	-2933	2	-5
NRM-AG-1_20181015_@05	0.00201729	0.00000021	5.68	0.21	-4194	-916	-12	4
NRM-AG-1_20181015_@06	0.00201665	0.00000019	5.36	0.20	-4194	-976	-12	4
JV1_20181005_@2	0.00204871	0.00000023	21.34	0.22	-4222	-3683	-10	-8
1652_20181005_@26b	0.00201690	0.00000018	5.49	0.20	-94	-3134	2	-8
1652_20181005_@25a	0.00201777	0.00000014	5.92	0.19	-827	-2668	4	-4
1652_20181005_@25b	0.00201759	0.00000021	5.83	0.21	-904	-2605	1	-4
1652_20181005_@25c	0.00201700	0.00000016	5.54	0.20	-946	-2540	0	-5
1652_20181005_@33a	0.00201727	0.00000013	5.67	0.19	-1754	-1028	-2	2
NRM-AG-1_20181015_@07	0.00201727	0.00000020	5.67	0.21	-4194	-1036	-9	3
NRM-AG-1_20181015_@08	0.00201696	0.00000018	5.52	0.20	-4194	-1096	-13	3
JV1_20181005_@3	0.00204748	0.00000016	20.73	0.20	-4222	-3743	-9	-8
1652_20181005_@33b	0.00201820	0.00000016	6.13	0.20	-1801	-1155	-2	1
1652_20181005_@34a	0.00201717	0.00000017	5.62	0.20	-688	-1335	0	2
1652_20181005_@34b	0.00201674	0.00000021	5.41	0.21	-653	-1524	0	1
1652_20181005_@42a	0.00201757	0.00000018	5.82	0.20	-962	85	0	7
1652_20181005_@42b	0.00201719	0.00000019	5.63	0.21	-1048	-9	-1	6
NRM-AG-1_20181015_@09	0.00201667	0.00000025	5.38	0.22	-4194	-1156	-12	2
NRM-AG-1_20181015_@10	0.00201635	0.00000026	5.21	0.22	-4194	-1216	-12	2
JV1_20181005_@4	0.00204712	0.00000021	20.55	0.21	-4222	-3803	-9	-9
1652_20181005_@42c	0.00201771	0.00000017	5.89	0.20	-1140	-89	-1	7
1652_20181005_@51a	0.00201728	0.00000019	5.68	0.21	-1167	911	0	11
1652_20181005_@51b	0.00201717	0.00000014	5.62	0.19	-1205	860	0	11
1652_20181005_@58a	0.00201688	0.00000025	5.48	0.22	-987	1840	2	15
1652_20181005_@58b	0.00201674	0.00000014	5.41	0.19	-1019	1761	2	15
NRM-AG-1_20181015_@12	0.00201618	0.00000019	5.13	0.21	-4194	-1336	-13	2
JV1_20181005_@5	0.00204779	0.00000017	20.89	0.20	-4222	-3863	-9	-8
1652_20181005_@58c	0.00201755	0.00000019	5.81	0.20	-1052	1681	2	15
1652_20181005_@65a	0.00201753	0.00000013	5.80	0.19	-1004	3097	9	19
1652_20181005_@65b	0.00201765	0.00000018	5.86	0.20	-1066	3078	9	17
1652_20181005_@65c	0.00201824	0.00000013	6.16	0.19	-1126	3056	8	17
1652_20181005_@52a	0.00201659	0.00000026	5.33	0.22	98	1726	4	13
NRM-AG-1_20181015_@13	0.00201651	0.00000021	5.29	0.21	-4307	-650	-12	4

NRM-AG-1_20181015_@14	0.00201723	0.00000014	5.65	0.19	-4307	-710	-13	4
JV1_20181005_@6	0.00204714	0.00000021	20.56	0.21	-4222	-3923	-10	-9
1652_20181005_@52b	0.00201759	0.00000024	5.83	0.22	14	1641	1	12
1652_20181005_@43a	0.00201725	0.00000021	5.66	0.21	87	210	0	5
1652_20181005_@43b	0.00201712	0.00000019	5.60	0.20	-38	86	-2	4
1652_20181005_@44a	0.00201666	0.00000014	5.37	0.19	922	-186	6	4
1652_20181005_@44b	0.00201738	0.00000016	5.73	0.20	873	-262	4	4
NRM-AG-1_20181015_@15	0.00201657	0.00000020	5.32	0.21	-4307	-770	-14	3
NRM-AG-1_20181015_@16	0.00201653	0.00000017	5.30	0.20	-4307	-1010	-12	3
JV1_20181005_@7	0.00204778	0.00000022	20.88	0.22	-4222	-3983	-10	-10
1652_20181005_@35a	0.00201660	0.00000015	5.34	0.20	353	-1131	0	3
1652_20181005_@35b	0.00201690	0.00000020	5.49	0.21	242	-1106	-1	3
1652_20181005_@27a	0.00201670	0.00000014	5.39	0.19	847	-1921	2	1
1652_20181005_@27b	0.00201685	0.00000021	5.46	0.21	787	-1921	0	0
1652_20181005_@27c	0.00201609	0.00000026	5.09	0.22	727	-1921	-1	0
NRM-AG-1_20181015_@17	0.00201631	0.00000025	5.19	0.22	-4307	-1070	-15	0
NRM-AG-1_20181015_@18	0.00201637	0.00000016	5.22	0.20	-4307	-1130	-19	0
JV1_20181005_@8	0.00204743	0.00000024	20.71	0.22	-4222	-4043	-11	-10
1652_20181005_@27d	0.00201737	0.00000016	5.72	0.20	607	-1921	-3	-2
1652_20181005_@28a	0.00201632	0.00000016	5.20	0.20	1882	-2234	0	-3
1652_20181005_@28b	0.00201565	0.00000014	4.86	0.19	1835	-2283	0	-3
NRM-AG-1_20181015_@18-2	0.00201746	0.00000024	5.77	0.22	-4266	-990	-7	-4
NRM-AG-1_20181015_@18-3	0.00201741	0.00000018	5.74	0.20	-4266	-1050	-8	-2
NRM-AG-1_20181015_@18-4	0.00201673	0.00000019	5.40	0.20	-4266	-1110	-8	-6
NRM-AG-1_20181015_@18-5	0.00201717	0.00000021	5.62	0.21	-4266	-1170	-8	-4
1652_20181005_@28c	0.00201662	0.00000015	5.35	0.20	1744	-2304	10	-9
1652_20181005_@28d	0.00201711	0.00000019	5.59	0.21	1690	-2367	9	-8
NRM-AG-1_20181015_@19	0.00201633	0.00000015	5.20	0.20	-4266	-1230	-7	-5
NRM-AG-1_20181015_@20	0.00201719	0.00000025	5.63	0.22	-4266	-1290	-8	-6
JV1_20181005_@9	0.00204772	0.00000016	20.85	0.20	-4180	-3629	-5	-17
1652_20181005_@28e	0.00201729	0.00000015	5.68	0.20	1622	-2428	8	-10
1652_20181005_@28f	0.00201715	0.00000013	5.61	0.19	1571	-2485	8	-10
1652_20181005_@28g	0.00201756	0.00000016	5.82	0.20	1436	-2613	9	-11
1652_20181005_@28h	0.00201751	0.00000013	5.79	0.19	1383	-2670	8	-12
1652_20181005_@36	0.00201710	0.00000023	5.59	0.22	1450	-1584	9	-6
NRM-AG-1_20181015_@21	0.00201687	0.00000017	5.47	0.20	-4266	-1350	-8	-5
NRM-AG-1_20181015_@22	0.00201712	0.00000020	5.60	0.21	-4266	-1410	-7	-7
JV1_20181005_@10	0.00204813	0.00000014	21.06	0.20	-4180	-3689	-3	-15
1652_20181005_@29a	0.00201662	0.00000018	5.35	0.20	2748	-2545	12	-9
1652_20181005_@29b	0.00201666	0.00000017	5.37	0.20	2704	-2635	12	-8
1652_20181005_@20a	0.00201698	0.00000013	5.53	0.19	2661	-3403	13	-11
1652_20181005_@20b	0.00201665	0.00000018	5.36	0.20	2587	-3421	13	-12
1652_20181005_@20c	0.00201605	0.00000013	5.07	0.19	2537	-3474	12	-14
NRM-AG-1_20181015_@23	0.00201680	0.00000017	5.44	0.20	-4266	-1470	-5	-6
NRM-AG-1_20181015_@24	0.00201684	0.00000013	5.46	0.19	-4266	-1530	-7	-7
JV1_20181005_@11	0.00204770	0.00000020	20.84	0.21	-4176	-3782	-3	-17
1652_20181005_@14a	0.00201660	0.00000017	5.34	0.20	1477	-4750	16	-22

1652_20181005_@14b	0.00201657	0.00000017	5.32	0.20	1480	-4815	17	-23
1652_20181005_@14c	0.00201628	0.00000014	5.18	0.20	1437	-4870	17	-23
1652_20181005_@14d	0.00201665	0.00000014	5.36	0.20	1437	-4930	18	-24
1652_20181005_@14e	0.00201696	0.00000021	5.52	0.21	1437	-4990	18	-24
NRM-AG-1_20181015_@25	0.00201693	0.00000024	5.50	0.22	-4389	-751	-6	-5
NRM-AG-1_20181015_@26	0.00201640	0.00000015	5.24	0.20	-4389	-811	-7	-6
JV1_20181005_@12	0.00204826	0.00000015	21.12	0.20	-4290	-3804	-3	-16
1652_20181005_@14f	0.00201632	0.00000022	5.20	0.21	1437	-5050	19	-24
1652_20181005_@14g	0.00201663	0.00000021	5.36	0.21	1437	-5110	20	-24
1652_20181005_@14h	0.00201660	0.00000020	5.34	0.21	1430	-5185	20	-26
1652_20181005_@55a	0.00201483	0.00000018	4.46	0.20	4053	1288	14	4
1652_20181005_@55b	0.00201622	0.00000021	5.15	0.21	4056	1233	13	4
NRM-AG-1_20181015_@27	0.00201706	0.00000013	5.57	0.19	-4389	-931	-7	-6
NRM-AG-1_20181015_@28	0.00201697	0.00000015	5.52	0.20	-4392	-1074	-8	-6
JV1_20181005_@13	0.00204797	0.00000020	20.98	0.21	-4290	-3864	-4	-16
1652_20181005_@55c	0.00201676	0.00000017	5.42	0.20	4056	1173	12	4
1652_20181005_@55d	0.00201626	0.00000020	5.17	0.21	4056	1113	12	3
1652_20181005_@55e	0.00201663	0.00000016	5.35	0.20	4056	1053	13	4
1652_20181005_@55f	0.00201661	0.00000016	5.34	0.20	4056	993	13	4
1652_20181005_@55g	0.00201638	0.00000013	5.23	0.19	4056	933	13	4
NRM-AG-1_20181015_@29	0.00201681	0.00000018	5.44	0.20	-4392	-1134	-8	-6
NRM-AG-1_20181015_@30	0.00201667	0.00000018	5.37	0.20	-4392	-1194	-9	-7
JV1_20181005_@14	0.00204762	0.00000017	20.80	0.20	-4320	-3922	-4	-17
1652_20181005_@55h	0.00201720	0.00000014	5.64	0.19	4056	873	12	3
1652_20181005_@55i	0.00201607	0.00000020	5.07	0.21	4056	813	12	3
1652_20181005_@54a	0.00201719	0.00000013	5.63	0.19	2967	722	14	1
1652_20181005_@54b	0.00201779	0.00000024	5.93	0.22	2967	662	13	2
1652_20181005_@54c	0.00201766	0.00000013	5.87	0.19	2967	602	14	1
NRM-AG-1_20181015_@31	0.00201763	0.00000020	5.85	0.21	-4392	-1254	-8	-7
NRM-AG-1_20181015_@32	0.00201707	0.00000020	5.57	0.21	-4392	-1374	-8	-7
JV1_20181005_@15	0.00204737	0.00000013	20.68	0.20	-4353	-3732	-8	-17
1652_20181005_@54d	0.00201682	0.00000017	5.45	0.20	2967	542	12	0
1652_20181005_@54e	0.00201613	0.00000013	5.11	0.19	2947	443	13	1
1652_20181005_@45a	0.00201705	0.00000015	5.57	0.20	2128	-335	12	-2
1652_20181005_@45b	0.00201704	0.00000013	5.56	0.19	2060	-359	11	-2
1652_20181005_@60a	0.00201718	0.00000013	5.63	0.19	2440	1822	14	5
1652_20181005_@60b	0.00201624	0.00000013	5.16	0.19	2351	1724	15	6
NRM-AG-1_20181015_@34	0.00201661	0.00000021	5.35	0.21	-4469	-681	-6	-4
NRM-AG-1_20181015_@35	0.00201689	0.00000019	5.48	0.21	-4469	-741	-6	-4
JV1_20181005_@16	0.00204771	0.00000014	20.85	0.20	-5522	-4200	-7	-15
1652_20181005_@80a	0.00201662	0.00000013	5.35	0.19	-602	4684	17	12
1652_20181005_@80b	0.00201730	0.00000030	5.69	0.23	-658	4670	16	12
1652_20181005_@80c	0.00201787	0.00000019	5.97	0.20	-723	4660	16	11
NRM-AG-1_20181015_@36	0.00201641	0.00000022	5.24	0.21	-4469	-801	-7	-4
NRM-AG-1_20181015_@37	0.00201700	0.00000020	5.54	0.21	-4476	-619	-8	-5
JV1_20181005_@17	0.00204816	0.00000014	21.07	0.20	-5522	-4260	-7	-16
1652_20181005_@80d	0.00201719	0.00000020	5.63	0.21	-791	4644	16	9

1652_20181005_@80e	0.00201709	0.00000013	5.58	0.19	-857	4630	17	10
1652_20181005_@80f	0.00201649	0.00000020	5.28	0.21	-925	4606	17	9
1652_20181005_@80g	0.00201789	0.00000013	5.98	0.19	-1094	4581	18	8
1652_20181005_@80h	0.00201796	0.00000015	6.02	0.20	-1067	4660	17	8
NRM-AG-1_20181015_@38	0.00201669	0.00000013	5.38	0.19	-4469	-861	-7	-4
NRM-AG-1_20181015_@39	0.00201691	0.00000019	5.49	0.20	-4469	-921	-7	-4
JV1_20181005_@18	0.00204810	0.00000021	21.04	0.21	-5522	-4320	-8	-14
1652_20181005_@79a	0.00201722	0.00000013	5.65	0.19	-1146	5085	16	10
1652_20181005_@79b	0.00201704	0.00000013	5.56	0.19	-1203	5071	15	9
1652_20181005_@79c	0.00201731	0.00000013	5.69	0.19	-1263	5071	15	9
1652_20181005_@79d	0.00201772	0.00000013	5.90	0.19	-1386	5054	15	7
1652_20181005_@79e	0.00201729	0.00000016	5.68	0.20	-1464	5044	15	7
NRM-AG-1_20181015_@40	0.00201645	0.00000013	5.26	0.19	-4469	-981	-7	-7
NRM-AG-1_20181015_@41	0.00201628	0.00000013	5.18	0.19	-4469	-1041	-8	-6
JV1_20181005_@19	0.00204885	0.00000018	21.42	0.21	-5522	-4380	-8	-16
1652_20181005_@79f	0.00201715	0.00000020	5.61	0.21	-1539	5015	17	5
1652_20181005_@79g	0.00201791	0.00000020	5.99	0.21	-1627	4990	17	5
1652_20181005_@79h	0.00201791	0.00000022	5.99	0.21	-1689	4971	17	5
1652_20181005_@79i	0.00201778	0.00000020	5.93	0.21	-1775	4942	17	3
1652_20181005_@79j	0.00201777	0.00000015	5.92	0.20	-1824	4893	18	3
NRM-AG-1_20181015_@42	0.00201718	0.00000013	5.63	0.19	-4469	-1101	-7	-5
NRM-AG-1_20181015_@43	0.00201687	0.00000024	5.47	0.22	-4469	-1161	-7	-5
JV1_20181005_@20	0.00204775	0.00000018	20.87	0.21	-5522	-4440	-7	-15
1652_20181005_@79k	0.00201826	0.00000013	6.17	0.19	-1777	4831	19	3
1652_20181005_@81a	0.00201668	0.00000013	5.38	0.19	-854	4412	17	8
1652_20181005_@81b	0.00201761	0.00000016	5.84	0.20	-929	4339	18	8
1652_20181005_@76a	0.00201714	0.00000018	5.61	0.20	1326	4059	16	11
1652_20181005_@76b	0.00201744	0.00000023	5.76	0.22	1237	4045	17	12
NRM-AG-1_20181015_@44	0.00201629	0.00000013	5.18	0.19	-4474	-1259	-8	-7
NRM-AG-1_20181015_@45	0.00201671	0.00000013	5.39	0.19	-4474	-1379	-8	-8
JV1_20181005_@21	0.00204791	0.00000016	20.95	0.20	-5522	-4500	-10	-18
1652_20181005_@76c	0.00201660	0.00000016	5.34	0.20	1151	4046	14	9
1652_20181005_@67a	0.00201717	0.00000019	5.62	0.21	1676	3114	14	9
1652_20181005_@67b	0.00201737	0.00000015	5.72	0.20	1615	3076	13	8
1652_20181005_@67c	0.00201614	0.00000015	5.11	0.20	1562	3042	12	7
1652_20181005_@61a	0.00201702	0.00000015	5.55	0.20	2608	2001	13	6
NRM-AG-1_20181015_@46	0.00201666	0.00000021	5.37	0.21	-4474	-1439	-8	-7
NRM-AG-1_20181015_@47	0.00201651	0.00000021	5.29	0.21	-4474	-1499	-7	-7
JV1_20181005_@22	0.00204794	0.00000014	20.96	0.20	-5522	-4560	-7	-15
1652_20181005_@61b	0.00201665	0.00000030	5.36	0.23	2555	1920	13	7
1652_20181005_@61c	0.00201691	0.00000015	5.49	0.20	2487	1777	13	6
1652_20181005_@46a	0.00201682	0.00000019	5.45	0.20	3200	1	13	0
1652_20181005_@46b	0.00201677	0.00000021	5.42	0.21	3166	-52	12	0
1652_20181005_@46c	0.00201572	0.00000017	4.90	0.20	3143	-109	12	0
NRM-AG-1_20181015_@48	0.00201731	0.00000021	5.69	0.21	-4474	-1559	-6	-5
NRM-AG-1_20181015_@49	0.00201736	0.00000022	5.72	0.21	-4530	-616	-8	-6
JV1_20181005_@23	0.00204831	0.00000019	21.15	0.21	-5609	-4194	-9	-15

1652_20181005_@46d	0.00201659	0.00000018	5.33	0.20	3394	-115	9	-1
1652_20181005_@46e	0.00201684	0.00000016	5.46	0.20	3364	-177	9	-2
1652_20181005_@46f	0.00201666	0.00000022	5.37	0.21	3340	-252	8	-2
1652_20181005_@47a	0.00201577	0.00000015	4.92	0.20	4492	-1128	10	-3
1652_20181005_@47b	0.00201593	0.00000022	5.00	0.21	4439	-1147	10	-2
NRM-AG-1_20181015_@50	0.00201680	0.00000022	5.44	0.21	-4534	-676	-10	-6
NRM-AG-1_20181015_@51	0.00201616	0.00000020	5.12	0.21	-4534	-796	-10	-6
JV1_20181005_@24	0.00204741	0.00000014	20.70	0.20	-5609	-4254	-11	-16
1652_20181005_@47c	0.00201518	0.00000021	4.63	0.21	4576	-1109	14	-2
1652_20181005_@47d	0.00201588	0.00000015	4.98	0.20	4517	-720	10	-2
1652_20181005_@47e	0.00201638	0.00000013	5.23	0.19	4517	-780	10	-2
1652_20181005_@47f	0.00201632	0.00000014	5.20	0.20	4517	-840	11	-1
1652_20181005_@48a	0.00201535	0.00000013	4.71	0.19	5787	-332	11	3
NRM-AG-1_20181015_@52	0.00201670	0.00000013	5.39	0.19	-4551	-926	-9	-4
NRM-AG-1_20181015_@53	0.00201656	0.00000018	5.32	0.20	-4551	-986	-9	-4
JV1_20181005_@25	0.00204800	0.00000017	20.99	0.20	-5609	-4314	-11	-16
1652_20181005_@48b	0.00201583	0.00000027	4.96	0.23	5787	-392	10	2
1652_20181005_@48c	0.00201602	0.00000021	5.05	0.21	5748	-482	10	2
1652_20181005_@48d	0.00201573	0.00000016	4.91	0.20	5498	-142	10	2
1652_20181005_@48e	0.00201694	0.00000017	5.51	0.20	5475	-196	10	1
1652_20181005_@48f	0.00201700	0.00000018	5.54	0.20	5450	-243	10	1
NRM-AG-1_20181015_@54	0.00201740	0.00000016	5.74	0.20	-4560	-1192	-10	-5
NRM-AG-1_20181015_@55	0.00201618	0.00000018	5.13	0.20	-4560	-1252	-10	-6
JV1_20181005_@26	0.00204803	0.00000016	21.01	0.20	-5609	-4374	-12	-16
1652_20181005_@40a	0.00201599	0.00000021	5.04	0.21	5521	-1569	12	-3
1652_20181005_@40b	0.00201658	0.00000015	5.33	0.20	5479	-1614	10	-3
1652_20181005_@22a	0.00201702	0.00000013	5.55	0.19	4344	-3751	14	-12
1652_20181005_@22b	0.00201712	0.00000020	5.60	0.21	4133	-3972	16	-14
1652_20181005_@16a	0.00201782	0.00000021	5.95	0.21	3815	-4539	19	-16
NRM-AG-1_20181015_@56	0.00201684	0.00000014	5.46	0.19	-4683	-578	-8	-4
NRM-AG-1_20181015_@57	0.00201618	0.00000019	5.13	0.20	-4683	-638	-9	-4
JV1_20181005_@27	0.00204769	0.00000015	20.84	0.20	-5609	-4554	-9	-16
1652_20181005_@16b	0.00201661	0.00000018	5.35	0.20	3788	-4614	18	-18
1652_20181005_@16c	0.00201711	0.00000017	5.59	0.20	3728	-4550	17	-19
1652_20181005_@16d	0.00201664	0.00000020	5.36	0.21	3439	-4728	17	-20
1652_20181005_@16e	0.00201615	0.00000013	5.11	0.19	3381	-4767	17	-20
1652_20181005_@16f	0.00201691	0.00000013	5.49	0.19	3452	-4642	17	-18
NRM-AG-1_20181015_@58	0.00201732	0.00000018	5.70	0.20	-4683	-698	-10	-5
NRM-AG-1_20181015_@59	0.00201745	0.00000015	5.76	0.20	-4683	-758	-10	-5
JV1_20181005_@28	0.00204812	0.00000031	21.05	0.24	-5609	-4614	-12	-17
1652_20181005_@15a	0.00201693	0.00000020	5.50	0.21	2674	-4922	17	-23
1652_20181005_@15b	0.00201645	0.00000015	5.27	0.20	2618	-4992	17	-22
1652_20181005_@15c	0.00201678	0.00000018	5.43	0.20	2587	-4899	17	-22
1652_20181005_@82a	0.00201749	0.00000015	5.78	0.20	1986	4946	19	17
1652_20181005_@82b	0.00201684	0.00000018	5.46	0.20	1985	4868	18	15
NRM-AG-1_20181015_@60	0.00201714	0.00000013	5.61	0.19	-4683	-818	-9	-3
NRM-AG-1_20181015_@61	0.00201718	0.00000013	5.63	0.19	-4683	-878	-10	-5

JV1_20181005_@29	0.00204874	0.00000014	21.36	0.20	-5609	-4674	-12	-16
1652_20181005_@82c	0.00201726	0.00000013	5.67	0.19	1985	4808	17	14
1652_20181005_@82d	0.00201697	0.00000015	5.53	0.20	1596	4955	17	15
1652_20181005_@82e	0.00201734	0.00000018	5.71	0.20	1596	4895	17	15
1652_20181005_@82f	0.00201593	0.00000014	5.00	0.19	1596	4835	17	15
1652_20181005_@83a	0.00201691	0.00000019	5.49	0.21	3060	4930	22	16
NRM-AG-1_20181015_@62	0.00201632	0.00000013	5.20	0.19	-4683	-938	-10	-4
NRM-AG-1_20181015_@63	0.00201692	0.00000017	5.50	0.20	-4683	-998	-11	-5
JV1_20181005_@30	0.00204786	0.00000016	20.92	0.20	-5609	-4734	-12	-17
1652_20181005_@83b	0.00201702	0.00000016	5.55	0.20	3060	4870	21	14
1652_20181005_@83c	0.00201657	0.00000022	5.32	0.21	3060	4810	20	13
1652_20181005_@78a	0.00201636	0.00000013	5.22	0.19	3881	4575	22	12
1652_20181005_@78b	0.00201672	0.00000018	5.40	0.20	3881	4515	22	12
1652_20181005_@78c	0.00201626	0.00000019	5.17	0.20	3881	4455	21	11
NRM-AG-1_20181015_@64	0.00201704	0.00000013	5.56	0.19	-4683	-1058	-10	-4
NRM-AG-1_20181015_@65	0.00201655	0.00000013	5.31	0.19	-4683	-1118	-10	-6
JV1_20181005_@31	0.00204771	0.00000019	20.85	0.21	-5737	-4470	-14	-17
1652_20181005_@59a	0.00201660	0.00000013	5.34	0.19	1813	2238	8	7
1652_20181005_@59b	0.00201670	0.00000020	5.39	0.21	1751	2187	8	7
1652_20181005_@59c	0.00201680	0.00000022	5.44	0.21	1691	2127	8	7
1652_20181005_@59d	0.00201806	0.00000017	6.07	0.20	1758	2342	8	8
1652_20181005_@59e	0.00201643	0.00000031	5.26	0.24	1702	2296	7	6
NRM-AG-1_20181015_@66	0.00201646	0.00000015	5.27	0.20	-4683	-1178	-12	-6
NRM-AG-1_20181015_@67	0.00201719	0.00000023	5.63	0.22	-4684	-1264	-11	-5
JV1_20181005_@32	0.00204830	0.00000025	21.14	0.22	-5763	-4554	-13	-13
1652_20181005_@59f	0.00201658	0.00000016	5.33	0.20	1643	2249	8	8
1652_20181005_@59g	0.00201758	0.00000020	5.83	0.21	1083	2254	10	8
1652_20181005_@59h	0.00201685	0.00000013	5.46	0.19	1034	2205	10	8
1652_20181005_@59i	0.00201682	0.00000017	5.45	0.20	987	2159	7	4
1652_20181005_@59j	0.00201744	0.00000017	5.76	0.20	1086	2143	8	5
NRM-AG-1_20181015_@68	0.00201689	0.00000013	5.48	0.19	-4684	-1444	-12	-8
NRM-AG-1_20181015_@69	0.00201681	0.00000013	5.44	0.19	-4684	-1504	-12	-9
NRM-AG-1_20181015_@70	0.00201677	0.00000027	5.42	0.23	-4684	-1684	-11	-9
NRM-AG-1_20181015_@71	0.00201712	0.00000013	5.60	0.19	-4684	-1744	-12	-10

Supplementary references

Aitcheson, S.J., Forrest, A.H., 1994. Quantification of crustal contamination in open magmatic systems. Journal of Petrology, 35(2):461-488. https://doi.org/10.1093/petrology/35.2.461.

Chang, Y-H., 2007. O-Isotopes as tracer for assimilation processes in different magmatic regimes (El Misti, S. Peru and Tapaaca, N. Chile). Dissertation, Diploma Thesis, Georg-August-Universität Göttingen, Germany.

Damm K.-W., Pichowiak S., Harmon R. S., Todt W., Omarini R., Niemeyer H., 1990. Pre-Mesozoic Evolution of the Central Andes; The basement revisited. in Kay, S.M., Rapela, C. W., eds., Plutonism from Antarctica to Alaska. Geological Society of America Special Paper 241:101-126.

Davidson, J.P., McMillan, N.J., Moorbath, S., Wörner, G., Harmon, R.S., Lopez-Escobar, L., 1990. The Nevados de Payachata volcanic region (18°S/69°W, N. Chile) II. Evidence for widespread crustal involvement in Andean magmatism. Contributions to Mineralogy and Petrology, 105(4):412-432. https://doi.org/10.1007/BF00286829.

DePaolo, D.J., 1981. Trace element and isotopic effects of combined wallrock assimilation and fractional crystallization. Earth and Planetary Science Letters, 53(2):189-202. https://doi.org/10.1016/0012-821X(81)90153-9.

Deruelle, B., 1982. Sairecabur volcano, a Plio-Quaternary calc-alkaline massif of the Andes of Atacama: Petrology. In Actas III Congreso Geológico Chileno, Concepción, Chile, D20-D40.

Eiler, J.M., Farley, K.A., Valley, J.W., Hauri, E., Craig, H., Hart, S.R., Stolper, E.M., 1997. Oxygen isotope variations in ocean island basalt phenocrysts. Geochimica et Cosmochimica Acta, 61(11):2281-2293. https://doi.org/10.1016/S0016-7037(97)00075-6.

Entenmann, J., 1994. Magmatic evolution of the Nevados de Payachata complex and the petrogenesis of basaltic andesites in the Central Volcanic Zone of northern Chile. Dissertation, Ph.D. Thesis, Johannes Gutenberg-Universität Mainz, Germany.

Feeley, T.C., Davidson, J.P., 1994. Petrology of calc-alkaline lavas at Volcán Ollagüe and the origin of compositional diversity at Central Andean stratovolcanoes. Journal of Petrology 35(5):1295-1340. https://doi.org/10.1093/petrology/35.5.1295.

Feeley, T.C., Sharp, Z.D., 1995. $^{18}O/^{16}O$ isotope geochemistry of silicic lava flows erupted from Volcán Ollagüe, Andean Central Volcanic Zone. Earth and Planetary Science Letters, 133(3-4):239-254. https://doi.org/10.1016/0012-821X(95)00094-S.

Figueroa, O., Déruelle, B., Demaiffe, D., 2009. Genesis of adakite-like lavas of Licancabur volcano (Chile—Bolivia, Central Andes). C. R. Geoscience, 341(4):310-318. https://doi.org/10.1016/j.crte.2008.11.008.

Francis, P.W., Roobol, M.J., Walker, G.P.L., Cobbold, P.R., Coward, M., 1974. The San Pedro and San Pablo volcanoes of northern Chile and their hot avalanche deposits. Geologische Rundschau, 63(1):357-388. https://doi.org/10.1007/BF01820994.

Francis, P.W., Sparks, R.S.J., Hawkesworth, C.J., Thorpe, R.S., Pyle, D.M., Tait, S.R., Mantovani, M.S., McDermott, F., 1989. Petrology and geochemistry of volcanic rocks of the Cerro Galan caldera, northwest Argentina. Geological Magazine, 126(5):515-547. https://doi.org/10.1017/S0016756800022834.

Freymuth, H., Brandmeier, M., Wörner, G., 2015. The origin and crust/mantle mass balance of Central Andean ignimbrite magmatism constrained by oxygen and strontium isotopes and erupted volumes. Contributions to Mineralogy and Petrology, 169(6):58. https://doi.org/10.1007/s00410-015-1152-5.

Godoy, B., 2014. Evolución petrológica de la Cadena Volcánica San Pedro-Linzor (21º30'S-22º10'S), norte de Chile, y su relación con la geodinámica Andina. Dissertation, Ph.D. Thesis, Universidad Católica del Norte, Chile.

Godoy, B., Lazcano, J., Rodríguez, I., Martínez, P., Parada, M.A., le Roux, P., Wilke, H.-G., Polanco, E., 2018. Geological evolution of Paniri volcano, Central Andes, northern Chile. Journal of South American Earth Sciences, 84:184-200. https://doi.org/10.1016/j.jsames.2018.03.013.

Godoy, B., Wörner, G., Le Roux, P., de Silva, S., Parada, M.A., Kojima, S., González-Maurel, O., Morata, D., Polanco, E., Martínez, P., 2017. Sr- and Nd- isotope variations along the Pleistocene San Pedro – Linzor volcanic chain, N. Chile: Tracking the influence of the upper crustal Altiplano-Puna Magma Body. Journal of Volcanology and Geothermal Research, 341:172-186. https://doi.org/10.1016/j.jvolgeores.2017.05.030.

Godoy, B., Wörner, G., Le Roux, P., de Silva, S., Parada, M.Á., Kojima, S., González-Maurel, O., Morata, D., Polanco, E., Martínez, P., 2017. Sr-and Nd-isotope variations along the Pleistocene San Pedro–Linzor volcanic chain, N. Chile: Tracking the influence of the upper crustal Altiplano-Puna Magma Body. Journal of Volcanology and Geothermal Research, 341:172-186. https://doi.org/10.1016/j.jvolgeores.2017.05.030.

Grocke, S.B., de Silva, S.L., Iriarte, R., Lindsay, J.M., Cottrell, E., 2017. Catastrophic caldera-forming (CCF) monotonous silicic magma reservoirs: Geochemical and petrological constraints on heterogeneity, magma dynamics, and eruption dynamics of the 3.49 Ma Tara Supereruption, Guacha II Caldera, SW Bolivia. Journal of Petrology, 58(2):227-260. https://doi.org/10.1093/petrology/egx012.

Harmon, R.S., Barreiro, B.A., Moorbath, S., Hoefs, J., Francis, P.W., Thorpe, R.S., Deruelle, B., McHugh, J., Viglino, J.A., 1984. Regional O-, Sr-, and Pb-isotope relationships in late Cenozoic calc-alkaline lavas of the Andean Cordillera. Journal of the Geological Society, 141(5):803-822. https://doi.org/10.1144/gsjgs.141.5.0803.

Harmon, R.S., Hoefs, J., 1995. Oxygen isotope heterogeneity of the mantle deduced from global ^{18}O systematics of basalts from different geotectonic settings. Contributions to Mineralogy and Petrology, 120(1):95-114. https://doi.org/10.1007/BF00311010.

Harmon, R.S., Thorpe, R.S., Francis, P.W., 1981. Petrogenesis of Andean andesites from combined O–Sr isotope relationships. Nature, 290(5805):396-399. https://doi.org/10.1038/290396a0.

Hofmann, A.W., 1988. Chemical differentiation of the Earth: the relationship between mantle, continental crust, and oceanic crust. Earth and Planetary Science Letters, 90(3):297-314. https://doi.org/10.1016/0012-821X(88)90132-X.

Ito, E., White, W.M., Göpel, C., 1987. The O, Sr, Nd and Pb isotope geochemistry of MORB. Chemical Geology, 62(3-4):157-176. https://doi.org/10.1016/0009-2541(87)90083-0.

Kaiser, J.F., 2014. Understanding Large Resurgent Calderas and Associated Magma Systems: The Pastos Grandes Caldera Complex, Southwest Bolivia. Dissertation, Ph.D. Thesis, Oregon State University, U.S.A.

Kay, S.M., Coira, B., Wörner, G., Kay, R.W., Singer, B.S., 2011. Geochemical, isotopic and single crystal $^{40}Ar/^{39}Ar$ age constraints on the evolution of the Cerro Galan ignimbrites. Bulletin of Volcanology, 73(10):1487-1511. https://doi.org/10.1007/s00445-010-0410-7.

Kay, S.M., Coira, B.L., Caffe, P.J., Chen, C.H., 2010. Regional chemical diversity, crustal and mantle sources and evolution of central Andean Puna plateau ignimbrites. Journal of Volcanology and Geothermal Research, 198(1-2):81-111. https://doi.org/10.1016/j.jvolgeores.2010.08.013.

Lister, J., 2019. Petrogenesis of lavas from Volcano Azufre, Northern Chile: evidence for crustal input. Dissertation, M.Sc. Thesis, University of Cape Town, South Africa.

Longstaffe, F.J., Clark, A.H., McNutt, R.H., Zentilli, M., 1983. Oxygen isotopic compositions of Central Andean plutonic and volcanic rocks, latitudes 26–29 south. Earth and Planetary Science Letters, 64(1):9-18. https://doi.org/10.1016/0012-821X(83)90048-1.

Lucassen, F., Becchio, R., Harmon, R., Kasemann, S., Franz, G., Trumbull, R., Wilke, H.G., Romer, R.L., Dulski, P., 2001. Composition and density model of the continental crust at an active continental margin—the Central Andes between 21° and 27°S. Tectonophysics, 341(1-4):195-223. https://doi.org/10.1016/S0040-1951(01)00188-3.

Mamani, M., Tassara, A., Wörner, G., 2008. Composition and structural control of crustal domains in the Central Andes. Geochemistry, Geophysics, Geosystems, 9(3):Q03006. https://doi.org/10.1029/2007GC001925.

Mamani, M., Wörner, G., Sempere, T., 2010. Geochemical variations in igneous rocks of the Central Andean orocline (13°S to 18°S): tracking crustal thickening and magma generation through time and space. Geological Society of America Bulletin, 122(1-2):162-182. https://doi.org/10.1130/B26538.1.

Matthews, S.J., Jones, A.P., Gardeweg, M.C., 1994. Lascar volcano, northern Chile: evidence for Steady-state disequilibrium. Journal of Petrology, 35(2):401-432. https://doi.org/10.1093/petrology/35.2.401.

Mattioli, M., Renzulli, A., Menna, M., Holm, P.M., 2006. Rapid ascent and contamination of magmas through the thick crust of the CVZ (Andes, Ollagüe region): Evidence from a nearly aphyric high-K andesite with skeletal olivines. Journal of Volcanology and Geothermal Research, 158(1-2):87-105. https://doi.org/10.1016/j.jvolgeores.2006.04.019.

Rogers, G., Hawkesworth, C.J., 1989. A geochemical traverse across the North Chilean Andes: evidence for crust generation from the mantle wedge. Earth and Planetary Science Letters, 91(3-4):271-285. https://doi.org/10.1016/0012-821X(89)90003-4.

Rollinson, H.R., 1993. Using Geochemical Data: Evaluation, Presentation, Interpretation. Longman Scientific and Technical (352 pp.).

Taussi, M., Godoy, B., Piscaglia, F., Morata, D., Agostini, S., le Roux, P., González-Maurel, O., Gallmeyer, G., Menzies, A., Renzulli, A., 2019. The upper crustal magma plumbing system of the Pleistocene Apacheta-Aguilucho Volcanic Complex area (Altiplano-Puna, northern Chile) as inferred from the erupted lavas and their enclaves. Journal of Volcanology and Geothermal Research, 373:179-198. https://doi.org/10.1016/j.jvolgeores.2019.01.021.

Trumbull, R.B., Wittenbrink, R., Hahne, K., Emmermann, R., Büsch, W., Gerstenberger, H., Siebel, W., 1999. Evidence for Late Miocene to Recent contamination of arc andesites by crustal melts in the Chilean Andes (25–26 S) and its geodynamic implications. Journal of South American Earth Sciences, 12(2):135-155. https://doi.org/10.1016/S0895-9811(99)00011-5.

van Alderwerelt, B.M.E.D., 2017. Diverse monogenetic volcanism across the main arc of the Central Andes, northern Chile. Dissertation, Ph.D. Thesis. The University of Iowa (Iowa), USA.

Walker, B.A., 2011. The geochemical evolution of the Aucanquilcha Volcanic Cluster: prolonged magmatism and its crustal consequences. Dissertation, Ph.D. Thesis. Oregon State University (Oregon), USA.

Wörner, G., Moorbath, S., Horn, S., Entenmann, J., Harmon, R. S., Davidson, J. P., Lopez-Escobar, L., 1994. Large- and fine-scale geochemical variations along the Andean arc of northern Chile (17.5°– 22°S). In Reutter KJ., Scheuber E., Wigger P.J. (Eds.) Tectonics of the Southern Central Andes. Springer, Berlin, Heidelberg. 77-92. https://doi.org/10.1007/978-3-642-77353-2_5.